

**WIRELESS POWER TRANSFER FOR WEARABLE AND
IMPLANTABLE MEDICAL DEVICES**

by
Binh Duc Truong

A dissertation submitted to the faculty of
The University of Utah
in partial fulfillment of the requirements for the degree of

Doctor of Philosophy

Department of Mechanical Engineering
The University of Utah

May 2021

Copyright © Binh Duc Truong 2021

All Rights Reserved

The University of Utah Graduate School

STATEMENT OF DISSERTATION APPROVAL

The dissertation of Binh Duc Truong
has been approved by the following supervisory committee members:

<u>Shadrach J. Roundy</u> ,	Chair(s)	<u>1/28/2021</u> Date Approved
<u>Stephen A. Mascaro</u> ,	Member	<u>12/14/2020</u> Date Approved
<u>Kam K. Leang</u> ,	Member	<u>12/14/2020</u> Date Approved
<u>Cynthia M. Furse</u> ,	Member	<u>12/14/2020</u> Date Approved
<u>Darrin J. Young</u> ,	Member	<u>12/14/2020</u> Date Approved

by Bruce Gale , Chair/Dean of
the Department/College/School of Mechanical Engineering
and by David B. Kieda , Dean of The Graduate School.

ABSTRACT

Biomedical implantable devices for health monitoring and therapeutic treatment have become more and more ubiquitous in human modern life. However, batteries can only power the implant for a certain amount of time and usually require surgical intervention for replacement. On the contrary, wireless power transfer (WPT) technology can provide a continuous and stable supply of power, making it an excellent alternative solution for powering bioelectronics. Methods for WPT include acoustic, capacitive coupling, and magnetic waves. This work will explore the utilization of magnetic waves for WPT to biomedical implants. Along with delivering sufficient power to maintain the system operation, the safety standards, which constraints the maximum allowable magnetic field strength that can be applied to the human body, are essential factors for consideration.

One of the most important objectives of the dissertation is to comprehend the fundamental dynamics, performance and limitations on transmitted power of different magnetic to electric energy conversion mechanisms. Throughout the study, theoretical modeling and power optimization are thoroughly investigated and validated with rigorous experiments. Although motivated by bioapplications, the developed models could also be used as a framework for further research in the field of wireless power transfer in general.

The first structure of interest is two-coil resonant inductive coupling (RIC) wireless power transfer system (WPTS), which is perhaps the most widely used technique in the literature. Under some circumstances, the influence of the parasitic capacitance of the coil on the dynamics cannot be neglected. The system now exhibits both resonance and antiresonance frequencies. This characteristic leads to different optimal choices of drive frequency in the weak coupling regime, depending on the electrical load.

Since the operating frequency of RIC devices is typically in the range of MHz, the allowable field could be as low as a few tens of μT , which significantly limits the power available for transfer. We then consider a magneto-mechano-electric (MME) architecture consisting of a piezoelectric transducer with a magnet tip mass as a receiver. Based on the

transverse vibration resulting from the interaction between the applied field and magnets, this configuration usually operates at a frequency below 1 kHz. In this case, the maximum permissible magnetic flux density may be up to several mT, making the method attractive. However, its disadvantages include weak coupling of the magnetic and mechanical domains, which leads to extremely low transmission efficiency ($< 10^{-2} \%$), and the employment of magnets could pose difficulties for miniaturization.

In order to compromise between the frequency of operation (with the aim to increase the permitted magnetic field amplitude) and the coupling strength, we propose to utilize a magnetoelectric composite consisting of magnetostrictive and piezoelectric phases as a receiver. For the first time, the potential of this mechanism in a WPTS is comprehensively analyzed. The performance of a ME-based WPTS is also evaluated taking into account several practical uncertainties such as alignment, orientation, and the effects of the field non-uniformity. A receiver prototype is constructed with Galfenol and PZT for experimental investigations. A maximum transferred-power of 4.91 mW is achieved at a distance of 30 mm between the centers of a circular coil transmitter and the ME receiver with the corresponding magnetic flux density of $225.8 \mu\text{T}$. This amount of power represents a sufficient supply for most biosensors.

For my wife and children,
"The best is yet to be" (Robert Browning).

CONTENTS

ABSTRACT	iii
LIST OF TABLES	viii
ACKNOWLEDGEMENTS	ix
CHAPTERS	
1. INTRODUCTION	1
1.1 Wireless Power Transfer Concepts and Operating Principles: With a Focus on Biomedical Applications	1
1.2 Research Objectives	6
1.3 Dissertation Outline	9
1.4 References	10
2. RESONANT INDUCTIVE COUPLED WIRELESS POWER TRANSFER SYSTEMS	12
2.1 Analysis of Resonance and Antiresonance Frequencies in a Wireless Power Transfer System: Analytical Model and Experiments	12
3. LOW-FREQUENCY ELECTROMECHANICAL- & ELECTRODYNAMIC-BASED WIRELESS POWER TRANSFER SYSTEMS	18
3.1 Experimentally Validated Model and Analytical Investigations on Power Optimization for Piezoelectric-Based Wireless Power Transfer Systems	18
3.2 Wireless Power Transfer System With Center-Clamped Magneto-Mechano- Electric (MME) Receiver: Model Validation and Efficiency Investigation	33
4. WIRELESS POWER TRANSFER WITH MAGNETOELECTRIC TRANSDUCERS	48
4.1 Experimentally Validated Model and Power Optimization of a Magnetolectric Wireless Power Transfer System in Free-Free Configuration	48
4.2 Magnetolectric Wireless Power Transfer for Biomedical Implants: Effects of Nonuniform Magnetic Field, Alignment and Orientation	64
5. GEOMETRY OPTIMIZATION FOR MAGNETOELECTRIC WIRELESS POWER TRANSFER SYSTEM	75
5.1 Introduction	75
5.2 A Summary of the Equivalent Circuit Model	76
5.3 Formulation of the Geometry Optimization Problem	77
5.4 Results and Discussions	83
5.5 Future Work	87

5.6	Conclusions	91
5.7	References	92
6.	APPROACHES TO SELF-BIASED MAGNETOELECTRIC TRANSDUCERS ..	94
6.1	Introduction	94
6.2	Self-Biased Magnetoelectric Composites	95
6.3	Proposals	100
6.4	References	102
7.	CONCLUSIONS	104

LIST OF TABLES

2.1	Coil parameters. Notation: f_0 - resonant frequency, f_1 - antiresonant frequency, superscript: T - transmitter, R - receiver.	15
3.1	Model parameters.	22
3.2	Model parameters, including material properties of (i) bimorph PZT-5A4E cantilever beam with brass substructure and (ii) neodymium magnets.	39
3.3	Corresponding definitions of the mechanical impedance, the electrical time scale and the stiffness difference of four transducer types used in formulas (3.21) and (3.22).	42
3.4	Model parameters (cont'd).	42
4.1	Material properties and device geometries.	56
4.2	Comparison of several WPT systems with different transferring mechanisms.	62
4.3	Coil parameters, material properties and magnetoelectric transducer geometries.	69
5.1	Material properties	77
5.2	Optimization results. Notations: Std. - Standard, Cstr. - Constraint, Gal - Galfenol, Met - Metglas. Constraints: (i) $Lw(t_p + 2t_m) \leq V_0$, and (ii) $(t_p + 2t_m) \geq 100 \mu\text{m}$	87
6.1	A summary of self-biased ME techniques. Notation: Met = Metglas, A-Met = Annealed Metglas and FCNSB = FeCuNbSiB.	101

ACKNOWLEDGEMENTS

First and foremost, I would like to express my deepest gratitude to my supervisor, Professor Shadrach Roundy, who not only served as my dissertation advisor, but who truly cares about me in many ways. Thank you for opening a new chapter in my life and career, for the valuable advice, support, and enthusiastic guidance, and for providing me the necessary freedom for my independent research. Above all, I have learned a lot from the culture you bring to the lab.

I wish to acknowledge the financial support from the National Science Foundation through the Center for Advanced Self-Powered Systems of Integrated Sensors and Technologies (ASSIST). I want to thank my committee members for spending their valuable time to evaluate this dissertation, and the staff of the Department of Mechanical Engineering, University of Utah, for their diligent administrative assistance.

I especially appreciate Professors Susan Trolier-McKinstry, Mehdi Kiani, and Berardi Sensale-Rodriguez for their valuable insights and comments, even beyond this dissertation.

I would like to extend my sincere gratitude to all the members of the ISS Lab. Tiancheng, Rob, Erik, and Hamid, you all have made my Ph.D. journey a lot more colorful and meaningful than just being a panda-nerd for 3 years. The wind blows away, but memories still stay.

I would love to deeply thank Becky and the Andersens for your kindness, your warm heart and spirit, and for making us feel at home in a strange land; it is my pleasure to get to know you all. I would also like to thank my friends in the University Village and many soccer mates across the U of U. In particular, Nghia-Trang, I appreciate all the fake parties (i.e., no alcohol, less meat, and much more vegetable) we have shared through the years.

I want to thank my parents and younger sister, who love me unconditionally and are always beside me no matter what life is. I am forever grateful. This dissertation belongs to them as much as it does to me.

For my wife, who has spent her whole youth and given up so many possible ships of life just to be with me (to the end of time): "After all, I am forever in your debt." This dissertation would not exist without her. Finally, for Albert: nothing is ever the same since you came into my life. You have messed it up quite a bit, but with you, I am living my dream.

CHAPTER 1

INTRODUCTION

This first chapter provides an overview of various wireless power transfer technologies that are under research with an emphasis on potential applications to biomedical wearable and implantable devices. It is then followed by the dissertation motivation and research objectives and dissertation outline.

1.1 Wireless Power Transfer Concepts and Operating Principles: With a Focus on Biomedical Applications

The Internet of Things (IoT) for healthcare has received worldwide research efforts related to a number of biomedical applications such as health monitoring, remote therapy, and chronic and acute disease treatment. Healthcare activities based on wireless sensor networks provide secure transmission and reception of medical signals both for early diagnosis and for real-time observation of health status. Surveys of this pervasive trend and its platform architecture can be found in [1]. The evolution is partly driven by the considerable developments of micro- and nanotechnologies for bioelectronic devices. A vision for bioelectronic medicines is one of miniaturized devices that can be mounted on the skin or implanted inside the human body to allow an interaction between medicine and technology, which is referred to as wearable-implantable medical devices (W-IMDs) [2]. The central role of the W-IMDs is to detect biological parameters and/or then to apply therapy solutions, thereby enhancing better treatments and diagnostics for increasing life quality.

An early well-known implant is a cardiac pacemaker. The cardiac implant is installed in the heart through a surgery to manage irregular rhythm, for instance tachycardia (too fast) or bradycardia (too slow) [3]. Figure 1.1 (a) shows an example of an IMD. The device is embedded in a blood vessel for monitoring multiple disease biomarkers in vivo [4]. Figure 1.1 (b) depicts a platform for multifunctional electronics conformally attached

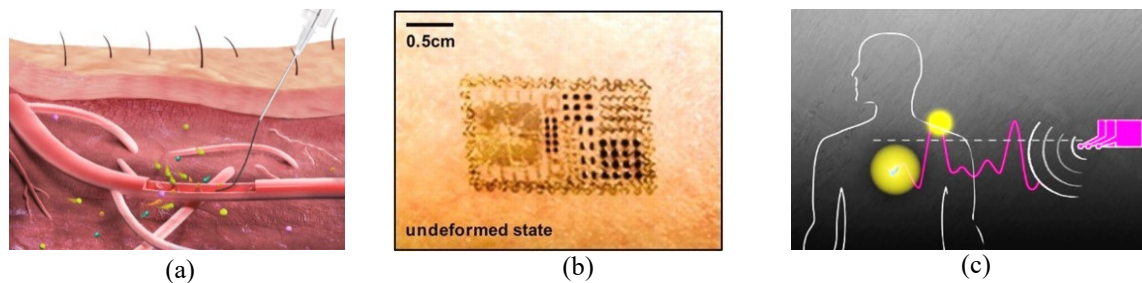


Figure 1.1. Examples of IMDs. (a) Functionalized helical fibre bundles of carbon nanotubes as electrochemical sensors (black cable device) [4], (b) multifunctional epidermal electronic system on skin [6], and (c) an illustration of WPT for W-IMDs [MIT News, 2018].

to the skin through van der Waals forces alone. A retinal implant for the bidirectional cordial brain-computer-interfacing providing sensory feedback is helpful for those suffering from paralysis [5]. Other W-IMDs can be found in several applications such as cochlear-, cortical-, spinal-implants and epidermal sensors on rough skin surfaces [6]. In the last decades, we have seen the extraordinary growth of W-IMD applications to attain better functionality and proper packaging for biological implantation. However, almost all W-IMDs have been so far powered by batteries that often occupy the majority of space in a worn/implanted system, posing a challenge for miniature integration as the devices get smaller. Limited-lifetime batteries have to be replaced or recharged regularly, which can be cumbersome and unsafe. In order to increase the operation longevity of an implanted system and eliminate the use of battery, WPT has become one of the most attractive technologies. It offers greater long-term sustainability, flexibility, reliability, and safety. WPT enables biomedical wearables and implantables by wave transmission through the air and/or multilayer tissue media (i.e., skin, fat, and muscle) as shown in Figure 1.1 (c).

WPT applications are categorized into the near-field and far-field techniques, depending on the frequency and application distance between the transmitter and the receiver. The far-field range has a typical distance beyond ~ 10 m, using propagating electromagnetic waves to transfer energy as radios transmit signals. The technique has limitations including the fact that the efficiency is rather low because the transmission is omnidirectional, which results in low power received by the wearables or implantables. The radiation of the high power radio frequency (RF) transmission can be potentially harmful to human

body, which is commonly limited in use by regulations [7]. Thus, the far-field technique is less attractive for the W-IMDs.

In near-field transmission, three well-established methods are (nonresonant) inductive coupling (IC), resonant inductive coupling (RIC, also known as strongly coupled magnetic resonance), and electrodynamic (ED) coupling. Figure 1.2 depicts the key concept of an inductive-based WPTS. A transmitter coil driven by an electric power source generates a time-varying electromagnetic field traveling through space, or some other medium, across a receiver coil where the electromagnetic energy is extracted and then supplied to an electrical load. IC WPT is only efficient over a very short range of a few millimeters (less than a wavelength), which is unsuitable for biomedical applications due to the large absorption rate in the human body [8]. RIC is a form of IC. However, in RIC the power is transferred between two transmitting and receiving resonators, in which each resonator consists of a coil connected to a capacitor. The two resonators are tuned to the same resonance frequency, which significantly enhances the power transfer. The magnetic induction between the transmitter and receiver is modeled by a mutual inductance M , which depends on the two coil geometries and their separation distance. A widely used dimensionless figure of merit is the coupling coefficient defined by $k = M/\sqrt{L_1L_2}$, which represents the fraction of magnetic flux density generated by L_1 that passes through L_2 when L_2 is in open circuit condition.

For ED systems, magnetic energy is transmitted from a transmitting coil to various types of receivers, where an electromechanical or electromagnetic resonator is used. The

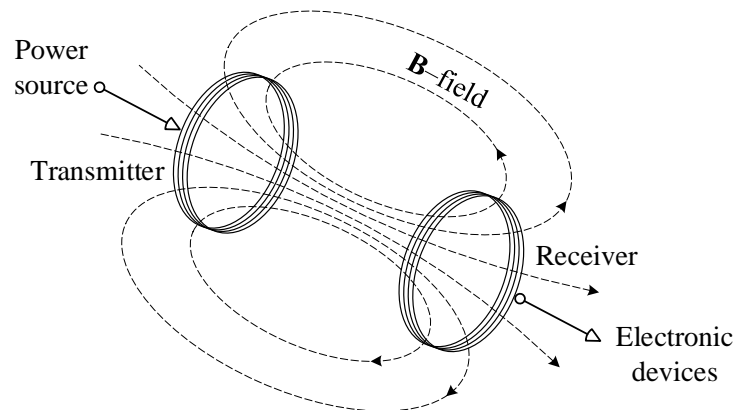


Figure 1.2. Inductive-based wireless power transfer concept.

device concept and model of an ED-based WPT system with the use of an electromagnetic transducer as a receiver is illustrated in Figure 1.3. The mechanical part of the electromagnetic generator is characterized by a linear mass-spring-damper system. A permanent magnet M_a is placed at the end of the spring, which is usually implemented as a cantilever beam. The magnetization direction is marked by a white arrow. When an external magnetic flux density (\mathbf{B} -field) is applied, the interactions between the magnet and the \mathbf{B} -field, or the magnetic flux gradient, cause a moment and/or a force acting on the resonator, depending on the relative orientation between the magnet magnetization and the applied field. Different transduction mechanisms could be used to convert the resulting mechanical oscillations to electrical power. In a common implementation, a pickup coil is mounted to the frame near the oscillating magnet. The relative displacement $x(t)$ between the magnet and coil results in a time-varying magnetic flux in the coil inducing an electrical potential, which then generates a current flowing to the load R_L . The coupling between the mechanical and electrical domain is typically modeled as a linear (two-port) transducer. In another common implementation, a piezoelectric transducer forms a part of the oscillating structure, as depicted in Figure 1.4. The stress in the piezoelectric material creates an electric field across the material which drives a current through a load R_L . When a piezoelectric transducer and a magnet tip mass are utilized as a receiver, the structure is also referred to as the magneto-mechano-electric (MME) mechanism in the literature.

A less well established near-field method for WPT utilizes a magnetolectric (ME) transducer as a receiver. The concept of a ME effect was first introduced by Röntgen in 1888 with his discovery that a dielectric material could be magnetized under a magnetic field

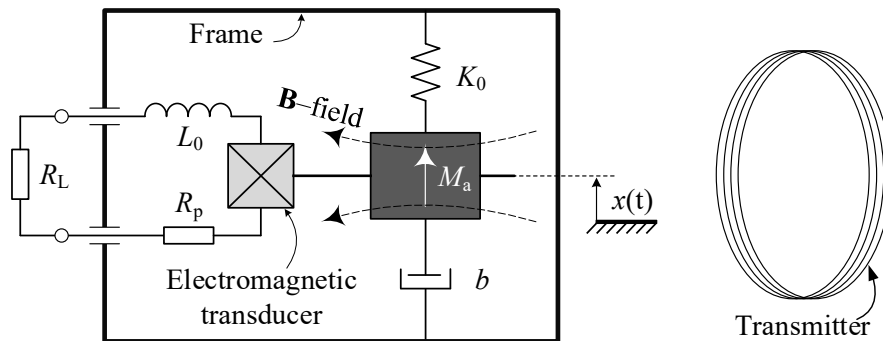


Figure 1.3. An example of the electrodynamic-based wireless power transfer concept, in which an electromagnetic transducer is used as a receiver.

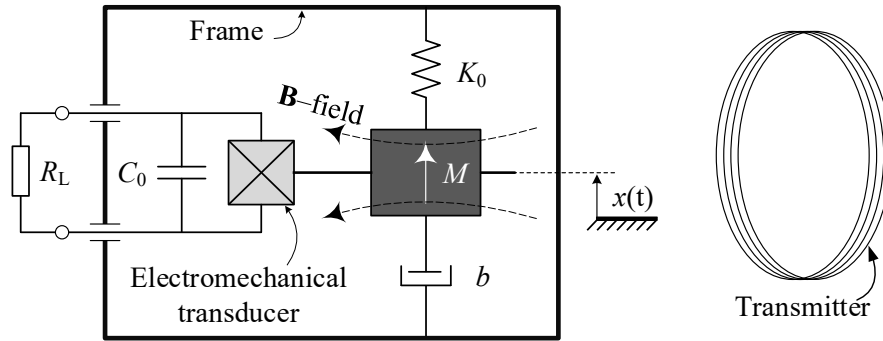


Figure 1.4. An example of the electrodynamic-based wireless power transfer concept, in which an electromechanical transducer is used as a receiver.

[9]. Since then, advances in ME multiferroic materials have triggered significant research interest [10]. The recent development of a ME antenna indicated that for a given frequency its wavelength could be five orders of magnitude shorter than the electromagnetic wavelength, leading to possibly dramatic miniaturization [11]. Furthermore, the typical operating frequency of ME systems is relatively low, in the range of tens/hundreds of kHz, which enables higher permissible applied \mathbf{B} -field than that of RIC WPTS [12]. These characteristics make a ME generator a promising alternative to other WPT technologies, especially for IMDs. The operational principle of a ME WPTS is illustrated in Figure 1.5, in which a ME laminated composite with two constituent materials (magnetostrictive and piezoelectric) serves as a receiver. When an external AC magnetic field is applied along the longitudinal axis of the laminate, a strain is excited in the two magnetostrictive phases, which is transferred to the piezoelectric layer through an interface coupling. As a result, the ME composite vibrates in the length direction, and its kinetic energy is transformed into electricity through the piezoelectric mechanism.

As the range of power transfer is from centimeters up to a few meters, the RIC, ED, and

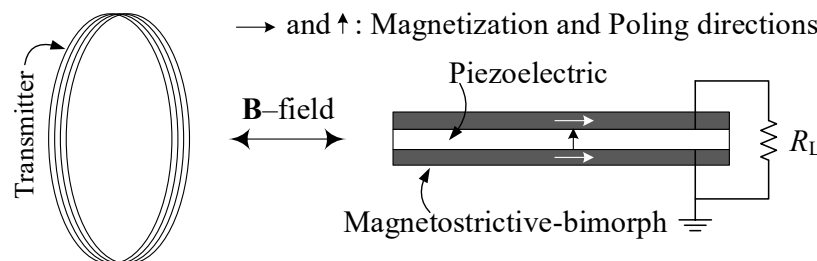


Figure 1.5. A configuration of a magnetoelastic-based wireless power transfer.

ME WPT systems are promising methods among the available solutions for the W-IMDs. Other, nonmagnetic means of WPT for biomedical implants exist but have significant drawbacks. For example, compared to capacitive coupling systems, a key advantage of RIC WPT is the ability to use the same link for simultaneously transferring power and data, while the other needs additional links for data communication [13]. Meanwhile, ultrasonic WPT requires that the transmitter have good contact to the skin, which is usually not very practical [14, 15]. A key advantage of ED and ME mechanisms is that they allow the size of the miniature wearables and implantables to be much less than a wavelength. Furthermore, ED and ME resonators typically operate at much lower frequency in the ranges of Hertz (Hz) or kilohertz (kHz). This allows the use of higher magnetic field while still remaining within safe limits for human exposure [16]. Due to these competitive advantages, the RIC, ED, and ME WPT systems are chosen as the main topics for research direction in this work.

1.2 Research Objectives

The central objective of the dissertation is to develop an analytical framework for each structure under investigation with an emphasis on optimizing the actual power delivered to an electrical load in addition to the transmission efficiency. For a given power available from a source, optimizing the efficiency may not result in maximum transferred power. Taking a two-coil series-series WPTS as an example, the optimal link efficiency is obtained at the primary resonance frequency; however, the power maxima are reached at two different frequencies nearby the secondary resonance frequencies [17]. This different point of view could shed new light on our understanding of the dynamics and performance of each system and get one step closer to realizing an optimal design. The research outcomes are also expected to stimulate future development and scientific innovation within the wireless transfer technology that provides an efficient, reliable and safe solution to power bioelectronics.

The RIC structure has been extensively studied in the literature. In a two-coil WPTS, depending on how the capacitors are connected to the coils, there are four basic compensation topologies, which are series-series (S-S), series-parallel (S-P), parallel-parallel (P-P), and parallel-series (P-S). Typically, the parasitic capacitances of the transmitter and

receiver coils are small and can be neglected. However, this assumption may not be valid for some systems. In an experimental S-S topology, we observe that the parasitic capacitance could be in the same range as the external capacitance. The fundamental dynamics and performance of the S-S system under this circumstance have not been reported and therefore are of interest to study.

Instead of inducing voltage on a receiver as two resonant inductively coupled coils do, Challa *et al.* proposed a near-field WPT system using an electromagnetic transducer to convert the kinetic energy from the oscillating magnet tip mass to electrical form [18]. The authors focused on analyzing the power transfer efficiency, which may not be a key parameter of many low-power systems such as biomedical implants. Furthermore, the transduction factor between the mechanical and electrical domains was not fully modeled, and its influence on the mechanical dynamics and maximum output power of the WPT system was not discussed. In related work, other authors reported several experimental observations indicating the potential application of piezoelectric devices with magnetic proof masses for harvesting power from \mathbf{B} -field around current-carrying conductors or ambient low-frequency magnetic fields [19, 20, 21]. However, the entire model for these designs has not been addressed in a systematic and complete manner.

A significant modeling effort which captures the performance of ME transducers was undertaken by Dong *et al.*, in which the ME effect was described by an equivalent circuit model [22, 23]. However, many essential errors have been found in their model, and the authors were only concerned with the open-circuit voltage for a sensing system. The actual power transferred to a load at a given external \mathbf{B} -field, which is of great interest for a WPTS, was not discussed. Figures of merit and the fundamental performance limits of the ME-based architecture are also of great interest to consider. A standard criterion to evaluate the ME effect is the ME coefficient (α_{ME}) defined by the rate of change of the electric field in terms of the applied magnetic field. Most studies in the literature so far have indicated a significant advantage in obtaining α_{ME} as high as possible [24]. While this argument may be true for magnetic field sensing applications, it is still questionable and needs to be clarified for a WPTS.

In order to fill the knowledge gaps presented above, this work accomplishes the following:

1. Thoroughly analyzing the essential effects of the parasitic capacitance of the coil on the behavior of a two-coil WPTS. In some practical circumstances, the parasitic capacitance is on the same range as the series-compensated capacitance and cannot be neglected. The considered system now exhibits both resonance and antiresonance frequencies. This property could offer more choices to optimize the output power at weak-coupling and also causes significant changes in system dynamics at high-coupling. Experiments are conducted to justify the established model.

Near-field RIC is currently the dominant method for WPT for biomedical implants. Objective 1 analyzes key aspects of inductive coupled WPT systems. The material presented here serves both as a theoretical basis for later comparisons to other types of WPT systems and provides novel insights into inductive-based WPT systems not previously explored.

2. Investigating a low-frequency WPTS utilizing a piezoelectric transducer with magnet tip mass as a receiver, which is referred to as magneto-mechano-electric (MME) mechanism. We aim to develop a complete equivalent circuit model, which is more convenient to approximately describe the behavior of distributed physical systems than a distributed-parameter solution without compromising the accuracy. Various aspects of the power optimization problem are discussed, providing a comprehensive view of the system fundamentals and an important premise for further study.
3. Fully evaluating the system efficiency of a MME device, considering both transmitting and receiving sides. Although the efficiency may not be a key metric for low power systems, it is still of interest and worthy of analysis, especially from a practical perspective when a certain amount of power is lost during the transfer process. The effect of the coil resistance on the transmission efficiency, as well as the impact of the transmitter size and the receiver geometry on the transduction factor between the magnetic-mechanical-electrical domains are studied.
4. Proposing an alternative approach for transferring power from a generic power source to an implant embedded inside the human body, utilizing the magnetoelectric effect. To our knowledge, this work is the first effort to thoroughly analyze a WPTS that utilizes a laminated composite ME-transducer as a receiver. A linear two-port

model is derived and experimentally validated, which is then used for analyzing a figure of merit and the fundamental performance limits of the architecture under consideration. Appropriate criteria for evaluating ME device performance are also investigated.

5. Assessing the feasibility of a ME-based WPTS in practice, accounting for the influence of the uncertainties of the receiver position, and the non-uniformity of the external magnetic field generated by a circular transmitter coil. These investigations are expected to provide additional insight into the operation of the ME WPTS in realistic scenarios, and partially answer the question on how to optimize the transmitter design to maximize the delivered power at a given distance between the transmitter and receiver. The key findings are validated by various sets of experiments.
6. Formulating an optimization problem to find the best set of geometric parameters of the ME laminated composite that yields the highest output power, primarily subject to total volume constraint (up to a few mm^3) and safety standards. Possible manufacturing limitations (such as minimum thin-film thickness) could be considered. Due to the high complexity of the problem and multiple local-optimal solutions may exist, a numerical global-optimization algorithm is utilized.
7. Seeking an appropriate method to eliminate the need for an external DC field bias. Although the ME generator has been proven to be an excellent candidate as a receiver for a WPTS, many magnetostrictive materials require a biased magnetic field for operation, which is a critical challenge in the miniaturization of biomedical devices. This study, along with the numerical analysis in 6, are essential for future work of the project.

1.3 Dissertation Outline

In Chapter 1, the thesis starts by introducing the concepts of different WPT technologies, the general motivation of the project, and the choice of research areas. Chapter 2 presents an analysis of the resonance- and antiresonance frequencies and their effects on the performance of a two-coil RIC WPTS. Chapter 3 focuses on MME WPT systems, in which an equivalent circuit model is developed and validated, the power optimization

principles are investigated, and the transfer efficiency is studied. In the same manner, Chapter 4 discusses a mathematical model of a ME WPTS, its fundamentals, limitations on transmitted power, and its performance in practice. The model presented in Chapter 4 is then extended in Chapter 5 to capture the dependence of the demagnetization effects on the laminate geometry in order to formulate a geometry optimization problem. Chapter 6 shows a possible pathway forward for the project by considering methods to eliminate the need for an external DC bias field. At the end, Chapter 7 represents the conclusion of the entire research.

1.4 References

- [1] S. M. R. Islam, D. Kwak, M. H. Kabir, M. Hossain, and K. Kwak, "The internet of things for health care: A comprehensive survey," *IEEE Access*, vol. 3, pp. 678–708, 2015.
- [2] J. Lueke, and W. A. Moussa, "MEMS-based power generation techniques for implantable biosensing applications," *Sensors*, vol. 11, no. 2, pp. 1433–1460, 2011.
- [3] S. Furman, and J. B. Schwedel, "An intracardiac pacemaker for stokes-adams seizures," *N. Engl. J. Med.*, vol. 261, no. 19, pp. 943–948, 1959, PMID: 13825713.
- [4] L. Wang *et al.*, "Functionalized helical fibre bundles of carbon nanotubes as electrochemical sensors for long-term in vivo monitoring of multiple disease biomarkers," *Nat. Biomed. Eng.*, vol. 4, pp. 159–171, 2019.
- [5] J. D. Weiland, and M. S. Humayun, "Visual prosthesis," *Proc. of the IEEE*, vol. 96, pp. 1076–1084, 2008.
- [6] D. Kim *et al.*, "Epidermal electronics," *Science*, vol. 333, no. 6044, pp. 838–843, 2011.
- [7] W. C. Brown, "The history of power transmission by radio waves," *IEEE Trans. Microw. Theory Techn.*, vol. 32, no. 9, pp. 1230–1242, Sep. 1984.
- [8] A. Kurs, A. Karalis, R. Moffatt, J. D. Joannopoulos, P. Fisher, and M. Soljačić, "Wireless power transfer via strongly coupled magnetic resonances," *Science*, vol. 317, no. 5834, pp. 83–86, 2007.
- [9] W. C. Röntgen, "Ueber die durch bewegung eines im homogenen electrischen felde befindlichen dielectricums hervorgerufene electrodynamische kraft," *Annalen der Physik*, vol. 271, no. 10, pp. 264–270, 1888.
- [10] N. Ortega, A. Kumar, J. F. Scott, and R. S Katiyar, "Multifunctional magnetoelectric materials for device applications," *J. Phys. Condens. Matter*, vol. 27, no. 50, pp. 504002, Nov 2015.
- [11] T. Nan *et al.*, "Acoustically actuated ultra-compact nems magnetoelectric antennas," *Nat. Commun.*, vol. 8, Dec 2017.

- [12] International Commission on Non-Ionizing Radiation Protection., "Guidelines for limiting exposure to time-varying electric, magnetic, and electromagnetic fields (up to 300 ghz).," *Health Physics*, vol. 75, Oct 1998.
- [13] M. Kiani and M. Ghovanloo, "A 13.56-mbps pulse delay modulation based transceiver for simultaneous near-field data and power transmission," *IEEE Trans. Biomed. Circuits Syst.*, vol. 9, no. 1, pp. 1–11, Feb 2015.
- [14] H. Basaeri, D. B. Christensen, and S. Roundy, "A review of acoustic power transfer for bio-medical implants," *Smart Mater. Struct.*, vol. 25, no. 12, pp. 123001, Nov 2016.
- [15] H. Basaeri, Y. Yu, D. Young, and S. Roundy, "A MEMS-scale ultrasonic power receiver for biomedical implants," *IEEE Sens. Lett.*, vol. 3, no. 4, pp. 1–4, April 2019.
- [16] A. Garraud and D. P. Arnold, "Advancements in electrodynamic wireless power transmission," in *2016 IEEE Sensors*, Oct 2016, pp. 1–3.
- [17] B. D. Truong, "Investigation on power optimization principles for series-configured resonant coupled wireless power transfer systems," *Int. J. Electron. Commun.*, vol. 106, pp. 67 – 81, 2019.
- [18] V. R. Challa, J. O. Mur-Miranda, and D. P. Arnold, "Wireless power transmission to an electromechanical receiver using low-frequency magnetic fields," *Smart Mater. Struct.*, vol. 21, no. 11, pp. 115017, 2012.
- [19] I. Paprotny, Q. Xu, W. W. Chan, R. M. White, and P. K. Wright, "Electromechanical energy scavenging from current-carrying conductors," *IEEE Sens. J.*, vol. 13, no. 1, pp. 190–201, Jan 2013.
- [20] G. Liu and S. Dong, "A magneto-mechano-electric coupling equivalent circuit of piezoelectric bimorph/magnets composite cantilever," *J. Appl. Phys.*, vol. 115, no. 8, pp. 084112, 2014.
- [21] J. Han, J. Hu, Z. Wang, S. X. Wang, and J. He, "Enhanced performance of magneto-electric energy harvester based on compound magnetic coupling effect," *J. Appl. Phys.*, vol. 117, no. 14, pp. 144502, 2015.
- [22] S. Dong, J. Li, and D. Viehland, "Longitudinal and transverse magnetoelectric voltage coefficients of magnetostrictive/piezoelectric laminate composite: theory," *IEEE Trans. Ultrason., Ferroelectr., Freq. Control*, vol. 50, no. 10, pp. 1253–1261, Oct 2003.
- [23] S. Dong, J. Li, and D. Viehland, "Longitudinal and transverse magnetoelectric voltage coefficients of magnetostrictive/piezoelectric laminate composite: experiments," *IEEE Trans. Ultrason., Ferroelectr., Freq. Control*, vol. 51, no. 7, pp. 794–799, July 2004.
- [24] C. M. Leung, J. Li, D. Viehland, and X. Zhuang, "A review on applications of magneto-electric composites: from heterostructural uncooled magnetic sensors, energy harvesters to highly efficient power converters," *J. Phys. D*, vol. 51, no. 26, pp. 263002, Jun 2018.

CHAPTER 2

RESONANT INDUCTIVE COUPLED WIRELESS POWER TRANSFER SYSTEMS

This chapter investigates the essential effects of the resonance and antiresonance frequencies on the dynamics and performance of a two-coil resonant inductive wireless power transfer system compensated in series-series.

2.1 Analysis of Resonance and Antiresonance Frequencies in a Wireless Power Transfer System: Analytical Model and Experiments

Most of the work in the literature neglects the parasitic capacitance (in parallel with the inductance) of the coil. However, we observe from experiments that, when such parasitic capacitance is in the same range of the added capacitance, the antiresonance frequency caused by this parasitic capacitance is close to the nominal resonance frequency. In this circumstance, the influence of the parasitic capacitance is considerable and the dynamic behavior of the system is thus of great interest to comprehensively analyze. Based on the two-port network theory, a compact model is developed and the analytical expression of the power delivered to the load is then derived. The mathematical model is validated by rigorous experiments, and therefore can be used for further analysis.

© 2019 IEEE. Reprinted, with permission from B. D. Truong, C. Roundy, E. Andersen, and S. Roundy, "Analysis of Resonance and Anti-Resonance Frequencies in a Wireless Power Transfer System: Analytical Model and Experiments," *IEEE Transactions on Circuits and Systems – II: Express Briefs*, vol. 66, no. 7, in July 2019.

Analysis of Resonance and Anti-Resonance Frequencies in a Wireless Power Transfer System: Analytical Model and Experiments

Binh Duc Truong¹, Caleb Roundy, Erik Andersen, and Shad Roundy

Abstract—This brief presents a magnetic coupling wireless power transfer system configured in a series-series topology and operating at both resonance and anti-resonance frequencies which occur due to the parasitic coil capacitances. It is shown that their effects on system dynamics cannot be ignored. A mathematical model based on circuit theory is developed and the analytical solution for the power transferred to an electrical load is derived. A technique for extracting coil parameters such as resistance, inductance and capacitance from impedance measurements is proposed. The complete model is first experimentally verified and then used for further numerical investigations.

Index Terms—Wireless power transfer, (anti-)resonance frequencies.

I. INTRODUCTION

WIRELESS power transfer systems utilizing magnetically coupled coils has gained more and more research interest due to its wide range of applications such as electric vehicles [1], wireless sensor networks [2], and implantable biomedical devices [3], [4]. Although the WPT concept has been explored at the beginning of the 20th century by Nikola Tesla [5], the recent work by a group at MIT [6] has led to a massive increase in research and commercial activity. In particular, the MIT group proposed an improved inductive power transfer system based on magnetic resonance coupling using a four-coil system which allows a more efficient operation over a farther distance range than similar previous methods [6]. This long distance operation has opened up many applications for charging electronic devices without annoying wires.

Different system architectures with three or four coils were widely reported [6], [7]. However, recently Dong-Wook *et al.* [8] revealed that three/four-coil systems do not necessarily perform better than two-coil type, without denying that the former could offer more degrees of freedom for optimization. In some particular circumstances when the device sizes are strictly constrained (e.g., an artificial

cardiac pacemaker), the simplicity of the two-coil structure is more appropriate. It is therefore the objective of this brief. In a two-coil WPTS, depending on how the capacitors are connected to the coils, there are four basic compensation topologies, which are series-series (SS), series-parallel (SP), parallel-parallel (PP) and parallel-series (PS) [9], [10]. When investigating their operation, the authors neglected the parasitic capacitance of the coil. However, we observe from experiments that for the SS topology the anti-resonant frequency caused by the parasitic capacitance in parallel with the coil inductance is close to the resonant frequency when such a parasitic capacitance is in the same range as the added capacitance. In this case, the impact of parasitic capacitance is considerable and the dynamic behavior of the system is thus of great interest to comprehensively analyze.

Coupled mode theory (CMT) addresses the clear physics of the power transfer process [6], however, most electrical researchers are more familiar with the circuit theory (CT) approach. Here we choose the CT as a means to study the WPTS given the fact that both methods are different but equivalent tools to describe the same phenomenon, meaning that the same conclusions are obtained regardless of approach [11], [12]. An advantage of the CT is to offer an explicit expression of the power delivered to a load, providing an efficient technique to design and optimize the system performance. In this brief, a compact analytical model is presented and validated by experiments, which is the premise for further analysis. Note that, we focus on power optimization issues in low-power systems rather than maximizing transmission efficiency.

II. THEORETICAL MODELING

Figure 1 shows the complete model of the two-coil WPT system configured in series-series topology, in which the parasitic capacitances of both transmitter and receiver coils (i.e., C_{p1} and C_{p2} respectively) are taken into account. The load coil L_2 is connected to a fixed capacitor C_2 and a resistor R_L in series. The load stray capacitance C_{pL} is included for a general model, which is typically neglected in the literature. The drive coil L_1 is excited by a power source V_S with output impedance R_S . A variable capacitor C_1 is utilized for resonance frequency matching. The magnetic interaction between the two coils is modeled as a mutual inductance $M = k\sqrt{L_1L_2}$ where $0 \leq k \leq 1$ is the coupling coefficient. R_1 and R_2 represents the parasitic resistances of L_1 and L_2 correspondingly. In practice, (R_1, L_1, C_{p1}) or (R_2, L_2, C_{p2}) are inseparable. However, in order to reduce the complexity of analytical computation without compromising the generality of the problem,

Manuscript received August 23, 2018; revised October 24, 2018; accepted October 25, 2018. Date of publication October 30, 2018; date of current version June 26, 2019. This work was supported by the National Science Foundation ASSIST Nanosystems ERC under Award EEC-1160483. This brief was recommended by Associate Editor S. C. Wong. (Corresponding author: Binh Duc Truong.)

B. D. Truong, E. Andersen, and S. Roundy were with the Department of Mechanical Engineering, University of Utah, Salt Lake, UT 84112 USA (e-mail: binh.d.truong@utah.edu; shad.roundy@utah.edu).

C. Roundy was with the Department of Bioengineering, University of Utah, Salt Lake, UT 84112 USA.

Color versions of one or more of the figures in this paper are available online at <http://ieeexplore.ieee.org>.

Digital Object Identifier 10.1109/TCSII.2018.2878662

1549-7747 © 2018 IEEE. Personal use is permitted, but republication/redistribution requires IEEE permission. See http://www.ieee.org/publications_standards/publications/rights/index.html for more information.

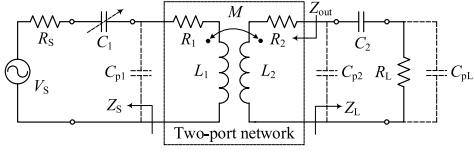


Fig. 1. Complete circuit model of the two-coil WPT system.

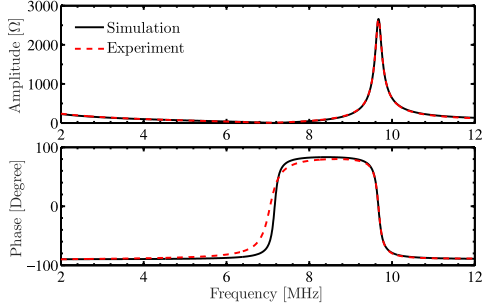


Fig. 2. Impedance amplitude and phase of the transmitter coil.

we conventionally define that the two-port network is formed only by (R_1, L_1) and (R_2, L_2) while the source impedance Z_S now includes both C_1 and C_{p1} , and the load impedance Z_L consists of C_2, C_{p2}, R_L and C_{pL} .

The expressions of these impedances, and the Z-parameters (i.e., the impedance matrix [13]) of the two-port network are

$$Z_{11} = R_1 + j\omega L_1, \quad (1)$$

$$Z_{22} = R_2 + j\omega L_2, \quad (2)$$

$$Z_{12} = Z_{21} = j\omega M, \quad (3)$$

$$Z_S = \left[j\omega C_{p1} + \left(R_S + \frac{1}{j\omega C_1} \right)^{-1} \right]^{-1}, \quad (4)$$

$$Z_L = \left[j\omega C_{p2} + \left(\frac{1}{j\omega C_2} + \left(j\omega C_{pL} + \frac{1}{R_L} \right)^{-1} \right)^{-1} \right]^{-1} \quad (5)$$

where ω is the driving angular frequency.

The power transferred to the load is then derived as follows

$$P_L = \frac{1}{2} |V_{th}|^2 \frac{|Z_{21}|^2 \Re\{Z_L\}}{|(Z_{11} + Z_S)(Z_{out} + Z_L)|^2} \quad (6)$$

$$\text{where } V_{th} = V_S \frac{\frac{1}{j\omega C_{p1}}}{\frac{1}{j\omega C_{p1}} + \frac{1}{j\omega C_1} + R_S} \quad (7)$$

$$\text{and } Z_{out} = Z_{22} - \frac{Z_{12}Z_{21}}{Z_{11} + Z_S}. \quad (8)$$

Here Z_{out} is the output impedance and V_{th} is the Thévenin equivalent voltage in series with Z_S (not shown in the Figure). The proposed mathematical technique can also be generalized and applied to obtain the closed-form of P_L for any similar structure or configuration, in which Z_S, Z_L and V_S are modified accordingly.

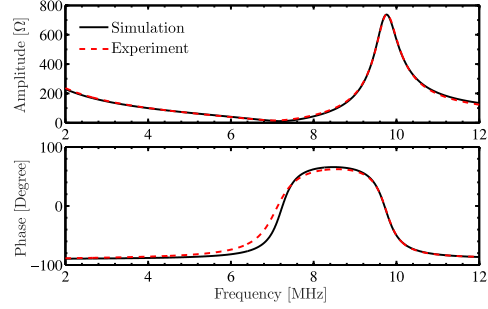


Fig. 3. Impedance amplitude and phase of the receiver coil.

III. EXPERIMENTAL VALIDATION

A. System Parameter Identification

In this section, we propose a numerical optimization scheme for identifying the electrical properties of each coil, which has been already connected to an external capacitor. In order to avoid any possible dynamic interferences between the two coils, we measure their impedances separately without integrating them on the complete experimental setup. Here, we denote R, L, C_p and C for both of transmitter and receiver coils since their models are identical.

The complex impedance of the coil, Z_c , and its amplitude $|Z_c|$ and phase ϕ are expressed as

$$Z_c = \frac{1}{j\omega C} + \frac{1}{\frac{j\omega C_p}{j\omega C_p + j\omega L + R}}, \quad (9)$$

$$|Z_c| = (\Re\{Z_c\}^2 + \Im\{Z_c\}^2)^{1/2}, \quad (10)$$

$$\phi = \tan^{-1} \frac{\Im\{Z_c\}}{\Re\{Z_c\}} \quad (11)$$

$$\text{where } \Re\{Z_c\} = \frac{R}{(\omega^2 L C_p - 1)^2 + (\omega R C_p)^2}, \quad (12)$$

$$\Im\{Z_c\} = -\frac{1}{\omega C} - \frac{\omega(\omega^2 L^2 C_p + R^2 C_p - L)}{(\omega^2 L C_p - 1)^2 + (\omega R C_p)^2}. \quad (13)$$

$|Z_c|$ and ϕ are measured by a network analyzer. It should be noted that the compensation capacitance C_2 is fixed at a chosen value while C_1 is tuned so that both coils have the same resonant frequency (i.e., at which the impedance amplitude is minimum). In contrast, the anti-resonant frequency (i.e., at which the impedance amplitude is maximum) depends on the parasitic capacitance, and therefore, is uncontrollable in such a circumstance.

The parametric identification problem is formulated as follows

$$\min_{R, L, C_p, C} \sum_{i=1}^n ({}^e|Z_c| - {}^s|Z_c|)^2 \quad (14)$$

where n is the number of experimental samples collected, ${}^e|Z_c|$ and ${}^s|Z_c|$ are experimental and simulated data respectively. To solve this nonlinear optimization problem with constraints placed on the value of the variables (i.e., all of them are positive), the nonlinear Interior Point (IP) or Sequential Quadratic

TABLE I
COIL PARAMETERS. NOTATION: f_0 - RESONANT FREQUENCY,
 f_1 - ANTI-RESONANT FREQUENCY, SUPERSCRIPIT:
T - TRANSMITTER, R - RECEIVER

Transmitter		Receiver	
C_1 , pF	334.32	C_2 , pF	333.82
C_{p1} , pF	406.25	C_{p2} , pF	407.08
L_1 , μ H	0.667	L_2 , μ H	0.692
R_1 , Ω	0.62	R_2 , Ω	2.20
f_0^T , MHz	7.037	f_0^R , MHz	7.056
f_1^T , MHz	9.675	f_1^R , MHz	9.762

Programming (SQP) methods are utilized [14]. Due to the fact that the resonance/anti-resonance frequencies are likely to result from various combinations of the inductance and capacitance, we not only consider the coil impedance around the resonance/anti-resonance frequencies but also account for a wide range of frequency. This consideration is expected to provide a unique solution to the two coil parameters. In order to test the accuracy of the method, we first use LT-SPICE simulation as a source of data with known parameters. Hence, these simulations play the role that measurements would do in a real experimental characterization. Comparison of “true” and estimated values shows that the approach can accurately recover the specified model parameters.

Figure 2 and 3 show a good agreement between results based on measured and estimated parameters for both drive and load coils, with a slight difference in phases only. The measurements are conducted from 2 MHz to 12 MHz where the maximum number of samples provided by the network analyzer is $n = 1601$. Note that, while the two coils exhibit the resonant and anti-resonant frequencies close to those of each other, their highest impedance amplitudes are recognizably different even when they are supposed to be identical in design. To be specific, $\max |Z_c| = 2.65 \text{ k}\Omega$ for the transmitter coil and $\max |Z_c| = 738.36 \Omega$ for the receiver coil. This can be explained by the difference between R_1 and R_2 due to errors during soldering and/or the property of two added capacitors (C_2 might have higher series resistance than C_1 does). However, this difference does not influence the general dynamics of the system, despite of the fact that it may slightly reduce the power delivered to the load. In addition, the resonance/anti-resonances of the WPTS can be approximately obtained by setting $\phi = 0$, or in other words $\Im\{Z_c\} = 0$. The two analytical solutions are presented in the Appendix. All the extracted parameters are listed in Table I, which will be used for all following simulations.

B. Measurement Results

Figure 4 depicts the transmit and receive coil setup, where a function generator is utilized as the source power to drive the transmitter coil and the voltage induced in the load V_L is captured by an oscilloscope. For the sinusoidal input signals, the average delivered power is calculated as $P_L = \frac{1}{2} \frac{|V_L|^2}{R_L}$. The output impedance of the source is set as $R_S = 50 \Omega$. The stray capacitance of the load resistor is measured equal to $C_{pL} \approx 15.5 \text{ pF}$, which can be changed from one to another resistor, however, the difference is typically small and negligible. The distance between the two coils is about 10 cm. The coupling factor is determined by fitting the model simulations

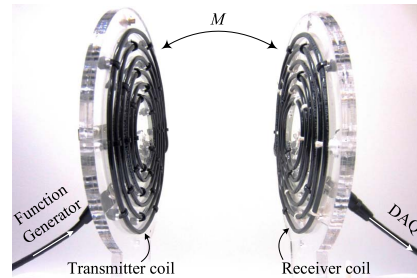


Fig. 4. Experiment setup.

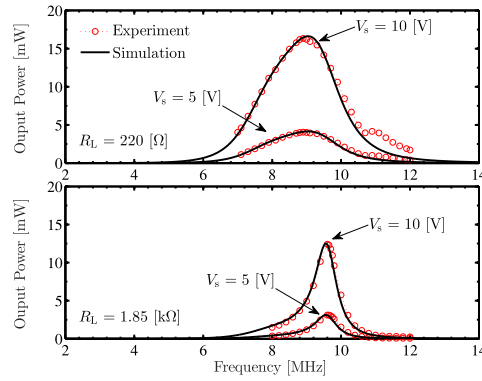


Fig. 5. Frequency responses with two different loads R_L and two source voltage V_S .

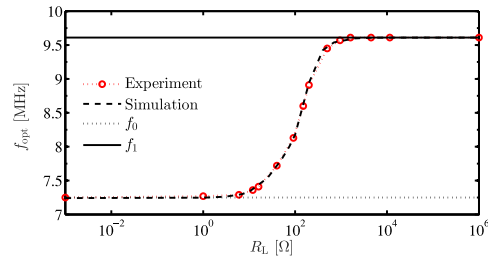


Fig. 6. Optimal frequency f_{opt} with respect to the electrical load R_L .

to the experimental data at $V_S = 5 \text{ V}$ and $R_L = 220 \Omega$, which results in $k = 57.19 \times 10^{-3}$. The squared magnetic coupling factor k^2 is often used to characterize the coupling since it is proportional to the transmission efficiency [15]. The value $k^2 = 2.7 \times 10^{-3}$ is then kept constant while verifying other cases.

Figure 5 shows a good agreement between the model predictions obtained from (6) and the measurement results, with different loads and input voltages. Since the system is operating at high frequencies, we choose to evaluate the steady-state performances with discrete frequencies instead of using frequency-swept signals. We also observe that the output power could drop down to $\sim 80\%$ in comparison with that of steady state due to the effect of sweep rate. As can be seen

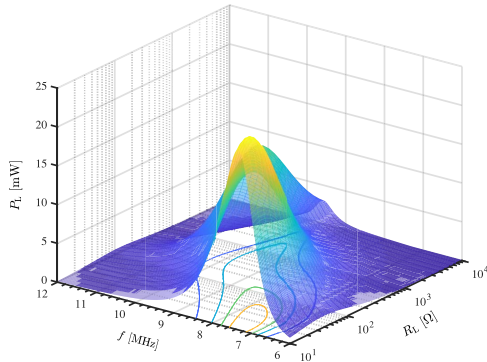


Fig. 7. Simulation results of the output power P_L as a function of the drive frequency f and the load resistance R_L in the weak coupling regime $k^2 = 2.7 \times 10^{-3}$.

in the same Figure, the optimal frequency f_{opt} changes with respect to the electrical load, in particular, $f_{\text{opt}} = 8.9$ MHz for $R_L = 220 \Omega$ and $f_{\text{opt}} = 9.6$ MHz for $R_L = 1.85$ k Ω .

For a further investigation, we vary the resistance and find its corresponding optimal frequency by examining the maximum voltage across the load. The obtained results are presented in Figure 6, showing that $f_{\text{opt}} \in [f_0, f_1]$ and f_{opt} increases with the load resistance. This particular property is present for all series-series WPTS, where the parasitic capacitance cannot be neglected, under the effects of the resonance and anti-resonance frequencies. This is the first time the phenomenon is reported in the field of WPT and it opens more options to optimize the transferred power depending on the loading conditions. Here, $f_0 = 7.25$ MHz and $f_1 = 9.61$ MHz, which are slightly different from $f_0^{T/R}$ and $f_1^{T/R}$ of each single coil reported in Table I.

IV. DISCUSSION

As demonstrated by the previous sections, the complete model based on the circuit theory formalism has captured the main physics of the complex WPTS well. It is, therefore, of great interest to utilize the model (i.e., mainly based on formula (6)) to further analyze other characteristics and to reveal a comprehensive physical insight of the system.

Figure 7 gives a more thorough picture of Figures 5 and 6, showing the variation of the output power as a function of the drive frequency and the load resistance with the same squared coupling factor $k^2 = 2.7 \times 10^{-3}$ and the input source voltage $V_S = 10$ V. The maximum power of 22.87 mW is achieved at $R_L = 12.2 \Omega$ when $f = f_0$. For $f = f_1$, the maximum power is 13.88 mW at $R_L = 605.0 \Omega$ approximately. Defining the transducer efficiency (i.e., transducer power gain) as a ratio of the power delivered to the load P_L to the power available from the source $P_{\text{avs}} = \frac{1}{8} \frac{|V_S|^2}{R_S}$, $\eta = \frac{P_L}{P_{\text{avs}}}$, the maximum efficiency achievable at this coupling coefficient is ~ 9.15 % where $P_{\text{avs}} = 250$ mW. Note, that P_{avs} is not the power actually taken from the source, the maximum power available at a given source voltage and resistance. P_{avs} is independent of the input impedance of the network [13], therefore it is much more convenient to compute the actual transferred power from

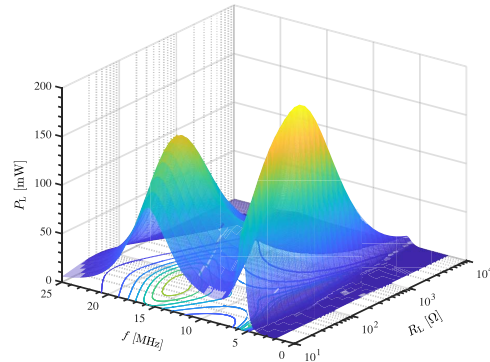


Fig. 8. Simulation results of the output power P_L as a function of the drive frequency f and the load resistance R_L in the strong coupling regime $k^2 = 0.565$.

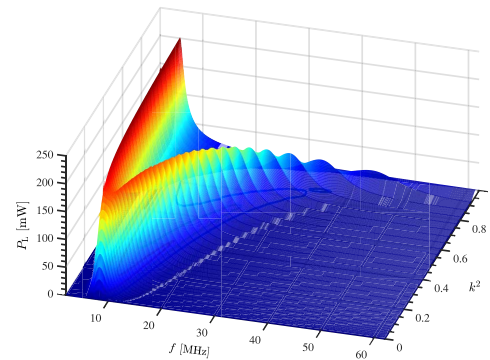


Fig. 9. Simulation results of the output power P_L as a function of the drive frequency f and the coupling factor k^2 .

known P_{avs} and η without determining the power input to the network.

The simulation results in Figure 8 are created using a higher squared coupling factor $k^2 = 0.565$ while keeping the same input voltage $V_S = 10$ V. It is revealed that the optimal frequency for each load is now no longer constrained by the resonant and anti-resonant frequencies. Instead, f_{opt} is dominantly affected by the frequency splitting phenomenon in the strong coupling regime that is well-known for four-coil systems [7]. For instance, the two extreme frequencies of $R_L = 110 \Omega$ are $f_l = 6.21$ MHz and $f_h = 17.51$ MHz which give $P_{L-l} = 199.68$ mW and $P_{L-h} = 132.34$ mW respectively. Although the maximum output power at f_h is ~ 33.72 % lower than that at f_l , the bandwidth around f_h is about ~ 3.15 times larger (i.e., $B_{f_h} = 7.63$ MHz in comparison with $B_{f_l} = 2.42$ MHz) as can be seen in the contour plot of Figure 8. The maximum achieved transducer efficiency at this coupling factor is 79.9 % with P_{L-l} .

The impact of the strong coupling on the system dynamics is depicted in Figure 9 with a fixed load of $R_L = 110 \Omega$ and $V_S = 10$ V. The critical coupling factor at which the frequency splitting phenomena start occurring is $k_{\text{cr}}^2 \approx 0.1$. Unlike what

has been described in [7], among others, the maximum output powers on the two extreme frequency branches are very asymmetric. The power on the high frequency branch drops significantly compared to that on the lower frequency branch as k^2 increases. In order to comprehend the reason behind this behavior, we theoretically compare three models: (i) Complete model presented in Section II, (ii) A model of a typical series-series configuration where the parasitic capacitance in parallel with the coil is eliminated, and (iii) A model only takes the parasitic capacitances into account while added capacitors are removed. The simulation results show that the investigated phenomenon only occurs when the parasitic capacitances are present, corresponding to cases (i) and (iii). For $f = f_1$ and $k_{cr}^2 \leq k^2 \leq 0.6$, the efficiency gradually rises from more than 70 % to 80 % and then remains almost unchanged for higher k^2 . By contrast, in the weak coupling regime, $k^2 \leq k_{cr}^2$, the maximum power to the load decreases dramatically. We found that applying the impedance matching approach to the source/load is a potential solution to overcome this challenge. However, performance of a system with and without impedance matching networks is very different. It is out of scope of this brief and is open for future analysis.

V. CONCLUDING REMARKS

We presented a theoretical study and experimental validation of a WPTS taking into consideration the resonance and anti-resonance frequencies of both the transmitter and receiver. That analysis led to an investigation of the optimal choice of drive frequency in the weak coupling regime, which depends on the electrical load. A closed-form analytical model developed based on the circuit theory was shown to be in good agreement with the measured data. The complete model was utilized as a means to thoroughly analyze the system dynamics. The numerical results showed that the efficiency of the WPTS under consideration could reach a high level without any optimization techniques in the strong coupling regime. While most of authors have considered a fixed load resistance (typically choose $R_L = R_S = 50 \Omega$), we offered another perspective when analyzing the system behavior in more general cases with load, frequency and coupling factor varying. It should be noted that the resonance and anti-resonance operation is completely different from the frequency splitting behavior reported in the literature. The former is dominant at low coupling coefficient and only occurs in presence of coil parasitic capacitances. In contrast, the latter was only observed in the high coupling regime regardless of whether those parasitic capacitances are present or not. Furthermore, in situations where parasitic capacitances are significant, they cause the asymmetric property of the frequency splitting phenomenon. These important findings have not been reported anywhere else.

APPENDIX

ANALYTICAL SOLUTION OF THE RESONANCE AND ANTI-RESONANCE FREQUENCIES

The resonance and anti-resonance are determined by the equation

$$-\frac{1}{\omega C} - \frac{\omega(\omega^2 L^2 C_p + R^2 C_p - L)}{(\omega^2 L C_p - 1)^2 + (\omega R C_p)^2} = 0, \quad (15)$$

which results in

$$f_0 = \frac{1}{2\pi} \left[\frac{C/2 + C_p}{L C_p (C + C_p)} - 2 \left(\frac{R}{L} \right)^2 - \frac{1}{2 L^2 C_p (C + C_p)} \sqrt{\sigma} \right]^{1/2}, \quad (16)$$

$$f_1 = \frac{1}{2\pi} \left[\frac{C/2 + C_p}{L C_p (C + C_p)} - 2 \left(\frac{R}{L} \right)^2 + \frac{1}{2 L^2 C_p (C + C_p)} \sqrt{\sigma} \right]^{1/2} \quad (17)$$

$$\text{where } \sigma = [R^2 C_p (C + C_p) - LC]^2 - 4L(RC_p)^2(C + C_p). \quad (18)$$

For instance, substituting C_1 , C_{p1} , L_1 and R_1 of the transmitter coil in Table I into (16) and (17), we get $f_0 = 7.163$ MHz and $f_1 = 9.666$ MHz. The difference between these analytical solutions and the measured results is less than 1.8%. A similar observation is obtained for the receiver coil.

In the case where the parasitic capacitance is negligibly small $C_p \approx 0$, (15) reduces to $1/(\omega C) + \omega L = 0$. Therefore there only exists the well-known resonance frequency of the series-series configuration $f^* = 1/(2\pi\sqrt{LC})$. The closed-form of f_0 and f_1 is much more complicated than that of f^* due to the presence of C_p .

REFERENCES

- [1] S. Y. Choi, B. W. Gu, S. Y. Jeong, and C. T. Rim, "Advances in wireless power transfer systems for roadway-powered electric vehicles," *IEEE J. Emerg. Sel. Topics Circuits Syst.*, vol. 3, no. 1, pp. 18–36, Mar. 2015.
- [2] L. Xie, Y. Shi, Y. T. Hou, and H. D. Sherali, "Making sensor networks immortal: An energy-renewal approach with wireless power transfer," *IEEE/ACM Trans. Netw.*, vol. 20, no. 6, pp. 1748–1761, Dec. 2012.
- [3] X. Li, Y. Li, C.-Y. Tsui, and W.-H. Ki, "Wireless power transfer system with $\Sigma\Delta$ -modulated transmission power and fast load response for implantable medical devices," *IEEE Trans. Circuits Syst. II, Exp. Briefs*, vol. 64, no. 3, pp. 279–283, Mar. 2017.
- [4] E. Y. Chow *et al.*, "Wireless powering and the study of RF propagation through ocular tissue for development of implantable sensors," *IEEE Trans. Antennas Propag.*, vol. 59, no. 6, pp. 2379–2387, Jun. 2011.
- [5] N. Tesla, "Apparatus for transmitting electrical energy," U.S. Patent 1119732A, May 1907.
- [6] A. Kurs *et al.*, "Wireless power transfer via strongly coupled magnetic resonances," *Science*, vol. 317, no. 5834, pp. 83–86, 2007.
- [7] A. P. Sample, D. T. Meyer, and J. R. Smith, "Analysis, experimental results, and range adaptation of magnetically coupled resonators for wireless power transfer," *IEEE Trans. Ind. Electron.*, vol. 58, no. 2, pp. 544–554, Feb. 2011.
- [8] S. Dong-Wook, L. Jae-Ho, and L. H. Soo, "Study on two-coil and four-coil wireless power transfer systems using Z-parameter approach," *ETRI J.*, vol. 38, no. 3, pp. 568–578, 2016.
- [9] S. Li and C. C. Mi, "Wireless power transfer for electric vehicle applications," *IEEE J. Emerg. Sel. Topics Circuits Syst.*, vol. 3, no. 1, pp. 4–17, Mar. 2015.
- [10] C. M. de Miranda and S. F. Pichorim, "A self-resonant two-coil wireless power transfer system using open bifilar coils," *IEEE Trans. Circuits Syst. II, Exp. Briefs*, vol. 64, no. 6, pp. 615–619, Jun. 2017.
- [11] M. Kiani and M. Ghovanloo, "The circuit theory behind coupled-mode magnetic resonance-based wireless power transmission," *IEEE Trans. Circuits Syst. I, Reg. Papers*, vol. 59, no. 9, pp. 2065–2074, Sep. 2012.
- [12] D. S. Ricketts, M. J. Chabalko, and A. Hillenius, "Experimental demonstration of the equivalence of inductive and strongly coupled magnetic resonance wireless power transfer," *Appl. Phys. Lett.*, vol. 102, no. 5, 2013, Art. no. 053904.
- [13] S. J. Orfanidis, *Electromagnetic Waves and Antennas*, ECE Dept., Rutgers Univ., New Brunswick, NJ, USA, 2016.
- [14] J. Nocedal and S. Wright, *Numerical Optimization* (Springer Series in Operations Research), 2nd ed. New York, NY, USA: Springer, 2006.
- [15] S. Assaworarith, X. Yu, and S. Fan, "Robust wireless power transfer using a nonlinear parity-time-symmetric circuit," *Nature*, vol. 546, pp. 387–390, Jun. 2017.

CHAPTER 3

LOW-FREQUENCY ELECTROMECHANICAL- & ELECTRODYNAMIC-BASED WIRELESS POWER TRANSFER SYSTEMS

In this chapter, the use of the magneto-mechano-electric energy conversion mechanism in wireless power transfer is studied.

3.1 Experimentally Validated Model and Analytical Investigations on Power Optimization for Piezoelectric-Based WPT Systems

Nonradiative wireless power transfer systems such as inductive or capacitive coupling are widely used to power biomedical wearable and implantable devices. However, the operating frequency (usually the resonance frequency) of these technologies is typically in the range of MHz, which constrains the amplitude of the magnetic fields that can be applied to humans due to safety limits. For instance, according to the IEEE standards, a maximum allowable magnetic flux density at 1 kHz is ~ 2 mT, 100 times larger than the ~ 20 μ T permissible at 1 MHz. One approach to overcome this challenge is to use an electromechanical or electrodynamic transducer as a receiver. The mechanical resonance frequency of those generator types can be designed much lower than 1 kHz, thus allowing much higher applied magnetic fields. In this part, a low-frequency wireless power transfer system utilizing a piezoelectric transducer with magnet tip mass as a receiver is investigated. A lumped-parameter model is developed and experimentally validated. A thorough analysis of how to optimize the delivered power is provided.

Reprinted, with permission from B. D. Truong, S. Williams, and S. Roundy, "Experimentally Validated Model and Analytical Investigations on Power Optimization for Piezoelectric-based Wireless Power Transfer Systems," *Journal of Intelligent Material Systems and Structures*, vol. 30, no. 16, 2019.



Experimentally validated model and analytical investigations on power optimization for piezoelectric-based wireless power transfer systems

Binh Duc Truong , Shane Williams and Shad Roundy

Journal of Intelligent Material Systems and Structures
2019, Vol. 30(16) 2464–2477
© The Author(s) 2019
Article reuse guidelines:
sagepub.com/journals-permissions
DOI: 10.1177/1045389X19862383
journals.sagepub.com/home/jim


Abstract

This article presents a near-field low-frequency wireless power transfer system utilizing a piezoelectric transducer with magnet tip mass as a receiver. The interaction moment between the uniform **B** field generated by a Helmholtz coil and the magnet is the means to deliver the electrical energy from the transmitter to an electrical load, which is therefore referred to as magneto-mechano-electric effect. This is the first time a complete equivalent circuit model of such a structure is developed and experimentally verified. Based on the lumped model, various aspects of the power optimization problem are thoroughly discussed, providing a comprehensive view of the system and an important premise for further study.

Keywords

wireless power transfer, magneto-mechano-electric effect, lumped-element model, power optimization, impedance matching

1. Introduction

With the rapid development of technology, the Internet of Things is beginning to shape the future of our modern world in which smart sensing systems require electronics that need not be plugged in or regularly recharged (Zhu et al., 2015; Hassan et al., 2017). Energy harvesting (EH) and wireless power transfer (WPT) hence become promising alternatives to the batteries currently in use (Roundy and Wright, 2004; Beeby et al., 2006; Mitcheson et al., 2008; Erturk et al., 2009; Kurs et al., 2007; Sample et al., 2011; Kiani and Ghovanloo, 2012; Pacini et al., 2017; Song et al., 2017). While the performance of EH systems is strongly dependent on the conditions of the environmental power source (Wei and Jing, 2017), WPT provides deterministic controllable techniques for actively transferring power from an optional source to desired electronic applications (Assaworarith et al., 2017; Paul and Sarma, 2018).

For biomedical applications, the amplitude of the magnetic field that can be applied to humans is constrained by the driving frequency due to safety standards (IEEE C95.1-2005, 2006; IEEE C95.6-2002, 2002). For instance, a maximum permissible field at 1 MHz is $\approx 200 \mu\text{T}$, while that at 1 kHz is $\approx 2\text{mT}$. This

relationship between maximum allowable magnetic field and frequency limits the potential of near-field WPT systems such as capacitive or inductive coupling (Huang et al., 2013; Barman et al., 2015), since the operating frequency of these devices is typically in the range of MHz.

Instead of inducing voltage on a receiver as two resonant inductively coupled coils do, Challa et al. (2012) proposed a near-field WPT system using an electromagnetic transducer to convert the mechanical energy from the oscillating magnet tip mass to electrical energy. The authors focused on analyzing the system efficiency (defined by the ratio of the power delivered to a load and the power input to the network), which may not be a key factor of a low-power system. Meanwhile, the electrodynamic coupling coefficient between the mechanical and electrical domains was not fully

Department of Mechanical Engineering, The University of Utah, Salt Lake City, UT, USA

Corresponding author:

Binh Duc Truong, Department of Mechanical Engineering, The University of Utah, 1495 E. 100 S., 1550 MEK, Salt Lake City, UT 84112, USA.
Email: Binh.D.Truong@utah.edu

modeled, and its influence on the mechanical dynamics and maximum output power of the WPT system was not discussed. In related works, other authors reported several experimental observations indicating the potential application of piezoelectric devices for harvesting power from current-carrying conductors or ambient low-frequency magnetic fields (Paprotny et al., 2013; Liu and Dong, 2014; Han et al., 2015). However, the entire model for these designs has not been addressed in a systematic and complete manner.

In the context of WPT, low-frequency systems gain more and more attractions in the last recent years. Garraud et al. (2014) introduced an alternative architecture, in which two torsional springs, a permanent magnet, and a coil were used as a receiver. It should be noted that the inductive coupling between the transmitter and receiver coils was shown to be negligible; the mechanical oscillation of the magnet generated most of the power at the receiver. Later prototypes by the same group demonstrated capabilities of utilizing two transmitting technologies: a coil-based transmitter and a rotating-magnet transmitter (Garraud et al., 2018). Experiments on through-body and multi-receiver transmissions were conducted, opening the way for biomedical implants and wearables. Another concept based on the continuous rotation of the permanent magnet was presented (Garraud et al., 2019). Under steady-state operation, the rotating magnet acts as a synchronous machine rather than a resonant system. This technique enables transferring power over a wide range of frequencies, as opposed to at a particular frequency nearby the mechanical resonance of the receiver.

Based on the Euler–Bernoulli beam theory, the closed-form distributed parameter solutions for piezoelectric EH from base excitations were obtained and thoroughly analyzed for both unimorph and bimorph cantilever configurations (Erturk & Inman, 2011, 2009). Apart from that, this article aims to present an explicit lumped-parameter model, which is widely used for modeling vibration-based energy harvesters and is convenient to approximately describe the behavior of distributed physical systems. For a cantilever beam, if the proof mass to the beam mass ratio is significantly large, the single degree-of-freedom lumped-element model and the distributed parameter model are considerably the same (Erturk and Inman, 2008a, 2008b). The explicit form of the transduction factor and the analytical solution of the power transferred to a load are derived as functions of the device dimensions and the external \mathbf{B} field. In addition to maximize the transmission efficiency, it is of great interest to understand how to optimize the generated power under different situations. This is therefore one of the central objectives of this study.

The outline of this article is as follows. First of all, we establish a complete equivalent circuit model of the piezoelectric-based low-frequency wireless power

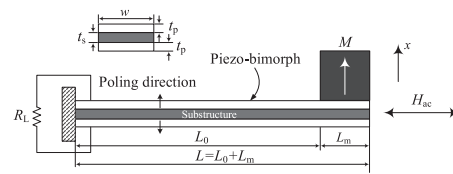


Figure 1. Schematic of MME transducer.

transfer system (WPTS) in section “Mathematical model.” We then experimentally validate the developed model in section “Experimental validation.” Based on the validated model, sections 4 and 5 further present analytical solutions of the power optimization problem, providing a comprehensive theoretical analysis under different standpoints. Various effects of (i) the thickness ratio constraint, (ii) material properties (e.g. the piezoelectric strain coefficient and Young’s modulus of the shim layer), and (iii) the leakage current of the piezoelectric transducer are given in section 6. Section 7 finally summarizes the study.

2. Mathematical model

Figure 1 illustrates the piezoelectric bimorph/magnet magneto-mechano-electric (MME) composite cantilever, including definition of the beam parameters such as w , t_p , t_s , L , L_0 , and L_m . The mechanism that transfers power to the MME transducer is similar to that of a piezoelectric energy harvester; however, it is different from an acoustic WPT system presented in the literature (in which ultrasonic waves are transmitted between two piezoelectric transducers). Assuming that the alternating current (AC) magnetic field H_{ac} of the Helmholtz coil is ideally uniform, a pure moment M_B acts on the magnet tip mass M , which is given by Liu and Dong (2014)

$$M_B = J_r C_M H_{ac} \quad (1)$$

where J_r is the remanent magnetic polarization and $C_M = L_m^3$ is the volume of the cubic magnet. Here, the vibration amplitudes are assumed to be small. The equivalent force positioned at the center of mass of M_B , which results in the same displacement, is (Bucciarelli, 2009)

$$F_M = \frac{3 M_B}{2 l_{eff}} \quad (2)$$

where the effective length is $l_{eff} = (L + L_0)/2$. It should be noted that for the use of thick single-coil (Challa et al., 2012), the moment M_B and a force F_B co-exist due to the field and the field gradient, respectively. Under such a circumstance, the pure force F_B acting on the magnet in the same vibration direction x is (Challa

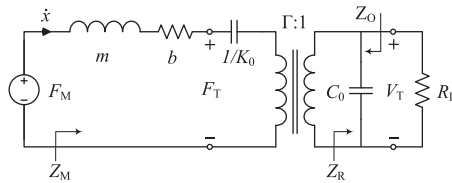


Figure 2. Equivalent two-port model.

et al., 2012) $F_B = J_r C_M (\partial H_{ac}(x) / \partial x)$. The total equivalent force is thus $F = F_M + F_B$. However, for the current case (i.e. we are considering a uniformed field), $F = F_M$ only, and the effect of F_B is out of scope of this article. The effective mass of the piezoelectric transducer consisting of the magnet mass M and the beam mass m_b is (Rao, 2010, section 2.5)

$$m = M + \frac{33}{140} m_b \tag{3}$$

where $m_b = wL(2t_p\rho_p + t_s\rho_s)$ and $M = \rho_M C_M$. ρ denotes the mass density of material. The effective short-circuit stiffness is approximated as (Erturk and Inman, 2011)

$$K_0 = \frac{3(YI)_c}{l_{eff}^3} \tag{4}$$

where $(YI)_c$ is the flexural rigidity of the composite beam.

$$q_m = \frac{24}{\{L_0[2L_m(4L_0^2 + 6L_0L_m + 3L_m^2) + q_r(3L_0^3 + 10L_0^2L_m + 12L_0L_m^2 + 6L_m^3)]\}}, \tag{10}$$

The expression of $(YI)_c$ for bimorph configuration is (Roundy and Wright, 2004)

$$(YI)_c = 2Y_p \left[\frac{wt_p^3}{12} + wt_p \left(\frac{t_s + t_p}{2} \right)^2 \right] + Y_s \frac{wt_s^3}{12} \tag{5}$$

where Y_p and Y_s are the elasticity constants of the piezoelectric layers and the substructure, respectively. The coupling between the electrical and mechanical domain is conveniently modeled as a linear two-port transducer, as depicted in Figure 2, where b is the mechanical damping coefficient and the electrical load is simply represented by a resistance R_L . The linear two-port equations for the piezoelectric transducer can be written as follows (Tilmans, 1996; Halvorsen, 2016)

$$F_T = K_1 x + \frac{\Gamma}{C_0} q, \tag{6}$$

$$V_T = \frac{\Gamma}{C_0} x + \frac{1}{C_0} q \tag{7}$$

where F_T is the transducer force, V_T is the voltage across the terminals of the electric port, $K_1 = K_0 + \Gamma^2 / C_0$ is the open-circuit stiffness, C_0 is the clamped capacitance, Γ is the transduction factor, and q is the charge on the positive electrical terminal.

Since the physical model studied in this work has a tip mass with appreciable length, the distribution of the tip mass over a finite span (i.e. L_m) is taken into account instead of a concentrated mass model. Adapted from Kim and Kim (2011), the static deflection shape function $\phi(y)$ can be expressed as two polynomial functions corresponding to two portions of the beam with and without the mass

$$0 \leq y \leq L_0 : \tag{8}$$

$$\phi_1(y) = q_m \left(\frac{L_m(L_0 + L)}{4} y^2 - \frac{L_m}{6} y^3 \right) + q_b \left(\frac{L^2}{4} y^2 - \frac{L}{6} y^3 + \frac{1}{24} y^4 \right),$$

$$L_0 \leq y \leq L : \tag{9}$$

$$\phi_2(y) = q_m \left(\frac{L_0 L_m L}{2} y - \frac{L_0^2 L_m (2L + L_m)}{12} \right) + q_b \left(\frac{L_0(L^2 + L_0 L_m + 2L_m^2)}{6} y - \frac{L_0^2(L^2 + 2L_0 L_m + 5L_m^2)}{24} \right)$$

where

$$q_b = q_m q_r, \tag{11}$$

$$q_r = \frac{L_m m_b}{LM}. \tag{12}$$

Depending on whether the wiring is in parallel or series (Erturk and Inman, 2011), C_0 and Γ are evaluated differently. For the case of series connection

$$s C_0 = \frac{1}{2} \epsilon_{33}^s \frac{wL}{t_p}, \tag{13}$$

$$s \Gamma = -e_{31} w \frac{t_p + t_s}{2} \frac{d\phi_1(y)}{dy} \Big|_{y=L_0} = \frac{-2e_{31} w (t_p + t_s) (3(M + m_b)L^2 - 3m_b L_0 L + m_b L_0^2)}{(6(M + m_b)L^3 - 6m_b L_0 L^2 + 2L_0^2 L (M + 2m_b) - L_0^3 m_b)} \tag{14}$$

where ϵ_{33}^s is the permittivity component at constant strain with the plane-stress assumption of a thin beam (i.e. $\epsilon_{33}^s = \epsilon_{33}^T - d_{31}^2 / s_{11}^E$ where d_{31} is the piezoelectric strain constant, s_{11}^E is the elastic compliance at constant electric field, and ϵ_{33}^T is the permittivity component at

constant stress). e_{31} is the effective piezoelectric stress constant, which can be given as $e_{31} = d_{31}/s_{11}^E$ based on the same assumption.

For the case of parallel connection

$${}^P C_0 = 4^S C_0, \quad (15)$$

$${}^P \Gamma = 2^S \Gamma. \quad (16)$$

It should be noted that the output power is independent of series/parallel configurations.

With a time harmonic drive force $F_M(t) = F_0 \cos(\omega t)$ of angular frequency ω and a resistance R_L directly connected to the electrical ports, the transverse velocity of the tip mass U_m and the output voltage V_T can be derived from the equivalent circuit model as

$$U_m = \frac{F_0}{Z_M}, \quad (17)$$

$$V_T = \frac{F_0 - \left(j\omega m + \frac{K_0}{j\omega} + b \right) U_m}{\Gamma} \quad (18)$$

where the impedance Z_M reads as

$$Z_M = \left(j\omega m + \frac{K_0}{j\omega} + b \right) + \Gamma^2 Z_R, \quad (19)$$

$$Z_R = \frac{\frac{1}{j\omega C_0} R_L}{\frac{1}{j\omega C_0} + R_L} = \frac{R_L}{1 + j\omega R_L C_0}. \quad (20)$$

The power transferred to the load is then given by

$$\begin{aligned} P &= \frac{1}{2} \frac{|V_T|^2}{R_L} \\ &= \frac{1}{2} \frac{\Gamma^2 F_0^2 |Z_R|^2}{R_L |Z_M|^2} = \frac{1}{2} \Delta K \frac{\omega^2 \tau}{1 + (\omega\tau)^2} \frac{F_0^2}{(\omega |Z_M|)^2} \\ &= \frac{1}{2} \Delta K \frac{\omega^2 \tau}{1 + (\omega\tau)^2} F_0^2 / \\ &\left\{ \left[\omega b + \Delta K \frac{\omega\tau}{1 + (\omega\tau)^2} \right]^2 + \left[K_1 - m\omega^2 - \Delta K \frac{1}{1 + (\omega\tau)^2} \right]^2 \right\} \end{aligned} \quad (21)$$

where the electrical time scale is $\tau = R_L C_0$; the difference between the highest and the lowest mechanical stiffness is denoted as $\Delta K = \Gamma^2 / C_0$ and $|X_0| = F_0 / (\omega |Z_M|)$ is the displacement amplitude of the tip mass. Formula (21) is the main objective to validate the model, where the frequency and **B**-field responses are the two most important aspects.

3. Experimental validation

Figure 3 shows the experimental setup, in which the circular Helmholtz coils are used as a transmitter. The

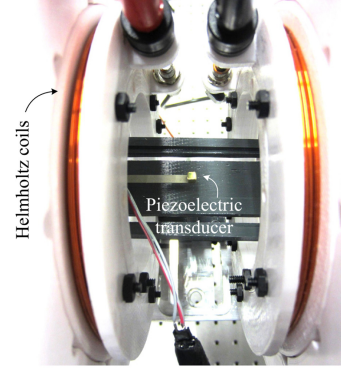


Figure 3. Experiment setup, in which a circular Helmholtz coil is used as a transmitter and the magnet tip mass of a piezoelectric-based receiver is placed at the center of the coil.

Table 1. Model parameters.

Parameters	Value
Permeability of free space, μ_0	$4\pi \times 10^{-7}$ H/m
Beam width, w	3.175 mm
Beam length, L	29.7 mm
Thickness of each PZT layer, t_p	0.14 mm
Elastic constant of PZT, Y_p	66×10^9 Pa
Piezoelectric constant, d_{31}	-190×10^{-12} m/V
Nominal capacitance, C_0	4.56 nF
Mass density of PZT, ρ_p	7800 kg/m ³
Thickness of center shim, t_s	0.1 mm
Elastic constant of center shim, Y_s	100×10^9 Pa
Mass density of center shim, ρ_s	8500 kg/m ³
Dimension of cubic magnet, L_m	3.175 mm
Mass density of Neodymium, ρ_M	8630 kg/m ³
Residual flux density of magnet, J_r	1.45 T
Mechanical damping coefficient, b	4.13×10^{-3} N s/m
Damping ratio, $\zeta_0 = b / (2m\omega_0)$	1.03%
Mechanical quality factor, Q_0	48.5

PZT: lead zirconate titanate.

generated **B** field is obtained using an AC milligauss meter (i.e. which is in root mean square (RMS) equivalent units). The receiver consists of a bimorph PZT-5A4E cantilever beam with a permanent magnet attached at its tip which is located in the center of the two coils. The Helmholtz coils are controlled by a Tektronix function generator connecting to a Rigol power amplifier. The induced voltage across the load resistance is measured by a laptop oscilloscope and the average output power is then computed as $P = \frac{1}{T} \int_0^T (V_T^2(t) / R_L) dt$. The mechanical damping coefficient b is determined by fitting the model to the experiment with $B = 40.5\sqrt{2} \mu\text{T}$ and $R_L = 1 \text{ M}\Omega$. The model parameters are now given and listed in Table 1, which is then used for validating all the following cases.

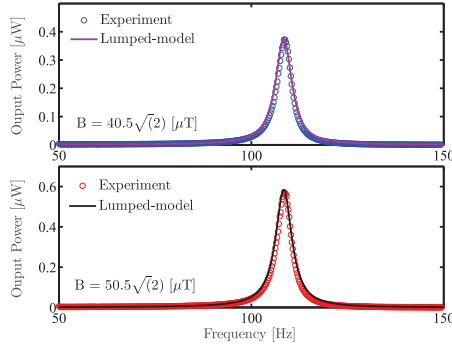


Figure 4. Frequency response comparisons between the experimental data and simulation results by the model.

Figure 4 shows a good agreement between the model results and the measurements for both $B = 40.5\sqrt{2} \mu\text{T}$ and $50.5\sqrt{2} \mu\text{T}$ when the drive frequency is swept from 50 to 150 Hz over a time duration of 40 s. Note that 40.5 and 50.5 are RMS values measured by the AC milligauss meter. The load resistance is $R_L = 1 \text{ M}\Omega$ and the corresponding optimal frequency is experimentally found at about $f_r = 108.5 \text{ Hz}$. Increase in the input magnetic field strength results in stronger moment acting on the magnet tip mass and therefore higher power delivered to the load. Figure 5 shows that the accuracy of the model is consistent when the applied magnetic flux density amplitude is discretely varied from 0 up to $B = 89.5 \mu\text{T}$. The load resistance is kept the same as that of in Figure 4 and the drive frequency is fixed at $f_r = 108.5 \text{ Hz}$. The transferred power obtained from experiments and simulations are almost identical, which is a quadratic function in terms of the \mathbf{B} -field amplitude. In summary, the lumped model has successfully predicted the two most important behavior that are frequency response and magnetic field response.

4. Power optimization principles: gradient descent method

We now utilize the developed model to further investigate the power optimization problem at a given applied \mathbf{B} field with respect to the load and the drive frequency for different possible cases. This is of interest not only from the mathematical point of view but also to provide a complete physical insight of the WPT system.

Case I. At $\omega = \omega_0 = \sqrt{K_0/m}$, the optimal load and the corresponding optimum output power are given by

$$R_L^{\text{opt}}|_{\omega = \omega_0} = \frac{1}{\omega_0 C_0 \sqrt{M_0^2 + 1}}, \quad (22)$$

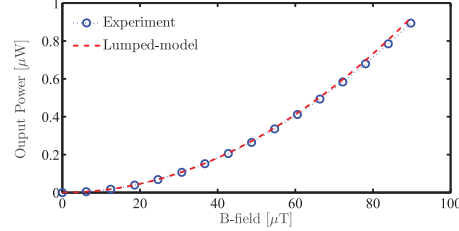


Figure 5. Comparisons of the external \mathbf{B} -field responses between the model simulations and experiments with $R_L = 1 \text{ M}\Omega$ and $f_r = 108.5 \text{ Hz}$.

$$P^{\text{opt}}|_{\omega = \omega_0} = \frac{F_0^2}{4b} M_0 \left(\sqrt{M_0^2 + 1} - M_0 \right). \quad (23)$$

Here, the resonator figure of merit is defined as $M_f = \Delta K/(b\omega)$ (Vittoz, 2010). In particular, at the resonant frequency $M_0 = \Delta K/(b\omega_0)$.

Case II. At $\omega = \omega_1 = \sqrt{K_1/m}$, we get

$$R_L^{\text{opt}}|_{\omega = \omega_0} = \frac{\sqrt{M_1^2 + 1}}{\omega_1 C_0}, \quad (24)$$

$$P^{\text{opt}}|_{\omega = \omega_0} = \frac{F_0^2}{4b} M_1 \left(\sqrt{M_1^2 + 1} - M_1 \right) \quad (25)$$

where $M_1 = \Delta K/(b\omega_1)$. In general, $P^{\text{opt}}|_{\omega = \omega_0}$ and $P^{\text{opt}}|_{\omega = \omega_1}$ are not identical; however, for moderately coupled systems $M_0 \approx M_1$, the two maximum powers approximately coincide.

Case III. The solution of the optimal load considered as a function of the drive frequency and the other system parameters is calculated by

$$R_L^{\text{opt}}|_{\omega} = \frac{1}{\omega C_0} \sqrt{\frac{(K_0 - m\omega^2)^2 + (\omega b)^2}{(K_1 - m\omega^2)^2 + (\omega b)^2}}. \quad (26)$$

We can observe that equation (26) reduces to equations (22) and (24) when $\omega = \omega_0$ and $\omega = \omega_1$ correspondingly.

Case 4. We now treat $\tau = R_L C_0$ as a constant (i.e. R_L is kept fixed) and consider ω to be a variable parameter. This investigation is motivated by the fact that the drive frequency can be easily subjected to control in WPT systems. Similarly, the stationary points of the power are determined by $dP/d\omega = 0$ or equivalently

$$2m\tau^2\omega^6 + \omega^4(b^2\tau^2 + m^2 - 2K_1m\tau^2) - K_0^2 = 0. \quad (27)$$

The (real) optimal frequency is derived as follows

$$\omega^{\text{opt}} = \left[\frac{1}{3\lambda_1} \left(\frac{\Lambda}{\sqrt[3]{2}} + \frac{\sqrt[3]{2}\lambda_2^2}{\Lambda} - \lambda_2 \right) \right]^{1/2} \quad (28)$$

where

$$\lambda_1 = 2(m\tau)^2, \quad (29)$$

$$\lambda_2 = b^2\tau^2 + m^2 - 2K_1m\tau^2, \quad (30)$$

$$\Lambda = \left(27(\lambda_1K_0)^2 - 2\lambda_2^3 + 3\sqrt{3}(\lambda_1K_0)\sqrt{27(\lambda_1K_0)^2 - 4\lambda_2^3} \right)^{1/3}. \quad (31)$$

Figure 6 shows a comprehensive picture of the transferred power with respect to the normalized angular frequency ω/ω_0 and the load resistance R_L . The corresponding power obtained by using equation (28) is also included, which is the maximum transferable power at each value of R_L .

Case V. Finally, we consider the condition in which both the load resistance R_L (and therefore, the parameterized time constant τ) and the drive frequency ω are simultaneously considered as objective control variables. Stationary point(s) of the general power optimization problem are given by solving $dP/d\tau = 0$ and $dP/d\omega = 0$ simultaneously. Substituting the optimal time constant $\tau^{\text{opt}} = R_L^{\text{opt}}C_0$ from equation (26) into equation (27), the latter equation reduces to

$$3\omega^8 - 4\alpha\omega^6 + (\alpha^2 + 2\beta)\omega^4 - \beta^2 = 0 \quad (32)$$

where

$$\alpha = (\omega_0^2 + \omega_1^2)(1 - 4\zeta_e^2), \quad (33)$$

$$\beta = (\omega_0\omega_1)^2, \quad (34)$$

$$\zeta_e = \frac{b}{2\sqrt{m(K_0 + K_1)}}. \quad (35)$$

Equation (32) can be rewritten as

$$[\omega^2(2\omega^2 - \alpha)]^2 = (\omega^4 - \beta)^2, \quad (36)$$

which results in three (positive) distinguished solutions

$$\omega_m = \left[\frac{\alpha + \sqrt{\alpha^2 + 12\beta}}{6} \right]^{1/2}, \quad (37)$$

$$\omega_{M1} = \left[\frac{\alpha - \sqrt{\alpha^2 - 4\beta}}{2} \right]^{1/2}, \quad (38)$$

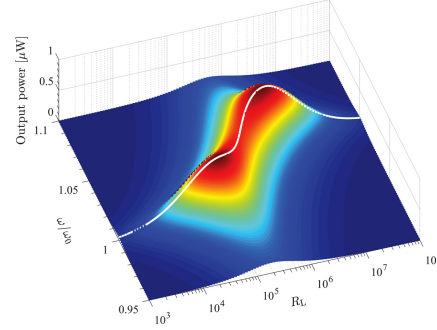


Figure 6. Output power as a function of driving frequency and load resistance. White solid line: corresponding power with analytical solution of the optimal frequency expressed in equation (28).

$$\omega_{M2} = \left[\frac{\alpha + \sqrt{\alpha^2 - 4\beta}}{2} \right]^{1/2}. \quad (39)$$

Here, ω_{M1} and ω_{M2} are real if and only if $\zeta_e \in \{(0, \zeta_1] \cup [\zeta_2, +\infty)\}$, where

$$\zeta_1^2 = \frac{1}{4} \frac{(\omega_1 - \omega_0)^2}{\omega_0^2 + \omega_1^2}, \quad (40)$$

$$\zeta_2^2 = \frac{1}{4} \frac{(\omega_1 + \omega_0)^2}{\omega_0^2 + \omega_1^2}. \quad (41)$$

The condition $\zeta_e \leq \zeta_1$ is equivalent to

$$k^2 \geq k_{\text{cr}}^2 = 1 - \frac{1}{(2\zeta_0 + 1)^2} \quad (42)$$

where the squared electromechanical coupling factor $0 \leq k^2 \leq 1$ and the damping ratio ζ_0 at the short-circuit resonant frequency ω_0 are given by

$$k^2 = \frac{\Gamma^2}{K_1C_0}, \quad (43)$$

$$\zeta_0 = \frac{b}{2\sqrt{mK_0}} = \frac{b}{2m\omega_0}. \quad (44)$$

Meanwhile, $\zeta_e \geq \zeta_2$ leads to $1 - k^2 > 1/(1 - 2\zeta_0)^2 > 1$, which cannot occur. Equation (36) has a unique positive solution ω_m when the coupling is lower than critical, $k^2 < k_{\text{cr}}^2$. Therefore, the optimum output power in this case is attained at ω_m . However, this power is less than the maximum achievable power when $k^2 \geq k_{\text{cr}}^2$. See Shu et al. (2007), Arroyo et al. (2012), and Liao and Sodano (2018) for an example. Note that the corresponding optimal load is computed by substituting the

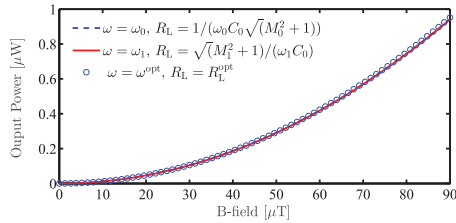


Figure 7. Maximum transferred power at different optimal conditions (Cases I, II, and V).

optimal frequency back into equation (26). The accuracy of these calculations is confirmed by an independent numerical method in Appendix 3.

In the currently studied device, the maximal power points achieved from Cases I, II, and V are considerably the same as depicted in Figure 7. However, we also found that in some circumstances, the maximum powers in Cases I and II can drop down to 95% or 92%, respectively, when compared to that of Case V. An example is discussed in Appendix 3 in which b , Γ , L , and t_p are mathematically adjusted for proving the statement. Supporting information for Cases I, II, III, IV, and V can also be found in Appendices 1 to 3.

5. Power optimization principles: impedance matching

In addition to the gradient descent method, impedance matching is a powerful approach for determining the condition of system parameters under which the power transferred to the load is maximized. We have shown that for an inductively coupled WPT system, the simultaneous optimization of load resistance and driving frequency generates almost identical output power compared to the case where the resonator impedance is matched to a particular load (Truong, 2019). However, a single-end conjugate-matched circuit at either source or load does not result in maximum power transfer through a physical two-port network in general. In other words, power delivered to a load is maximized by simultaneous conjugate matching at both ends (source and load; Truong, 2019). These findings lead to a question of how the piezoelectric-magnet WPT system performs under different conjugate matching conditions. In this section, solutions of impedance matching problems in comparison with the results presented in section 4 are addressed.

5.1. Impedance matching to the load

From the equivalent circuit model shown in Figure 2, the output impedance Z_O is calculated as

$$Z_O = \frac{\frac{1}{j\omega C_0} \left[\frac{1}{\Gamma^2} \left(j\omega m + \frac{K_0}{j\omega} + b \right) \right]}{\frac{1}{j\omega C_0} + \left[\frac{1}{\Gamma^2} \left(j\omega m + \frac{K_0}{j\omega} + b \right) \right]}. \quad (45)$$

Based on the impedance matching technique shown in Challa et al. (2012), the optimal load is given by

$$R_L^{\text{opt}} = |Z_O| = \frac{1}{\omega C_0} \sqrt{\frac{(K_0 - m\omega^2)^2 + (\omega b)^2}{(K_1 - m\omega^2)^2 + (\omega b)^2}}, \quad (46)$$

which is the same as in equation (26) (Case III).

Given the fact that the formula $R_L^{\text{opt}} = |Z_O|$ does not fully reflect the maximum power transfer theorem followed by the impedance matching condition $Z_L = Z_O^*$ (Kong, 1995; here, Z_L denotes the general load impedance), we now consider the complete case where $\Im\{Z_O\} = 0$ and $R_L = \Re\{Z_O\}$. The former equation results in

$$\omega_- = \left[\frac{\omega_0^2 + \omega_1^2}{2} + \frac{\kappa - b^2}{2m^2} \right]^{1/2}, \quad (47)$$

$$\omega_+ = \left[\frac{\omega_0^2 + \omega_1^2}{2} - \frac{\kappa + b^2}{2m^2} \right]^{1/2} \quad (48)$$

where

$$\kappa^2 = [(m(\omega_0 + \omega_1))^2 - b^2][(m(\omega_0 - \omega_1))^2 - b^2]. \quad (49)$$

The latter equation yields

$$R_L = \frac{\Delta K}{C_0} \frac{b}{(K_1 - m\omega^2)^2 + (\omega b)^2}. \quad (50)$$

We find that $\omega_- = \omega_{M_1}$ and $\omega_+ = \omega_{M_2}$ and the optimum power obtained by the two methods (complete impedance matching to the load, and gradient algorithm Case V) are identical.

An attempt to maximize the generated power for a piezoelectric energy harvester with the presence of an additional inductor L_a in parallel/series with the load resistance R_L was proposed in Renno et al. (2009). However, this method is not appropriate in practice since it leads to the optimal inductance in the range of a few H , not yet to mention that its high parasitic resistance may significantly reduce the power delivered to the load.

5.2. Bi-conjugate impedance matching

The equivalent circuit model in Figure 2 can be generalized for any lossless two-port network as shown in Figure 8. The applied force F_M and the mechanical damping coefficient b form an effective power source for the two-port network whose output port is connected to a load resistance R_E in the later stage. Given a constant amplitude of the applied magnetic flux

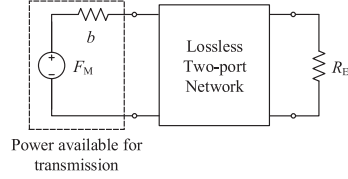


Figure 8. Generalized equivalent circuit model for any lossless two-port network.

density, based on the two-port theory (Gonzalez, 1996), the power available for transmission is determined by

$$P_{\text{avs}} = \frac{1}{8} \frac{F_0^2}{b}. \quad (51)$$

In other words, P_{avs} is the largest possible power that can be delivered to the two-port network and therefore is the power limit transferred into the load. Without loss of generality, we consider a lossless network formed by reactances jX and jY as shown in Figure 9. The source, input, output, and load impedances are

$$Z_s = b, \quad (52)$$

$$Z_{\text{in}} = jX + \frac{jYR_E}{jY + R_E}, \quad (53)$$

$$Z_{\text{out}} = \frac{jY(b + jX)}{b + j(X + Y)}, \quad (54)$$

$$Z_L = R_E \quad (55)$$

respectively. The output voltage and power induced in the load R_E are computed as

$$V_E = F_0 \frac{jYR_E}{(bR_E - XY) + j(bY + XR_E + YR_E)}, \quad (56)$$

$$P_E = \frac{1}{2} \frac{|V_E|^2}{R_E} = \frac{1}{2} F_0^2 Y^2 R_E \left/ \left[(bR_E - XY)^2 + j(bY + XR_E + YR_E)^2 \right] \right. \quad (57)$$

and

$$P_{E, \text{lim}} = P_{\text{avs}}.$$

The bi-conjugate impedance matching conditions are $Z_{\text{in}} = Z_s^*$ and $Z_{\text{out}} = Z_L^*$, which leads to

$$\Im\{Z_{\text{in}}\} = \Im\{Z_{\text{out}}\} = 0, \quad (58)$$

$$\Re\{Z_{\text{in}}\} = \frac{Y^2 R_E}{Y^2 + R_E^2} = b, \quad (59)$$

$$\Re\{Z_{\text{out}}\} = \frac{Y^2 b}{(X + Y)^2 + b^2} = R_E. \quad (60)$$

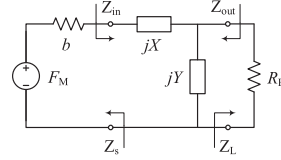


Figure 9. A circuit model with reactance two-port network.

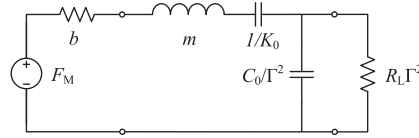


Figure 10. An equivalent circuit of the linear two-port model.

Equation (58) is equivalent to

$$X(R_E^2 + Y^2) + YR_E^2 = 0, \quad (61)$$

$$b^2 + X(X + Y) = 0. \quad (62)$$

Since X and Y must have opposite sign ($XY < 0$), one possible solution with $Y < 0$ is

$$X = \sqrt{b(R_E - b)}, \quad (63)$$

$$Y = -\frac{R_E \sqrt{b}}{\sqrt{R_E - b}} \quad (64)$$

with the assumption that $R_E > b$. Surprisingly, these solutions of X and Y also satisfy the other two conditions (equations (59) and (60)). Therefore, equations (63) and (64) are the final solution of the bi-conjugate impedance matching problem. Substituting equations (59) and (60) into equation (57), the optimum power transferred to the load is

$$P_E|_{\text{opt}} = \frac{1}{8} \frac{F_0^2}{b} = P_{E, \text{lim}}. \quad (65)$$

We have proved that the limitation of the output power is reached by a bi-conjugate impedance matched system. In general, this conclusion holds for any lossless two-port network.

We then apply the analysis above to the particular piezoelectric resonator used in this article which is assumed to be a lossless transducer. Using the reflected impedance technique (Orfanidis, 2016), the linear two-port model in Figure 2 can be represented by an equivalent circuit depicted in Figure 10. Letting $X = \omega m - K_0/\omega$, $Y = -\Gamma^2/(\omega C_0)$, and $R_E = R_L \Gamma^2$, we recover the case explored in Figure 9. Note that the power in equation (21) is the same as the power

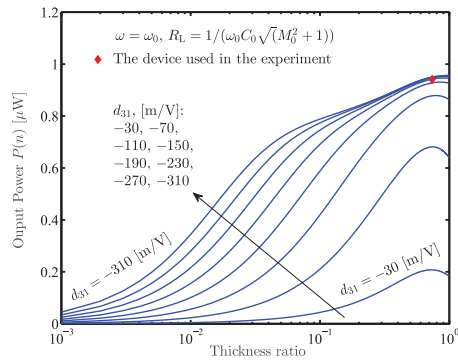


Figure 11. Maximum transferred power as a function of the thickness ratio $n = 2t_p/t_0$ with different values of d_{31} . The total thickness of the composite laminate t_0 is kept fixed $t_0 = 0.38$ mm and $Y_s = 100$ GPa (see Table 1).

delivered to the reflected resistance $R_L \Gamma^2$. Expressions (63) and (64) are written in terms of two variables R_L and ω as follows

$$R_L = \frac{1}{bC_0} \left(m - \frac{K_0}{\omega^2} \right), \quad (66)$$

$$\omega^2 \left(m - \frac{K_0}{\omega^2} \right)^2 - \Delta K \left(m - \frac{K_0}{\omega^2} \right) + b^2 = 0. \quad (67)$$

Equation (67) has two solutions that are identical to equations (47) and (48). The corresponding maximum output power is exactly equal to $P_{E, \text{lim}}$.

Up to this point, we are able to conclude that *three approaches (1) optimal load and frequency by the gradient descent analysis, (2) impedance matching to the load, and (3) bi-conjugate impedance matching collapse to the same solution, in which the output power attains the maximum transferable power (for a given applied magnetic field)*. The same result was observed for vibration energy harvesters under displacement-unconstrained operation (Renaud et al., 2012; Halvorsen et al., 2013). From a physics standpoint, optimizing the load and frequency in this circumstance is fully equivalent to applying the bi-conjugate impedance matching principle to the piezoelectric-based WPT system under investigation. This conclusion does not always hold true in general. With a lossy two-port network, such as a two-coil magnetically coupled resonator, optimal load and frequency is not able to reach the maximum possible power. Additional impedance matching circuits are required for maximizing the output power to the load. See Heeb et al. (2014) and Kim et al. (2015) for examples.

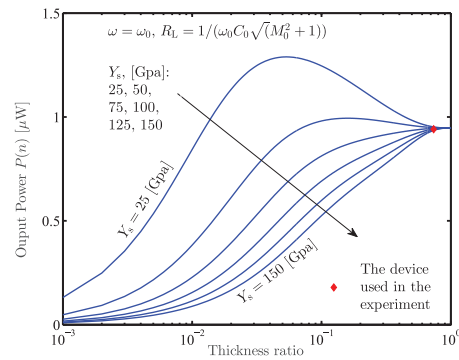


Figure 12. Maximum transferred power as a function of the thickness ratio $n = 2t_p/t_0$ with different values of Y_s . The total thickness of the composite laminate t_0 is kept fixed.

6. Discussion

6.1. Thickness ratio–constrained operation

Many researchers are focused on improving the performance of piezoelectric materials. However, constraints on the geometry of the device are also important. Geometric constraints may not be problematic for macro-scale prototypes because the dimensions of the beam (i.e. piezoelectric and substrate layers) are easily controllable. However, in the case of microfabricated generators, where the thickness ratio between piezoelectric and substrate layers is constrained by microfabrication technologies, the power output could be significantly affected. Figure 11 depicts the variations in the generated power with the changes in the thickness ratio defined as $n = 2t_p/t_0$, while the total thickness t_0 and the other parameters are unchanged. The optimal thickness ratio slightly changes with the decrease in $|d_{31}|$, for instance, $n^{\text{opt}} \approx 0.73$ with $d_{31} = -30$ m/V and $n^{\text{opt}} \approx 0.91$ with $d_{31} = -190$ m/V. Furthermore, the maximum output power (obtained at corresponding n^{opt}) is nearly saturated with $|d_{31}| \geq 190$ m/V for relatively large n (in particular, $n \geq 0.2$). Here, we assume that the mechanical damping coefficient is nearly unchanged. This assumption is reasonable since the air damping mainly depends on the ambient pressure and the beam length and width (which are kept fixed in this case).

6.2. Material properties

In addition to the piezoelectric strain constant d_{31} , the elastic Young's modulus of the shim Y_s also has a strong influence on both the optimal thickness ratio and the generated power. This issue has not been fully explored in the literature. Figure 12 shows the

dependencies of P^{opt} and n^{opt} on Y_s , in which P^{opt} increases and n^{opt} reduces with the decrease in Y_s . For instance, at an elastic modulus of $Y_s = 100$ GPa, $P^{\text{opt}} = 0.95 \mu\text{W}$ and $n^{\text{opt}} = 0.909$, while those at $Y_s = 25$ GPa are $P^{\text{opt}} = 1.29 \mu\text{W}$ and $n^{\text{opt}} = 0.053$. In a general trend, lower Y_s results in higher power transferred to the load at the same thickness ratio. Here, the total thickness and the mechanical quality factor at short-circuit resonant frequency of the composite laminate are kept fixed, $t_0 = 0.38$ mm and $Q_0 = 48.5$ (taken from Table 1). The damping coefficient is calculated by $b = \sqrt{mK_0}/Q_0$. This observation can explain the experimental results reported in Annapureddy et al. (2016, 2018) where an optimum power obtained by a Fe-Ga MME generator was approximately 430% higher than that of a Ni-based MME prototype. Both devices have a similar structure and dimensions. The increase is due to the fact that Young's modulus of Nickel at the room temperature is higher than that of Fe-Ga, ${}^{\text{Ni}}Y_s \approx 200$ GPa (Luo et al., 2004) in comparison with ${}^{\text{Fe-Ga}}Y_s \approx 140$ GPa (Li et al., 2018). If we choose to keep b fixed and express Q_0 as a function of b , the same trend is observed.

6.3. Leakage current and effective figure of merit

In practice, piezoelectric transducers may have leakage current that cannot be neglected. This parasitic loss is modeled as a resistance connected in parallel with the clamped capacitance of the piezoelectric generator (Arroyo et al., 2012; Halvorsen, 2016). The power delivered to the resistive load now becomes

$$P_L = \frac{1}{2} \left(1 - \frac{\tau}{\tau_p} \right) \frac{\Delta K \omega^2 \tau}{1 + (\omega\tau)^2} \frac{F_0^2}{(\omega Z_M + b)^2} \quad (68)$$

where

$$Z_M = j \left(m\omega - \frac{K_0}{\omega} \right) + \Delta K \frac{\tau}{1 + j\omega\tau}, \quad (69)$$

$$\tau_L = R_L C_0, \quad \tau_p = R_p C_0, \quad \frac{1}{\tau} = \frac{1}{\tau_L} + \frac{1}{\tau_p}. \quad (70)$$

With arbitrary operating frequencies, the optimal load is

$$\tau_L^{\text{opt}} = \frac{\tau_p [(K_0 - m\omega^2)^2 + (\omega b)^2]^{1/2}}{[(K_0 - m\omega^2)^2 + (K_1 - m\omega^2)^2 + (\omega b)^2 (1 + (\omega\tau_p)^2) + 2\Delta K (\omega^2 b \tau_p)]^{1/2}}. \quad (71)$$

At resonance frequency $\omega = \omega_0$, equation (71) reduces to

$$\tau_L^{\text{opt}} = \frac{1}{\omega_0} \frac{1}{\sqrt{1 + (M_0 + 1/(\omega_0\tau_p))^2}}. \quad (72)$$

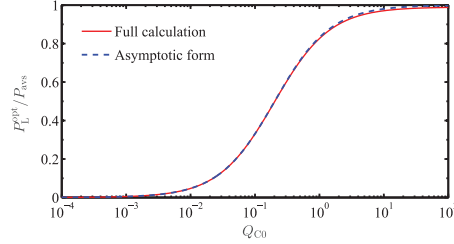


Figure 13. Solutions of the ratio between the optimum output power P_L^{opt} and its limit P_{avs} as functions of Q_{C0} , computed by equations (74) and (75), respectively.

Since $\Delta K = k^2 K_1$, we can write $M = k^2 Q_1 \omega_1 / \omega$ or $M = k_c^2 Q_0 \omega_0 / \omega$, where the Q factors are $Q_0 = m\omega_0 / b$ and $Q_1 = m\omega_1 / b$, and the expedient coupling coefficient is $k_c^2 = k^2 / (1 - k^2)$. Denoting $M|_{\omega=\omega_0} = M_0$, we have $M_0 = \Delta K / (\omega_0 b) = k_c^2 Q_0$. By introducing the electrical quality factor, $Q_{C0} = \omega_0 \tau_p$, equation (72) results in

$$\tau_L^{\text{opt}} = \frac{\tau_p}{\sqrt{(M_c + 1)^2 + Q_{C0}^2}}. \quad (73)$$

The effective (overall) figure of merit is defined by $M_c = M_0 Q_{C0} = k_c^2 Q_0 Q_{C0}$. The optimum delivered power is

$$P_L^{\text{opt}} = \frac{1}{8} \frac{F_0^2}{b} \frac{2M_c}{M_c + 1 + \sqrt{(M_c + 1)^2 + Q_{C0}^2}}. \quad (74)$$

For moderate or high coupling, $M_c \gg Q_{C0}$, and the asymptotic form of the maximum transferable power is

$$P_L^{\text{opt}} \approx P_{\text{avs}} \frac{M_c}{M_c + 1}. \quad (75)$$

When $R_p \rightarrow \infty$ ($\tau_p \rightarrow \infty$), both equations (74) and (75) collapse to the case without the parasitic resistance as shown in equation (65).

The effects of the electrical quality factor Q_{C0} on the optimal output power are depicted in Figure 13. Other

parameters such as the coupling coefficient $k = 0.3$ and the mechanical quality factor $Q_0 = 48.5$ are taken from Table 1. In this particular case, the discrepancy between equations (74) and (75) is negligible. The question on

how to determine R_p (and therefore Q_{C0}) is out of scope of this article.

6.4. Transmission efficiency

Although the efficiency is not a key factor of a low-power system (e.g. sensor nodes or wearable/implantable applications), it is still of interest to study. We found that the transmission efficiency of the MME configuration is relatively low in comparison with other WPT system such as inductively coupled resonators (Truong and Roundy, 2018). Despite this obvious drawback, an advantage of the MME system is that the applied magnetic field can be higher at the low frequencies required by the MME system while still remaining within safe limits. According to the IEEE standards, a maximum allowable field at 1 kHz is 2 mT, 10 times larger than the 200 μ T permissible at 1 MHz (IEEE C95.1-2005, 2006; IEEE C95.6-2002, 2002). In the case that the receiver is blocked by a metal plate, high-frequency devices such as inductive/capacitive coupled systems cannot be utilized due to the effects of eddy currents (i.e. also called Foucault currents, which flow in closed loops within conductors and in planes perpendicular to the applied magnetic field).

7. Conclusion

The main aim of this work was to present an experimentally validated lumped-parameter model for a piezoelectric-based WPT system, providing thorough analyses on how to optimize the delivered power and reveal the essential role of the device thickness ratio. The electromechanical transduction factor was given as an explicit formula of device geometry, rather than a derivative (or integral) function reported in the literature. The solution of the optimal load at the resonance/anti-resonance frequency (*Case I/II*), the general optimal load at an arbitrary frequency (*Case III*), the optimal driving frequency with respect to the load (*Case IV*), and the simultaneous optimal load and frequency (*Case V*) were analytically derived in explicit forms. It was shown that for the system under consideration, optimizing the load and frequency is equivalent to bi-conjugate impedance matching. The fundamental maximum transferable power for a given external \mathbf{B} field was revealed, which can be reached by concurrently tuning the driving frequency and adapting the load resistance. The model can also be utilized as a means for further investigations, including the effect of material properties such as the piezoelectric strain coefficient and Young's modulus of the shim layer.

Declaration of conflicting interests

The author(s) declared no potential conflicts of interest with respect to the research, authorship, and/or publication of this article.

Funding

The author(s) disclosed receipt of the following financial support for the research, authorship, and/or publication of this article: This work was supported by the National Science Foundation ASSIST Nanosystems ERC under Award Number EEC-1160483.

ORCID iD

Binh Duc Truong  <https://orcid.org/0000-0001-7108-4713>

References

- Annapureddy V, Kim M, Palneedi H, et al. (2016) Low-loss piezoelectric single-crystal fibers for enhanced magnetic energy harvesting with magnetolectric composite. *Advanced Energy Materials* 6(24): 1601244.
- Annapureddy V, Na SM, Hwang GT, et al. (2018) Exceeding milli-watt powering magneto-mechano-electric generator for standalone-powered electronics. *Energy & Environmental Science* 11: 818–829.
- Arroyo E, Badel A, Formosa F, et al. (2012) Comparison of electromagnetic and piezoelectric vibration energy harvesters: model and experiments. *Sensors and Actuators A: Physical* 183: 148–156.
- Assaworrorarit S, Yu X and Fan S (2017) Robust wireless power transfer using a nonlinear parity-time-symmetric circuit. *Nature* 546: 387–390.
- Barman SD, Reza AW, Kumar N, et al. (2015) Wireless powering by magnetic resonant coupling: recent trends in wireless power transfer system and its applications. *Renewable and Sustainable Energy Reviews* 51: 1525–1552.
- Beeby SP, Tudor MJ and White NM (2006) Energy harvesting vibration sources for microsystems applications. *Measurement Science and Technology* 17(12): R175–R195.
- Bucciarelli L (2009) *Engineering Mechanics for Structures* (Dover Civil and Mechanical Engineering). New York: Dover Publications.
- Challa VR, Mur-Miranda JO and Arnold DP (2012) Wireless power transmission to an electromechanical receiver using low-frequency magnetic fields. *Smart Materials and Structures* 21(11): 115017.
- D'hulst R, Mitcheson PD and Driesen J (2006) CMOS buck-boost power processing circuitry for powerMEMS generators. In: *PowerMEMS 2006 technical digest*, Berkeley, CA, 29 November–1 December, pp. 215–218. Available at: <http://cap.ee.ic.ac.uk/pdm97//powermems/2006/pdfs/215-218%20P43%20dhulst.pdf>
- D'hulst R, Sterken T, Puers R, et al. (2010) Power processing circuits for piezoelectric vibration-based energy harvesters. *IEEE Transactions on Industrial Electronics* 57(12): 4170–4177.
- Erturk A and Inman DJ (2008a) On mechanical modeling of cantilevered piezoelectric vibration energy harvesters. *Journal of Intelligent Material Systems and Structures* 19(11): 1311–1325.
- Erturk A and Inman DJ (2008b) Issues in mathematical modeling of piezoelectric energy harvesters. *Smart Materials and Structures* 17(6): 065016.
- Erturk A and Inman DJ (2009) An experimentally validated bimorph cantilever model for piezoelectric energy

- harvesting from base excitations. *Smart Materials and Structures* 18(2): 025009.
- Erturk A and Inman DJ (2011) *Piezoelectric Energy Harvesting*. Chichester: Wiley.
- Erturk A, Hoffmann J and Inman DJ (2009) A piezomagnetoelastic structure for broadband vibration energy harvesting. *Applied Physics Letters* 94: 254102.
- Garraud A, Jimenez JD, Garraud N, et al. (2014) Electrodynamic wireless power transmission to rotating magnet receivers. *Journal of Physics: Conference Series* 557: 012136.
- Garraud N, Alabi D, Chyczewski S, et al. (2018) Extending the range of wireless power transmission for bio-implants and wearables. *Journal of Physics: Conference Series* 1052: 012023.
- Garraud N, Garraud A, Munzer D, et al. (2019) Modeling and experimental analysis of rotating magnet receivers for electrodynamic wireless power transmission. *Journal of Physics D: Applied Physics* 52(18): 185501.
- Gonzalez G (1996) *Microwave Transistor Amplifiers: Analysis and Design*. 2nd ed. Upper Saddle River, NJ: Prentice-Hall.
- Halvorsen E (2016) Optimal load and stiffness for displacement-constrained vibration energy harvesters. *arXiv*. Available at: <https://arxiv.org/abs/1603.01909>
- Halvorsen E, Le CP, Mitcheson PD, et al. (2013) Architecture-independent power bound for vibration energy harvesters. *Journal of Physics: Conference Series* 476(1): 012026.
- Han J, Hu J, Wang Z, et al. (2015) Enhanced performance of magnetoelectric energy harvester based on compound magnetic coupling effect. *Journal of Applied Physics* 117(14): 144502.
- Hassan Q, Khan A and Madani S (2017) *Internet of Things: Challenges, Advances, and Applications* (Chapman & Hall/CRC Computer and Information Science Series). Boca Raton, FL: CRC Press.
- Heebl JD, Thomas EM, Penno RP, et al. (2014) Comprehensive analysis and measurement of frequency-tuned and impedance-tuned wireless non-radiative power-transfer systems. *IEEE Antennas and Propagation Magazine* 56(5): 131–148.
- Huang L, Hu AP, Swain A, et al. (2013) An overview of capacitively coupled power transfer—a new contactless power transfer solution. In: *2013 IEEE 8th conference on industrial electronics and applications (ICIEA)*, Melbourne, VIC, Australia, 19–21 June, pp. 461–465. New York: IEEE.
- IEEE C95.1-2005 (2006) IEEE standard for safety levels with respect to human exposure to radio frequency electromagnetic fields, 3 kHz to 300 GHz (Revision of IEEE Std C95.1-1991).
- IEEE C95.6-2002 (2002) IEEE standard for safety levels with respect to human exposure to electromagnetic fields, 0-3 kHz.
- Jorge Nocedal SW (2006) *Numerical Optimization* (Springer Series in Operations Research). 2nd ed. New York: Springer.
- Khaligh A, Zeng P and Zheng C (2010) Kinetic energy harvesting using piezoelectric and electromagnetic technologies-state of the art. *IEEE Transactions on Industrial Electronics* 57(3): 850–860.
- Kiani M and Ghovanloo M (2012) The circuit theory behind coupled-mode magnetic resonance-based wireless power transmission. *IEEE Transactions on Circuits and Systems I: Regular Papers* 59(9): 2065–2074.
- Kim J, Kim DH and Park YJ (2015) Analysis of capacitive impedance matching networks for simultaneous wireless power transfer to multiple devices. *IEEE Transactions on Industrial Electronics* 62(5): 2807–2813.
- Kim YY and Kim JE (2011) Analysis of piezoelectric energy harvesters of a moderate aspect ratio with a distributed tip mass. *Journal of Vibration Acoustics Stress and Reliability in Design* 133: 041010.
- Kong CS (1995) A general maximum power transfer theorem. *IEEE Transactions on Education* 38(3): 296–298.
- Kurs A, Karalis A, Moffatt R, et al. (2007) Wireless power transfer via strongly coupled magnetic resonances. *Science* 317(5834): 83–86.
- Li J, Li M, Mu X, et al. (2018) Temperature and magnetic field dependencies of the Young's modulus in magnetostriuctive Fe-Ga alloys. *Journal of Applied Physics* 123(7): 075102.
- Liao Y and Sodano H (2018) Optimal power, power limit and damping of vibration based piezoelectric power harvesters. *Smart Materials and Structures* 27(7): 075057.
- Liu G and Dong S (2014) A magneto-mechano-electric coupling equivalent circuit of piezoelectric bimorph/magnets composite cantilever. *Journal of Applied Physics* 115(8): 084112.
- Luo J, Flewitt A, Spearing S, et al. (2004) Young's modulus of electroplated Ni thin film for MEMS applications. *Materials Letters* 58(17): 2306–2309.
- Mitcheson PD, Yeatman EM, Rao GK, et al. (2008) Energy harvesting from human and machine motion for wireless electronic devices. *Proceedings of the IEEE* 96(9): 1457–1486.
- Moss SD, Payne OR, Hart GA, et al. (2015) Scaling and power density metrics of electromagnetic vibration energy harvesting devices. *Smart Materials and Structures* 24(2): 023001.
- Orfanidis SJ (2016) *Electromagnetic Waves and Antennas*. Online ed. Piscataway, NJ: ECE Department, Rutgers University. Available at: <http://eceweb1.rutgers.edu/~orfanidi/ewa/>
- Pacini A, Costanzo A, Aldhaher S, et al. (2017) Load- and position-independent moving MHz WPT system based on GaN-distributed current sources. *IEEE Transactions on Microwave Theory and Techniques* 65(12): 5367–5376.
- Paprotny I, Xu Q, Chan WW, et al. (2013) Electromechanical energy scavenging from current-carrying conductors. *IEEE Sensors Journal* 13(1): 190–201.
- Paul K and Sarma AK (2018) Fast and efficient wireless power transfer via transitionless quantum driving. *Scientific Reports* 8: 4134.
- Popovic Z, Falkenstein EA, Costinett D, et al. (2013) Low-power far-field wireless powering for wireless sensors. *Proceedings of the IEEE* 101(6): 1397–1409.
- Rao SS (2010) *Mechanical Vibrations*. 5 ed. Upper Saddle River, NJ: Prentice Hall.
- Renaud M, Elfrink R, Jambunathan M, et al. (2012) Optimum power and efficiency of piezoelectric vibration energy harvesters with sinusoidal and random vibrations. *Journal of Micromechanics and Microengineering* 22(10): 105030.

- Renno JM, Daqaq MF and Inman DJ (2009) On the optimal energy harvesting from a vibration source. *Journal of Sound and Vibration* 320(1–2): 386–405.
- Roundy S and Wright PK (2004) A piezoelectric vibration based generator for wireless electronics. *Smart Materials and Structures* 13(5): 1131–1142.
- Sample AP, Meyer DT and Smith JR (2011) Analysis, experimental results, and range adaptation of magnetically coupled resonators for wireless power transfer. *IEEE Transactions on Industrial Electronics* 58(2): 544–554.
- Shu YC, Lien IC and Wu WJ (2007) An improved analysis of the SSHI interface in piezoelectric energy harvesting. *Smart Materials and Structures* 16(6): 2253–2264.
- Song M, Belov P and Kapitanova P (2017) Wireless power transfer inspired by the modern trends in electromagnetics. *Applied Physics Reviews* 4(2): 021102.
- Tilmans HAC (1996) Equivalent circuit representation of electromechanical transducers: I. Lumped-parameter systems. *Journal of Micromechanics and Microengineering* 6: 157–176.
- Truong BD and Roundy S (2018) Wireless power transfer system with center-clamped magneto-mechano-electric (MME) receiver: model validation and efficiency investigation. *Smart Materials and Structures* 28(1): 015004.
- Truong BD (2019) Investigation on power optimization principles for series-configured resonant coupled wireless power transfer systems. *AEU: International Journal of Electronics and Communications* 106: 67–81.
- Vittoz E (2010) *Low-Power Crystal and MEMS Oscillators: The Experience of Watch Developments* (Integrated Circuits and Systems). Dordrecht: Springer.
- Wei C and Jing X (2017) A comprehensive review on vibration energy harvesting: modelling and realization. *Renewable and Sustainable Energy Reviews* 74: 1–18.
- Zhu C, Leung VCM, Shu L, et al. (2015) Green internet of things for smart world. *IEEE Access* 3: 2151–2162.

Appendix I

Cases I, II and III: a comparison

Figure 14 gives us a bigger picture than the first two cases with a wide frequency range. We note that when the input frequency is far away from ω_0 and ω_1 , the optimal load can be approximated by $R_{\text{off}}^{\text{opt}} = 1/(\omega C_0)$.

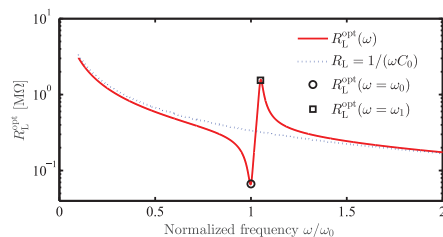


Figure 14. General solution of the optimal load as a function of the drive frequency, the other parameters are taken from Table I.

This analysis can also be applied for non-resonant transducers.

Appendix 2

Case IV: optimal frequency as a function of load resistance

Figure 15 presents the changes of the optimal frequency when the load varies from 1Ω to $100 \text{ M}\Omega$. It is to be expected that the optimal frequency of high resistances approaches the anti-resonance (i.e. open-circuit resonant frequency) and that of low resistances tends to coincide with the resonant (short-circuit) frequency. However, when $R_L \in [100 \text{ k}\Omega, 5 \text{ M}\Omega]$ roughly, the optimal frequency is in between $f_0 = \omega_0/(2\pi)$ and $f_1 = \omega_1/(2\pi)$ and is given by formula (28). Once again, the model predicts exactly where the drive frequency should be for the specific load used in the experiments.

Appendix 3

Case V: numerical solutions

Figure 16 presents the optimum power at each driving frequency with the corresponding optimal load given by equation (26). The global maximum output power is achieved either at ω_{M_1} or ω_{M_2} , while a local minimum is observed at ω_m . Given the facts that asynchronously switched electronic interfaces (e.g. buck-boost converters) can be utilized as an effective load resistance (i.e. by tuning the duty cycle of the switching circuit; D'hulst et al., 2006, 2010) and the driving frequency of a WPT system is able to be adjusted easily, the exact solutions presented in this section offer a convenient means for realizing an optimal system in practice.

In order to check the accuracy of the analytical calculation procedure, we also develop a numerical approach to solve the general power optimization problem (Case V) based on equation (21). It is formulated as follows

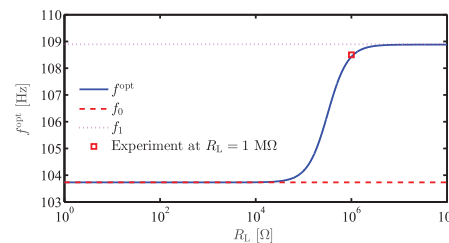


Figure 15. General solution of the optimal frequency for an arbitrary load resistance.

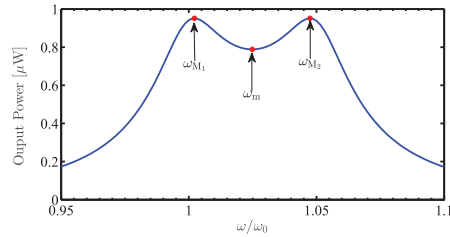


Figure 16. Maximum transferred power as a function of the driving frequency and the optimal load calculated by equation (26). Solid dot: analytical solutions of the optimal frequencies (equations (37) to (39)).

$$\max_{\omega, \tau} P \text{ subject to } \omega > 0, \tau > 0. \quad (76)$$

To deal with such a nonlinear optimization problem with inequality constraints, the nonlinear Interior Point and Sequential Quadratic Programming methods can be used (Jorge Nocedal, 2006). The numerical solutions are exactly the same as those obtained from analytical closed form, showing that the optimal loads and frequencies are either close to but not necessarily identical to *Cases I and II*. The differences between them are strongly dependent on system parameters such as beam geometry, parasitic damping coefficient, and transduction factor.

Figure 17 shows two normalized numerical solutions of the general power optimization problem addressed in equation (76), note that $\omega_1/\omega_0 = 1.05$. Here, we denote R_L^0 and R_L^1 as the loads expressed in equations (22) and (24), respectively. With the particular prototype used for these measurements, the optimal solutions of *Case V* are not so different from those of *Cases I and II*. Therefore, the obtained power outputs of three mentioned cases are considerably indistinguishable. This indicates that for practical convenience, either ω_0 or ω_1 can be used to drive moderately coupled systems, while the load is optimized to maximize the output power.

However, we mathematically point out an example shown in Figure 18 where the maximum powers given by equations (23) and (25) are more clearly different from the solution of equation (76). Pseudo parameters $b_s, t_{p-s}, L_s, \Gamma_s$ are set for simulations by multiplying the actual ones (in Table 1) with a chosen factor as seen in Figure 18. The aim of this study is to realize that the resonant/anti-resonant frequencies are not always the optimal value, which depends on particular system

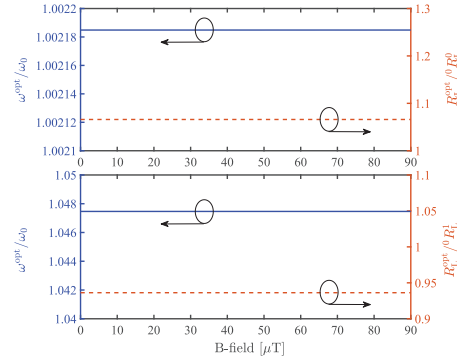


Figure 17. Numerical solutions of the optimal load and frequency, which is independent on the applied **B** field.

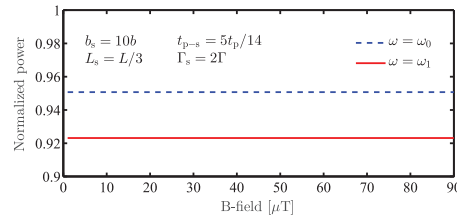


Figure 18. An example indicates the difference when the power obtained from *Cases I and II* are compared to that of *Case V*.

parameters. Finally, it should be noted that all theoretical results reported in this article can be independently affirmed by dynamic simulations using SPICE simulators.

While the particular beam used in these measurements only generated a few μW , the power density was about $152 \mu\text{W}/\text{cm}^3$ at $B_{ac} = 300 \mu\text{T}$, which is typical with the use of piezoelectric technologies (Khaligh et al., 2010; Moss et al., 2015) and is comparable to that of far-field wireless powering systems (Popovic et al., 2013). Furthermore, our simulations indicate that if we double the magnet volume and halve the length of the piezoelectric cantilever, the power density could be significantly higher, with a factor of ~ 3.8 potential improvement.

3.2 Wireless Power Transfer System With Center-Clamped Magneto-Mechano-Electric (MME) Receiver: Model Validation and Efficiency Investigation

The equivalent circuit model presented in Section 3.1 is now extended to a symmetric structure when the bimorph piezoelectric beam is clamped at the middle and two magnet masses are attached at the two ends. For many low power applications, the transmission efficiency is not a key metric for evaluating the performance of a wireless power transfer system; however, it is still of interest and worthy of analysis. A complete system model accounting for the dynamics of both transmitting and receiving sides is essentially required for such purpose. Due to the similarity of the electromechanical, and electrodynamic transduction mechanisms: piezoelectric, electrostatic, electromagnetic, and magnetoelectric, we aim to develop a unified model in which a single analysis can cover all of the four transducer types. All the findings are validated by experimental results.

© 2018 IOP Publishing Ltd. Reprinted, with permission from B. D. Truong and S. Roundy, "Wireless power transfer system with center-clamped magneto-mechano-electric (MME) receiver: model validation and efficiency investigation," *Smart Materials and Structures*, vol. 28, in November 2018.

Wireless power transfer system with center-clamped magneto-mechano-electric (MME) receiver: model validation and efficiency investigation

Binh Duc Truong  and Shad Roundy

Department of Mechanical Engineering, University of Utah, 1495 E. 100 S., 1550 MEK, Salt Lake City, UT 84112, United States of America

E-mail: Binh.D.Truong@utah.edu

Received 6 July 2018, revised 21 October 2018

Accepted for publication 25 October 2018

Published 20 November 2018



Abstract

This paper presents a complete equivalent circuit model for a wireless power transfer concept utilizing a center-clamped piezoelectric cantilever beam with magnetic tip masses as a receiver. The analytical solution for the power delivered to a load resistance is given as a function of material properties, beam characteristics and external magnetic field strength. The lumped element model is experimentally verified. The efficiency of the system is thoroughly investigated and validated. The essential effect of the coil resistance is highlighted. The analyses show that optimization of transmitter coil size and geometry of the piezoelectric transducer has a significant impact on the transduction factor between the magnetic-mechanical-electrical domains, which greatly improves the transmission efficiency. Finally, the model for evaluating the efficiency is generalized for other similar structures.

Keywords: wireless power transfer, energy conversion/generation, transmission efficiency

(Some figures may appear in colour only in the online journal)

Nomenclature

H_{ac}	AC magnetic field of the Helmholtz coils	ϵ_{33}^S	permittivity component at constant strain
M_B	pure moment acts on the magnet tip mass M	e_{31}	piezoelectric stress constant
J_r	remanent magnetic polarization	d_{31}	piezoelectric charge constant
V_M	volume of the magnet tip mass	b	mechanical damping coefficient
F_M	equivalent force corresponding to the moment induced by magnetic field	L_m	dimension of the cubic magnet
l_{eff}	effective length	M	magnet mass
m	effective mass of the piezoelectric transducer	$2L_g$	total width of the anchor
m_b	beam mass	K_0	short circuit stiffness
$(YI)_c$	flexural rigidity of the composite beam	K_1	open circuit stiffness
$Y_p (t_p)$	elasticity constants (thickness) of the piezoelectric layers	Γ_p	electromechanical transduction factor
$Y_s (t_s)$	elasticity constants (thickness) of the shim	Γ_M	electrodynamical transduction factor
w	beam width	C_0	nominal capacitance of the piezoelectric transducer
		R_L	load resistance

ζ	dimensionless damping ratio, $\zeta = b/(2m\omega_0)$
L_H	total inductance of the Helmholtz coil
R_H	parasitic resistance of the Helmholtz coil
V_s	source voltage
R_s	source resistance
Ψ	electromagnetic transduction factor
L_0	internal inductance of electromagnetic transducer

1. Introduction

Energy harvesting (EH) and wireless power transfer (WPT) provide means to power electronics while avoiding battery replacement, especially for autonomous wireless sensor nodes and wearable or implantable devices [1–6]. Toward sensing systems for human health monitoring, it should be noted that the power obtained from EH systems strongly depends on human activities, which vary remarkably during the day [7, 8]. Meanwhile, WPT provides the advantage that power from a source can be controlled and delivered to an electrical load actively and directly [9]. The latter technique, therefore, has gained more and more attention from researchers in the last decade.

Non-radiative (or near-field) WPT/charging systems are used in a wide variety of applications such as smart phones, unmanned aerial vehicles and biomedical electronics [10], utilizing capacitive or inductive coupling [11, 12]. However, the operating frequency of these technologies is typically in the range of MHz, which constrains the amplitude of the magnetic fields that can be applied to humans due to safety standards [13, 14].

One approach to overcome this challenge was to use an electromagnetic (electrodynamical) transducer as a receiver [9]. The authors later developed similar methods to extend the transmission range for bio-implants and wearables with torsional springs and a rotating magnet mass [15–17]. For harvesting energy from current-carrying conductors [18] or ambient low-frequency magnetic fields [19, 20], an alternative technique is to utilize a piezoelectric cantilever beam (either d_{31} or d_{33} coupling) with a permanent magnet placed at its tip. The mechanical resonance frequency of the electromechanical and electrodynamic receivers can be designed much lower than 1 kHz, allowing much higher external magnetic flux densities. Besides, the piezoelectric and electromagnetic generators can also scavenge energy from vibrations when the user is moving and there is no power transmitted. Several authors mentioned above have attempted to model those structures. However, these developments were either specific to particular devices and did not reflect the generalized problem, or lack of details in describing the complete model.

A more recent WPT architecture is based on the magneto-electric (ME) effect in composites of magnetostrictive and piezoelectric materials [21–24]. Most authors only investigated the power transferred to a load resistance through experiments, and did not fully address the system efficiency. In addition, observing that there is a similarity among the four

resonator types (i.e. electrostatic, electromagnetic, piezoelectric and ME transducers), we are motivated to explore a complete unified-model considering both transmitting and receiving sides that can cover all four types.

In this work, we propose a symmetric structure when the bimorph piezoelectric beam is clamped at the middle and two magnet masses are attached at the two ends. We develop a theoretical lumped element model to analyze and predict system performance, which is then verified by an experimental prototype. Although the transmission efficiency is not a key metric for low power systems, it is still of interest and worthy of analysis. Both the output power and the system efficiency are derived from the equivalent circuit models.

2. Lumped-parameter model of the piezoelectric receiver

2.1. Linear two-port model

Figure 1 shows the proposed configuration where the bimorph piezoelectric beam is clamped at the middle and is utilized as a receiver for the WPT system. Two permanent magnets are positioned at the two ends of the beam. Their magnetic directions are parallel and in opposite direction to each other. With the use of a circular Helmholtz (CH) coil as a transmitter, a uniform magnetic field generated along the longitudinal axis induces a torque of equal magnitude on each magnet mass, but in opposite directions (i.e. clockwise/anticlockwise and vice versa). As a consequence, two portions of the cantilever beam vibrate like a bird's flapping wings.

The operation of the structure can be represented by an equivalent circuit model as shown in figure 2. The linear two-port equations describing the relation of the transducer force F_T , the charge on the positive electrical terminal q , the displacement at the center of tip mass x and the voltage across the electric terminals V_T are [25, 26]

$$F_T = K_0 x + \Gamma_P V_T, \quad (2.1)$$

$$q = -\Gamma_P x + C_0 V_T, \quad (2.2)$$

where Γ_P is the transduction factor between the mechanical and electrical domains.

The lumped elements of the model are determined as follows [27]

$$M_B = J_r V_M H_{ac}, \quad (2.3)$$

$$F_M = \frac{3 M_B}{2 l_{eff}}, \quad (2.4)$$

$$l_{eff} = \frac{L + L_0}{2}, \quad (2.5)$$

$$m = M + \frac{33}{140} m_b, \quad (2.6)$$

$$K_0 = \frac{3(YI)_c}{l_{eff}^3}, \quad (2.7)$$

$$(YI)_c = 2Y_p \left[\frac{wt_p^3}{12} + wt_p \left(\frac{t_s + t_p}{2} \right)^2 \right] + Y_s \frac{wt_s^3}{12}, \quad (2.8)$$

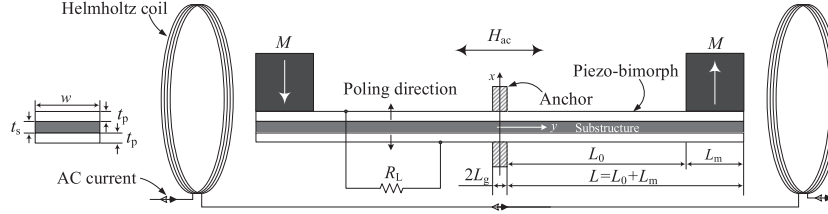


Figure 1. Schematic of the center-clamped bimorph piezoelectric transducer with two magnet tip masses used as a receiver for a low-frequency WPT system.

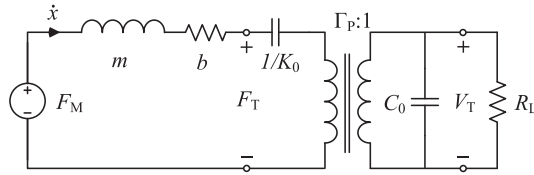


Figure 2. Equivalent two-port model of the piezoelectric transducer.

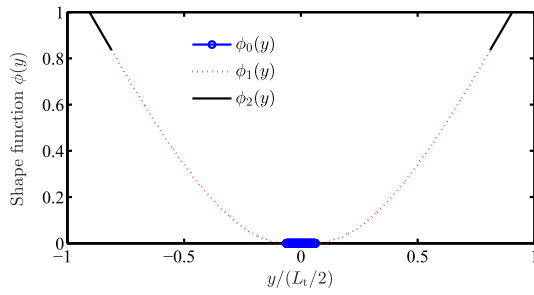


Figure 3. Static deflection shape function $\phi(y)$, here L_t is the total length of the beam, $L_t = 2(L + L_g)$.

$$C_0 = \epsilon_{33}^S \frac{w(L + L_g)}{t_p}, \quad (2.9)$$

where L and L_0 are the intermediate lengths defined as in figure 1, $m_b = wL(2t_p\rho_p + t_s\rho_s)$, $M = \rho_M V_M$, the definitions of other parameters can be found in the Nomenclature section. Differing from our previous work [27], the cantilever beam is

2.2. Static shape function

In the same manner presented by Kim *et al* [28] and Wang *et al* [29], the tip mass is treated as a distributed mass rather than a point mass. While the authors in [28, 29] investigated a piezoelectric EH using the distributed-parameter model, we develop an equivalent linear two-port model instead (it is perhaps the most widely used model for piezoelectric-based devices). An advantage of this method is to express the output power by an explicit form, which is convenient to further interpret the system performance. Assume that the structure is symmetric about the x -axis, the static deflection shape function $\phi(y)$ can be described as follows

$$\begin{aligned} 0 \leq |y| \leq L_g: \quad & \phi_0(y) = 0, \\ L_g \leq |y| \leq (L_0 + L_g): \quad & \phi_1(y) \\ & = q_m \left(\frac{L_m(L_0 + L)}{4} |y - L_g \text{sign}(y)|^2 \right. \\ & \quad \left. - \frac{L_m}{6} |y - L_g \text{sign}(y)|^3 \right) \\ & + q_b \left(\frac{L^2}{4} |y - L_g \text{sign}(y)|^2 - \frac{L}{6} |y - L_g \text{sign}(y)|^3 \right. \\ & \quad \left. + \frac{1}{24} |y - L_g \text{sign}(y)|^4 \right), \quad (L_0 + L_g) \leq |y| \\ \leq (L + L_g): \quad & \phi_2(y) = q_m \left(\frac{L_0 L_m L}{2} |y - L_g \text{sign}(y)| \right. \\ & \quad \left. - \frac{L_0^2 L_m (2L + L_m)}{12} \right) + q_b \left(\frac{L_0 (L^2 + L_0 L_m + 2L_m^2)}{6} \right. \\ & \quad \left. |y - L_g \text{sign}(y)| - \frac{L_0^2 (L^2 + 2L_0 L_m + 5L_m^2)}{24} \right), \end{aligned} \quad (2.10)$$

where

$$\begin{aligned} q_m &= \frac{24}{L_0 [2L_m (4L_0^2 + 6L_0 L_m + 3L_m^2) + q_r (3L_0^3 + 10L_0^2 L_m + 12L_0 L_m^2 + 6L_m^3)]}, \\ q_b &= q_m q_r, \quad \text{and } q_r = \frac{L_m m_b}{LM}. \end{aligned} \quad (2.11)$$

clamped at the center instead of one end. In addition, this paper focuses more on the efficiency of a complete transmission system than investigating power optimization issues.

The final static shape function is depicted in figure 3. It should be noted that the vibration displacement of each branch (i.e. $y \leq 0$ or $y \geq 0$) is exactly the same as using a

single piezoelectric beam correspondingly. However, in a realistic application, if we use two piezoelectric resonators, the electronic interface circuit is required to deal with the challenge of multiple outputs. This may require a more sophisticated complete system. Therefore, utilizing the center-clamped cantilever beam as an alternative is an appropriate option to avoid that issue.

2.3. Modal coupling coefficient

The electromechanical coupling factor is derived based on the static shape function as [30, 31]

$$\begin{aligned}\Gamma_P &= -e_{31}w \frac{t_p + t_s}{2} \int_{-(L+L_g)}^{(L+L_g)} \frac{d^2\phi(y)}{dy^2} dy \\ &= -e_{31}w \frac{t_p + t_s}{2} \int_{-(L+L_g)}^{(L+L_g)} \left[\frac{d^2\phi_0(y)}{dy^2} + \frac{d^2\phi_1(y)}{dy^2} + \frac{d^2\phi_2(y)}{dy^2} \right] dy.\end{aligned}\quad (2.12)$$

Note that $\phi_0(y) = 0$ for all y such that $0 \leq |y| \leq L_g$ and $\phi_2(y)$ is a first order polynomial of y for all y such that $(L_0 + L_g) \leq |y| \leq (L + L_g)$, therefore $d^2\phi_0(y)/dy^2 = d^2\phi_2(y)/dy^2 = 0$ and (2.12) reduces to

$$\begin{aligned}\Gamma_P &= -e_{31}w \frac{t_p + t_s}{2} \\ &\times \left[\int_{-(L_0+L_g)}^{-L_g} \frac{d^2\phi_1(y)}{dy^2} dy + \int_{L_g}^{(L_0+L_g)} \frac{d^2\phi_1(y)}{dy^2} dy \right] \\ &= -e_{31}w \frac{t_p + t_s}{2} \\ &\times \left[\frac{d\phi_1(y)}{dy} \Big|_{y=-(L_0+L_g)}^{y=-L_g} + \frac{d\phi_1(y)}{dy} \Big|_{y=L_g}^{y=(L_0+L_g)} \right].\end{aligned}\quad (2.13)$$

Denote $\kappa = |y - L_g \text{sign}(y)| \geq 0$, we can re-write $\phi_1(y)$ as a function of κ as follows

$$\begin{aligned}\phi_1(\kappa) &= q_m \left(\frac{L_m(L_0 + L)}{4} \kappa^2 - \frac{L_m}{6} \kappa^3 \right) \\ &+ q_b \left(\frac{L^2}{4} \kappa^2 - \frac{L}{6} \kappa^3 + \frac{1}{24} \kappa^4 \right).\end{aligned}\quad (2.14)$$

This implies that

$$\frac{d\phi_1(\kappa)}{d\kappa} \Big|_{\kappa=0} = 0.\quad (2.15)$$

In addition, $\kappa \xrightarrow{y \rightarrow \pm L_g} 0$, we infer that

$$\frac{d\phi_1(y)}{dy} \Big|_{y=-L_g} = \frac{d\phi_1(y)}{dy} \Big|_{y=L_g} = 0.\quad (2.16)$$

These results collide with the fact that the cantilever beam is clamped at $y = \pm L_g$ and therefore the derivative of the static displacement $\phi_1(y)$ with respect to y at these positions must equal zero by following the boundary conditions.

Formula (2.13) then becomes

$$\Gamma_P = -e_{31}w \frac{t_p + t_s}{2} \frac{d\phi_1(y)}{dy} \Big|_{y=-(L_0+L_g)}^{y=(L_0+L_g)}.\quad (2.17)$$

Due to the symmetric property of $\phi_1(y)$, we get

$$\frac{d\phi_1(y)}{dy} \Big|_{y=-(L_0+L_g)} = -\frac{d\phi_1(y)}{dy} \Big|_{y=(L_0+L_g)}.\quad (2.18)$$

The explicit form of the electromechanical coupling is hence expressed as

$$\begin{aligned}\Gamma_P &= -e_{31}w(t_p + t_s) \frac{d\phi_1(y)}{dy} \Big|_{y=(L_0+L_g)} = -4e_{31}w(t_p + t_s) \\ &\times \frac{3(M + m_b)L^2 - 3m_bL_0L + m_bL_0^2}{6(M + m_b)L^3 - 6m_bL_0L^2 + 2L_0^2L(M + 2m_b) - L_0^3m_b}.\end{aligned}\quad (2.19)$$

Now all the lumped parameters and functions necessary for the model have been obtained.

2.4. Power delivered to a load resistance

Assuming that the piezoelectric resonator is driven by a time harmonic force $F_M(t) = F_0 \cos(\omega t)$ of angular frequency ω , the steady-state average power delivered to a load resistance is computed as

$$P_L = \frac{1}{T} \int_0^T \frac{V_T^2(t)}{R_L} dt = \frac{1}{2} \frac{|V_0|^2}{R_L},\quad (2.20)$$

where $T = 1/f = 2\pi/\omega$ is the period of the sinusoidal function $F_M(t)$.

The linear two-port model shown in figure 2 is commonly described by two equations (2.1) and (2.2) [25, 26] where x and V_T are independent variables. Other formulations such as the one with x and q as independent variables are [26, 32]

$$F_T = K_I x + \frac{\Gamma_P}{C_0} q,\quad (2.21)$$

$$V_T = \frac{\Gamma_P}{C_0} x + \frac{1}{C_0} q.\quad (2.22)$$

Taking the time derivatives of both sides of equation (2.22) and note that $\dot{q} = -I_L = -V_T/R_L$ (i.e. R_L is the load resistance connected directly to the electrical ports and I_L is the current through it), we have

$$\dot{V}_T = \frac{\Gamma_P}{C_0} \dot{x} - \frac{V_T}{R_L C_0}.\quad (2.23)$$

Equation (2.23) in the frequency domain is represented by

$$V_0 \left(j\omega + \frac{1}{R_L C_0} \right) = j\omega \frac{\Gamma_P}{C_0} X_0,\quad (2.24)$$

where V_0 and X_0 are the complex amplitudes of V_T and x respectively. A closed-form of V_0 as a function of X_0 is

$$V_0 = \frac{\Gamma_P}{C_0} \frac{j\omega R_L C_0}{1 + j\omega R_L C_0} X_0.\quad (2.25)$$

From (2.20), the output power can be written as

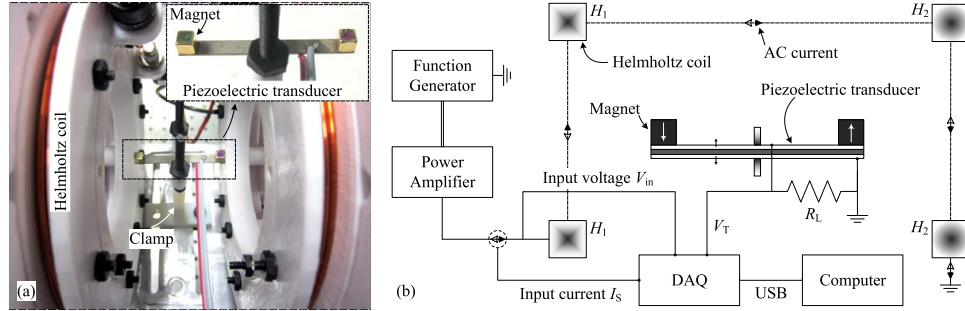


Figure 4. (a) Experimental prototype of the Helmholtz transmitting coil and the piezoelectric/magnet receiver. (b) Sketch of the electrical setup for measuring the input voltage/current V_{in}/I_s and the output voltage V_L across the load resistance R_L . The two coils connected in series are marked by notations H_1 and H_2 .

$$P_L = \frac{1}{2} \frac{\Gamma_P^2}{C_0} \frac{\omega^2 R_L C_0}{1 + (\omega R_L C_0)^2} |X_0|^2 = \frac{1}{2} \Delta K \frac{\omega^2 \tau}{1 + (\omega \tau)^2} |X_0|^2, \quad (2.26)$$

where the electrical time scale, the open-circuit stiffness and the difference between the highest and lowest stiffnesses are

$$\tau = R_L C_0, \quad (2.27)$$

$$K_1 = K_0 + \Delta K, \quad (2.28)$$

$$\Delta K = \frac{\Gamma_P^2}{C_0} \quad (2.29)$$

respectively.

Based on equation (2.2), the complex amplitude of the charge Q_0 in the frequency domain is

$$\begin{aligned} Q_0 &= -\Gamma_P X_0 + C_0 V_0 = -\Gamma_P X_0 + \Gamma_P \frac{j\omega \tau}{1 + j\omega \tau} X_0 \\ &= -\frac{\Gamma_P}{1 + j\omega \tau} X_0. \end{aligned} \quad (2.30)$$

From (2.21), the equation of motion in the mechanical domain is rearranged as

$$m\ddot{x} = -K_1 x - b\dot{x} - \frac{\Gamma_P}{C_0} q + F_0 \cos(\omega t). \quad (2.31)$$

Similarly, the equivalent equation in the frequency domain reads as

$$\begin{aligned} -m\omega^2 X_0 &= -K_1 X_0 - j\omega b X_0 - \frac{\Gamma_P}{C_0} Q_0 + F_0 \\ &= -K_1 X_0 - j\omega b X_0 + \Delta K \frac{1}{1 + j\omega \tau} X_0 + F_0, \end{aligned} \quad (2.32)$$

which results in

$$X_0 = \frac{F_0}{K_1 - m\omega^2 + j\omega b - \Delta K \frac{1}{1 + j\omega \tau}}. \quad (2.33)$$

The squared amplitude of the displacement has the following form

$$|X_0|^2 = \frac{F_0^2}{\left[\omega b + \Delta K \frac{\omega \tau}{1 + (\omega \tau)^2} \right]^2 + \left[K_1 - m\omega^2 - \Delta K \frac{1}{1 + (\omega \tau)^2} \right]^2}. \quad (2.34)$$

Finally, the explicit form of the output power is

$$\begin{aligned} P_L &= \frac{1}{2} \Delta K \frac{\omega^2 \tau}{1 + (\omega \tau)^2} \\ &\times \frac{F_0^2}{\left[\omega b + \Delta K \frac{\omega \tau}{1 + (\omega \tau)^2} \right]^2 + \left[K_1 - m\omega^2 - \Delta K \frac{1}{1 + (\omega \tau)^2} \right]^2}. \end{aligned} \quad (2.35)$$

Formula (2.35) is the main objective to validate the model, where the frequency and \mathbf{B} -field responses are the most important aspects.

2.5. Measurement and validation

Figure 4(a) shows the Helmholtz coils (transmitter) and the middle-clamped piezoelectric transducer (receiver) used in the experiments, and figure 4(b) illustrates the complete electrical setup. The receiver consists of a bimorph PZT-5A4E cantilever beam with two Neodymium (NdFeB) permanent magnets attached at its tips. The material properties can be found from the datasheets on Piezo System Inc. and K&J Magnetics Inc. websites. The two coils are driven by a Rigol power amplifier while a Tektronix function generator acts as a control unit. The \mathbf{B} -field generated by the Helmholtz coils is measured by an AC milligauss meter. The current I_s and voltage V_{in} inputted to the coils along with the output voltage V_L induced in the load R_L are collected by a data acquisition (DAQ) unit connected to a computer through USB communication protocol. The average output power is then calculated as $P_L = \frac{1}{T} \int_0^T \frac{V_L^2(t)}{R_L} dt$. The mechanical damping coefficient b is determined by fitting the model simulations to the experimental data at $B_{ac} = 50.77 \mu\text{T}$ and $R_L = 1 \text{ M}\Omega$. All the model parameters are now identified and listed in table 1, which are then used for validating all following cases.

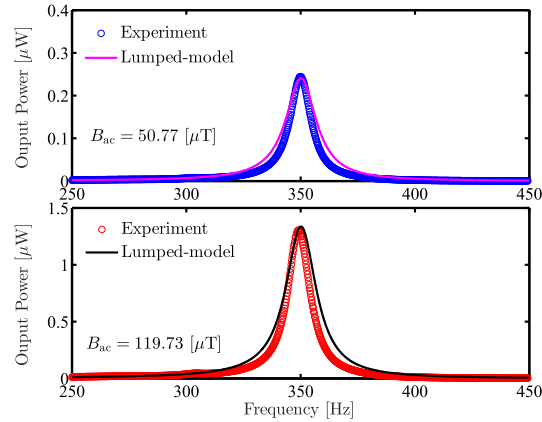


Figure 5. Performance of the WPT system under swept-frequency conditions over a time duration of 60 s.

Table 1. Model parameters, including material properties of (i) Bimorph PZT-5A4E cantilever beam with brass substructure and (ii) neodymium magnets.

Parameters	Value
μ_0	$4\pi \times 10^{-7} \text{ H m}^{-1}$
w	3.175 mm
$L_t = 2(L + L_g)$	32.55 mm
$2L_g$	1.90 mm
t_p	0.14 mm
Y_p	$66 \times 10^9 \text{ Pa}$
d_{31}	$-190 \times 10^{-12} \text{ m V}^{-1}$
C_0	4.83 nF
ρ_p	7800 kg m^{-3}
t_s	0.1 mm
Y_s	$100 \times 10^9 \text{ Pa}$
ρ_s	8500 kg m^{-3}
L_m	3.175 mm
ρ_M	8630 kg m^{-3}
J_r	1.45 T
b	$18.92 \times 10^{-3} \text{ Nsm}^{-1}$
ζ	1.7%

Figure 5 presents the frequency response of the system with different amplitudes of the applied \mathbf{B} -field, $B_{ac} = 50.77$ and $119.73 \mu\text{T}$. The load is fixed at $1 \text{ M}\Omega$. The measured data are compared to the model predictions by formula (2.20), which shows a good agreement between them. In particular, the optimal frequencies f_r observed in experiment and simulation at $B_{ac} = 50.77 \mu\text{T}$ are the same at 350 Hz while the other case, $B_{ac} = 119.73 \mu\text{T}$, indicates a slight difference of 1 Hz (i.e. $f_r = 349 \text{ Hz}$ from the experimental results). This can be explained by the fact that the structure is not perfectly symmetric and the anchor is not completely rigid as assumptions of the model. These imperfections could lead to possible slight non-linearity on the transducer behaviors and energy lost due to plastic deformation. Their effect on system performance is clearer with increasing the external magnetic field (or in other words, the torques acting on the two magnets).

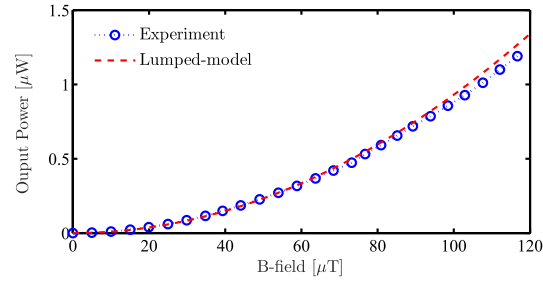


Figure 6. System response with discrete variation of the applied \mathbf{B} -field while the drive frequency is kept fixed at 350 Hz.

In order to verify the consistency of the model, we choose to drive the WPT system at the fixed frequency $f_r = 350 \text{ Hz}$ and only vary the \mathbf{B} -field amplitude in a wide range from 0 up to $120 \mu\text{T}$. The model-predicted simulations are still in a good agreement with the experimental results as shown in figure 6. It is also confirmed that higher strengths of magnetic field cause larger errors between the predictions and measurements due to slight differences in the actual optimal frequency and the chosen f_r . Although, these differences can be considered almost negligible in practice. In summary, the lumped element model has been successful in explaining behavioral characteristics of the WPT system.

3. Investigation on the efficiency of a WPT system

3.1. Theoretical model

Since the efficient operating frequency range of the center-clamped configuration is typically much less than 1 kHz, the system is considered electromagnetically quasi-static, and therefore the electromagnetic radiation from the coils is neglected. Figure 7 shows a model for investigating the transmission efficiency of a WPT system. Here, V_s and R_s are the source voltage and internal resistance. L_H and R_H represent the total inductance and resistance of the Helmholtz coils. Γ_M is the coupling factor relating the source current I_s and the electromotive force V_{EMF} to the force acting on the piezoelectric-beam F_M and its tip mass velocity \dot{x} respectively. Note that L_H is the sum of each coil inductance L_{C_i} (configured in series) and the mutual inductance M_C between the two coils, i.e. $L_H = L_{C_1} + L_{C_2} + M_C$ [33]. With the fact that the generated \mathbf{B} -field is proportional to the current through the Helmholtz coil which is dependent on the total inductance L_H , determining specific values of $L_{C_{i/2}}$ and M_C does not affect on the final result, and is not the objective of this paper.

Due to the similarity of the electromechanical/electrodynamic transduction mechanisms: piezoelectric, electrostatic, electromagnetic and ME [26, 34], we aim to develop a unified model that is able to evaluate the system efficiency when one of these resonator types is used as a receiver. Despite the apparent differences, the first three architectures can be described by similar mathematical equations and it is possible to obtain the output power of all the three transducers on the same form, i.e.

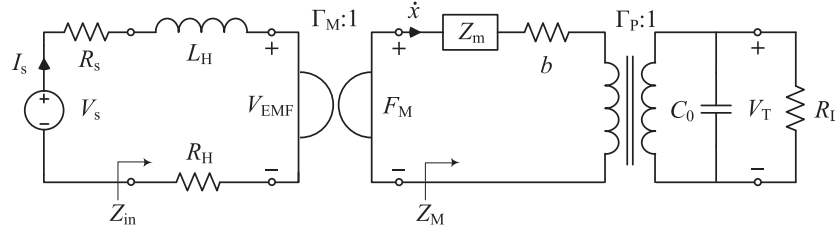


Figure 7. Schematic of lumped element model for wireless power transfer systems with piezoelectric transducer as a receiver.

(2.35). For the electrostatic and piezoelectric generators, the electrical time scale τ and the stiffness difference ΔK are defined by (2.27) and (2.29) respectively. In the case of using the electromagnetic transducer, we perform the following substitutions to get the corresponding output power

$$\tau \rightarrow \tau_e = \frac{L_0}{R_L}, \quad (3.1)$$

$$\Delta K \rightarrow \Delta K_e = \frac{\Psi^2}{L_0}, \quad (3.2)$$

where L_0 is the clamped inductance and Ψ is the electromagnetic transduction factor. Details of these analyses were thoroughly presented in [26]. We also provide an alternative model along with derivations of the output power and the efficiency in appendix A.

It is worthwhile to note that, for the structure under consideration, the mechanical impedance is explicitly expressed as a mass-spring system

$$Z_m = j(\omega m - K_0/\omega). \quad (3.3)$$

However, in general Z_m is an inseparable function of frequency and material properties. For instance, the impedance of the bimorph piezoelectric/magnetostrictive laminated composite beam vibrating longitudinally under applied magnetic field due to the ME effect is

$$Z_m \rightarrow Z_e = j\bar{\nu}\bar{\rho}A \left(\tan \frac{kL_e}{2} - \frac{1}{\sin(kL_e)} \right). \quad (3.4)$$

An example of the ME device is presented in appendix B.

The generalized forms $Z_m = jZ_0$, τ and ΔK thus will be used for further derivations. The impedance Z_M and Z_{in} in figure 7 are given as follows

$$Z_M = Z_m + b + \Gamma_P^2 \frac{R_L}{1 + j\omega R_L C_0} = jZ_0 + b + \Delta K \frac{\tau}{1 + j\omega\tau}, \quad (3.5)$$

$$Z_{in} = j\omega L_H + R_H + \frac{\Gamma_M^2}{Z_M}, \quad (3.6)$$

$$\Re\{Z_{in}\} = R_H + \frac{(\alpha\varphi_m)^2 \left[b + \Delta K \frac{\tau}{1 + (\omega\tau)^2} \right]}{\left[-Z_0 + \Delta K \frac{\omega\tau^2}{1 + (\omega\tau)^2} \right]^2 + \left[b + \Delta K \frac{\tau}{1 + (\omega\tau)^2} \right]^2}, \quad (3.7)$$

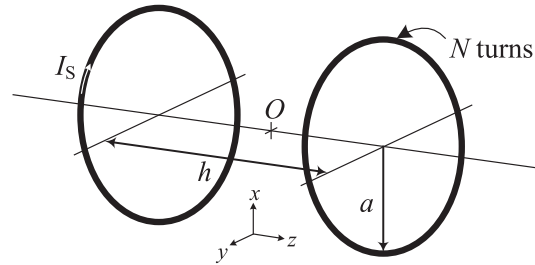


Figure 8. Configuration of circular Helmholtz coil, where the radius of each coil and the distance between them are denoted by a and h respectively which are the same as in [35] for convenience of following derivations.

$$\Im\{Z_{in}\} = \omega L_H - \frac{(\alpha\varphi_m)^2 \left[-Z_0 + \Delta K \frac{\omega\tau^2}{1 + (\omega\tau)^2} \right]}{\left[-Z_0 + \Delta K \frac{\omega\tau^2}{1 + (\omega\tau)^2} \right]^2 + \left[b + \Delta K \frac{\tau}{1 + (\omega\tau)^2} \right]^2}. \quad (3.8)$$

The power input to the network and the transmission efficiency are then determined by

$$P_{in} = \frac{1}{2} |V_s|^2 \frac{\Re\{Z_{in}\}}{|Z_{in} + Z_s|^2} = \frac{1}{2} |V_s|^2 \frac{\Re\{Z_{in}\}}{(R_s + \Re\{Z_{in}\})^2 + (\Im\{Z_{in}\})^2}, \quad (3.9)$$

$$\eta_t = \frac{P_L}{P_{in}}. \quad (3.10)$$

In the considered circumstance, the source impedance is real, $Z_s = R_s$ for the sake of simplification.

We are now considering the CH coil depicted in figure 8, here O is the origin of the rectangular coordinates $Oxyz$. Assume the CH coils are driven by a sinusoidal source, the amplitude of the magnetic flux density \mathbf{B} right at the middle of the two coils is [35]

$$B_{ac} = B_{ac|x=y=z=0} = \mu_0 \alpha |I_s| \quad (3.11)$$

where $\alpha = \frac{N}{2}a^2$

$$\begin{aligned} & \times \left[\frac{1}{\left(a^2 + \left(z + \frac{h}{2}\right)^2\right)^{3/2}} + \frac{1}{\left(a^2 + \left(z - \frac{h}{2}\right)^2\right)^{3/2}} \right] \\ & = N \frac{a^2}{\left(a^2 + \left(\frac{h}{2}\right)^2\right)^{3/2}}, \end{aligned} \quad (3.12)$$

$$\text{and } |I_s| = \left| \frac{V_s}{Z_{in} + R_s} \right| = \frac{|V_s|}{\sqrt{(R_s + \Re\{Z_{in}\})^2 + (\Im\{Z_{in}\})^2}}. \quad (3.13)$$

The constant ratio α may be different for various geometries of the coils and the distance between them. However, the relation between the magnetic field strength \mathbf{H} and the current through the coils can always be written in the form

$$H_{ac} = H_{ac|x=y=z=0} = \alpha |I_s|. \quad (3.14)$$

The matrix representation of the linear two-port gyrator and the electrodynamic coupling coefficient are

$$\begin{bmatrix} F_M \\ V_{EMF} \end{bmatrix} = \begin{bmatrix} \Gamma_M & 0 \\ 0 & \Gamma_M \end{bmatrix} \begin{bmatrix} I_s \\ \dot{x} \end{bmatrix}, \quad (3.15)$$

$$\Gamma_M = \frac{|F_M|}{|I_s|} = \frac{F_0}{|I_s|}. \quad (3.16)$$

Based on the analysis in the previous section, the relationship between the force on the input mechanical port and the \mathbf{H} -field is derived as follows

$$|F_M| = \varphi_m H_{ac}, \quad (3.17)$$

$$\text{where } \varphi_m = \frac{3 J_r V_M}{2 l_{\text{eff}}}. \quad (3.18)$$

Substituting (3.14) and (3.17) into (3.16), we get

$$\Gamma_M = \alpha \varphi_m. \quad (3.19)$$

The amplitude of the force F_M now takes the form

$$F_0 = \alpha \varphi_m \frac{|V_s|}{\sqrt{(R_s + \Re\{Z_{in}\})^2 + (\Im\{Z_{in}\})^2}}. \quad (3.20)$$

The analytical solution of the power transferred to the load is re-written from (2.20) as

$$\begin{aligned} P_L &= \frac{1}{2} \Delta K \frac{\omega^2 \tau}{1 + (\omega \tau)^2} \\ & \times \frac{F_0^2}{\left[-\omega Z_0 + \Delta K \frac{(\omega \tau)^2}{1 + (\omega \tau)^2}\right]^2 + \left[\omega b + \Delta K \frac{\omega \tau}{1 + (\omega \tau)^2}\right]^2}, \end{aligned} \quad (3.21)$$

where $Z_0 = \omega m - K_0/\omega$. From (3.9), (3.20) and (3.21), the efficiency is provided by

$$\begin{aligned} \eta_t &= \frac{1}{\Re\{Z_{in}\}} \Delta K \frac{\omega^2 \tau}{1 + (\omega \tau)^2} \\ & \times \frac{(\alpha \varphi_m)^2}{\left[-\omega Z_0 + \Delta K \frac{(\omega \tau)^2}{1 + (\omega \tau)^2}\right]^2 + \left[\omega b + \Delta K \frac{\omega \tau}{1 + (\omega \tau)^2}\right]^2}. \end{aligned} \quad (3.22)$$

Since Γ_M is relatively small, the reflected loads from the transmitter onto the piezoelectric cantilever beam and vice versa are neglected, and F_0 is considered as a constant and independent on R_L for the sake of simplification. At the resonance frequency $\omega = \omega_0$, the optimal load and maximum power are

$$\text{opt}_\tau = \frac{1}{\omega_0 \sqrt{M_0^2 + 1}}, \quad \text{opt}_R = \frac{1}{\omega_0 C_0 \sqrt{M_0^2 + 1}}, \quad (3.23)$$

$$\text{opt}_P = \frac{1}{4} F_0^2 \frac{M_0}{b} (\sqrt{M_0^2 + 1} - M_0), \quad (3.24)$$

where the resonator figure of merit is defined as a function of frequency

$$M_f = \frac{\Gamma_p^2}{b \omega C_0} \quad (3.25)$$

and at $\omega = \omega_0$, $M_0 = \Gamma_p^2 / (b \omega_0 C_0) = \Delta K / (b \omega_0)$. The corresponding efficiency is

$$\eta_t = \frac{1}{2} \frac{(\alpha \varphi_m)^2 M_0}{\Re\{Z_{in}\} b} (\sqrt{M_0^2 + 1} - M_0) \quad (3.26)$$

$$\text{where } \Re\{Z_{in}\} = R_H + (\alpha \varphi_m)^2 \left(2 - \frac{M_0}{\sqrt{M_0^2 + 1}} \right). \quad (3.27)$$

$\Re\{Z_{in}\}$ is obtained by substituting $\omega = \omega_0$, $\Delta K = b \omega_0 M_0$ and (3.23) into (3.7).

The analytical model (i.e. formulas (3.21) and (3.22)) can be used as a general framework for estimating the output power and the transfer efficiency of any electromechanical/electrodynamic-based WPT system. A summary of the corresponding definitions of Z_0 , τ (τ_c) and ΔK (ΔK_c) for different types of generators is listed in table 2.

3.2. Experimental validation

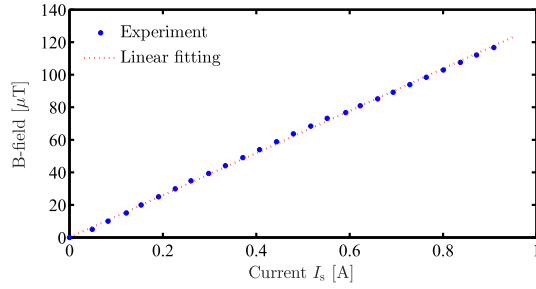
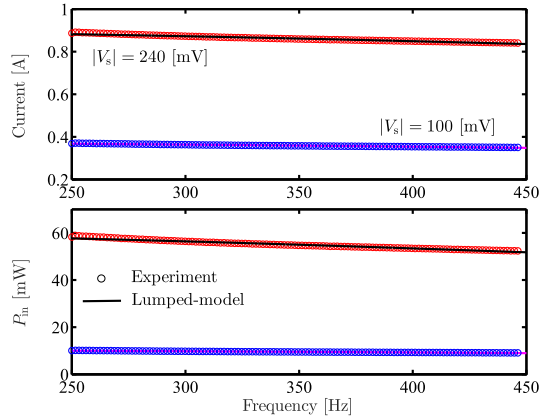
The aim of this section is to describe the characterization of the Helmholtz coils along with identification of the electrodynamic coupling factor and to validate the complete lumped-element model for predicting the efficiency.

The electrical properties of the transmitter, such as the coil inductance L_H and resistance R_H , as well as the source impedance R_s , are measured separately without mounting them on the experimental setup to avoid any possible dynamic interferences with the magnets. Meanwhile, the coefficient α is extracted after construction of the complete system. To be more specific, α is achieved by a linear fit between measured data of the input current I_s and the generated \mathbf{B} -field as shown in figure 9. The average-experimental-input power is calculated as $P_{in} = \frac{1}{2} |V_{in}| |I_s| \cos \phi$ where the method to measure V_{in} and I_s is presented in figure 4 and ϕ [rad s⁻¹] is the phase difference between them. The experimental efficiency is then simply obtained by (3.10). The additional system parameters are listed in table 3.

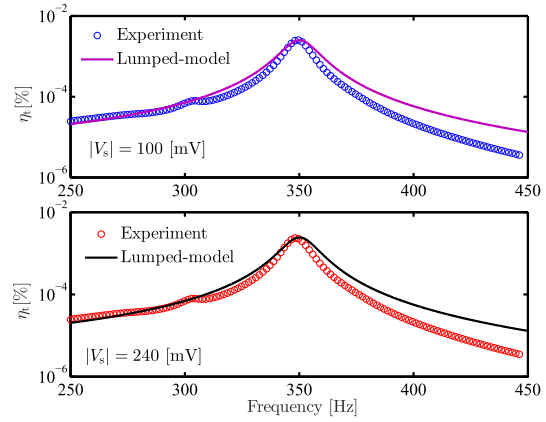
Figure 10 presents the variation of the input current and power in terms of frequency with different values of the voltage source amplitude $|V_s| = 100$ mV and 240 mV. Since the main purpose is to verify the proposed model, $|V_s|$ is chosen arbitrarily and the \mathbf{B} -field amplitude is measured

Table 2. Corresponding definitions of the mechanical impedance, the electrical time scale and the stiffness difference of four transducer types used in formulas (3.21) and (3.22).

Parameters	Magnetolectric	Piezoelectric/Electrostatic	Electromagnetic
Z_0	$\bar{v}\bar{\rho}A(\tan(kL_c/2) - 1/\sin(kL_c))$	$\omega m - K_0/\omega$	$\omega m - K_0/\omega$
τ (τ_c)	$R_L C_0$	$R_L C_0$	L_0/R_L
ΔK (ΔK_c)	Γ_p^2/C_0	Γ_p^2/C_0	Ψ^2/L_0

**Figure 9.** Linear fit of the relationship between the input current I_s and the generated **B**-field.**Figure 10.** Comparison between the measured current amplitude $|I_s|$ and average power P_{in} input to the network and the predictions from model.

accordingly. We use the internal resistance of the DAQ unit (1 M Ω) as the load resistance in order to avoid the error as much as possible. The corresponding input voltage amplitudes of the two cases are $|V_{in}| \approx 150$ and 30 mV, and the cosine of the phase difference between the input voltage and the input current is $\cos \phi \approx 0.89$, approximately. The experimental results are compared to those of the model computed using (3.9) and (3.13), showing a good agreement between the theoretical results and measurements. The analytical model (i.e. formula (3.22)) also accurately predicts the measured efficiency as can be seen in figure 11. It should be noted that η_t is independent of the strength of the applied **B**-field, or in other words, the current input to the two coils. Therefore,

**Figure 11.** Frequency responses of the transmission efficiency with different source voltages.**Table 3.** Model parameters (cont'd).

Parameters	Value
R_H	148.16 m Ω
L_H	39.10 μ H
R_s	116.82 m Ω
α	129.60 μ T A $^{-1}$

the transfer efficiency is a constant with respect to AC magnetic flux density.

3.3. Essential influence of the transmitter coil resistance

For a given system where the parameters and properties of the transmitter coil and the piezoelectric-resonator receiver are determined, (3.24) and (3.26) describe the maximum power delivered to the load (**B**-field dependent) and the corresponding optimum efficiency (**B**-field independent). For convenience, we denote the real part of the input impedance in (3.27) as $\Re\{Z_{in}\} = R_H + \nu\Gamma_M^2 = R_H + \nu(\alpha\varphi_m)^2$ where $\nu = 2 - M_0/\sqrt{M_0^2 + 1}$. In a weak coupling regime $\Gamma_M \rightarrow 0$, the second term of $\Re\{Z_{in}\}$ is nearly negligible comparing to the coil resistance $R_H \gg \nu\Gamma_M^2$, thus $\Re\{Z_{in}\} \approx R_H$. This observation indicates that

$$\eta_t \approx \frac{1}{2} \frac{(\alpha\varphi_m)^2 M_0}{R_H b} (\sqrt{M_0^2 + 1} - M_0) \quad (3.28)$$

and therefore $\eta_t \propto \frac{1}{R_H}$.

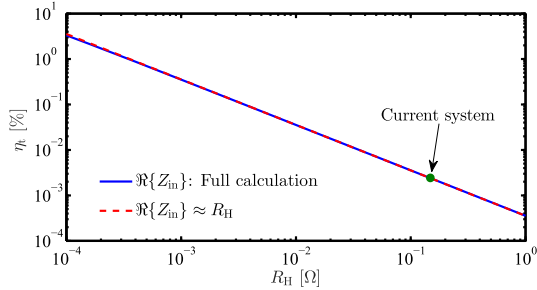


Figure 12. Efficiency as a function of the parasitic resistance R_H of the coil. The maximum output power is given by (3.24) with the optimal load (3.23). The optimum efficiency is computed by (3.26) for two cases: (i) full calculation of $\Re\{Z_{in}\}$ using (3.27), and (ii) an approximation $\Re\{Z_{in}\} \approx R_H$.

In particular, figure 12 shows the theoretical computation of the efficiency as a function of total parasitic resistance of the two coils R_H using (3.26) and (3.28). The obtained results are almost identical for the two cases, hence (3.28) can be utilized as an alternative to estimate the efficiency of a loosely coupled system. The effect of R_H on η_h is significant while that of R_s is almost zero. This is to be expected since we define η_h as a ratio between the power delivered to the load P_L and the power input to the network P_{in} rather than the power available from the source $P_{avs} = \frac{1}{8} \frac{|V_s|^2}{\Re\{Z_s\}} = \frac{1}{8} \frac{|V_s|^2}{R_s}$. It is observed that, for instance, η_h increases by more than two orders of magnitude in comparison to the presented experimental system if R_H decreases to 1 m Ω . Using a higher conductivity material for the coils is not practical. Instead, a doubling of the wire diameter could increase the efficiency by a factor of 4 approximately (i.e. the change of the coil geometry is neglected).

In comparison with other types of WPT systems (e.g. magnetic resonance/induction coupling, capacitive coupling), the efficiency of the proposed structure is low. Despite this obvious drawback, an advantage of the MME system under investigation is that the applied magnetic field can be higher at the low frequencies required by the MME system while still remaining within safe limits [36]. According to the IEEE standards, a maximum allowable field at 1 kHz is ≥ 2 mT [13], 10 times larger than the ~ 200 μ T permissible at 1 MHz [14]. Especially in the case that the receiver is blocked by a metal plate, high frequency devices such as inductive/capacitive coupled systems cannot be utilized due to the effects of eddy currents (i.e. also called Foucault currents, which flow in closed loops within conductors, and in planes perpendicular to the applied magnetic field) [37]. Meanwhile, the MME receiver is able to operate effectively since its resonance frequency is typically lower than 1 kHz and can be reduced to the range of a few hundred Hz by adjusting the structure geometry.

3.4. Method to increase the electrodynamic transduction factor: an example

From (3.19), (3.26) and (3.27), we see that, when $\Gamma_M \rightarrow +\infty$ (or large enough), the second term in (3.27) is dominant,

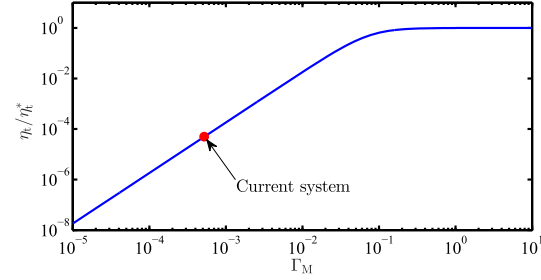


Figure 13. Variations of the efficiency as a function of the electrodynamic transduction factor.

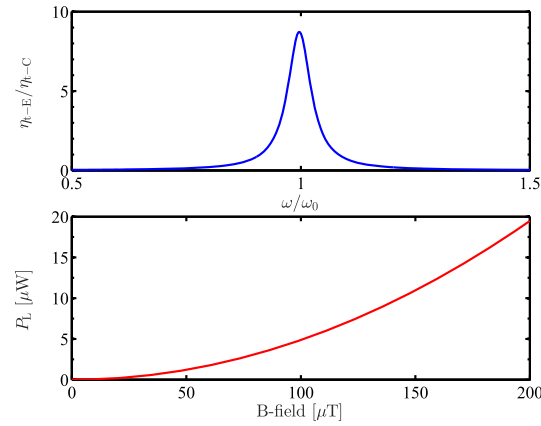


Figure 14. Simulation results of the example structure, denoting the simulated efficiency and the maximum efficiency of the system used in measurements as η_{h-E} and η_{h-C} respectively.

$\nu\Gamma_M^2 \gg R_H$, therefore $\Re\{Z_{in}\} \approx \nu\Gamma_M^2$ and

$$\begin{aligned} \eta_h \rightarrow \eta_h^* &= \frac{1}{2} \frac{M_0}{\nu b} (\sqrt{M_0^2 + 1} - M_0) \\ &= \frac{M_0 (\sqrt{M_0^2 + 1} - M_0)^2 + 1}{2 \sqrt{M_0^2 + 1} - M_0}. \end{aligned} \quad (3.29)$$

Considering Γ_M as a variable and treating the other parameters such as ω_0 , C_0 , b and Γ_P as constants, the variation of η_h over a wide range of Γ_M is depicted in figure 13.

Obviously, there is still significant room for improvement of the transmission efficiency by increasing Γ_M . An example is presented as follows.

Based on the dependency of the electrodynamic coupling factor Γ_M on the geometry of the Helmholtz coil (a , h), volume of the magnet tip mass V_M and effective length l_{eff} of the piezoelectric cantilever beam (i.e. as presented in (3.12), (3.18) and (3.19)), we found that the efficiency η_h can be increased by a factor of ~ 8.7 if we simultaneously double magnet volume ${}^sV_M = 2V_M$, halve the beam length ${}^sL_t = L_t/2$ and optimize the coil radius ${}^sa = h\sqrt{2}/2$, where sa is the stationary point of α and is determined by $\partial\alpha/\partial a = 0$. Here, values with a superscript (i.e. sX) are used for

simulations. The Helmholtz coil used in experiments has the ratio of $a \approx 2h$, and the optimal coil provides $\alpha = 1.65\alpha$. The final simulated results of the example are shown in figure 14. The frequency response of the efficiency is normalized by the ratio between the obtained efficiency η_{t-E} and the maximum efficiency of the current system η_{t-C} . The optimal load is given in (3.23). The maximum output power of the optimized system is about $19.5 \mu\text{W}$ at the magnetic field amplitude of $200 \mu\text{T}$, which is sufficient to power various body wireless sensors [38]. This model-based study suggests a potential of significant improvement in the delivered power and is the preliminary work for realizing an optimal system.

In order to prove the feasibility of the optimization method in practice, we investigate the output power when utilizing the same piezoelectric resonator and doubling the magnet volume, in which two magnet masses are placed on top and bottom (symmetric about the y -axis) in each portion of the beam. The measured power in this case is $P_L = 4.93 \mu\text{W}$ attained at a resonance frequency of $f_0 = 259.8 \text{ Hz}$, which is very close to that predicted by the model, $P_L = 4.95 \mu\text{W}$ at $f_0 = 256.0 \text{ Hz}$. The applied \mathbf{B} -field amplitude is $B_{ac} = 129 \mu\text{T}$ and the load resistance is $R_L = 1 \text{ M}\Omega$. The obtained power is 3.2 times as large as that of the original prototype.

It should be noted that, η_t^* is not the upper bound of the efficiency. η_t^* is the limit of η_t only for the case in which (i) the transducer characteristics (ω_0 , C_0), the mechanical damping coefficient b and the electromechanical transduction factor Γ_p were defined, and (ii) the optimal load in (3.23) is used. Furthermore, (3.26) is expressed in terms of architecture-independent parameters such as the resonance frequency ω_0 or the resonator figure of merit M_0 (i.e. at $\omega = \omega_0$). In general, when maximizing the transmission efficiency that is subject to particular limitations or requirements of a realistic application, all geometry-dependent relations (e.g., the dependency of the coil resistance on its length, radius and material properties) need to be taken into consideration. This design problem is out of scope of the paper and is open for future work. However, the analyses reported in section 3.1 can still be used as a framework to solve for the global optimal solution of η_t . For instance, one can describe α , ω_0 and M_0 in (3.26) as functions of geometry, then optimize the corresponding efficiency in terms of those geometric parameters, subject to their constraints (if any).

4. Conclusions

In this work, we presented a WPT device concept using a center-clamped piezo-bimorph transducer with two magnet tip masses as a receiver and a Helmholtz coil as a transmitter. Two equivalent circuit models for exploring the power delivered to the load and the transmission efficiency were developed and experimentally validated. Comparisons between the theoretical simulations and experimental data for different cases (i.e. frequency/ \mathbf{B} -field responses) showed the accuracy and consistency of both models. Note that the proposed structure requires deliberately aligning so that the piezoelectric beam is clamped at

the center. Otherwise, the length difference between the two halves may lead to their mis-matched resonance frequencies. As a consequence, they may have a small phase difference at the operational frequency, which reduces the output power. While the paper analyzed the piezoelectric generator, other electro-mechanical mechanisms (electrostatic and electromagnetic) or a ME device can be utilized as well and the two models still hold for those energy conversion techniques due to their similarities. Several methods were mentioned to improve the system efficiency such as increasing the wire diameter or the electrodynamic coupling factor. Enhancing electromechanical coupling factor by the use of appropriate piezoelectric materials could be also a potential solution, however, this issue is beyond the scope of the paper and is open for further study.

Acknowledgments

The authors want to thank the anonymous reviewers for their comments on the manuscript.

This work was supported by the National Science Foundation ASSIST Nanosystems ERC under Award Number EEC-1160483.

Appendix A. A model for electromagnetic (electrodynamic) transducer

The physical analogy between the electromagnetic, electrostatic and piezoelectric generators was thoroughly explained in [26] where the three types of resonators were modeled as a lossless transformer. Differing from that, we presents an alternative model of the electromagnetic transducer using an ideal gyrator [25], and then utilize a circuit-theory-based technique to obtain the same closed-form of the output power and efficiency as in (3.21) and (3.22).

The complete model is shown in figure A1, in which the complex amplitudes of the tip mass velocity, the force on the mechanical port and the voltage induced on the electrical port are denoted by V_m , F_Ψ and V_Ψ respectively. The impedance Z_M is calculated as

$$Z_M = j\left(\omega m - \frac{K_0}{\omega}\right) + b + \frac{\Psi^2}{j\omega L_0 + R_L} = jZ_0 + b + \Delta K_e \frac{\tau_e}{1 + j\omega\tau_e}, \quad (\text{A.1})$$

where τ_e and ΔK_e are defined in (3.1) and (3.2). We see that the compact form of (A.1) is identical to (3.5), and therefore the expression of the input impedance Z_{in} is unchanged. With a time harmonic drive force $F_M(t) = F_0 \cos(\omega t)$ of angular frequency ω , the transverse velocity of the tip mass is

$$V_m = \frac{F_0}{Z_M}. \quad (\text{A.2})$$

The relation between the mechanical velocity and the induced voltage is

$$V_\Psi = \Psi V_m. \quad (\text{A.3})$$

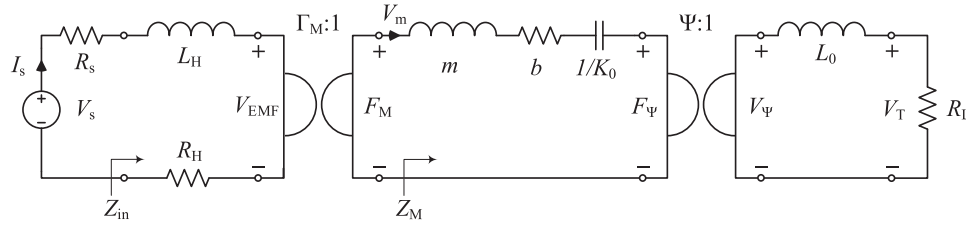


Figure A1. Schematic of lumped element model for wireless power transfer systems with electromagnetic (electrodynamics) transducer as a receiver.

The transducer voltage across the load resistance is

$$V_T = \frac{V_\Psi R_L}{j\omega L_0 + R_L}. \quad (\text{A.4})$$

The power transferred to the load is then given by

$$\begin{aligned} P_L &= \frac{1}{2} \frac{|V_T|^2}{R_L} = \frac{1}{2} \frac{|V_\Psi|^2}{L_0} \frac{L_0/R_L}{1 + (\omega L_0/R_L)^2} \\ &= \frac{1}{2} \Delta K_e \frac{\omega^2 \tau_e}{1 + (\omega \tau_e)^2} \frac{F_0^2}{(\omega |Z_M|)^2} \\ &= \frac{1}{2} \Delta K_e \frac{\omega^2 \tau_e}{1 + (\omega \tau_e)^2} \\ &\quad \times \frac{F_0^2}{\left[-\omega Z_0 + \Delta K_e \frac{(\omega \tau_e)^2}{1 + (\omega \tau_e)^2} \right]^2 + \left[\omega b + \Delta K_e \frac{\omega \tau_e}{1 + (\omega \tau_e)^2} \right]^2}, \end{aligned} \quad (\text{A.5})$$

whose form is exactly the same as (3.21).

Either the two-port equations shown in section 2.4 or the circuit theory-based approach presented here can be applied to investigate the output power and the transmission efficiency of any transducer presented in this paper. Both methods yield identical results due to the fact that they are just different techniques of describing the same physical mechanism. While the former clearly describes the insight through the Newton's second law and the Ohm's law, the latter is more convenient and easier for derivations and is more familiar to electrical engineers. Finally, a single expression of each P_L and η_h obtained in section 3.1 can cover all four different types of generators.

Appendix B. ME WPT system

Figure B1 illustrates a configuration of the ME generator, in which two piezoelectric layers are parallel poled in transverse direction (y-axis) and a magnetostrictive shim is magnetized in longitudinal direction (z-axis). When a time-harmonic external magnetic field is applied longitudinally, a longitudinal vibration is excited in the shim due to magnetostrictive effect. It is then elastically coupled to the two piezoelectric layers, causing a forced oscillation in them and inducing a voltage across the load resistance R_L . Similar to the work published by Dong *et al* [34, 39, 40], the complete ME-based WPT system can be modeled by an equivalent circuit shown in figure 7 (note that \dot{x} now denotes the mechanical velocity in the longitudinal

direction instead of the transverse vibration). However, differing from those works, the ME cantilever beam is clamped at one end rather than utilizing the free-free configuration (which is widely used in sensing systems). Furthermore, while those authors concerned with the ME voltage coefficient (i.e. the relation between the open circuit voltage and the applied magnetic field or magnetic flux density), we focus more on the power delivered to the load which makes the derivations more complicated.

Following the same procedure reported in [34], the model parameters are derived as follows

$$n = \frac{2t_p}{2t_p + t_m}, \quad 0 < n < 1, \quad (\text{B.1})$$

$$\bar{\rho} = \rho_p n + \rho_m (1 - n), \quad (\text{B.2})$$

$$\bar{\nu}^2 = \left(\frac{n}{s_{11}^E} + \frac{1-n}{s_{33}^H} \right) / \bar{\rho}, \quad (\text{B.3})$$

$$k^2 = \frac{\omega^2}{\bar{\nu}^2}, \quad (\text{B.4})$$

$$\Gamma_p = w \frac{d_{31,p}^E}{s_{11}^E}, \quad (\text{B.5})$$

$$\varphi_m = w t_m \frac{d_{33,m}^H}{s_{33}^H}, \quad (\text{B.6})$$

$$C_0 = \frac{1}{2} \epsilon_{33}^S \frac{w L_e}{t_p}, \quad (\text{B.7})$$

$$A = (2t_p + t_m) w, \quad (\text{B.8})$$

$$Z_e = j\bar{\nu} \bar{\rho} A \left(\tan\left(\frac{kL}{2}\right) - \frac{1}{\sin(kL)} \right), \quad (\text{B.9})$$

where ρ_p and ρ_m are the mass densities of the piezoelectric and the magnetostrictive layers respectively, the definitions of w , t_p and t_m are shown in figure B1, ω is the angular driving frequency, s_{11}^E is the elastic compliance of the piezoelectric material under constant electric field, $d_{31,p}^E$ is the transverse electric constant, s_{33}^H is the elastic compliance at constant magnetic field, $d_{33,m}^H$ is the longitudinal piezoelectric constant, ϵ_{33}^S is the permittivity component at constant strain with the plane-stress assumption of a thin beam. Γ_M is calculated as in (3.19). The resonance frequency is attained by setting $Z_e = 0$, resulting in

$$\omega_0 = \frac{\pi \bar{\nu}}{2 L_e}. \quad (\text{B.10})$$

After determining all the key parameters, the explicit solutions of the output power and the transmission efficiency can be obtained

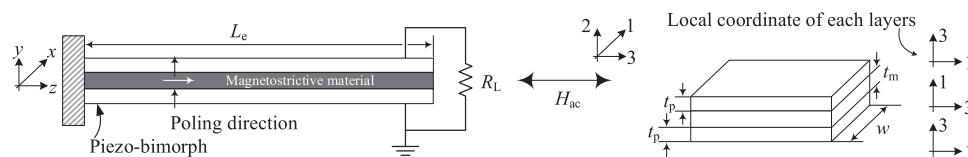


Figure B1. Schematic of magneto-electric transducer and geometric dimensions of the composite laminate.

by substituting them into (3.21) and (3.22). This example completes the analysis in section 3.1.

ORCID iDs

Binh Duc Truong  <https://orcid.org/0000-0001-7108-4713>

References

- [1] Roundy S and Wright P K 2004 A piezoelectric vibration based generator for wireless electronics *Smart Mater. Struct.* **13** 1131–42
- [2] Mitcheson P 2010 Energy harvesting for human wearable and implantable bio-sensors *Annual International Conference of the IEEE Engineering in Medicine and Biology (31 Aug–4 Sept 2010)* **3432–36**
- [3] Erturk A and Inman D 2011 *Piezoelectric Energy Harvesting* (New York: Wiley) (<https://doi.org/10.1002/9781119991151>)
- [4] Kurs A, Karalis A, Moffatt R, Joannopoulos J D, Fisher P and Soljačić M 2007 Wireless power transfer via strongly coupled magnetic resonances *Science* **317** 83–6
- [5] Sid A, Xiaofang Y and Shanhuai F 2017 Robust wireless power transfer using a nonlinear parity-time-symmetric circuit *Nature* **546** 6
- [6] Paul K and Sarma A K 2018 Fast and efficient wireless power transfer via transitionless quantum driving *Sci. Rep.* **8** 12
- [7] Riemer R and Shapiro A 2011 Biomechanical energy harvesting from human motion: theory, state of the art, design guidelines, and future directions *J. NeuroEng. Rehabil.* **8** 22
- [8] Ylli K, Hoffmann D, Willmann A, Becker P, Folkmer B and Manoli Y 2015 Energy harvesting from human motion: exploiting swing and shock excitations *Smart Mater. Struct.* **24** 025029
- [9] Challa V R, Mur-Miranda J O and Arnold D P 2012 Wireless power transmission to an electromechanical receiver using low-frequency magnetic fields *Smart Mater. Struct.* **21** 115017
- [10] Song M, Belov P and Kapitanova P 2017 Wireless power transfer inspired by the modern trends in electromagnetics *Appl. Phys. Rev.* **4** 021102
- [11] Huang L, Hu A P, Swain A, Kim S and Ren Y 2013 An overview of capacitively coupled power transfer—a new contactless power transfer solution *2013 IEEE 8th Conf. on Industrial Electronics and Applications (ICIEA)* pp 461–5
- [12] Barman S D, Reza A W, Kumar N, Karim M E and Munir A B 2015 Wireless powering by magnetic resonant coupling: recent trends in wireless power transfer system and its applications *Renew. Sustain. Energy Rev.* **51** 1525–52
- [13] IEEE 2002 IEEE standard for safety levels with respect to human exposure to electromagnetic fields, 0–3 kHz *IEEE Std C95.6-2002* pp 1–0
- [14] IEEE 2006 IEEE standard for safety levels with respect to human exposure to radio frequency electromagnetic fields, 3 kHz to 300 GHz *IEEE Std C95.1-2005 (Revision of IEEE Std C95.1-1991)* pp 1–238
- [15] McEachern K M and Arnold D P 2013 Electrodynamic wireless power transmission to a torsional receiver *J. Phys.: Conf. Ser.* **476** 012004
- [16] Garraud A, Jimenez J D, Garraud N and Arnold D P 2014 Electrodynamic wireless power transmission to rotating magnet receivers *J. Phys.: Conf. Ser.* **557** 012136
- [17] Garraud N, Alabi D, Chyczewski S, Varela J D, Arnold D P and Garraud A 2018 Extending the range of wireless power transmission for bio-implants and wearables *J. Phys.: Conf. Ser.* **1052** 012023
- [18] Paprotny I, Xu Q, Chan W W, White R M and Wright P K 2013 Electromechanical energy scavenging from current-carrying conductors *IEEE Sens. J.* **13** 190–201
- [19] Guoxi L, Penghong C and Shuxiang D 2014 Energy harvesting from ambient low-frequency magnetic field using magneto-mechano-electric composite cantilever *Appl. Phys. Lett.* **104** 032908
- [20] Han J, Hu J, Wang S X and He J 2014 Magnetic energy harvesting properties of piezofiber bimorph/ndfeb composites *Appl. Phys. Lett.* **104** 093901
- [21] Lasheras A, Gutiérrez J, Reis S, Sousa D, Silva M, Martins P, Lanceros-Mendez S, Barandiarán J M, Shishkin D A and Potapov A P 2015 Energy harvesting device based on a metallic glass/pvdf magnetolectric laminated composite *Smart Mater. Struct.* **24** 065024
- [22] Ming L C, Xin Z, Junran X, Srinivasan G, Jiefang L and Viehland D 2016 Power conversion efficiency and resistance tunability in coil-magnetolectric gyrators *Appl. Phys. Lett.* **109** 202907
- [23] Reis S, Silva M P, Castro N, Correia V, Rocha J G, Martins P, Lasheras A, Gutierrez J and Lanceros-Mendez S 2016 Electronic optimization for an energy harvesting system based on magnetolectric metglas/poly(vinylidene fluoride)/metglas composites *Smart Mater. Struct.* **25** 085028
- [24] Malleron K, Gensbittel A, Talleb H and Ren Z 2018 Experimental study of magnetolectric transducers for power supply of small biomedical devices *Microelectronics Journal* 1–6 Article in press
- [25] Tilmans H A C 1996 Equivalent circuit representation of electromechanical transducers: I. Lumped-parameter systems *J. Micromech. Microeng.* **6** 157–76
- [26] Halvorsen E 2016 Optimal load and stiffness for displacement-constrained vibration energy harvesters arXiv:1603.01909
- [27] Truong B D, Williams S and Roundy S 2018 Experimentally validated model and power optimization for piezoelectric-based wireless power transfer systems (in preparation)
- [28] Kim J E and Kim Y Y 2011 Analysis of piezoelectric energy harvesters of a moderate aspect ratio with a distributed tip mass *J. Vibr. Acoust. Stress Reliab. Des.* **133**

- [29] Wang Y, He H and Xu R 2015 An analytical model for a piezoelectric vibration energy harvester with resonance frequency tunability *Adv. Mech. Eng.* **7**
- [30] Erturk A and Inman D J 2009 An experimentally validated bimorph cantilever model for piezoelectric energy harvesting from base excitations *Smart Mater. Struct.* **18** 025009
- [31] Kim M, Hoegen M, Dugundji J and Wardle B L 2010 Modeling and experimental verification of proof mass effects on vibration energy harvester performance *Smart Mater. Struct.* **19** 045023
- [32] Le C P and Halvorsen E 2012 Mems electrostatic energy harvesters with end-stop effects *J. Micromech. Microeng.* **22** 074013
- [33] Javor E R and Anderson T 1998 Design of a helmholtz coil for low frequency magnetic field susceptibility testing 1998 *IEEE EMC Symp. Int. Symp. on Electromagnetic Compatibility. Symp. Record (Cat. No.98CH36253)* vol 2 pp 912–7
- [34] Dong S, Li J-F and Viehland D 2003 Longitudinal and transverse magnetoelectric voltage coefficients of magnetostrictive/piezoelectric laminate composite: theory *IEEE Trans. Ultrason., Ferroelectr. Freq. Control* **50** 1253–61
- [35] Restrepo A F, Franco E, Cadavid H and Pinedo C R 2017 A comparative study of the magnetic field homogeneity for circular, square and equilateral triangular helmholtz coils 2017 *Int. Conf. Electrical, Electronics, Communication, Computer, and Optimization Techniques (ICEECCOT)* pp 13–20
- [36] Garraud A and Arnold D P 2016 Advancements in electrodynamic wireless power transmission 2016 *IEEE Sensors* pp 1–3
- [37] Ding-Xin Y, Zheng H, Hong Z, Hai-Feng H, Yun-Zhe S and Bao-Jian H 2015 Through-metal-wall power delivery and data transmission for enclosed sensors: a review *Sensors* **15** 12
- [38] Rajan R 2012 Ultra-low power short range radio transceivers White Paper—Microsemi https://www.microsemi.com/document-portal/doc_view/127466-white-paper-ultra-low-power-short-range-radio-transceivers
- [39] Dong S, Li J-F and Viehland D 2003 Giant magneto-electric effect in laminate composites *IEEE Trans. Ultrason., Ferroelectr. Freq. Control* **50** 1236–9
- [40] Liu G, Zhang C, Chen W and Dong S 2013 Eddy-current effect on resonant magnetoelectric coupling in magnetostrictive-piezoelectric laminated composites *J. Appl. Phys.* **114** 027010

CHAPTER 4

WIRELESS POWER TRANSFER WITH MAGNETOELECTRIC TRANSDUCERS

This chapter explores the potential use of the magnetoelectric energy conversion mechanism in wireless power transfer.

4.1 Experimentally Validated Model and Power Optimization of a Magnetoelectric Wireless Power Transfer System in Free-Free Configuration

The magneto-mechano-electric (MME) devices presented in Chapter 3 operate at low frequencies that allow them to be exposed to high magnetic field strengths. However, the weak coupling between the magnetic and mechanical domains of the MME resonator, which is realized by the interaction of a permanent magnet and the B-field, results in extremely low transmission efficiency ($\sim 2.5 \times 10^{-3}$ %). Furthermore, the power transferred to the load is proportional to the square of the total magnet volume, making this method challenging to miniaturize for use on implants. In order to overcome the limitations of such architecture, in this Chapter, we introduce an alternative wireless power transfer system that utilizes a magnetoelectric (ME) transducer as a receiver. This approach exhibits a higher coupling than MME structures and requires lower frequencies than resonant-inductive-coupling (RIC) systems. Therefore, it is possible to transfer energy into an implanted medical device more efficiently (than MME transducers) and at higher magnetic fields (than RIC) without violating the safety standards.

© 2020 IOP Publishing Ltd. Reprinted, with permission from B. D. Truong and S. Roundy, "Experimentally validated model and power optimization of a magnetoelectric wireless power transfer system in free-free configuration," *Smart Materials and Structures*, vol. 29, in July 2020.

Experimentally validated model and power optimization of a magnetoelectric wireless power transfer system in free-free configuration

Binh Duc Truong  and Shad Roundy

Department of Mechanical Engineering, University of Utah, 1495 E. 100 S., 1550 MEK, Salt Lake City, Utah, 84112, United States of America

E-mail: Binh.D.Truong@utah.edu

Received 19 February 2020, revised 13 April 2020

Accepted for publication 6 May 2020

Published 21 July 2020



CrossMark

Abstract

This article presents a thorough analysis and an equivalent circuit model of a wireless power transfer system utilizing magnetoelectric (ME) effects. Based on two-port theory, explicit analytical solutions of, (i) the ME coefficient α_{ME} (defined by the derivative of the generated electric field with respect to the applied magnetic field), and (ii) the power transferred to a load resistance, are derived and rigorously validated by experiments. The compact closed-forms of the optimal load and its corresponding maximum output power are developed. In our particular experimental system, a power of ~ 10 mW is attained at an applied magnetic flux density of $318.9 \mu\text{T}$ with a laminated composite made by two Galfenol and one PZT layers. While α_{ME} is widely used in the literature as a standard criterion to evaluate the performance of a ME transducer, we reveal that larger α_{ME} does not always ensure higher optimum power delivered to the load. Instead, we quantify the essential influences of each magnetostrictive and piezoelectric phases on the maximum obtainable power. We show that the transduction factor between the magnetic and mechanical domains is often more critical for power optimization than the mechanical-electrical transduction factor as it determines and limits the maximum power available for transfer to a resistive load.

Keywords: wireless power transfer, magneto-electric effect, longitudinal vibration, equivalent circuit model, power optimization

(Some figures may appear in colour only in the online journal)

1. Introduction

Wireless power transfer (WPT) with a focus on biomedical applications has received significant attention recently as it provides the promise of a safe approach to deliver power to implantable medical devices (IMDs). Resonant inductive coupling (RIC) wireless power transfer systems (WPTS) are perhaps the most prevalent technology to realize this vision. However, as the size of IMDs decreases, RIC systems may be less successful because of the need to operate at high frequency, which results in high attenuation in soft tissue. In addition, subject to the International Commission on Non-Ionizing

Radiation Protection (ICNIRP) Safety Standards [1, 2], the maximum allowable amplitude of the magnetic flux density (i.e. \mathbf{B} -field) that can be applied to humans is restricted by the driving frequency. For example, largest permissible \mathbf{B} -field at 6.78 MHz is $0.29 \mu\text{T}$ whereas at 100 kHz it is $100 \mu\text{T}$. These safety constraints reduce the potential of RIC approach when applied to very small biomedical systems.

Low-frequency near-field techniques are attractive alternatives to RIC for powering biomedical devices. Electrodynamic (ED) and Magneto-Mechano-Electric (MME) WPT systems were proposed and thoroughly investigated, including both linear and rotational vibration [3–6]. In these mechanisms, either

an electromagnetic transducer or a piezoelectric generator along with one or more permanent magnets form a receiver. Meanwhile, a coil or a rotation magnet is utilized as a transmitter. Typical operating frequencies of the ED and MME devices are well below 1 kHz, which allows the application of a maximum \mathbf{B} -field of ~ 2 mT [7]. A disadvantage of these structures is a relatively low efficiency due to the weak coupling between the magnetic and mechanical domains that is realized by the interaction of magnet and magnetic field. Moreover, the magnetic-to-mechanical transduction factor, and therefore, the maximum possible power transferred to an electrical load, depends on the magnet volume. Given the fact that implantable integrated systems are desired to be as small as possible, the required use of permanent magnets may be challenging in the miniaturization of implants.

Mid-field and far-field electromagnetic WPT systems (referred to here as RF WPTS) have been widely employed to power pacemakers [8–10]. However, this technique can induce significant heating caused by RF wave absorption in the human body. This absorption both reduces system efficiency and can pose a health risk to users. According to the ICNIRP regulation [1, 11], the maximum specific absorption rate (SAR) is set to be 2 W/kg per 10 g of tissue in order to avoid the safety risk that these systems could pose.

Acoustic power transfer is another possible solution, whose advantages include lower absorption and shorter wavelength enabling smaller transducers [12]. However, the acoustic transmitter must be in direct contact with the skin, and the transmission of acoustic power through the bone seems to be minimal since the large acoustic impedance mismatch between soft tissue and bone results in most of the acoustic energy being reflected.

With the limitations of the available WPT technologies (including ED, MME, RIC, RF, and ultrasonic waves) pointed out, we are seeking another approach for powering biomedical implantable electronics that is able to overcome those obstacles. A mechanism that operates at low frequency with an acceptable transfer efficiency is considered appropriate. We believe that a WPTS utilizing the magnetoelectric (ME) effects possesses such potential.

Advances in ME multiferroic materials have triggered significant research interest [13]. With a shift of focus from fundamental material discoveries to translational research, the field of multiferroics and magnetoelectrics is anticipated to make further application-oriented breakthroughs over the next few years [14]. The recent development of a ME antenna indicated that for a given frequency its wavelength could be five orders of magnitude shorter than the electromagnetic wavelength, leading to possibly dramatic miniaturization [15]. Furthermore, the typical operating frequency of ME systems is relatively low, in the range of tens of kHz, which enables higher permissible applied \mathbf{B} -field than that of RIC WPTS [1]. These characteristics make ME generator a promising alternative to other WPT technologies, especially for IMDs.

The concept of a ME effect was first introduced by Röntgen in 1888 with his discovery that a dielectric material could be magnetized under a magnetic field [16]. In the next 100

years, various ME architectures and materials have been discovered and studied, with most studies focused on single-phase and two-phase ME composites [17, 18]. In 2001, Ryu *et al* proposed a ME laminated composite combined by two radial-magnetized Terfenol-D and one thickness-polarized PZT disks [19]. Since then, laminated structures have become preferable due to their strong ME coupling, and high reproducibility and reliability. A significant modeling effort which captures the performance of ME transducers was undertaken by Dong *et al*, in which the ME effect was described by an equivalent circuit model [20, 21]. However, the authors were only concerned with the open-circuit voltage for a sensing system. The actual power transferred to a load at a given external \mathbf{B} -field was not addressed.

ME laminated composites have been widely utilized in many applications, such as magnetic field sensors [22–24], ME Random Access Memory (MERAM) [25–27] and electronic components [28–30]. However, its potential in WPT has not been thoroughly explored. To the authors' knowledge, this work is one of the first efforts to utilize a laminated composite ME-transducer as a receiver for a WPTS, adding to the efforts of [31, 32]. In this article, we further develop a linear two-port model of a ME-based WPTS, together with corrections to essential errors found in [20]. The model is experimentally validated, which is then used for analyzing a figure of merit and the fundamental performance limits of the architecture under consideration. A standard criterion to evaluate the ME effect is the ME coefficient (denoted as α_{ME}) defined by the rate of change of the electric field in response to the applied magnetic field. Most studies in the literature so far have indicated a significant advantage in obtaining α_{ME} as high as possible [33–35]. While this statement may hold true for magnetic field sensing devices, it is still questionable for a WPTS. Clarifying this issue is also one of the central objectives of the paper.

2. Mathematical analysis and essential equations

As shown in figure 1, we consider a ME laminated composite with two constituent materials, magnetostrictive and piezoelectric, bonded together by conductive epoxy. The piezoelectric and magnetostrictive phases are poled and magnetized in the thickness and length directions, respectively. The global coordinates of the beam are denoted by (x, y, z) . Local coordinates of each layer are also included, where z -axis is always parallel to the polarization and magnetization vectors, \vec{P} and \vec{M} . L and w are the length and width of the ME generator. t_p and t_m accordingly represent the thicknesses of the magnetostrictive and piezoelectric layers. In order to evaluate the transferred power capability, the output port of the ME transducer is connected to a resistor R_L , for the convenience and simplification. When an external AC magnetic field H_{ac} is applied along the longitudinal axis of the laminate, $(H_{\text{ac}} \parallel \vec{M}) \perp \vec{P}$, a strain is excited in the two magnetostrictive phases, which is then transferred to the piezoelectric layer through an interface coupling. As a result, the laminated composite vibrates in the z -direction.

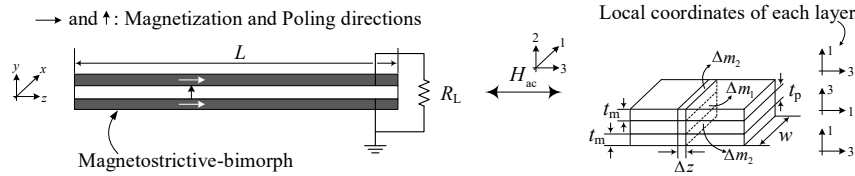


Figure 1. Schematic of ME transducers and geometric dimensions of the laminated composite.

The piezoelectric constitutive equations for the thickness poling are

$$S_{1p} = s_{11}^E T_{1p} + d_{31,p} E_3, \quad (1)$$

$$D_3 = d_{31,p} T_{1p} + \epsilon_{33}^T E_3 \quad (2)$$

where T_{1p} and S_{1p} are the stress and strain of the piezoelectric layer imposed by the magnetostrictive layer, D_3 and E_3 are the electric displacement and electric field in the piezoelectric layer along z , respectively, s_{11}^E is the elastic compliance of the piezoelectric material under constant electric field E , $d_{31,p}$ is the transverse electric constant and ϵ_{33}^T is the dielectric permittivity under constant stress T .

The magnetostrictive constitutive equations for the longitudinal strain S_{3m} and the magnetic field flux density B_3 are

$$S_{3m} = s_{33}^H T_{3m} + d_{33,m} H_3, \quad (3)$$

$$B_3 = d_{33,m} T_{3m} + \mu_{33,m}^T H_3 \quad (4)$$

where H_3 is the AC applied magnetic field (i.e. H_{ac} in figure 1), T_{3m} is the stress in the magnetostrictive layer, s_{33}^H is the elastic compliance at constant H , $d_{33,m}$ is the piezomagnetic constant and $\mu_{33,m}^T$ is the magnetic permeability at constant stress T .

Assume that an applied magnetic field H_3 is sinusoidal with angular frequency ω (e.g. $H_3 = H_0 \cos(\omega t)$), the corresponding vibration of the laminate is a harmonic motion along the longitudinal direction z . We denote (i) the displacements of the piezoelectric and magnetostrictive mass units (Δm_1 and $2\Delta m_2$) in the laminate are $u_{1p}(z)$ and $u_{3m}(z)$ respectively, and (ii) the corresponding strain components along z are

$$S_{1p} = \partial u_{1p} / \partial z, \quad (5)$$

$$S_{3m} = \partial u_{3m} / \partial z. \quad (6)$$

Here, in the same manner as in [36–39], we introduce an interface coupling coefficient, $0 \leq \kappa \leq 1$, which relates the strain transfer between the two phases (magnetostrictive and piezoelectric) such that $S_{1p} = \kappa S_{3m}$, and therefore $u_{1p} = \kappa u_{3m}$. With the presence of κ , all of the following derivations are, in general, different from the well-known results established in the literature [20, 40, 41], in which the authors only considered the ideal case $\kappa = 1$.

Based on the Newton's second law, the equation of motion of the laminate is given by

$$\Delta m_1 \frac{\partial^2 u_{1p}}{\partial t^2} + 2\Delta m_2 \frac{\partial^2 u_{3m}}{\partial t^2} = \Delta T_{1p} A_1 + 2\Delta T_{3m} A_2 \quad (7)$$

where

$$\Delta m_1 = \rho_p A_1 \Delta z, \quad \Delta m_2 = \rho_m A_2 \Delta z, \quad (8)$$

$$A_1 = t_p w, \quad A_2 = t_m w. \quad (9)$$

ρ_p and ρ_m are the mass densities of the piezoelectric and the magnetostrictive layers respectively. The geometric definitions of Δm_1 , Δm_2 , w , Δz , t_p and t_m are shown in figure 1. Considering an element of infinitesimal length, $\Delta z \rightarrow 0$, and with notice that $\partial^2 u_{3m} / \partial t^2 = (\partial^2 u_{1p} / \partial t^2) / \kappa$, equation (7) can be re-written as

$$\bar{\rho} \frac{\partial^2 u}{\partial t^2} = n \frac{\partial T_{1p}}{\partial z} + (1-n) \frac{\partial T_{3m}}{\partial z} \quad (10)$$

where the variable of interest is $u = u_{1p}$,

$$n = \frac{A_1}{A_1 + 2A_2} = \frac{t_p}{t_p + 2t_m}, \quad 0 < n < 1, \quad (11)$$

$$\bar{\rho} = \frac{\rho_p A_1 + 2\rho_m A_2 / \kappa}{A_1 + 2A_2}. \quad (12)$$

Based on the piezoelectric constitutive equations, the partial derivative of the stress with respect to the position in the length direction is computed as

$$\frac{\partial T_{1p}}{\partial z} = \left(s_{11}^E - \frac{d_{31,p}^2}{\epsilon_{33}^T} \right)^{-1} \left(\frac{\partial S_{1p}}{\partial z} - \frac{d_{31,p}}{\epsilon_{33}^T} \frac{\partial D_3}{\partial z} \right), \quad (13)$$

$$\frac{\partial T_{3m}}{\partial z} = \left(s_{33}^H - \frac{d_{33,m}^2}{\mu_{33,m}^T} \right)^{-1} \left(\frac{\partial S_{3m}}{\partial z} - \frac{d_{33,m}}{\mu_{33,m}^T} \frac{\partial B_3}{\partial z} \right). \quad (14)$$

It should be noted that, the constitutive equations of piezoelectric and magnetostrictive materials are written under the assumption that all field components do not vary through the width and thickness directions, which means

$\partial D_1/\partial x = \partial D_2/\partial y = 0$ and $\partial B_1/\partial x = \partial B_2/\partial y = 0$. In addition, Maxwell's magnetostatic and electrostatic equations in magnetostrictive and piezoelectric materials (also known as Gauss's laws for magnetism) are given by

$$\text{rot } \vec{E} = 0, \text{div } \vec{D} = 0, \quad (15)$$

$$\text{div } \vec{B} = 0, \text{rot } \vec{H} = 0. \quad (16)$$

Hence $\partial D_3/\partial z = 0$ and $\partial B_3/\partial z = 0$. Equations (13) and (14) now become

$$\frac{\partial T_{1p}}{\partial z} = \left(s_{11}^E - \frac{d_{31,p}^2}{\epsilon_{33}^T} \right)^{-1} \frac{\partial^2 u}{\partial z^2} = \frac{1}{s_{11}^D} \frac{\partial^2 u}{\partial z^2}, \quad (17)$$

$$\frac{\partial T_{3m}}{\partial z} = \left(s_{33}^H - \frac{d_{33,m}^2}{\mu_{33,m}^T} \right)^{-1} \frac{1-n}{\kappa} \frac{\partial^2 u}{\partial z^2} = \frac{1-n}{\kappa s_{33}^B} \frac{\partial^2 u}{\partial z^2}. \quad (18)$$

By substituting (17) and (18) into (10), the motion equation can be written

$$\frac{1}{\bar{v}^2} \frac{\partial^2 u}{\partial t^2} = \frac{\partial^2 u}{\partial z^2} \quad (19)$$

where

$$\begin{aligned} \bar{v}^2 &= \frac{1}{\rho} \left[n \left(s_{11}^E - \frac{d_{31,p}^2}{\epsilon_{33}^T} \right)^{-1} + \frac{1-n}{\kappa} \left(s_{33}^H - \frac{d_{33,m}^2}{\mu_{33,m}^T} \right)^{-1} \right] \\ &= \frac{1}{\rho} \left(\frac{n}{s_{11}^D} + \frac{1-n}{\kappa s_{33}^B} \right). \end{aligned} \quad (20)$$

The expression of \bar{v}^2 is slightly different from the formula presented by Dong *et al* [20], since the authors neither took Maxwell's equations into consideration nor the effects of the electric field E_3 and the magnetic flux density B_3 on the strains S_{1p} and S_{3m} respectively. Only in the cases where $s_{11}^D \approx s_{11}^E$, $s_{33}^B \approx s_{33}^H$ and $\kappa = 1$, (17) and (18) recover the equations reported in [20].

Under harmonic motion, the general solution of the one-dimensional wave equation (19) in the time domain is

$$u(z, t) = Y(z)T(t), \quad (21)$$

$$Y(z) = A \cos(kz) + B \sin(kz), \quad (22)$$

$$T(t) = C \cos(\omega t) + D \sin(\omega t) \quad (23)$$

where the squared wave number is defined as

$$k^2 = \frac{\omega^2}{\bar{v}^2}. \quad (24)$$

The real constants A and B are determined by boundary conditions, while C and D depends on initial conditions. Solving for $\{A, B, C, D\}$ is not the objective of this paper, however, this time-domain solution is a preliminary step for further analysis in the frequency domain in the following sections.

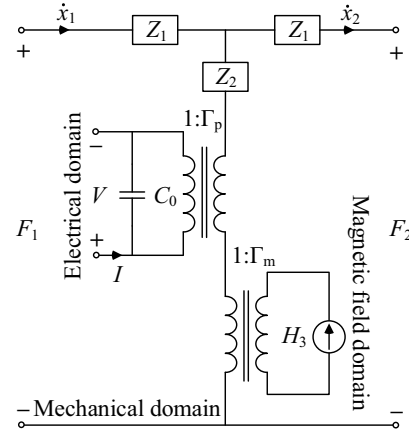


Figure 2. Equivalent circuit model of magnetolectric wireless power transfer system.

3. Equivalent two-port model

The linear two-port network is one of the most widely used models for ED, MME, and RIC WPT systems. Under the right circumstances (e.g. small vibration amplitude or single transmitter-receiver configuration), it is a convenient method of describing dynamical characteristics and interpreting the fundamental performance without compromising the accuracy of the model. The main aim of this section is to simplify a multi-port model of the original system when configured in the free-free condition and develop its two-port equivalent circuit.

The driving frequency of WPT systems can be controlled at the transmitter side. Therefore, investigating and optimizing the frequency responses of the system is of great interest. In order to avoid any possible misunderstanding that might arise for the readers, frequency-domain variables are denoted with a hat on top of a character rather than using the same notations for both the time and frequency domains as seen in [20, 21]. From this point on, all the derivations are carried out in the frequency domain, unless stated explicitly.

The complex amplitude of the displacement, \hat{X} , is a function of z only, $\hat{X}(z) = Y(z)$ where $Y(z)$ is given in (22). The boundary conditions given in terms of the face velocities of the composite laminate (denoted as \hat{V}_1 and \hat{V}_2) are

$$\hat{V}_1|_{z=0} = j\omega \hat{X}(0) = j\omega A, \quad (25)$$

$$\hat{V}_2|_{z=L} = j\omega \hat{X}(L) = j\omega (A \cos(kL) + B \sin(kL)), \quad (26)$$

Assuming that the boundary conditions \hat{V}_1 (\hat{V}_2) at $z=0$ ($z=L$) were determined, two constant coefficients A (B) and the complex amplitude of the displacement are computed as

$$A = \frac{\hat{V}_1}{j\omega}, \quad (27)$$

$$B = \frac{\widehat{V}_2 - \widehat{V}_1 \cos(kL)}{j\omega \sin(kL)}, \quad (28)$$

$$\widehat{X}(z) = \frac{\widehat{V}_1}{j\omega} \cos(kz) + \frac{\widehat{V}_2 - \widehat{V}_1 \cos(kL)}{j\omega \sin(kL)} \sin(kz). \quad (29)$$

The complex amplitude of the strains at the faces are

$$\widehat{S}_{1p}(0) = \left. \frac{d\widehat{X}}{dz} \right|_{z=0} = \frac{\widehat{V}_2 - \widehat{V}_1 \cos(kL)}{j\bar{\nu} \sin(kL)}, \quad (30)$$

$$\widehat{S}_{1p}(L) = \left. \frac{d\widehat{X}}{dz} \right|_{z=L} = \frac{\widehat{V}_2 \cos(kL) - \widehat{V}_1}{j\bar{\nu} \sin(kL)}, \quad (31)$$

$$\widehat{S}_{3m}(0) = \frac{1}{\kappa} \widehat{S}_{1p}(0), \widehat{S}_{3m}(L) = \frac{1}{\kappa} \widehat{S}_{1p}(L). \quad (32)$$

The corresponding forces related to the face stresses are

$$\begin{aligned} \widehat{F}_1 &= -A_1 \widehat{T}_{1p}|_{z=0} - 2A_2 \widehat{T}_{3m}|_{z=0} \\ &= -A_1 \frac{1}{s_{11}^E} (\widehat{S}_{1p}(0) - d_{31,p} \widehat{E}_3) - 2A_2 \frac{1}{s_{33}^H} (\widehat{S}_{3m}(0) - d_{33,m} \widehat{H}_3) \\ &= -\left(\frac{A_1}{s_{11}^E} + \frac{1}{\kappa} \frac{2A_2}{s_{33}^H} \right) \frac{\widehat{V}_2 - \widehat{V}_1 \cos(kL)}{j\bar{\nu} \sin(kL)} + \frac{A_1 d_{31,p}}{s_{11}^E} \widehat{E}_3 + \frac{2A_2 d_{33,m}}{s_{33}^H} \widehat{H}_3, \end{aligned} \quad (33)$$

$$\begin{aligned} \widehat{F}_2 &= -A_1 \widehat{T}_{1p}|_{z=L} - 2A_2 \widehat{T}_{3m}|_{z=L} \\ &= -A_1 \frac{1}{s_{11}^E} (\widehat{S}_{1p}(L) - d_{31,p} \widehat{E}_3) - 2A_2 \frac{1}{s_{33}^H} (\widehat{S}_{3m}(L) - d_{33,m} \widehat{H}_3) \\ &= -\left(\frac{A_1}{s_{11}^E} + \frac{1}{\kappa} \frac{2A_2}{s_{33}^H} \right) \frac{\widehat{V}_2 \cos(kL) - \widehat{V}_1}{j\bar{\nu} \sin(kL)} + \frac{A_1 d_{31,p}}{s_{11}^E} \widehat{E}_3 + \frac{2A_2 d_{33,m}}{s_{33}^H} \widehat{H}_3. \end{aligned} \quad (34)$$

The coupling voltage \widehat{V} produced at the two surfaces of the piezoelectric layer is determined as

$$\widehat{V} = \int_0^{t_p} \widehat{E}_3 dy = \widehat{E}_3 t_p \quad (35)$$

where y is the thickness direction. The forces \widehat{F}_1 and \widehat{F}_2 in (33) and (34) now can be rewritten as follows

$$\widehat{F}_1 = Z_1 \widehat{V}_1 - (\widehat{V}_2 - \widehat{V}_1) Z_2 - \Gamma_p \widehat{V} + \Gamma_m \widehat{H}_3, \quad (36)$$

$$\widehat{F}_2 = -Z_1 \widehat{V}_2 - (\widehat{V}_2 - \widehat{V}_1) Z_2 - \Gamma_p \widehat{V} + \Gamma_m \widehat{H}_3 \quad (37)$$

where Z_1 and Z_2 are referred to the mechanical characteristic impedances, Γ_p is the electromechanical transduction factor of the piezoelectric layer and Γ_m is the magneto-elastic (also known as electrodynamic) transduction factor of the magnetostrictive layer. These parameters are given by

$$Z_1 = -\left(\frac{n}{s_{11}^E} + \frac{1-n}{\kappa s_{33}^H} \right) \frac{A \tan(kL/2)}{j\bar{\nu}}, \quad (38)$$

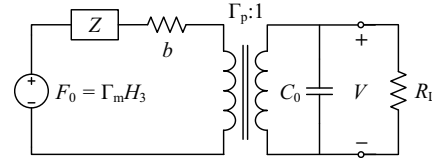


Figure 3. Simplified model with free-free conditions.

$$Z_2 = \left(\frac{n}{s_{11}^E} + \frac{1-n}{\kappa s_{33}^H} \right) \frac{A}{j\bar{\nu} \sin(kL)}, \quad (39)$$

$$\Gamma_p = -\frac{A_1 d_{31,p}}{t_p s_{11}^E} = -w \frac{d_{31,p}}{s_{11}^E}, \quad (40)$$

$$\Gamma_m = 2w t_m \frac{d_{33,m}}{s_{33}^H}. \quad (41)$$

The piezoelectric constant $d_{31,p}$ is usually a negative number, thus $\Gamma_p > 0$. The coupling current \widehat{I} produced by an equivalent piezoelectric layer is

$$\widehat{I} = j\omega C_0 \widehat{V} - \Gamma_p \widehat{V}_m \quad (42)$$

where $C_0 = \epsilon_{33}^S \frac{wL}{t_p}$ is the equivalent nominal capacitance of the piezoelectric transducer and ϵ_{33}^S is the permittivity component at constant strain with the plane-stress assumption of a thin narrow beam (i.e. $\epsilon_{33}^S = \epsilon_{33}^T - d_{31,p}^2 / s_{11}^E$). Here, we denote $\widehat{V}_m = \widehat{V}_2 - \widehat{V}_1$. The complete equivalent circuit is developed as shown in figure 2 where notations of the forces, applied magnetic field and output voltage are in the time domain for a general view.

Under free-free conditions, $\widehat{F}_1 = \widehat{F}_2 = 0$ (which leads to mechanical short-circuit). The lumped-model is then simplified to that depicted in figure 3, where

$$Z = Z_1/2 + Z_2 = \frac{1}{2} \left(\frac{n}{s_{11}^E} + \frac{1-n}{\kappa s_{33}^H} \right) \frac{A}{j\bar{\nu}} \cot(kL/2). \quad (43)$$

The damping coefficient b (not shown in figure 2) represents the mechanical loss. Additionally, the electrical terminals are now connected to a load resistance R_L . The input equivalent 'force' is defined as $\widehat{F}_0 = \Gamma_m \widehat{H}_3$ (or $F_0 = \Gamma_m H_3$ in the time domain). The short-circuit resonance frequency, is determined by the condition $Z = 0$, or equivalently

$$\cos\left(\frac{\omega L}{2\bar{\nu}}\right) = 0, \quad (44)$$

which results in

$$\omega_0 = \pi \frac{\bar{\nu}}{L}. \quad (45)$$

The resonance frequency depends on the beam length, the thickness ratio, and the material properties, but not on the

width of the beam. This property is distinguished from the bending operation of a cantilever beam with a tip mass, in which the bending resonance frequency is a function of the beam width [5].

4. Magnetolectric coefficient

We now consider the ratio of the electric field E_3 to the external magnetic field H_3 . Under open circuit operation (i.e. $R_L \rightarrow +\infty$),

$$\hat{I}_\infty = 0, \quad (46)$$

$$\hat{V}_\infty = \frac{\Gamma_p \hat{V}_m}{C_0 j\omega} = \frac{\Gamma_p \hat{X}}{C_0} = \frac{\Gamma_p}{C_0} \frac{\hat{F}_0}{j\omega(Z+b) + \frac{\Gamma_p}{C_0}} \quad (47)$$

Therefore, the ME coefficient is

$$\alpha_{ME} = \left| \frac{d\hat{E}_{3,\infty}}{d\hat{H}_3} \right| = \frac{\Gamma_p}{t_p C_0} \frac{\Gamma_m}{\sqrt{(\omega b)^2 + (\bar{Z} + \Gamma_p^2/C_0)^2}} \quad (48)$$

where $\bar{Z} = j\omega Z$ is a real function of the drive frequency ω , as follows

$$\bar{Z} = \frac{1}{2} \left(\frac{n}{s_{E1}^2} + \frac{1-n}{\kappa s_{H3}^2} \right) \frac{A}{V} \omega \cot\left(\frac{\omega L}{2v}\right). \quad (49)$$

The anti-resonance frequency (i.e. the open-circuit resonance frequency), denoted by ω_1 , is determined by

$$\bar{Z} + \Delta K = 0 \quad (50)$$

where $\Delta K = \Gamma_p^2/C_0$. Equation (50) has a general form of $X \cot(X) = C$ where X is a variable and C is a constant. There does not exist any analytical solution for this problem, hence, using a numerical method is more suitable. At $\omega = \omega_1$, the ME coefficient is reduced to

$$\alpha_{ME,1} = \frac{\Gamma_p \Gamma_m}{t_p C_0 \omega_1 b}. \quad (51)$$

For moderate electromechanical coupling of the piezoelectric phase $\omega_1 \approx \omega_0$, so $\alpha_{ME,1}$ is approximately $\Gamma_p \Gamma_m / (t_p C_0 \omega_0 b)$. In principle, $\alpha_{ME,1}$ is the maximum possible ME coefficient that can be obtained for a given ME transducer. The compact form in (51) is maybe the most convenient means to evaluate the performance of a ME composite from a material perspective (in other words, from an application-independent point of view).

5. Power optimization

5.1. Analytical solution of output power

We now utilize the equivalent circuit model developed in section 3 to investigate the transferred power in terms of the load resistance, the drive frequency, and the applied \mathbf{B} -field. The complex amplitude of the output voltage is derived as

$$\hat{V} = \frac{\Gamma_p}{C_0} \frac{j\omega R_L C_0}{1 + j\omega R_L C_0} \hat{X} = \frac{\Gamma_p}{C_0} \frac{j\omega \tau}{1 + j\omega \tau} \hat{X} \quad (52)$$

where the electrical time constant is $\tau = R_L C_0$. The complex displacement amplitude is

$$\hat{X} = \frac{\hat{V}_m}{j\omega} = \frac{\hat{F}_0}{j\omega(Z+b) + \frac{\Gamma_p^2}{C_0} \frac{j\omega \tau}{1 + j\omega \tau}}. \quad (53)$$

Assuming that, in the time domain, the applied magnetic field has the form of $H_3 = H_0 \cos(\omega t)$, the average output power is obtained as

$$P = \frac{1}{2} \frac{|\hat{V}|^2}{R_L} = \frac{1}{2} \Delta K \frac{\omega^2 \tau}{1 + (\omega \tau)^2} |\hat{X}|^2 \quad (54)$$

where the square of the displacement amplitude in the frequency domain is given by

$$|\hat{X}|^2 = \frac{(\Gamma_m H_0)^2}{\left[\bar{Z} + \Delta K \frac{(\omega \tau)^2}{1 + (\omega \tau)^2} \right]^2 + \left[\omega b + \Delta K \frac{\omega \tau}{1 + (\omega \tau)^2} \right]^2}. \quad (55)$$

From (54) and (55), we observe that the power delivered to the load is proportional to the square of both the magnetic field strength and the magneto-elastic transduction factor. For a given external magnetic field, magnetostrictive materials with higher $d_{33,m}$ are preferable as they provide stronger Γ_m , and as a consequence, higher output power.

5.2. Optimum power at resonance and anti-resonance frequencies

Typically, optimal operating frequencies of a resonant generator, such as piezoelectric energy harvesters [5], are close to either the resonance or anti-resonance frequency. Therefore, the maximum output power of the ME WPTS can also be estimated by considering the system performance at these specific frequencies.

At the resonance frequency $\omega = \omega_0$ and $\bar{Z} = 0$. By using the gradient descent method, the optimal load and the corresponding optimum output power are determined as follows:

$$\text{opt } R_L|_{\omega=\omega_0} = \frac{1}{\omega_0 C_0 \sqrt{M_0^2 + 1}}, \quad (56)$$

$$P_0 = \text{opt } P|_{\omega=\omega_0} = \frac{(\Gamma_m H_0)^2}{4b} M_0 (\sqrt{M_0^2 + 1} - M_0). \quad (57)$$

M_f is a resonator figure of merit, defined as $M_f = \Delta K / (b\omega)$. In particular, at the resonance frequency $M_0 = \Delta K / (b\omega_0)$. We can write $M_0 = k_c^2 Q_{0,p}$ where k_c is the expedient coupling coefficient (or the generalized electromechanical coupling coefficient) and $Q_{0,p}$ is the mechanical quality factor of the piezoelectric phase at the resonance frequency ω_0 . The details of the derivation are presented in appendix B. A high figure-of-merit is achieved when a piezoelectric material shows strong electromechanical coupling and low mechanical losses, simultaneously. With the same applied magnetic field, based on (41), we can infer the following properties, increasing the amount of the magnetostrictive material or the ratio of the piezomagnetic coefficient to the compliance constant ($d_{33,m}/s_{33}^H$), results in higher output power.

In the same manner, at the anti-resonance frequency $\omega = \omega_1$ (and thus $Z = -\Delta K$), we get

$$\text{opt} R_L|_{\omega=\omega_1} = \frac{\sqrt{M_1^2 + 1}}{\omega_1 C_0}, \quad (58)$$

$$P_1 = \text{opt} P|_{\omega=\omega_1} = \frac{(\Gamma_m H_0)^2}{4b} M_1 (\sqrt{M_1^2 + 1} - M_1) \quad (59)$$

where $M_1 = \Delta K / (b\omega_1)$. In general, P_0 and P_1 are not identical, however for moderately coupled systems $M_0 \approx M_1$, the two maximum powers approximately coincide $P_0 \approx P_1$. It should be noted that the inequality $M_1(\sqrt{M_1^2 + 1} - M_1) < 1/2$ always holds true for all $M_i > 0$ ($i \in \{1, 2\}$), therefore P_0 and P_1 are less than $P_{\text{avt}} = (\Gamma_m H_0)^2 / (8b)$ which is the maximum power available for transfer [5]. As M_0 and M_1 increase, the two ratios P_0/P_{avt} and P_1/P_{avt} approach unity.

6. Model validations

6.1. Experimental setup

Figure 4 shows the experimental setup used for validating the equivalent two-port model. The Helmholtz coil is a transmitter that produces a uniform magnetic flux density as a means of power transfer. The receiver is a magnetoelectric laminated composite, consisting of two TdVib Galfenol and one PZT-5A layers. The magnetostrictive and piezoelectric phases are bonded together by a conductive epoxy, EPO-TEK H20S. Four permanent magnets placed on top, bottom, and two sides (not shown in the figure) of the ME transducer provide a DC bias field for its operation. The two Galfenol layers are magnetized in the length axis; meanwhile, the PZT-5A layer is poled in the thickness direction. The Helmholtz coil is controlled by a Tektronix function generator connecting to an E&I 210 L RF power amplifier. The induced voltage across the load resistance is measured and collected by a Tektronix oscilloscope. The average output power is then computed as $P = \frac{1}{T} \int_0^T \frac{v^2(t)}{R_L} dt$. The geometry of the ME generator, the Helmholtz coil, and the material properties are listed in table 1, except the interface coupling coefficient κ and the longitudinal piezomagnetic constant $d_{33,m}$, which are determined by fitting to experiments in the next Sections.

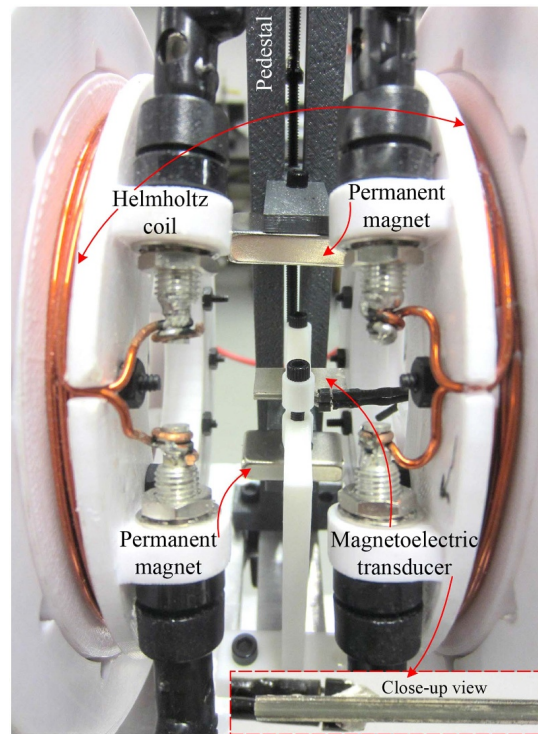


Figure 4. Experimental setup, in which a circular Helmholtz coil is used as a transmitter, the magnetoelectric transducer is placed at the center of the coil, and four permanent magnets are utilized as DC field bias.

6.2. Parameter identifications

Since the piezomagnetic coefficient $d_{33,m}$ is a function of the DC bias field, the possible optimal value of $d_{33,m}$ can be obtained by manually adjusting the distances between the permanent magnets and the ME laminated composite. The DC field that yields the maximum open-circuit voltage generated by the ME transducer is considered as optimal. Here, the bias field is read by the DC Gaussmeter Model GM1-ST (AlphaLab, Inc.), and the open-circuit output voltage is approximately measured with Tektronix 10 M Ω probes. By varying the drive frequency, the anti-resonance frequency, at which the open-circuit voltage reaches its maximum, is determined. The optimal DC bias field and the corresponding anti-resonance frequency are ~ 13.31 mT and $f_1 \approx 70.47$ kHz respectively. The interface coupling coefficient κ is then estimated by fitting the solution ω_1 of equations (49) and (50) to the experimental value, which results in $\kappa = 62.2\%$.

We note that, the output voltage is proportional to the displacement of the laminated composite. Considering a damped harmonic oscillation of the open-circuit voltage shown in figure 5, the damping ratio ξ can be extracted with an exponential fit through the local maxima of this underdamped response ($\xi < 1$). The least-squares method is formulated as follows

Table 1. Material properties and device geometries.

Parameters	Value
PZT-5A4E	
Elastic constant, Y_{11}^E	66, GPa
Elastic compliance, s_{11}^E	$1/Y_{11}^E$, m^2/N
Piezoelectric constant, $d_{31,p}$	-190×10^{-12} , m/V
Dielectric permittivity, $\epsilon_{33}^T/\epsilon_0$	1800
Mass density, ρ_p	7800 kg/m ⁻³
TdVib Galfenol	
Elastic constant, Y_{33}^H	40, GPa
Elastic compliance, s_{33}^H	$1/Y_{33}^H$, m^2/N
Magnetic permeability, $\mu_{33,m}^T/\mu_0$	100
Mass density, ρ_m	7800 kg/m ⁻³
ME transducer geometry	
PZT thickness, t_p	1.02, mm
Galfenol thickness (each layer), t_m	370, μm
Total thickness, $t_0 = t_p + 2t_m$	1.76, mm
Laminated composite width, w	10, mm
Laminated composite length, L	20, mm
Helmholtz coil geometry	
Diameter (center of cross-section)	91, mm
Nominal cross-section	49×49 , mm ²
Wire gauge	16
Number of turns	9

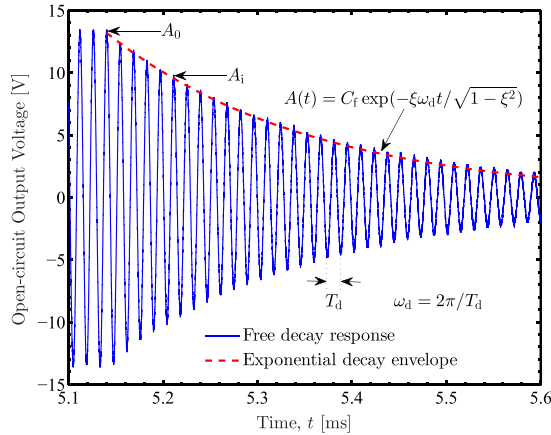


Figure 5. A comparison of (i) free decay response of the open-circuit output voltage, and (ii) exponential decay envelope through local maxima A_i , where $i \in \mathbb{N}$. A_0 is the highest maximum and $C_f = 2.12 \times 10^{11}$ is a fitted constant.

$$\min_{\xi > 0, C_f > 0} \sum_{i=0}^N [A(t_i) - A_i(t_i)]^2 \quad (60)$$

where $(N + 1)$ is the number of experimental samples collected. The decay envelope is characterized by the exponential function $A(t) = C_f \exp(-\xi \omega_d t / \sqrt{1 - \xi^2})$ where C_f is an unknown constant. The angular damped resonance frequency

is calculated as $\omega_d = 2\pi/T_d$, where T_d is the damped period. The discrete oscillation maxima, denoted as A_i ($i \in \mathbb{N}$), with their corresponding time of occurrence t_i , are obtained from the decaying waveform. To solve this non-linear problem with inequality constraints, the non-linear Interior Point and Sequential Quadratic Programming approaches can be used [42]. The fitting procedure gives $\xi \approx 10.68 \times 10^{-3}$; accordingly, the mechanical quality factor around the resonance is $Q_m \approx 46.81$.

For a mass-spring-damper system, the damping ratio is defined as $\xi = b/(2\sqrt{mK_0})$ where b is the damping coefficient which represents total mechanical losses, K_0 is the short-circuit stiffness and m is the mass. However, the mechanical impedance Z of the ME generator is an indispensable function of the material properties and the geometry. Therefore, in order to evaluate the damping constant, we approximate Z by an equivalent mass-spring model, where K_0 and m are found by the least-squares optimization scheme

$$\min_{K_0 > 0, m > 0} \sum \left[\left(\omega m - \frac{K_0}{\omega} \right) - |Z| \right]^2 \quad (61)$$

where the angular drive frequency ω is chosen in a range around the resonance frequency ω_0 . The numerical minimization yields the following results, $K_0 = 81.48$ MN m⁻¹ and $m = 445.8$ mg, which leads to $b = 4.22$ Ns m⁻¹.

From (47) and (50), the open-circuit voltage amplitude at the anti-resonance frequency is derived as

$$V_{\infty,1} = \Gamma_m \frac{H_0 \Gamma_p}{C_0 \omega_1 b} \quad (62)$$

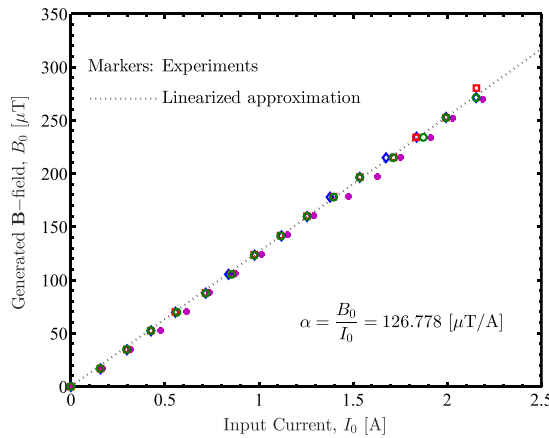


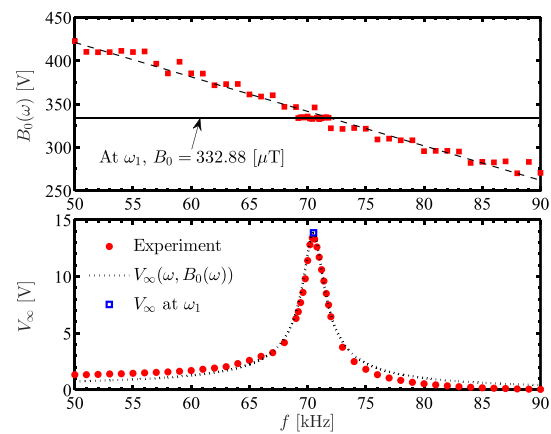
Figure 6. Characterization of the **B**-field generated at the center of the Helmholtz coil, with respect to the current input to the coil. B_0 and I_0 are the amplitude values.

where Γ_m is a function of $d_{33,m}$. The piezomagnetic constant $d_{33,m}$ is approximated by fitting the model prediction in (62) to the measured value, giving us a coefficient of $d_{33,m} = 7.77 \times 10^{-9}$ Wb/N, which is within the range reported by other authors, e.g. 1.85×10^{-9} Wb N^{-1} in [43] and 16.5×10^{-9} Wb N^{-1} in [44]. The measured nominal capacitance of the piezoelectric layer is $C_0 = 2.95$ nF. Up to this point, all the model coefficients are given. This same set of parameters is then used for validating all following cases.

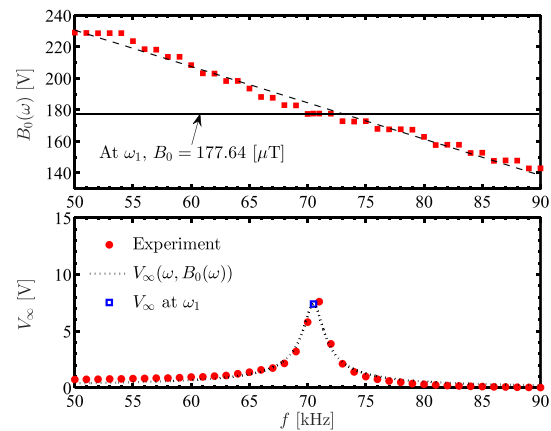
6.3. Experimental validations

(i) Due to the difficulty in measuring the **B**-field while conducting experiments, and (ii) to avoid any possible interference of the permanent magnets (used as the bias field), the relationship between the magnetic flux density strength and the input current is quantified before completing the experimental setup. Four sets of measurements are carried out. The current through the Helmholtz coil and the **B**-field generated at the coil center are captured by the Rigol RP1001C current probe and the AC milliGauss meter model UHS2, respectively. Note, the value displayed on the Gauss meter is in root mean square (RMS) form. The obtained results are shown in figure 6. The relationship between the two parameters is expressed by a linearized approximation, $\alpha = B_0/I_0 = 126.3778 \mu\text{T A}^{-1}$, which is then utilized to map the external **B**-field amplitude from the measured current in further experiments.

Figure 7 presents the frequency response of the open-circuit voltage amplitude with two different ranges of the applied **B**-field. Comparisons between the experimental data and the simulation results (predicted by the equivalent two-port model) show a consistently good agreement for both cases. The output voltage is measured at the steady-state with discrete drive frequencies. It should be noted that the impedance of the Helmholtz coil is dependent on the frequency. Therefore, given the same source voltage, the input current decreases with respect to the increase of the operating frequency, which



(a) $B_0 \in [422.64 \rightarrow 270.06] [\mu\text{T}]$



(b) $B_0 \in [229.05 \rightarrow 142.85] [\mu\text{T}]$

Figure 7. Frequency response comparisons between the experimental data and simulation results by the model. V_∞ is the open-circuit output voltage, measured with $10 \text{ M}\Omega$ probes. $V_{\infty,1}$ (V_∞ at the anti-resonance frequency ω_1) is determined from (62), in which $B_0 = 332.88 \mu\text{T}$ and $177.64 \mu\text{T}$ are used for the two cases.

hence reduces the **B**-field strength. In the simulations, V_∞ is computed as a function of both the drive frequency and its corresponding **B**-field amplitude, $V_\infty = V_\infty(\omega, B_0(\omega))$.

Figure 7 also reveals that (50) is the exact equation to solve for the anti-resonance frequency ω_1 , and $V_{\infty,1}$ computed by (62) can be used to estimate the maximum possible open-circuit voltage. Since $\alpha_{\text{ME}} \propto V_\infty$, this means $\alpha_{\text{ME},1}$ is the highest magnetoelectric coefficient that can be achieved. α_{ME} is widely used as a critical criterion for the magnetoelectric coupling properties in multiferroic materials. However, most of the expressions of α_{ME} reported in the literature concern the operation of a ME device at low-frequency ranges (far below the resonance), which may lead to unfair comparisons among ME transducers (e.g. [45, 46]). Therefore, from

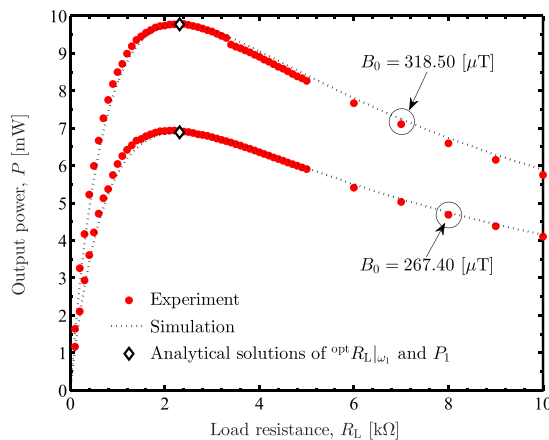


Figure 8. Output power with respect to load resistance with different applied magnetic flux density: Comparisons between experimental data and simulation results. The drive frequency is at the anti-resonance frequency, $f_1 = 70.47$ kHz. The analytical solutions of ${}^{\text{opt}}R_L|\omega_1$ and P_1 are obtained from (58) and (59), respectively.

the material point of view, $\alpha_{\text{ME},1}$ is perhaps a more appropriate and efficient alternative means to theoretically evaluate the performance of a ME-based system. Although α_{ME} is not the main objective of this work, its corresponding frequency response is presented in appendix A.

Figure 8 shows the variation of the output power with respect to the load resistance for two \mathbf{B} -field amplitudes. The drive frequency is set at the anti-resonance frequency, $f_1 = \omega_1/(2\pi) = 70.47$ kHz, for all measurements. The difference between experiments and simulations is negligible. A maximum transferred power of $\max\{P\} = 9.78$ mW is achieved at $B_0 = 318.50 \mu\text{T}$, with an optimal load of ${}^{\text{opt}}R_L \in [2.1, 2.5]$ k Ω (note that any value of R_L in this resistance range produces almost the same output power). The corresponding analytical solutions derived from the model are $P_1 = 9.77$ mW and ${}^{\text{opt}}R_L|\omega_1 = 2.3$ k Ω , attained from (58) and (59), respectively. The model accuracy is consistent with $B_0 = 267.40 \mu\text{T}$. As expected, (i) The optimum electrical load is independent of B_0 , and (ii) Higher input magnetic field strength results in stronger interaction acting on the Galfenol layers, and as a consequence, higher power delivered to the load.

Figure 9 presents the variation of the output power P with respect to the external magnetic flux density B_0 . The drive frequency is fixed at f_1 . The experimental and theoretical results are in good agreement in both cases, with the optimal load of ${}^{\text{opt}}R_L|\omega_1 = 2.5$ k Ω and with an arbitrary load of $R_L = 12.5$ k Ω . As predicted by the theory, P is a quadratic function of B_0 . The optimum power delivered to the load at the anti-resonance frequency P_1 and the power limit P_{avt} are very close to each other. This observation can be explained by figure 10. It shows the ratio of $P_{0/1}$ to the power bound, P_{avt} , as a function of the resonator figure of merit $M_{0/1}$. For the device under consideration, $M_0 = 2.95$ and $M_1 = 2.85$, which leads to

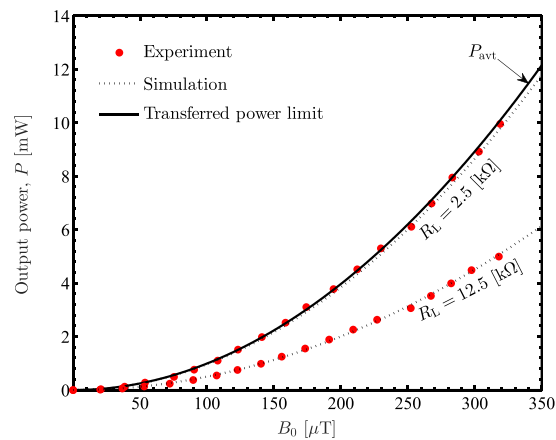


Figure 9. Comparisons of the external \mathbf{B} -field responses between the model simulations and measured results with the optimal load of ${}^{\text{opt}}R_L|\omega_1 = 2.5$ k Ω and an arbitrary load of $R_L = 12.5$ k Ω . The maximum power available for transfer is $P_{\text{avt}} = (\Gamma_m H_0)^2 / (8b)$.

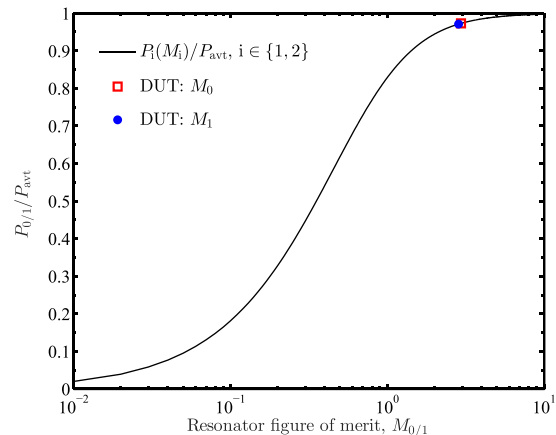


Figure 10. Ratio between the optimum output power attained at the (anti-)resonance frequency $P_{0/1}$ and the power limit P_{avs} as functions of the resonator figure of merit $M_{0,1}$, computed by (57) and (59). The particular values of $M_{0,1}$ and their corresponding power ratios of the investigated ME transducer are included. Notation: DUT = Device Under Test.

$P_0/P_{\text{avt}} \approx P_1/P_{\text{avt}} \approx 97\%$. In general, $M_{0/1} \approx 2$ or higher is a sufficient condition such that $P_{0/1}$ approaches its physical limit P_{avt} . From practical point of view, determining and operating the ME transducer at its anti-resonance frequency along with the corresponding optimal load is perhaps the most convenient technique to approach the power limit.

For the system in use, the overall efficiency is relatively low, $\eta \approx 0.12\%$. The details of this experimental study are presented in appendix C, in order to keep the article focused on the power delivered to the load at a given incident magnetic field, regardless of how the field is produced or the power

required to generate it. The question on how to improve the transfer efficiency is out of the scope of this work and is open for further investigation.

Despite the apparent complexity of the multi-domain energy conversion property of the ME WPTS, the equivalent circuit model has been consistently accurate in predicting all of the essential behaviors related to frequency, load, and magnetic field responses. The developed model is reliable in capturing both of the ME coefficient and the actual power transferred to the load.

The simulation results obtained from the model reveal the following characteristics. When the length of the composite changes (half or double, for instance), only the corresponding optimal load is adjusted, the power available for transfer P_{avt} , and the maximum output power $P_{0/1}$ are kept the same, given an applied magnetic field strength. An advantage of the longer beam is that its resonance and anti-resonance frequencies are lower, which allows higher permissible external magnetic flux density, and thus results in higher transferred power. Meanwhile, a shorter beam achieves higher power density, with identical incident \mathbf{B} -field. The increase of the width allows the laminate to capture more magnetic flux (i.e. inducing higher Γ_m), which enhances both P_{avt} and $P_{0/1}$. Similar effects are observed when increasing the Galfenol thickness. However, further increasing the thickness of PZT does not give a significant benefit as the current thickness can already approach the physical power limit. In a general trend, decrease of t_m and t_p leads to smaller Γ_m and Γ_p , respectively, and drop of $P_{0/1}$. In the circumstance where the total thickness t_0 is constrained, there exists an optimal ratio of t_p to t_0 , $n = t_p/t_0$; for the material properties shown in this article, the optimum value is $n_{\text{opt}} = 0.14$ with the maximum output power of $P_{0/1} = 33.72$ mW at $B_0 = 318.5 \mu\text{T}$. The effects of the material constants, such as $d_{31,p}$ and $d_{33,m}$, are discussed in the next section.

7. Discussions

The ME coefficient α_{ME} has been widely used as a standard to evaluate the performance of ME-based devices; the higher α_{ME} , the stronger the ME effect, and the better the quality of the ME materials. However, is it true that higher α_{ME} always gives better output power? The main aim of this section is to seek the answer to that question, based on the equivalent circuit model validated in the previous section.

The electrodynamic and electromechanical transduction factors, Γ_m and Γ_p , represent the energy transfer mechanisms between the magnetic-mechanical-electrical domains. Considering the analytical solutions for the optimum ME coefficient and output power in (51) and (59), we observe that both $\alpha_{\text{ME},1}$ and P_1 are functions of Γ_m and Γ_p . The behavior of $\alpha_{\text{ME},1}$ and P_1 in terms of Γ_m are shown in figure 11, where Γ_m is treated as a variable and the other model parameters, such as Γ_p , C_0 , ω_1 and b , are kept unchanged. In a general trend, $\alpha_{\text{ME},1}$ and P_1 always increase with the increase of Γ_m . However, while $\alpha_{\text{ME},1}$ is linearly proportional to Γ_m , P_1 is a quadratic function of Γ_m . It is essential to note that higher

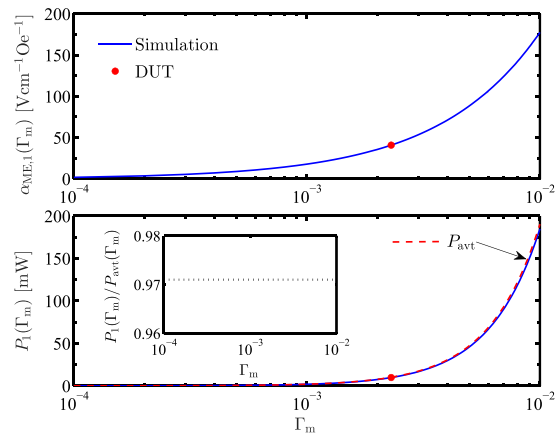


Figure 11. Optimum output power and ME coefficient, P_1 and $\alpha_{\text{ME},1}$, with respect to the electrodynamic transduction factor Γ_m . The ratio of P_1 to P_{avt} , and the measured results of the DUT are also included for comparisons.

Γ_m leads to higher power available for transfer, given a constant applied \mathbf{B} -field. Nonetheless, the discrepancy between P_1 and P_{avt} is negligible. The ratio of P_1 to P_{avt} is close to unity for all Γ_m as depicted in the sub-figure; in particular, $P_1/P_{\text{avt}} = 97.1\%$. At $\Gamma_m^* = 10^{-2}$, which is 4.35 times of that of the DUT, the maximum output power reaches $P_1^* = 190.3$ mW. In practice, this can be achieved with the use of other magnetostrictive materials instead of Galfenol. Among those, Metglas and FeGaB thin film are two promising alternatives, as their piezomagnetic coefficients, $d_{33,m}$, are much higher than that of Galfenol (denoted as G) [34], and therefore result in higher Γ_m . For example, the piezomagnetic coefficient and elastic compliance of Metglas (M) are $d_{33,m}(\text{M}) = 50.3 \times 10^{-9} \text{ m A}^{-1}$ and $s_{33}^{\text{H}}(\text{M}) = 40 \times 10^{-12} \text{ m}^2 \text{ N}^{-1}$ [34], and the ratio between the two electrodynamic transduction factors is $\Gamma_m(\text{M})/\Gamma_m(\text{G}) = 4.05$, given the same geometry. From the efficiency perspective, P_1^* is still far below the input power, which is approximately 8.2 W. Thus, there remains considerable room for the improvement of η associated with material development.

By definition, the longitudinal piezomagnetic coefficient is the rate of change of the magnetostrictive strain along the axial direction ε with respect to the DC bias magnetic field H_b . In particular, $d_{33,m} = d\varepsilon(M)/dH_b$ where M is the magnetization and is induced by H_b [47]. Both ε and $d_{33,m}$ are zero before the magnetostrictive material is magnetized. ε increases with M and then reaches its saturation value when the magnetization is saturated. Due to this behavior of ε , initially, $d_{33,m}$ increases. However, there exists a certain strength of H_b at which $d_{33,m}$ attains a maximum. Beyond that point, $d_{33,m}$ decreases. Since the physical limitations of $d_{33,m}$, and thus Γ_m , are determined by the magnetic properties of the material, the power available for transfer P_{avt} cannot increase infinitely for a given \mathbf{B} -field. Furthermore, P_{avt} is rigorously constrained by the power input to the transmitter coil P_i . However, with the range of Γ_m shown

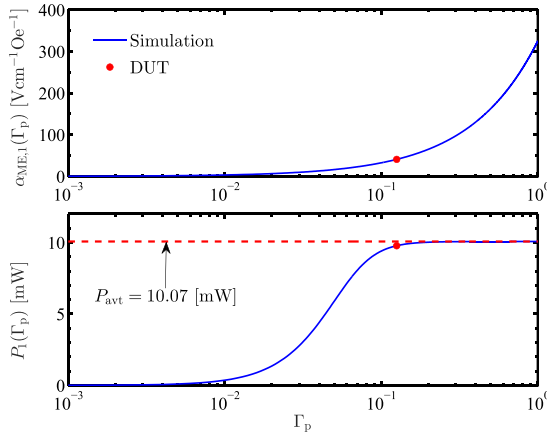


Figure 12. Variations of the optimum output power and ME coefficient, P_1 and $\alpha_{ME,1}$, with respect to the electromechanical transduction factor Γ_p . The measured results of the DUT are also included for comparisons. P_{avt} is a constant.

in figure 11, $P_1 \approx P_{avt} \ll P_i$, therefore, the limit of P_{avt} is not seen.

In the same manner, the influence of Γ_p on the performance of $\alpha_{ME,1}$ and P_1 is presented in figure 12. The roles of Γ_m and Γ_p are now switched and Γ_p becomes a variable. Similarly, $\alpha_{ME,1}$ is a linear function of Γ_p . However, P_1 saturates to P_{avt} when Γ_p is large enough. In this case, Γ_m is a constant, and hence P_{avt} is unchanged with respect to Γ_p . Moreover, with the use of PZT-5A4E as in the experiments, we get $P_1 \approx P_{avt}$. Alternating PZT-5A4E by another piezoelectric material that has higher $d_{31,p}$, and therefore higher Γ_p , does not make any significant improvement on the output power as it nearly approaches its physical limit. This finding demonstrates that an increase in the ME coefficient does not ensure increased power delivered to the load. Only considering α_{ME} as a critical criterion to anticipate the performance of a ME WPTS may be not appropriate. Instead, separately assessing the role of each phase, magnetostrictive and piezoelectric, is a more comprehensive view. While Γ_m defines the physical bound of the power that can be transferred to the load, Γ_p (as an alternative to the figure of merits $M_{0/1}$) indicates whether the device is able to reach that limit or not. Note that, when the mechanical damping coefficient b decreases, the required value of Γ_p , at which $M_1 \approx 2$ and P_1 starts to saturate, also decreases due to the relationship $M_1 = \Gamma_p^2 / (b\omega_1 C_0)$. We hope this recommendation is able to clarify possible misunderstandings in the literature, and have an impact on the design considerations of a ME WPTS.

8. Conclusions

We have presented a comprehensive mathematical modeling framework and analytical solutions to the power optimization problem for a WPTS utilizing a ME transducer as a

receiver. An equivalent two-port model was derived and validated by different sets of rigorous experiments. Several techniques for identifying unknown parameters were discussed. The model developed was able to sufficiently capture and predict the behavior of the device with respect to the drive frequency, load resistance, and applied magnetic flux density, despite the apparent sophisticated-dynamics of a multiple-domain system. We especially emphasized the essential role of the electrodynamic (also known as magneto-elastic) transduction factor in determining the maximum possible power generated at the load with a constant external B-field. We simultaneously showed that this power bound can be approached if the two following conditions are satisfied. (i) The ME generator is operating at the anti-resonance frequency, and the electrical load is optimized correspondingly. (ii) The electromechanical transduction factor reaches a particular range. These alternative criteria (for both transduction mechanisms) are more appropriate for evaluating the performance of a ME WPTS than the ME coefficient that has been widely utilized in the literature.

Acknowledgment

This work was supported by the National Science Foundation ASSIST Nanosystems ERC under Award Number EEC-1160483.

Appendix A. Frequency response of the magnetoelastic coefficient α_{ME}

Figure A1 shows the frequency response of the ME coefficient α_{ME} with the unit of $Vcm^{-1}Oe^{-1}$ that is the most common use in the material science community. The simulation results are calculated from (48) and the measured data are given by $(V_\infty/t_p)/H_0$, which are in good agreement. The analytical solution of the ME constant at the anti-resonance frequency, $\alpha_{ME,1}$, is able to predict exactly the maximum attainable of α_{ME} for a given ME transducer. The consistency of the equivalent circuit model is demonstrated by two sets of experiments with different ranges of the applied B-field. As shown in figure 7, these two intervals are dependent on the drive frequency and the initial values of B_0 (or in other words, the power input to the Helmholtz coil). The optimum ME coefficient of the device under test is $\max\{\alpha_{ME}\} \approx 40.8 Vcm^{-1}Oe^{-1}$.

Appendix B. Resonator figure-of-Merit

At the resonance frequency ω_0 , the figure of merit M_f of the piezoelectric generator is given by

$$M_0 = \frac{\Delta K}{\omega_0 b} = \frac{\Gamma_p^2}{C_0} \frac{1}{\omega_0 b} = k_c^2 \left(\frac{wt_p}{s_{11}^E \pi v} \right) \frac{1}{b} \quad (B1)$$

where Γ_p , C_0 and ω_0 are taken from (40), (42) and (45), respectively, and the squared expedient electromechanical

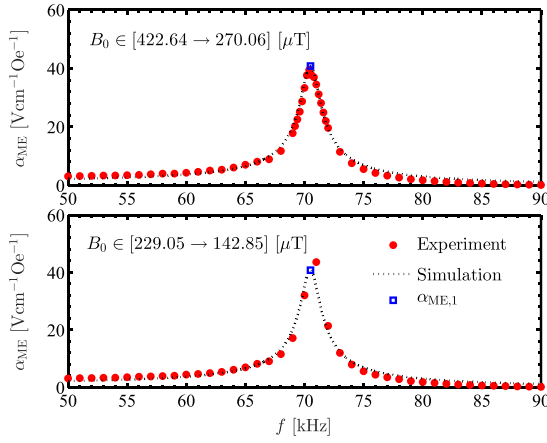


Figure A1. Frequency response of the ME coefficient: Comparisons between the experimental data and simulation results. $\alpha_{ME,1}$ (α_{ME} at ω_1) is achieved from (51). Unit conversion of magnetic field: $1 \text{ A/m} = 4\pi \times 10^{-3} \text{ Oe}$.

coupling coefficient is

$$k_c^2 = \frac{d_{31,p}^2}{s_{11}^E \epsilon_{33}^S}. \quad (\text{B2})$$

Introducing an effective compliance s_e , which is determined by

$$\frac{1}{s_e} = \frac{n}{s_{11}^D} + \frac{1-n}{\kappa s_{33}^B}, \quad (\text{B3})$$

we can write

$$\bar{v}^2 = (\bar{\rho} s_e)^{-1}. \quad (\text{B4})$$

The effective mass of the piezoelectric layer can then be defined as

$$m_{e,p} = \left(\frac{s_e}{\pi^2 s_{11}^E} \right) (wt_p L) \bar{\rho} = \frac{wt_p L}{s_{11}^E (\pi \bar{v})^2}. \quad (\text{B5})$$

The mechanical quality factor of the piezoelectric resonator at ω_0 is derived as follows

$$Q_{0,p} = \frac{m_{e,p} \omega_0}{b} = \frac{1}{b} \frac{wt_p L}{s_{11}^E (\pi \bar{v})^2} \frac{\pi \bar{v}}{L} = \frac{1}{b} \frac{wt_p}{s_{11}^E \pi \bar{v}}. \quad (\text{B6})$$

From (B1) and (B6), we get

$$M_0 = k_c^2 Q_{0,p}. \quad (\text{B7})$$

Besides k_c^2 , M_0 is widely used as an alternative to distinguish the low- and high-coupling regime.

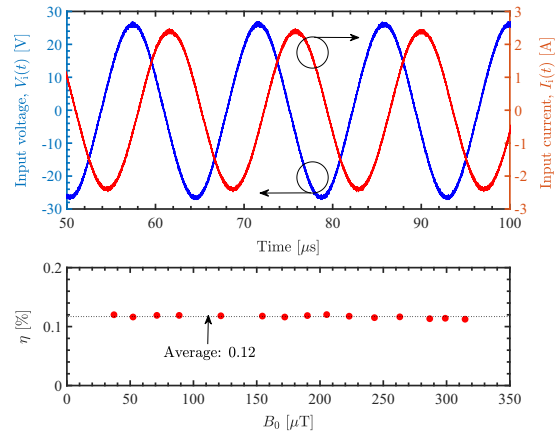


Figure C2. Top: Waveforms of the voltage and current input to the Helmholtz coil that producing a magnetic flux density amplitude of $B_0 = 314.62 \mu\text{T}$. Bottom: Efficiency of the ME WPTS, measured with different values of input power (and therefore generated \mathbf{B} -field).

Appendix C. An experimental study on transfer efficiency

For low-power applications such as implantable medical devices and wireless sensor networks, the efficiency is often not the central objective. Instead, the ultimate goal is to maximize the power delivered to the load. However, it is still of interest to investigate the transmission efficiency of the ME WPTS.

Figure C2 shows an example of the input voltage and current waveforms that generate a corresponding \mathbf{B} -field amplitude of $B_0 = 314.62 \mu\text{T}$. The average input power is numerically calculated as

$$P_i = \frac{1}{t_2 - t_1} \int_{t_1}^{t_2} p_i(t) dt \quad (\text{B8})$$

where $[t_1, t_2]$ is the measured time interval, and $p_i(t)$ is the instantaneous power, $p_i(t) = V_i(t)I_i(t)$. The system efficiency is then determined by the ratio between the power induced on the load and the power input to the network,

$$\eta = \frac{P}{P_i}. \quad (\text{B9})$$

The measurement is repeated with various values of P_i (which results in an alteration of the input \mathbf{B} -field strengths accordingly). As seen in the same figure, η is independent of B_0 since both of P_i and P are proportional to B_0^2 . The average efficiency of the device under test is $\eta \approx 0.12\%$, which is relatively lower than that of an inductively coupled wireless power transfer device [48–50], though, is comparable to an acoustic or RF energy transmission system [12]. However, the power transfer efficiency of the inductive coupling WPTS drops dramatically as the dimensions of the receiver scale down to mm or μm ranges [51]. Details of a brief quantitative comparison are

Table C1. Comparison of several WPT systems with different transferring mechanisms.

Article	Method	Frequency	Receiver size	Distance	Efficiency
[51], 2016	RIC	200 MHz	1 mm (diameter)	12 mm	0.56 %
[52], 2011	RIC	8 MHz	10 × 10 mm ²	10 mm	54.98 %
[53], 2010	RF	1 GHz	2 × 2 mm ²	40 mm	0.2 %
[54], 2014	RF	1.6 GHz	2 mm (diameter)	50 mm	0.04 %
[55], 2014	Acoustic	1 MHz	5 × 10 mm ²	105 mm	1.6 %
[56], 2019	Acoustic	88 kHz	2 × 2 mm ²	20 mm	0.33 %
[4], 2018	MME	350 Hz	71.28 mm ³	–	2.5 × 10 ⁻³ %
[6], 2019	ED	514 Hz	3 cm ³	10 mm	7 %
This work, 2019	ME	70.47 kHz	352 mm ³	–	0.12 %

presented in table C1. Here, we are not trying to cover all the WPT-related work reported in the literature. Instead, we only choose the latest and the most relevant papers focusing on bio-medical applications as representatives.

For a given operating frequency, an efficient ME receiver can be a few orders of magnitude smaller than that of inductive coupling and RF WPT systems [15]. This advantage of the ME transducer makes it promising for miniaturization, especially for implantable medical devices. Furthermore, it is important to note that the Helmholtz coil is not tuned to the mechanical (anti-)resonance of the ME laminated composite. This means the transmitter is subject to more electrical loss during transfer, thus reducing the overall efficiency. The question of how to improve η is open for further analysis in future work.

ORCID iD

Binh Duc Truong  <https://orcid.org/0000-0001-7108-4713>

References

- [1] Int. Commission on Non-Ionizing Radiation Protection 1998 Guidelines for limiting exposure to time-varying electric, magnetic and electromagnetic fields (up to 300 ghz) *Health Phys.* **75** 494–522
- [2] Int. Commission on Non-Ionizing Radiation Protection 2010 Guidelines for limiting exposure to time-varying electric and magnetic fields (1 hz to 100 khz) *Health Phys.* **99** 818–36
- [3] Garraud A, Jimenez J D, Garraud N and Arnold D P 2014 Electrodynamic wireless power transmission to rotating magnet receivers *J. Phys.: Conf. Ser.* **557** 012136
- [4] Truong B D and Roundy S 2018 Wireless power transfer system with center-clamped magneto-mechano-electric (MME) receiver: model validation and efficiency investigation *Smart Mater. Struct.* **28** 015004
- [5] Truong B D, Williams S and Roundy S 2019 Experimentally validated model and analytical investigations on power optimization for piezoelectric-based wireless power transfer systems *J. Intell. Mater. Syst. Struct.* **30** 2464–77
- [6] Garraud N, Garraud A, Munzer D, Althar M and Arnold D P 2019 Modeling and experimental analysis of rotating magnet receivers for electrodynamic wireless power transmission *J. Phys. D: Appl. Phys.* **52** 185501
- [7] IEEE 2006 IEEE standard for safety levels with respect to human exposure to radio frequency electromagnetic fields, 3 khz to 300 ghz *IEEE Std C95.1-2005 (Revision of IEEE Std C95.1-1991)* 1–238
- [8] Lee S, Su M Y, Liang M, Chen Y, Hsieh C, Yang C, Lai H, Lin J and Fang Q 2011 A programmable implantable microstimulator soc with wireless telemetry: Application in closed-loop endocardial stimulation for cardiac pacemaker *IEEE Trans. Biomed. Circuits Syst.* **5** 511–22
- [9] Monti G, Arcuti P and Tarricone L 2015 Resonant inductive link for remote powering of pacemakers *IEEE Trans. Microw. Theory Tech.* **63** 3814–22
- [10] Campi T, Cruciani S, Palandrani F, De Santis V, Hirata A and Feliziani M 2016 Wireless power transfer charging system for airds and pacemakers *IEEE Trans. Microw. Theory Tech.* **64** 633–42
- [11] McRobbie D 2011 Concerning guidelines for limiting exposure to time-varying electric, magnetic and electromagnetic fields (1 hz-100 khz) *Health Phys.* **100** 04
- [12] Basaeri H, Christensen D B and Roundy S 2016 A review of acoustic power transfer for bio-medical implants, *Smart Mater. Struct.* **25** 123001
- [13] Ortega N, Kumar A, Scott J F and Katiyar R S 2015 Multifunctional magnetoelectric materials for device applications *J. Phys.: Condens. Matter.* **27** 504002
- [14] Spaldin N A and Ramesh R 2019 Advances in magnetoelectric multiferroics *Nat. Mater.* **18** 203–12
- [15] Nan T *et al* 2017 Acoustically actuated ultra-compact nems magnetoelectric antennas *Nat. Commun.* **8** 12
- [16] Röntgen W C 1888 Ueber die durch bewegung eines im homogenen elektrischen felde befindlichen dielectricums hervorgerufene electrodynamische kraft *Ann. Phys., Lpz.* **271** 264–70
- [17] Debye P 1926 Bemerkung zu einigen neuen versuchen über einen magneto-elektrischen richteffekt *Z. für Phys.* **36** 300–1
- [18] van Suchtelen J 1972 Product properties: A new application of composite materials *Philips Res. Rep.* **27** 28–37
- [19] Ryu J, Carazo A V, Uchino K and Kim H-E 2001 Magnetolectric properties in piezoelectric and magnetostrictive laminate composites *Japan. J. Appl. Phys.* **40** 4948–51
- [20] Dong S, Li J-F and Viehland D 2003 Longitudinal and transverse magnetoelectric voltage coefficients of magnetostrictive/piezoelectric laminate composite: theory *IEEE Trans. Ultrason. Ferroelectr. Freq. Control* **50** 1253–61
- [21] Dong S, Jie-Fang Li and Viehland D 2004 Longitudinal and transverse magnetoelectric voltage coefficients of magnetostrictive/ piezoelectric laminate composite: experiments *IEEE Trans. Ultrason. Ferroelectr. Freq. Control* **51** 794–9
- [22] Gao J, Gray D, Shen Y, Li J and Viehland D 2011 Enhanced dc magnetic field sensitivity by improved flux concentration in magnetoelectric laminates *Appl. Phys. Lett.* **99** 153502
- [23] Wang Y, Li M, Hasanyan D, Gao J, Li J and Viehland D 2012 Geometry-induced magnetoelectric effect enhancement and

- noise floor reduction in metglas/piezofiber sensors *Appl. Phys. Lett.* **101** 092905
- [24] Wang Z *et al* 2016 Highly sensitive flexible magnetic sensor based on anisotropic magnetoresistance effect *Adv. Mater.* **28** 9370–7
- [25] Gajek M, Bibes M, Fusil S, Bouzouane K, Fontcuberta J, Barthèlèmy A and Fert A 2007 Tunnel junctions with multiferroic barriers *Nat. Mater.* **6** 296–302
- [26] Yang F, Zhou Y C, Tang M H, Liu F, Ma Y, Zheng X J, Zhao W F, Xu H Y and Sun Z H 2009 Eight-logic memory cell based on multiferroic junctions *J. Phys. D: Appl. Phys.* **42** 072004
- [27] Hu J-M, Li Z, Chen L-Q and Nan C-W 2011 High-density magnetoresistive random access memory operating at ultralow voltage at room temperature *Nat. Commun.* **2** 553
- [28] Geiler A L *et al* 2010 Multiferroic heterostructure fringe field tuning of meander line microstrip ferrite phase shifter *Appl. Phys. Lett.* **96** 053508
- [29] Lee J, Hong Y-K, Lee W, Abo G S, Park J, Neveu N, Seong W-M, Park S-H and Ahn W-K 2012 Soft m-type hexaferrite for very high frequency miniature antenna applications *J. Appl. Phys.* **111** 07A520
- [30] Liu M, Howe B M, Grazulis L, Mahalingam K, Nan T, Sun N X and Brown G J 2013 Voltage-impulse-induced non-volatile ferroelastic switching of ferromagnetic resonance for reconfigurable magnetoelectric microwave devices *Adv. Mater.* **25** 4886–92
- [31] O'Handley R C, Huang J K, Bono D C and Simon J 2008 Improved wireless, transcutaneous power transmission for in vivo applications *IEEE Sens. J.* **8** 57–62
- [32] Newacheck S and Youssef G 2019 Wireless energy transfer based on strain-mediated composite multiferroics, *Smart Mater. Struct.* **29** 015014
- [33] Leung C M, Li J, Viehland D and Zhuang X 2018 A review on applications of magnetoelectric composites: from heterostructural uncooled magnetic sensors, energy harvesters to highly efficient power converters *J. Phys. D: Appl. Phys.* **51** 263002
- [34] Chu Z, Pourhosseini Asl M and Dong S 2018 Review of multi-layered magnetoelectric composite materials and devices applications *J. Phys. D: Appl. Phys.* **51** 243001
- [35] Cheng Y, Peng B, Hu Z, Zhou Z and Liu M 2018 Recent development and status of magnetoelectric materials and devices *Phys. Lett.* **382** 3018–25
- [36] Sirohi J and Chopra I 2000 Fundamental understanding of piezoelectric strain sensors *J. Intell. Mater. Syst. Struct.* **11** 246–57
- [37] Bichurin M I, Petrov V M and Srinivasan G 2002 Theory of low-frequency magnetoelectric effects in ferromagnetic-ferroelectric layered composites *J. Appl. Phys.* **92** 7681–3
- [38] Osaretin I A and Rojas R G 2010 Theoretical model for the magnetoelectric effect in magnetostrictive/piezoelectric composites *Phys. Rev. B* **82** 174415 p
- [39] Subhani S M, Chelvane J A and Arockiarajan A 2018 Experimental investigation of performance of tri-layered magnetoelectric composites under thermal environment *J. Phys. D: Appl. Phys.* **51** 295001
- [40] Bian L, Wen Y, Li P, Gao Q and Zheng M 2009 Magnetolectric transducer with high quality factor for wireless power receiving *Sensors Actuators A: Phys.* **150** 207–11
- [41] Wang Y, Hasanyan D, Li M, Gao J, Li J, Viehland D and Luo H 2012 Theoretical model for geometry-dependent magnetoelectric effect in magnetostrictive/piezoelectric composites *J. Appl. Phys.* **111** 124513
- [42] Jorge Nocedal S W 2006 *Numerical Optimization* (New York: Springer)
- [43] Domann J P, Loeffler C M, Martin B E and Carman G P 2015 High strain-rate magnetoelasticity in galferol *J. Appl. Phys.* **118** 123904
- [44] Summers E, Meloy, R and Restorff J B 2009 Galferol alloying additions and the effects on uniaxial anisotropy generation *J. Appl. Phys.* **106** 024914
- [45] Chang C-M and Carman G P 2007 Experimental evidence of end effects in magneto-electric laminate composites *J. Appl. Phys.* **102** 124901
- [46] Zhao C P, Fang F and Yang W 2010 A dual-peak phenomenon of magnetoelectric coupling in laminated terfenol-d/PZT/terfenol-d composites, *Smart Mater. Struct.* **19** 125004
- [47] Zhou H-M, Li M-H, Li X-H and Zhang D-G 2016 An analytical and explicit multi-field coupled nonlinear constitutive model for terfenol-d giant magnetostrictive material *Smart Mater. Struct.* **25** 085036
- [48] Kurs A, Karalis A, Moffatt R, Joannopoulos J D, Fisher P and Soljačić M 2007 Wireless power transfer via strongly coupled magnetic resonances *Science* **317** 83–6
- [49] Moore J, Castellanos S, Xu S, Wood B, Ren H and Tse Z T H 2018 Applications of wireless power transfer in medicine: State-of-the-art reviews *Ann. Biomed. Eng.* **47** 22–38
- [50] Schormans M, Valente V and Demosthenous A 2018 Practical inductive link design for biomedical wireless power transfer: A tutorial *IEEE Trans. Biomed. Circuits Syst.* **12** 1112–30
- [51] Ahn D and Ghovanloo M 2016 Optimal design of wireless power transmission links for millimeter-sized biomedical implants *IEEE Trans. Biomed. Circuits Syst.* **10** 125–37
- [52] Silay K M, Dehollain C and Declercq M 2011 Inductive power link for a wireless cortical implant with two-body packaging *IEEE Sens. J.* **11** 2825–33
- [53] Poon A S Y, O'Driscoll S and Meng T H Optimal frequency for wireless power transmission into dispersive tissue *IEEE Trans. Antennas Propag.* **58** 1739–50 2010
- [54] Ho J S, Yeh A J, Neofytou E, Kim S, Tanabe Y, Patlolla B, Beygui R E and Poon A S Y 2014 Wireless power transfer to deep-tissue microimplants *Proc. Natl Acad. Sci.* **111** 7974–9
- [55] Mazzilli F, Lafon C and Dehollain C 2014 A 10.5 cm ultrasound link for deep implanted medical devices *IEEE Trans. Biomed. Circuits Syst.* **8** 738–50
- [56] Basaeri H, Yu Y, Young D and Roundy S 2019 A mems-scale ultrasonic power receiver for biomedical implants *IEEE Sensors Lett.* **3** 1–4

4.2 Magnetolectric Wireless Power Transfer for Biomedical Implants: Effects of Nonuniform Magnetic Field, Alignment and Orientation

In practice, the position and orientation of biomedical implants cannot be perfectly controlled. In addition, it is nearly impossible to provide a uniform magnetic field throughout the space from the transmitter to the receiver. Any variations in the receiver location may lead to a significant drop in the delivered power, making it insufficient for powering the implanted medical devices. Therefore, evaluating the effects of the field nonuniformity, receiver misalignment and misorientation is essential. These influences were thoroughly investigated for resonant inductive coupling power transmission systems. However, there has been no such study on the magnetolectric wireless power transfer system in the literature. Addressing all of those concerns is the central objective of this Section. Furthermore, comprehending the performance of a complete system, from the transmitter to the receiver side, is required to design an optimal structure and bridge the gap between ideal operation and realistic scenarios.

© 2020 Elsevier. Reprinted, with permission from B. D. Truong, E. Andersen, C. Casados, and S. Roundy, "Magnetolectric Wireless Power Transfer for Biomedical Implants: Effects of Non-Uniform Magnetic Field, Alignment and Orientation," *Sensors and Actuators: A. Physical*, vol. 316, 1 December 2020.



Magnetolectric wireless power transfer for biomedical implants: Effects of non-uniform magnetic field, alignment and orientation

Binh Duc Truong, Erik Andersen, Curtis Casados, Shad Roundy

Department of Mechanical Engineering, University of Utah, Salt Lake, UT 84112, USA



ARTICLE INFO

Article history:

Received 11 May 2020

Received in revised form 16 July 2020

Accepted 6 August 2020

Available online 28 August 2020

Keywords:

Magnetolectric transducer

Wireless power transfer

Non-Uniform magnetic field

Power optimization

Mis-alignment/orientation

ABSTRACT

This article presents experimental validation of a generalized equivalent two-port model for a magnetolectric-based wireless power transfer system (WPTS) that utilizes a circular multi-turn coil as a transmitter, with a focus on potential application to biomedical implantable devices. The central objective of the work is to investigate the performance of the power delivered to a resistive load under uncertainties in magnetolectric receiver position and orientation. In addition, the effects of a non-uniform applied magnetic field are considered. For the particular experimental system being studied, a maximum transferred power of 4.91 mW is obtained at a distance of 3 cm between the centers of the coil and the magnetolectric (ME) transducer, in which the corresponding magnetic flux density is 225.8 μT . As the distance increases to 6 cm, the generated power drops to 1.97 mW. Furthermore, we find that the output power is proportional to the squared cosine of the misorientation angle, compared to the power achieved at the nominal (zero-angle) position. Meanwhile, as expected, the delivered power is less sensitive to misalignment since the width of the receiver is relatively small in comparison with the diameter of the transmit coil. In general, the power produced at the load is a quadratic function of the effective magnetic field that is projected onto the operating direction of the ME laminated composite (i.e., the longitudinal axis in this case). All findings are expected to provide a universal comprehensive picture of the dynamics and performance of the ME WPTS. The presented device concept could open an alternative pathway for powering implants.

© 2020 Elsevier B.V. All rights reserved.

1. Introduction

The Internet of Things (IoT) for healthcare has received worldwide research effort for many biomedical applications such as health monitoring and therapeutic treatment of dysfunctional organs. Healthcare activities based on wireless sensor networks provide secure transmission and reception of medical signals both for early diagnosis and for real-time observation of health status [1,2]. A well-known early implant is a cardiac pacemaker, which is installed in the heart through surgery to manage irregular rhythm, for instance, tachycardia (too fast) or bradycardia (too slow) [3]. In the last decades, the rapid progress of implantable medical devices (IMDs) has seen extraordinary growth to have functionality and packaging proper for biological implantations [4]. However, almost all IMDs so far have been powered by batteries that occupy the majority of space in an implanted system, posing a challenge to effort to miniaturize the entire implanted system. The battery has to be replaced or recharged regularly due to its limited lifetime. In

order to increase the longevity of IMDs, efforts to power the implant by alternative contactless means has become more prevalent. Central to this ongoing advancement is wireless power transfer (WPT) [5]; a technology that offers not only long-term sustainability but also greater flexibility, reliability, and safety [6,7].

A wireless power transfer system (WPTS) enables the biomedical implant by wave transmission through the air and multi-layer tissue media. The WPT methods are generally categorized into two schemes, near-field and far-field, depending on the operating frequency and the transfer distance between the transmitter and receiver [8]. In lossy dielectrics (e.g., skin, fat, and muscle), the far-field waves suffer from significant path loss as a result of high energy absorption [9]. Furthermore, the higher frequency waves used in far-field transmission, resulting in higher energy absorption in human tissue, are potentially more harmful to the human body, and so are more tightly limited by standard regulations [10–13]. By contrast, near-field systems are more efficient (i.e., lower power dissipation) in lossy media [14], and therefore are generally more suitable for bio-implantable applications.

Two well-established methods using electromagnetic fields are inductive coupled resonators [15,16] and electrodynamic coupling

E-mail address: Binh.D.Truong@utah.edu (B.D. Truong).

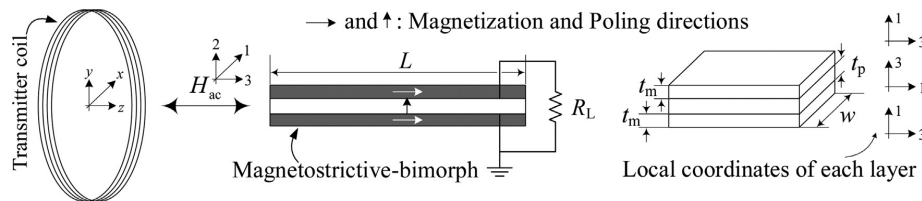


Fig. 1. Schematic of the WPTS utilizing a circular multi-turn coil as a transmitter and a magnetoelastic (ME) transducer as a receiver. The geometric dimensions of the ME laminated composite are included. (x, y, z) and $(1, 2, 3)$ are the global and local coordinates, respectively.

[17,18]. The latter is referred to here as the magneto-mechano-electric (MME) mechanism. Each technique has its own merits and drawbacks. The typical operating frequency of a resonant inductive coupling (RIC) system is in a range of MHz, which limits the maximum allowable magnetic flux density (\mathbf{B} -field) that can be applied to humans. By contrast, MME devices operate at much lower frequencies which allow them to be exposed to much higher field strengths. For instance, the permissible \mathbf{B} -field at 1 kHz is $\sim 300 \mu\text{T}$, in comparison with $0.29 \mu\text{T}$ at 6.78 MHz, according to [12,13]. However, the weak coupling between the magnetic and mechanical domains of the MME resonator, which is realized by the interaction of a permanent magnet and the \mathbf{B} -field, results in extremely low transmission efficiency. In order to overcome the limitations of those architectures, in this work, we introduce an alternative WPTS that utilizes a magnetoelastic (ME) transducer as a receiver. This approach manifests a higher coupling than MME structures and requires lower frequencies than RIC systems; therefore, it is possible to transfer energy into an implanted medical device more efficiently (than MME transducers) and at higher magnetic fields (than RIC) without violating the safety standards.

In practice, the position and orientation of IMDs cannot be perfectly controlled. Furthermore, it is almost impossible to generate a uniform \mathbf{B} -field throughout the space from the transmitter to the receiver. Any variations in the receiver location may lead to a significant drop in the delivered power, making it insufficient for powering the IMDs. Thus, comprehending the effects of the field non-uniformity, device misalignment and misorientation is essential. These influences were thoroughly investigated for RIC and acoustic power transmission systems [19,20]. However, there has been no such a study on the ME WPTS in the literature. Addressing all of these concerns is the central objective of the article.

In a previous work [21], we presented in detail a two-port model for the receiver (a ME transducer), with an assumption that the external \mathbf{B} -field is ideally uniform along the length of the laminated composite. To verify the model predictions, a Helmholtz coil was utilized as a transmitter, and the ME resonator was located at its center. In contrast, in this paper, the developed model is further generalized and validated for the case where a non-uniform magnetic field is employed. By making use of a circular multi-turn coil as a transmitter, the effects of the coil geometry on the distribution of the \mathbf{B} -field now cannot be disregarded. Understanding the performance of a complete structure that takes into account the dynamics of both transmitting and receiving sides is important to design an optimal system and bridge the gap between ideal operation and realistic scenarios. With the aim to power low-power bioelectronics, we treat the actual transferred power as a key factor of the investigation, while leaving the transfer efficiency open for further consideration.

2. Device concept and Equivalent circuit model

Different from a RIC architecture, in which the magnetic energy is captured on the principle of Faraday's law of induction, a ME

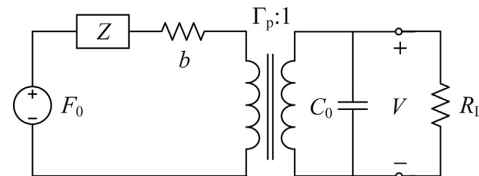


Fig. 2. Simplified equivalent circuit model for free-free ends configuration.

WPTS first converts the magnetic waves to mechanical vibrations through the interaction between the field and magnetostrictive material. The kinetic energy is then transformed into electrical energy at the final stage of conversion due to the piezoelectric effect. The overall ME coupling is dependent on not only the receiver geometry but also the intrinsic properties of materials in use. This characteristic could provide more degrees of freedom for transducer design and optimization in order to achieve a given desired power.

Fig. 1 shows the WPTS that is under consideration, in which a ME transducer is utilized as a receiver while a circular multi-turn coil is a transmitter. The ME laminate used for this study is composed of one PZT layer placed in between two Galfenol layers, bonded together by a conductive adhesive. The magnetostrictive material is magnetized in the length direction while the piezoelectric phase is poled in the thickness axis. The geometric dimensions of the ME generator are defined as in the figure; L , w , t_m and t_p are the beam length, width, and thicknesses of the two phases. (x, y, z) are the system global coordinates while the material local axes are denoted as $(1, 2, 3)$. The positive z -axis is coming out of the coil plane towards the ME laminate. The transmitter can be modeled as a thick coil that uses the current density instead of the current itself in order to eliminate the number of turns.

Under an external AC magnetic field (\mathbf{H} -field) applied along the z -axis, a strain is induced inside the magnetostrictive material, which is then transferred to the piezoelectric layer through the bonding interfaces. As a consequence, the entire composite structure vibrates along the length direction, which is also the local axis 3 and 1 of the magnetostrictive and piezoelectric phases, respectively. Since the magnetization and polarization vectors are in parallel with the 3-direction, Galfenol and PZT operates in the longitudinal ($d_{33,m}$) and transversal ($d_{31,p}$) coupling. The power generation capability of the ME WPTS is evaluated by measuring the voltage across a resistor that is connected to the output terminals of the ME receiver.

The equivalent circuit model of the free-free configuration is shown in Figure 2, which was derived and experimentally validated in [21] under the condition that the applied magnetic flux density is uniform. Here, $F_0 = \Gamma_m H_0 \cos(\omega t)$ is the equivalent force input to the mechanical domain where Γ_m is the magneto-elastic transduction factor. The excitation magnetic field is sinusoidal with angular frequency ω , $H_{ac} = H_0 \cos(\omega t)$. We denote Z and b as the mechanical impedance and damping coefficient, respectively. Γ_p is the elec-

tromechanical transduction factor, C_0 is the nominal capacitance of the piezoelectric resonator, and V is the voltage generated on the resistor R_L .

The model parameters are given by

$$\Gamma_m = 2wt_m \frac{d_{33,m}}{s_{33}^H}, \quad (1)$$

$$Z = \frac{1}{2} \left(\frac{n}{s_{11}^E} + \frac{1-n}{\kappa s_{33}^H} \right) \frac{A}{j\bar{v}} \cot \left(\frac{\omega L}{2\bar{v}} \right), \quad (2)$$

$$\Gamma_p = -w \frac{d_{31,p}}{s_{11}^E}, \quad (3)$$

$$C_0 = \epsilon_{33}^T \frac{wL}{t_p} \quad (4)$$

where κ is the interface coupling coefficient representing the strain percentage transferred to the piezoelectric material from the magnetostrictive layers,

$$n = \frac{t_p}{t_p + 2t_m}, \quad 0 < n < 1, \quad (5)$$

$$A_1 = t_p w, \quad A_2 = t_m w, \quad A = (t_p + 2t_m)w, \quad (6)$$

$$\bar{v}^2 = \frac{1}{\bar{\rho}} \left[n \left(s_{11}^E - \frac{d_{31,p}^2}{\epsilon_{33}^T} \right)^{-1} + \frac{1-n}{\kappa} \left(s_{33}^H - \frac{d_{33,m}^2}{\mu_{33,m}^T} \right)^{-1} \right], \quad (7)$$

$$\bar{\rho} = \frac{\rho_p A_1 + 2\rho_m A_2 / \kappa}{A_1 + 2A_2}. \quad (8)$$

The definitions of the material properties are as follows. ρ_p and ρ_m – mass densities of the piezoelectric and magnetostrictive phases, respectively. s_{11}^E – elastic compliance of the piezoelectric material under constant electric field. $d_{31,p}$ – transverse piezoelectric charge constant. ϵ_{33}^T – dielectric permittivity under constant stress. ϵ_{33}^S – permittivity component at constant strain with the plane-stress assumption of a thin narrow beam (i.e., $\epsilon_{33}^S = \epsilon_{33}^T - d_{31,p}^2 / s_{11}^E$). s_{33}^H – elastic compliance of the magnetostrictive material at constant magnetic field. $d_{33,m}$ – piezomagnetic constant. $\mu_{33,m}^T$ – magnetic permeability at constant stress.

Based on the derivations presented in [21], the two-port model is now generalized for the case of a non-uniform external magnetic field and an arbitrary position of the ME receiver. The complex amplitude of the open-circuit voltage, $R_L \rightarrow +\infty$, is determined as

$$\hat{V}_\infty = \frac{\Gamma_p}{C_0} \frac{\Gamma_m(H_0)}{j\omega(Z+b) + \Delta K} \quad (9)$$

where $\Delta K = \Gamma_p^2 / C_0$ and $\langle H_0 \rangle$ is the effective \mathbf{H} -field amplitude. Denoting H_i as the projection of the total magnetic field acting on an infinitesimal mass element m_i onto the length direction of the laminated composite, $\langle H_0 \rangle$ is then averaged over the entire volume of the magnetostrictive material,

$$\langle H_0 \rangle = \frac{1}{N} \sum_{i=1}^N H_i \quad (10)$$

where N is the number of computational samples. The ME coefficient is defined by the rate of change of the open-circuit electric field $\hat{E}_{3,\infty}$ in response to the applied magnetic field \hat{H}_3 ,

$$\alpha_{ME} = \left| \frac{d\hat{E}_{3,\infty}}{d\hat{H}_3} \right| = \frac{\Gamma_p}{t_p C_0} \frac{\Gamma_m}{\sqrt{(\omega b)^2 + (\bar{Z} + \Delta K)^2}} \quad (11)$$

where the subscript {3} denotes the local coordinate of both piezoelectric and magnetostrictive phases, and $\bar{Z} = j\omega Z$ is a real function of the drive frequency ω ,

$$\bar{Z} = \frac{1}{2} \left(\frac{n}{s_{11}^E} + \frac{1-n}{\kappa s_{33}^H} \right) \frac{A}{\bar{v}} \omega \cot \left(\frac{\omega L}{2\bar{v}} \right). \quad (12)$$

α_{ME} is independent of the applied magnetic field, but it is a function of operating frequency.

The power delivered to the load is derived as

$$P = \frac{1}{2} \frac{|\hat{V}|^2}{R_L} = \frac{1}{2} \Delta K \frac{\omega^2 \tau}{1 + (\omega \tau)^2} \Gamma_m^2 \langle H_0^2 \rangle / \left\{ \left[\bar{Z} + \Delta K \frac{(\omega \tau)^2}{1 + (\omega \tau)^2} \right]^2 + \left[\omega b + \Delta K \frac{\omega \tau}{1 + (\omega \tau)^2} \right]^2 \right\} \quad (13)$$

where $\tau = C_0 R_L$ is the electrical time constant, and

$$\langle H_0^2 \rangle = \frac{1}{N} \sum_{i=1}^N H_i^2. \quad (14)$$

Validating equations (9), (11) and (13) are the main objectives of the article, taking into account the effects of non-uniform \mathbf{H} -field, alignment and orientation.

3. Experimental validations

3.1. Experimental setup

Figure 3 shows the complete electrical setup to evaluate the output power of the ME WPTS. A single-coil, connected to an E&I 210L RF power amplifier, is used as a transmitter that generates a magnetic field as a means of power transmission. The receiver is a ME laminated composite, consisting of one PZT-5A and two TdVib Galfenol layers. The two materials are bonded together by EPO-TEK H20S, a conductive epoxy. Two rectangular K&J neodymium magnets are placed above and below the ME transducer to produce a DC magnetic field (as a bias) for its operation. The drive frequency and the power input to the transmitter are controlled by a Tektronix function generator. The output voltage is measured with a Tektronix 10 M Ω probe and collected by a Tektronix oscilloscope. In experiments, the average transferred power is determined by

$$P = \frac{1}{T} \int_0^T \frac{V^2(t)}{R_L} dt \quad (15)$$

where $V(t)$ is the waveform taken over a sampling period of time T . Under the open-circuit operation, $R_L \rightarrow +\infty$ and $P \rightarrow 0$. A 10-M Ω probe is used for approximating the open-circuit output voltage. All the model parameters are extracted from [21] and are listed in Table 1. This same set of constants is utilized to validate all following cases. The damping coefficient is computed from a damped harmonic oscillation of the measured open-circuit voltage. The interface coupling, which relates the strain transfer between the two phases (magnetostrictive and piezoelectric), is estimated by fitting the predicted anti-resonance frequency to its experimental value.

3.2. Open-circuit voltage and magnetoelectric coefficient

The ME coefficient, α_{ME} , is the most widely used factor for evaluating the performance of a ME transducer as it shows the direct relation between the induced electric field and the applied magnetic field. While α_{ME} is a material-oriented criterion, the open-circuit output voltage is the actual physical parameter that

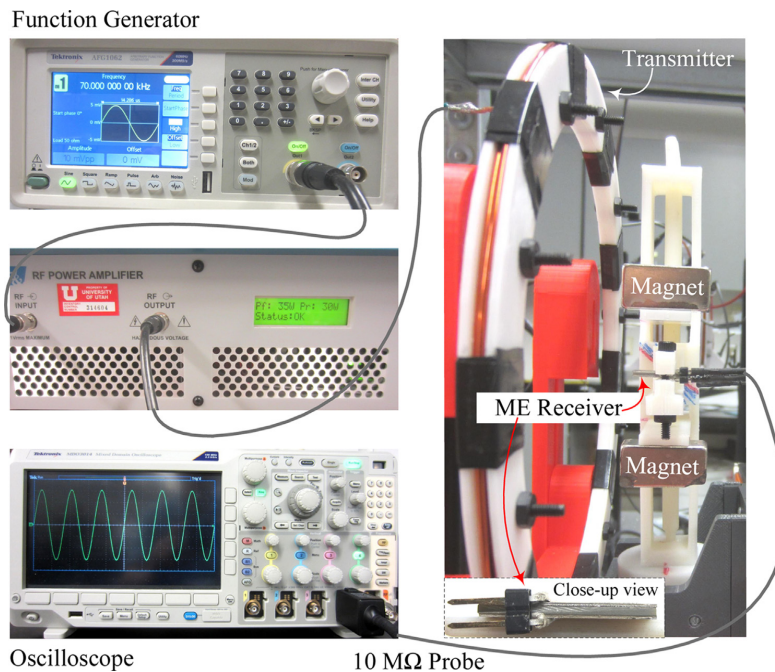


Fig. 3. Sketch of the electrical setup for measuring the power transferred to the load, including the experimental prototypes of the transmitting coil, the ME receiver and its close-up view.

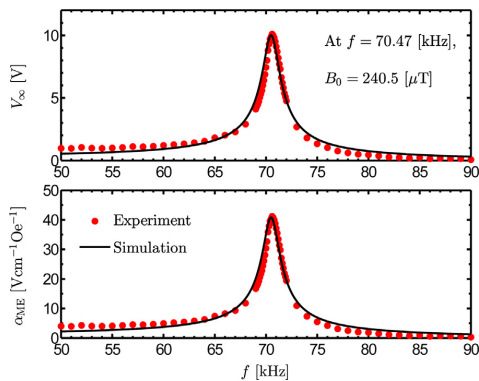


Fig. 4. Frequency responses of the open-circuit voltage V_{∞} and the ME coefficient α_{ME} : Comparisons between the experimental data and simulation results. Unit conversion of magnetic field: $1 \text{ A/m} = 4\pi \times 10^{-3} \text{ Oe}$.

magnetic field sensing applications concern. Therefore, it is worthwhile to investigate these aspects, although they are not the main aims of the work.

As proven in [18], operating an electromechanical-based WPTS at its anti-resonance frequency together with the corresponding optimal load is the most convenient method to approach the power transfer limit (i.e., the maximum power available at the mechanical domain). The anti-resonance frequency f_1 , also known as the open-circuit resonance frequency, can be determined by considering the frequency responses of the open-circuit voltage amplitude V_{∞} that are presented in Figure 4. A magnetic field sensor (model MC110A) is used to measure the \mathbf{B} -field amplitude generated by the trans-

mitter at $f = f_1$. The obtained results are $f_1 = 70.47 \text{ kHz}$, $B_0 = 240.5 \mu\text{T}$ and $\max\{V_{\infty}\} = 10.10 \text{ V}$. Note that, the impedance of the transmit coil is a function of frequency. Hence, given the same source voltage, the input current decreases with respect to the increase of the operating frequency, which hence reduces the \mathbf{B} -field strength. However, for the particular transmitter and frequency range in use, this effect can be neglected. In the simulations, the same value of B_0 is employed and V_{∞} is calculated as $V_{\infty} = |\hat{V}_{\infty}|$ with \hat{V}_{∞} given in (9). The measured capacitance of the PZT layer is $C_0 = 2.95 \text{ nF}$. A comparison between the experiments and predictions shows a good agreement. The frequency performance of the ME coefficient is included in the same figure, in which a $\max\{\alpha_{ME}\} = 41.17 \text{ Vcm}^{-1}\text{Oe}^{-1}$ is attained at the anti-resonance frequency.

In order to investigate the alteration of V_{∞} over the change of the relative distance between the transmitter and receiver, we first use an analytical model of a thick coil to generate a map of the magnetic field strength along the coil centerline $(x, y, z) = (0, 0, z)$. The model is reliable for further studies as it was both numerically and experimentally validated [22,23]. This method relaxes the demand for the precise measurements of the \mathbf{H} -field with a large number of sampling points (i.e., N in (10)) over a short distance range, which is challenging to implement due to the large size of the magnetic field sensor (MC110A). A summary of the theoretical formulation developed in [23] is presented in Appendix A.

Applying equation (18) for the transmitter and receiver geometries in Table 1, we find that, given the same z , the variation of the magnetic field in the longitudinal direction, $H_z(x, y, z)$, is negligible for $x^* \in [x - w/2, x + w/2]$ and $y^* \in [y - t/2, y + t/2]$ where $t = t_p + 2t_m$ is the total thickness of the ME laminate. In other words, $H_z(x^*, y^*, z) \approx H_z(x, y, z)$. Meanwhile, at the same x and y , the non-uniformity along the z -axis is more significant and cannot be neglected, $H_z(x, y, z^*) \neq H_z(x, y, z)$ for $z^* \in [z - L/2, z + L/2]$.

Table 1
Coil parameters, material properties and magnetolectric transducer geometries.

Parameters	Value
Transmitter	
Inner radius, r_1	7.78, cm
Outer radius, r_2	8.35, cm
Lower height, z_1	-1.65, mm
Upper height, z_2	1.65, mm
Number of turns, N_c	9
Wire diameter, d_w	1.291, mm
PZT-5A4E	
Elastic constant, Y_{11}^E	66, GPa
Elastic compliance, s_{11}^E	$1/Y_{11}^E$, m^2/N
Piezoelectric constant, $d_{31,p}$	-190×10^{-12} , m/V
Dielectric permittivity, $\epsilon_{33}^T/\epsilon_0$	1800
Mass density, ρ_p	7800 kg/m ³
TdVib Gallenol	
Elastic constant, Y_{33}^H	40, GPa
Elastic compliance, s_{33}^H	$1/Y_{33}^H$, m^2/N
Piezomagnetic coefficient, $d_{33,m}$	7.77×10^{-9} , Wb/N
Magnetic permeability, $\mu_{33,m}^T/\mu_0$	100
Mass density, ρ_m	7800, kg/m ³
Receiver Geometry	
PZT thickness, t_p	1.02, mm
Gallenol thickness (each layer), t_m	370, μm
Total thickness, $t_0 = t_p + 2t_m$	1.76, mm
Laminated composite width, w	10, mm
Laminated composite length, L	20, mm
Mechanical characteristics	
Damping coefficient, b	4.22, Ns/m
Interface coupling, κ	62.2%

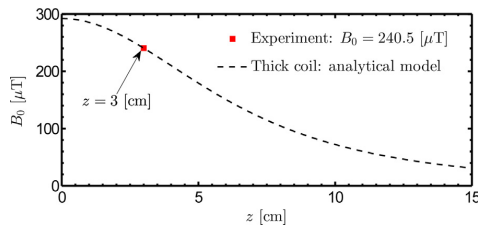


Fig. 5. Magnetic flux density amplitude B_0 : Measured value at $z = 3$ cm and those obtained by the analytical model of a thick coil.

Therefore, for the sake of simplification, we only consider the change of the \mathbf{H} -field with respect to z without compromising the final results.

Figure 5 shows the profile of the magnetic flux density strength along z . The current flowing into the transmitter coil (\mathbf{I} in (18)) is adjusted, such that the simulation and experimental results of B_0 at $z = 3$ cm are identical. Figure 6 presents the influence of the non-uniform magnetic field on the open-circuit output voltage. The effective \mathbf{H} -field amplitude (H_0) is averaged over the length of the ME transducer with $N = 2000$, based on the prediction data obtained in Figure 5. The operating frequency is at the anti-resonance frequency, $f = f_1$. The experimental and simulation results (marked by solid red dot and blue square, respectively) are in good agreement. In addition, we observe that V_∞ can also be anticipated with the use of the \mathbf{H} -field amplitude at the origin of the ME receiver instead of (H_0), while not compromising the accuracy of the theoretical model. In this case, we assume that the \mathbf{H} -field is distributed uniformly over the volume of the beam. This finding is explained by the fact that the size of the receiver is relatively small compared to that of the transmitter. Hence, the applied \mathbf{H} -field varies almost linearly from one end to the other end of the ME

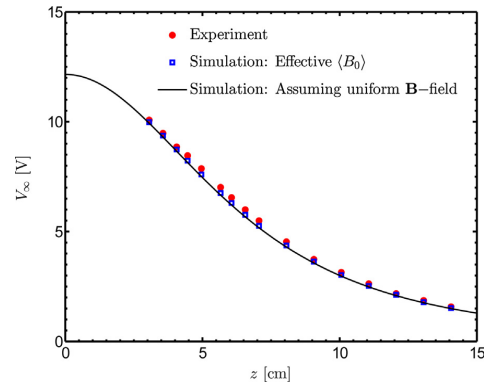


Fig. 6. Effects of non-uniform magnetic field on the open-circuit voltage along the z direction. Note, $(B_0) = \mu_0(H_0)$.

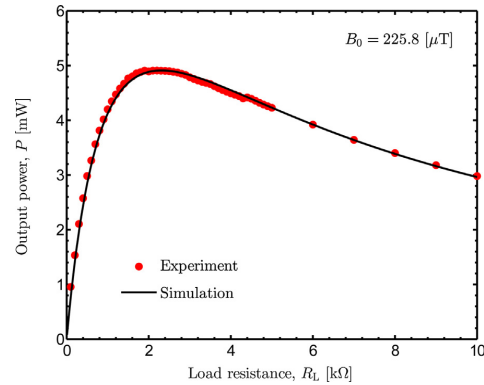


Fig. 7. Output power with respect to load resistance: Comparison between experimental data and simulation results. The drive frequency is kept fixed at the anti-resonance frequency $f = f_1 = 70.47$ kHz, for all measurements.

laminates, which allows us to approximate (H_0) by the value of H_0 taken at the beam center. This statement may not hold in general. However, it is applicable to a smaller receiver (e.g., which is in a dimension of mm or μm) with the same or similar transmitter used.

It is important to note that α_{ME} is only a function of the constitutive material properties and the operating frequency. Therefore, α_{ME} achieves the value of $41.17 \text{ Vcm}^{-1}\text{Oe}^{-1}$ and is unchanged for all V_∞ seen in Figure 6.

3.3. Transferred power

The most important goals of the paper are to validate equation (13) and to assess the maximum power transferred of the ME WPTS under the effects of the field non-uniformity, misalignment, and misorientation. These concerns are to be addressed in this section.

Following the principle of impedance matching to optimize the delivered power, the load resistance is varied to experimentally determine its optimum, as shown in Figure 7. The drive frequency is set at the anti-resonance frequency f_1 . Under a \mathbf{B} -field amplitude of $B_0 = 225.8 \mu T$, a maximum output power of $\max\{P\} = 4.91$ mW is attained with the optimal load of $R_{L-opt} = 2.2 \text{ k}\Omega$. The difference between the experimental and predicted data is negligibly small. For a low coupling between the magnetic and mechanical domains, R_{L-opt} is isolated from the impedance of the thick coil.

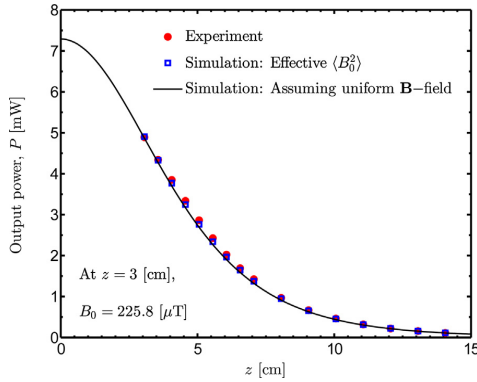


Fig. 8. Effects of non-uniform magnetic field on the power delivered to the load in the z -axis. Conversion: $\langle B_0^2 \rangle = \mu_0 \langle H_0^2 \rangle$.

Meanwhile, f_1 is only dependent on the natural mechanical characteristics of the laminate and the electromechanical coupling. The pair of (f_1, R_{L-opt}) is unchanged against the receiver location or the applied magnetic field, which is hence utilized for the remaining investigations on the performance of the ME WPTS in this Section.

Figure 8 shows the responses of the output power to the decrease of the applied \mathbf{B} -field when moving the ME generator away from the transmit coil. Similar to estimating $\langle H_0 \rangle$, the effective \mathbf{H} -field amplitude squared $\langle H_0^2 \rangle$ (or $\langle B_0^2 \rangle$, equivalently) is computed from equations (14) and (18) with $N = 2000$. The characteristics inferred from analyzing V_∞ in Figure 6 still hold true and are applicable to the transferred power P ; in which using H_0^2 acquired at the ME transducer center (with an assumption of uniform magnetic field distribution inside the magnetostrictive material) is sufficient to describe the dynamics of P . The simulation results in both cases follow closely with those of measurements. In a general trend, the received power decreases faster at a distance range that is closer to the transmitter; it is coincident with the property of the \mathbf{B} -field produced by the thick coil. At $z = 3$ cm, $P = 4.89$ mW, and when z equals to the diameter of the transmit antenna, $z \approx 15$ cm, P drops to nearly zero.

In order to quantify the influence of the alignment between the transmitter centerline and the longitudinal axis of the ME laminate to the behavior of the generated power, we adjust the location of the receiver only in the x -direction ($y = 0$) while keeping it at a fixed distance of $z = 4$ cm from the coil origin. The experimental and simulation data for $x \in [-10, 10]$ cm are compared in Figure 9, which, overall, are in good agreement. The discrepancy observed in the right-hand side of the figure could be due to the imperfect symmetry of the coil that might occur during the winding process. Despite that, the model is still able to capture the main essence of the considered system. Note that, at $x = 0$, the corresponding power is $P_{x_0} = 3.85$ mW, which is identical to that measured at the same gap of $z = 4$ cm in Figure 8. There is a certain range of the misalignment, $x \in \mathbb{X} = [-x_c, x_c]$, such that $P/P_{x_0} \geq 90\%$. The specific value of x_c depends on z . The set \mathbb{X} is broader at smaller z and becomes narrower with an increase of z . In the case of $z = 4$ cm, $x_c/r_c \approx 1/2$ where r_c is the coil radius and $r_c = (r_1 + r_2)/2$. Comparing the whole span of \mathbb{X} to the width of the laminate, we get a ratio of $2x_c/w \approx 8$, which means the receiver can be located in a space that is much bigger than its size without losing any significant power. However, outside this region, P is sensitive to the alignment error and reduces substantially with only a small further increase of $|x|$.

Figure 10 shows an experimental setup for evaluating the effects of the orientation angle θ on the output power P , in which the ME

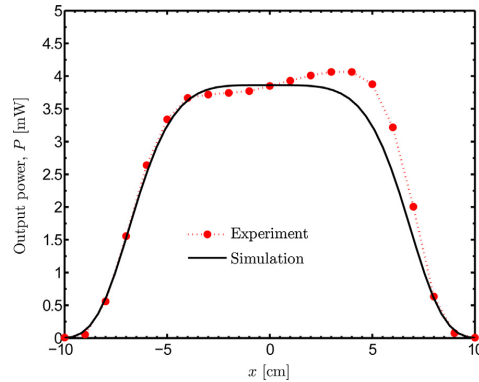


Fig. 9. Effects of alignment on the output power with respect to the lateral position (x -axis). The distance between the transmitter and receiver centers is $z = 4$ cm. The \mathbf{B} -field amplitude at $x = 0$ cm is $B_0 = 197.2 \mu\text{T}$.

receiver is rotated about the global coordinate x at its origin O_t . An experimental example with $\theta = 20^\circ$ is depicted. The relative locations of the two permanent magnets and the laminated composite are fixed, such that the DC bias field strength is kept unchanged during the measurement.

Let us consider a magnetic field vector that is oriented with the z -axis, H_z . The effective \mathbf{H} -field acting on the magnetostrictive material, which is a projection of H_z onto the length direction of the transducer, is given by

$$H_\theta = H_z \cos \theta. \quad (16)$$

Denoting the power delivered to the load at the nominal position (i.e., $\theta = 0$) as P_0 , based on equations (13) and (16), the generated power for an arbitrary angle can be written as

$$P_\theta = P_0 (\cos \theta)^2. \quad (17)$$

It is apparent that, $P_\theta \rightarrow P_0$ as $\theta \rightarrow 0$ and $P_\theta \rightarrow 0$ if $\theta \rightarrow \pi/2$ (or 90° equivalently). The accuracy of the prediction by (17) is presented in Figure 11, in which the measured and simulated data are nearly identical for all $\theta \in [0, \pi/2]$. In this case, the nominal power is $P_0 = 4.89$ mW, attained at $z = 3$ cm. Since the ratio P_θ/P_0 is only dependent on θ , and not z , equation (17) is simple but efficient to anticipate the behavior of the induced power with respect to the misorientation angle.

4. Discussion

As the validity of the complete system model has been demonstrated in previous sections, we proceed with further analysis. The direct influence of the transmitter geometry and configuration on the generated power are of interest. In particular, attempts to reduce the effects of the field non-uniformity and the misorientation are theoretically considered.

$$H_z(r, z) = \frac{J}{4\pi} \int_{r_1}^{r_2} \int_{\varphi_1}^{\varphi_2} \int_{z_1}^{z_2} \frac{(\vec{r} - r \cos \varphi) \vec{r}}{(r^2 + \vec{r}^2 - 2r\vec{r} \cos \varphi + (z - \vec{z})^2)^{3/2}} d\vec{r} d\varphi dz$$

$$\text{where } J = \frac{I}{(z_2 - z_1)(r_2 - r_1)}. \quad (18)$$

Figure 12 shows the change of the power delivered to the load along the transmitter center axis, $(x, y, z) = (0, 0, z)$, with different radii of the transmitting coil, $r_c/2$, r_c and $2r_c$ where r_c is the nominal radius of the coil currently in use in experiments. For this comparison, the (effective) input current I is altered accordingly

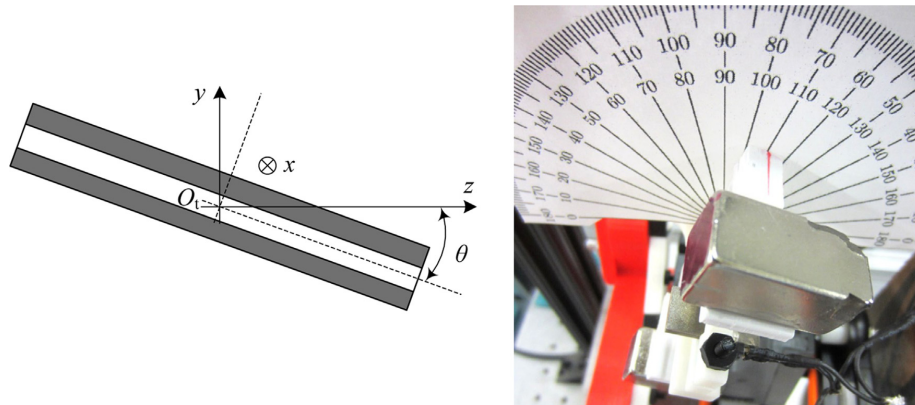


Fig. 10. Experimental setup used for investigating the effects of the orientation between the longitudinal direction of the ME transducer and the centerline of the transmit coil. The ME laminate is rotated about the x -axis while O_t is kept fixed.

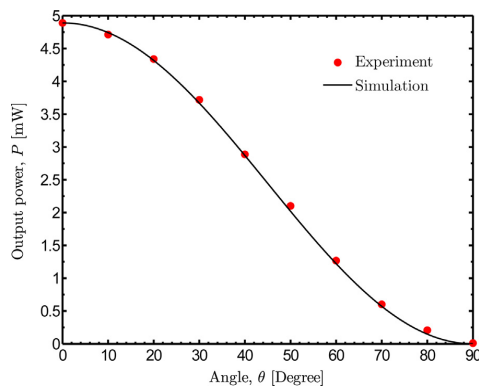


Fig. 11. Effects of the orientation of the receiver to the transmitter on the output power. The transmitter-to-receiver distance is $z = 3$ cm. At $\theta = 0$, the \mathbf{B} -field amplitude is $B_0 = 225.8 \mu\text{T}$.

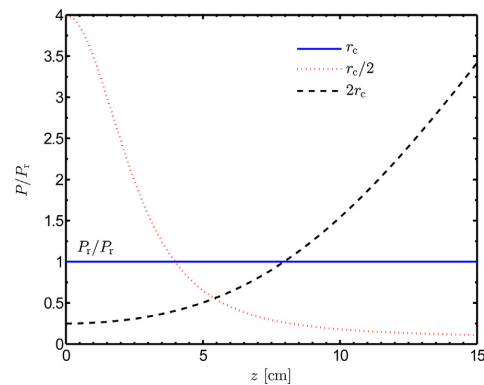


Fig. 13. Comparison of transferred power for different coil radii with the same arbitrary input current, characterized by the ratio P/P_t , where P_t is the output power of the current coil design used as a reference power. $r_c = (r_1 + r_2)/2 = 8.07$ cm, and P_t is also a function of z .

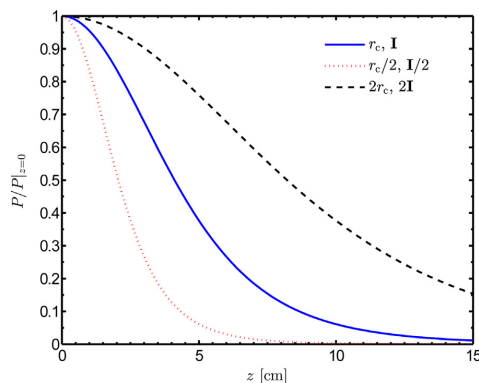


Fig. 12. Effects of coil radius on the power delivered to the load with respect to the transfer distance z , assuming perfect alignment and orientation, $x = y = 0$, $\theta = 0$. $P_t|_{z=0}$ are identical for all three cases, and $r_c = (r_1 + r_2)/2 = 8.07$ cm.

to keep the \mathbf{B} -field strength produced at $z = 0$ identical. In general, the transferred power drops faster with smaller coils as the transfer distance increases. However, bigger coil requires higher \mathbf{I} to generate the same $B_0|_{z=0}$, and the change (increase or decrease) of \mathbf{I} is proportional to that of the radius. For instance, doubling r_c leads to a doubling of \mathbf{I} . Therefore, a trade-off between the coil size and input current needs to be balanced in an effort of minimizing the effects of the field non-uniformity on the output power P .

In another perspective, we now consider the behavior of P with respect to z when the input current \mathbf{I} is set to be equal to an arbitrary value, regardless of the coil radius. The obtained results are shown in Figure 13 for three coil radii, in which the power corresponding to the current design of the transmitter is chosen as a reference, P_t . In order to maximize the power transferred to the load, the choice of the coil diameter depends upon the transfer distance. At close range, a smaller coil is more suitable with higher power generated. However, a bigger coil is preferable for a larger transfer range. This universal tendency is less apparent in a RIC WPTS when a small coil may not give any benefit to the received power at a short separation [24].

Figure 14 presents the simultaneous influences of the transfer distance and the orientation angle on the delivered power,

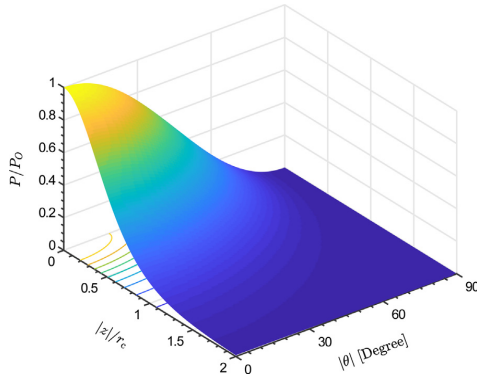


Fig. 14. Combined influences of both the transfer distance and orientation on the actual power delivered to the load, characterized by the ratio P/P_0 where $P_0 = P|_{|x=y=z=0, \theta=0}$ is the power obtained at the transmitter origin O without any misorientation.

expressed by $|\theta|$ and two normalized parameters P/P_0 and $|z|/r_c$, where the reference power and coil radius are $P_0 = P|_{|x=y=z=0, \theta=0}$ and $r_c = (r_1 + r_2)/2 = 8.07$ cm, respectively. The input current, \mathbf{I} , is the same as used for Figure 8. As an apparent trend, any increase of either $|z|$ or $|\theta| \in [0, \pi/2]$ results in a significant drop of the output power. The combined effects even lead to a faster decrease of P . Moreover, the contours (also known as level sets) in the $z - \theta$ plane show that there exist different positions of the ME receiver yielding the same power.

Due to the characteristic shown in (17), a possible configuration to reduce the effects of misorientation is to utilize two transmitting coils electrically connected in series such that their center lines are perpendicular to each other and approximately intersect at the location of the receiver. Under this circumstance, only one input current \mathbf{I} is required for operation, and the obtained power becomes $P_\theta = P_0 \cos^2(\theta) + P'_0 \cos^2(\pi/2 - \theta) = P_0 \cos^2(\theta) + P'_0 \sin^2(\theta)$, where P_0 and P'_0 are the nominal power at zero-distance corresponding to the two transmitters ($z = 0$ and $z' = 0$). Especially, if $z \approx z'$, $P_0 \approx P'_0$, and as a consequence, $P_\theta \approx P_0$. However, the power losses increase due to the series parasitic resistance of the second inductor, which might lead to a decrease in the transfer efficiency. If the two coils are identical, the total power dissipated in the stray resistances is double that of when using one single transmitter. It should be noted that the efficiency of a ME WPTS is rather low, $\sim 0.12\%$ as reported in [21]. However, for many low-power systems such as wireless sensor networks, efficiency may not be the key factor of interest, but the actual delivered power instead.

The maximum possible received power is bounded by the power input to the mechanical domain, and is determined by $P_{avt} = F_0^2/(8b)$, where F_0 is a product of the magnetic field amplitude H_0 and the electrodynamic transduction factor Γ_m . For a given distance z and input current \mathbf{I} , H_0 is merely dependent on the dimension of the transmitting coil, and Γ_m is only a function of the geometry and material properties of the magnetostrictive phase. Thus, F_0 (and accordingly, P_{avt}) can be maximized by optimizing the transmitter and the receiver independently. On the contrary, the magnetic induction between two coils of a RIC WPTS is modeled by a mutual inductance M that simultaneously depends on both coil geometries [25]. Therefore, this approach is more challenging to apply for RIC architecture. Furthermore, while the conventional receiver antenna relies on the electromagnetic wavelength, a ME antenna

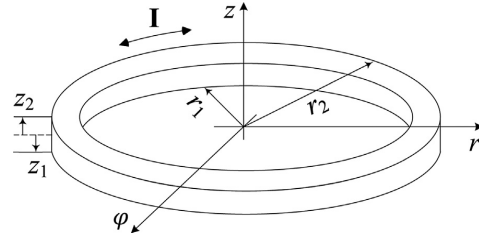


Fig. 15. Geometry of a thick coil carrying a uniform current density. Here, \mathbf{I} is the current flowing in the coil.

is not limited by the size of an electromagnetic wave. It hence can be much smaller than the state-of-the-art antenna designs [26]. This critical fact could lead to dramatic miniaturization of the implanted receiver. As a ME WPTS usually operates at a low-frequency range ($\ll 1$ MHz), the human body is nearly transparent to the applied magnetic field [27]. The energy absorbed by the tissues and the frequency shift phenomenon are negligible. All these advantages make the ME transducer a promising alternative solution to the RIC WPTS and pave a new way for powering biomedical devices.

Subject to the IEEE safety standards [10,11], at 70.47 kHz the largest allowable amplitude of the \mathbf{B} -field that can be applied to humans is $205 \mu\text{T}$. With the same operating frequency and maximum magnetic field strength, the system under investigation is able to transfer up to 4.16 mW to a load resistance (which is equivalent to 3.85 mW with $197.2 \mu\text{T}$ as shown in Figure 9). This amount of power is sufficient to supply most of the biosensors. These observations further enhance the potential use of a ME WPTS in biomedical applications.

5. Conclusions

We have investigated how the non-uniformity of the applied magnetic field, and the misalignment/misorientation between the transmitter and receiver, affect the maximum power transferred to the load. The analytical models for both transmitting and receiving sides presented in this work were proven to be sufficiently and consistently accurate to capture the fundamental dynamics of the ME WPTS under consideration. The spatial distribution of the magnetic field generated by the transmit coil is the most important factor, as it determines the capability of the power transmission for a given ME transducer. The output power is more sensitive to the change of the orthogonal distance from the ME laminate origin to the coil plane than to the variation of the alignment in parallel with the coil diameter. We also found that the delivered power is proportional to the squared cosine of the orientation angle. The findings were validated by different sets of experiments.

For small-scale ME transducers used in implantable biomedical applications, as long as the effective \mathbf{B} -field at the receiver location is maximized (subject to some safety constraints), the field uniformity is not essentially required.

Author statement

Binh Duc Truong and Shad Roundy conceptualized the project; Erik Andersen and Curtis Casados designed and implemented the transmitter; Binh Duc Truong developed the theoretical model, performed experiments and simulations, and analyzed results; Binh Duc Truong and Shad Roundy wrote the manuscript.

Conflict of interests

The authors declare that there is no conflict of interests regarding the publication of this article.

Declaration of Competing Interest

The authors report no declarations of interest.

Acknowledgments

This material is based upon work supported by the National Science Foundation under Grant Number ECCS-1651438. The authors would like to thank website <https://www.kindpng.com/> for providing an open-source image used in the Graphical Abstract.

Appendix A. Magnetic field produced by a thick coil with rectangular cross section [23]

Figure 15 shows the geometric dimensions of a thick coil that carries a uniform current density \mathbf{J} . In particular, r_1 and r_2 are the inner and outer radii, z_1 and z_2 are the lower and upper heights. Usually, $z_1 = -z_2 = t_c/2$ where t_c is the total thickness of the coil. Without losing the generality, the cylindrical coordinates are used to describe the magnetic field in the z -direction, denoted as $H_z(r, z)$, which is of our interest in this paper. Another formulation with the Cartesian coordinate system was presented in [22]. Both approaches give the same results, thus which formulation to choose is a matter of convenience, not of physics. The role of the r -axis is now the same as that of x - or y -coordinate in Figure 1. The analytical solution of $H_z(r, z)$ is expressed in equation (18), where \tilde{r} , $\tilde{\varphi}$ and \tilde{z} are the integration variables, $\varphi_1 = 0$ and $\varphi_2 = 2\pi$. This three-dimensional integral can be numerically computed by the function [integral3] in MATLAB.

References

- [1] D.-H. Kim, N. Lu, R. Ma, Y.-S. Kim, R.-H. Kim, S. Wang, J. Wu, S.M. Won, H. Tao, A. Islam, K.J. Yu, T.-i. Kim, R. Chowdhury, M. Ying, L. Xu, M. Li, H.-J. Chung, H. Keum, M. McCormick, P. Liu, Y.-W. Zhang, F.G. Omenetto, Y. Huang, T. Coleman, J.A. Rogers, Epidermal electronics, *Science* 333 (6044) (2011) 838–843.
- [2] S.M.R. Islam, D. Kwak, M.H. Kabir, M. Hossain, K. Kwak, The internet of things for health care: a comprehensive survey, *IEEE Access* 3 (2015) 678–708.
- [3] S. Furman, J.B. Schwedel, An intracardiac pacemaker for Stokes-Adams seizures, *N. Engl. J. Med.* 261 (19) (1959) 943–948, PMID: 13825713.
- [4] R. Bashirullah, Wireless implants, *IEEE Microwave Mag.* 11 (2010) S14–S23.
- [5] M. Song, P. Belov, P. Kapitanova, Wireless power transfer inspired by the modern trends in electromagnetic, *Appl. Phys. Rev.* 4 (2) (2017) 021102.
- [6] K. Agarwal, R. Jegadeesan, Y. Guo, N.V. Thakor, Wireless power transfer strategies for implantable bioelectronics, *IEEE Rev. Biomed. Eng.* 10 (2017) 136–161.
- [7] H. Kim, H. Hirayama, S. Kim, K.J. Han, R. Zhang, J. Choi, Review of near-field wireless power and communication for biomedical applications, *IEEE Access* 5 (2017) 21264–21285.
- [8] Z. Zhang, H. Pang, A. Georgiadis, C. Cecati, Wireless power transfer—an overview, *IEEE Trans. Ind. Electron.* 66 (2019) 1044–1058.
- [9] A.I. Al-Kalbani, M.R. Yuze, J. Redouté, A biosafety comparison between capacitive and inductive coupling in biomedical implants, *IEEE Antennas Wirel. Propag. Lett.* 13 (2014) 1168–1171.
- [10] IEEE, IEEE standard for safety levels with respect to human exposure to electromagnetic fields, 0–3 kHz, IEEE Std C95.6-2002, 2002, pp. 1–0.
- [11] IEEE, IEEE standard for safety levels with respect to human exposure to radio frequency electromagnetic fields, 3 kHz to 300 GHz, IEEE Std C95.1-2005 (Revision of IEEE Std C95.1-1991), 2006, pp. 1–238.
- [12] International Commission on Non-Ionizing Radiation Protection, Guidelines for limiting exposure to time-varying electric, magnetic, and electromagnetic fields (up to 300 GHz), *Health Phys.* 75 (1998).

- [13] International Commission on Non-Ionizing Radiation Protection, Guidelines for limiting exposure to time-varying electric and magnetic fields (1 Hz to 100 kHz), *Health Phys.* 99 (2010).
- [14] M. Manteghi, A.A.Y. Ibraheem, On the study of the near-fields of electric and magnetic small antennas in lossy media, *IEEE Trans. Antennas Propag.* 62 (2014) 6491–6495.
- [15] A. Kurs, A. Karalis, R. Moffatt, J.D. Joannopoulos, P. Fisher, M. Soljacic, Wireless power transfer via strongly coupled magnetic resonances, *Science* 317 (2007).
- [16] A.P. Sample, D.T. Meyer, J.R. Smith, Analysis, experimental results, and range adaptation of magnetically coupled resonators for wireless power transfer, *IEEE Trans. Ind. Electron.* 58 (2011) 544–554.
- [17] V.R. Challa, J.O. Mur-Miranda, D.P. Arnold, Wireless power transmission to an electromechanical receiver using low-frequency magnetic fields, *Smart Mater. Struct.* 21 (11) (2012) 115017.
- [18] B.D. Truong, S. Williams, S. Roundy, Experimentally validated model and analytical investigations on power optimization for piezoelectric-based wireless power transfer systems, *J. Intell. Mater. Syst. Struct.* 30 (16) (2019) 2464–2477.
- [19] H. Basaeri, Y. Yu, D. Young, S. Roundy, Acoustic power transfer for biomedical implants using piezoelectric receivers: effects of misalignment and misorientation, *J. Micromech. Microeng.* 29 (2019) 084004.
- [20] G. Ke, Q. Chen, W. Gao, S. Wong, C.K. Tse, Z. Zhang, Research on IPT resonant converters with high misalignment tolerance using multicoil receiver set, *IEEE Trans. Power Electron.* 35 (2020) 3697–3712.
- [21] B.D. Truong, S. Roundy, Experimentally validated model and power optimization of a magnetolectric wireless power transfer system in free-free configuration, *Smart Mater. Struct.* (2020).
- [22] S. Babic, Z. Anđjelic, B. Krstajic, S. Salon, Analytical calculation of the 3d magnetostatic field of a toroidal conductor with rectangular cross section, *IEEE Trans. Magn.* 24 (1988) 3162–3164.
- [23] R. Ravaut, G. Lemarquand, V. Lemarquand, S. Babic, C. Akyel, Calculation of the magnetic field created by a thick coil, *J. Electromagn. Waves Appl.* 24 (10) (2010) 1405–1418.
- [24] B.H. Waters, B.J. Mahoney, G. Lee, J.R. Smith, Optimal coil size ratios for wireless power transfer applications, in: 2014 IEEE International Symposium on Circuits and Systems (ISCAS) (2014) 2045–2048.
- [25] S. Raju, R. Wu, M. Chan, C.P. Yue, Modeling of mutual coupling between planar inductors in wireless power applications, *IEEE Trans. Power Electron.* 29 (2014) 481–490.
- [26] T. Nan, H. Lin, Y. Gao, A. Matyushov, G. Yu, H. Chen, N. Sun, S. Wei, Z. Wang, M. Li, X. Wang, A. Belkessam, R. Guo, B. Chen, J. Zhou, Z. Qian, Y. Hui, M. Rinaldi, M.E. McConney, B.M. Howe, Z. Hu, J.G. Jones, G.J. Brown, N.X. Sun, Acoustically actuated ultra-compact NEMS magnetolectric antennas, *Nat. Commun.* 8 (2017).
- [27] K.L. Kaiser, *Electromagnetic shielding*, CRC/Taylor and Francis, Boca Raton, London, 2006, This material was previously published in *The Electromagnetic Compatibility Handbook*, CRC Press, 2004.

Biographies



Binh Duc Truong received the B.E. degree in Mechatronics from the Ho Chi Minh City University of Technology, Vietnam, in 2012 and the M.Sc. degree in Micro- and Nano System Technology from the Buskerud and Vestfold University College, Norway, in 2015. He is currently pursuing the Ph.D. degree with Department of Mechanical Engineering, University of Utah, focusing on energy harvesting and wireless power transfer systems.



Erik Andersen received his Bachelor of Science and Masters of Mechanical Engineering from the University of Utah in 2018. He is currently a Ph.D. candidate under Dr. Shad Roundy at the University of Utah, Salt Lake City, Utah. His research interests include wireless power transfer (specifically for implantable biomedical devices), system design and optimization, and magnetolectric transducers.



Curtis Casados received his Bachelor of Science in Mechanical Engineering from the University of Utah in 2020 and is continuing his Masters of Computer Science at the University of Southern California. He assisted in Dr. Shad Roundy's lab at the University of Utah, Salt Lake City, Utah. His research interests include wireless power transfer as well as energy harvesting.



Shad Roundy received the M.S. and Ph.D. degrees in mechanical engineering from the University of California, Berkeley, Berkeley, CA, USA in 2000 and 2003, respectively. He joined the faculty at the University of Utah in 2012 where he is currently an Associate Professor in the Department of Mechanical Engineering. From 2005 to 2012 he worked in the MEMS industry developing tire pressure sensors, accelerometers, gyroscopes, and energy harvesters. From 2003 to 2005 he was a Senior Lecturer at the Australian National University. His research interests include energy harvesting, wireless power transfer, and more generally MEMS sensors and actuators.

CHAPTER 5

GEOMETRY OPTIMIZATION FOR MAGNETOELECTRIC WIRELESS POWER TRANSFER SYSTEM

This chapter presents a framework to optimize the geometry of a magnetolectric (ME) laminated composite. It aims to maximize both the magnetic energy captured by magnetostrictive material and the power transferred to a load resistance. A nonlinear-constrained global optimization algorithm is utilized for such purpose. The outcomes of this study could serve as a preliminary step towards implementing a microscale magnetolectric wireless power transfer system for biomedical applications.

5.1 Introduction

The concept of using a ME transducer as a receiver of a wireless power transfer system has been successfully demonstrated in Chapter 4. However, its potential for use as a power unit that is embedded inside the human body along with bioelectronics is still questionable. Miniaturization is critical for realizing an implanted device, and the decrease in the size of the ME generator could lead to a significant drop in the output power. Therefore, it is of great interest to optimize and evaluate the performance of a ME receiver when subject to some mild volume (and perhaps geometry-dimension) constraints.

Furthermore, due to safety concerns, the maximum magnetic field strength that can be applied is limited. In particular, the field amplitude varies with the choice of the operating frequency (usually at/around the resonance or antiresonance frequency of the ME laminate). Changing the transducer geometry could lead to an adjustment of the maximum permissible field-excitation, which results in a variation of the magnetic power input to the system as well as the power delivered to the load. Thus, safety standards are closely related to the geometry optimization problem.

The primary goals of this study are as follows: (i) to understand the general trend of

the power response to the laminate dimensions, and (ii) to find an appropriate geometry that yields the highest-possible generated power while maintaining its manufacturability.

5.2 A Summary of the Equivalent Circuit Model

What follows are the essential parameters used in the optimization problem and their corresponding definitions, summarized from the model developed in Chapter 4.

Geometries and mass densities of the ME laminate are as follows:

$$\bar{\rho} = \frac{\rho_p A_1 + 2\rho_m A_2 / \kappa}{A_1 + 2A_2}, \quad (5.1)$$

$$n = \frac{A_1}{A_1 + 2A_2} = \frac{t_p}{t_p + 2t_m}, 0 < n < 1, \quad (5.2)$$

$$A_1 = t_p w, A_2 = t_m w, A = A_1 + 2A_2. \quad (5.3)$$

The squared speed of sound in the composite is as follows:

$$\begin{aligned} \bar{v}^2 &= \frac{1}{\bar{\rho}} \left[n \left(s_{11}^E - \frac{d_{31,p}^2}{\epsilon_{33}} \right)^{-1} + \frac{1-n}{\kappa} \left(s_{33}^H - \frac{d_{33,m}^2}{\mu_{33,m}} \right)^{-1} \right] \\ &= [n/s_{11}^D + (1-n)/(\kappa s_{33}^B)] / \bar{\rho}, \end{aligned} \quad (5.4)$$

Electrodynamic and electromechanical transduction factors are as follows:

$$\Gamma_m = 2wt_m d_{33,m} / s_{33}^H, \quad (5.5)$$

$$\Gamma_p = -wd_{31,p} / s_{11}^E. \quad (5.6)$$

Mechanical impedance and nominal capacitance of the piezoelectric layer are as follows:

$$Z = \frac{1}{2} \left(\frac{n}{s_{11}^E} + \frac{1-n}{\kappa s_{33}^H} \right) \frac{A}{j\bar{v}} \cot \frac{kL}{2}, \quad (5.7)$$

$$C_0 = \epsilon_{33}^S wL / t_p \quad (5.8)$$

where $k^2 = \omega^2 / \bar{v}^2$.

The optimal load and the corresponding optimum output power at the resonance frequency ω_0 are as follows:

$${}^{\text{opt}}R_L|_{\omega=\omega_0} = \frac{1}{\omega_0 C_0 \sqrt{M_0^2 + 1}}, \quad (5.9)$$

$$P_0 = {}^{\text{opt}}P|_{\omega=\omega_0} = \frac{(\Gamma_m H)^2}{4b} M_0 (\sqrt{M_0^2 + 1} - M_0) \quad (5.10)$$

where b is the mechanical damping coefficient, H is the effective applied magnetic field, $\Delta K = \Gamma_p^2 / C_0$, $M_0 = \Delta K / (b\omega_0)$ and $\omega_0 = \pi\bar{v} / L$.

And at the antiresonance frequency ω_1

$$\text{opt} R_L|_{\omega=\omega_1} = \frac{\sqrt{M_1^2 + 1}}{\omega_1 C_0}, \quad (5.11)$$

$$P_1 = \text{opt} P|_{\omega=\omega_1} = \frac{(\Gamma_m H)^2}{4b} M_1 (\sqrt{M_1^2 + 1} - M_1) \quad (5.12)$$

where $M_1 = \Delta K / (b\omega_1)$. The material constants are defined in Chapter 4 and are listed in Table 5.1. Either P_0 or P_1 can be chosen as the objective of the optimization problem with almost no difference between the two.

5.3 Formulation of the Geometry Optimization Problem

5.3.1 An approximate mass-spring model and mechanical damping coefficient

Quality factor (Q -factor) – a dimensionless parameter – is theoretically defined as the ratio of total stored energy to dissipated energy per cycle in a resonator. In engineering, it is one of the most important metrics and widely used as a criterion to examine the efficiency of a mechanical system [1]. In this investigation, we assume that the mechanical quality factor is a geometry-independent constant to make the comparison as fair as possible. The mechanical damping coefficient b is then computed based on the Q -factor.

Table 5.1. Material properties

Piezoelectric Material	PZT-5A4E	PMN-PT
Elastic constant, Y_{11}^E	66, GPa	20, GPa
Elastic compliance, s_{11}^E	$1/Y_{11}^E$, m^2/N	$1/Y_{11}^E$, m^2/N
Piezoelectric constant, $d_{31,p}$	-190×10^{-12} , m/V	-1500×10^{-12} , m/V
Dielectric permittivity, $\epsilon_{33}^T/\epsilon_0$	1800	10^4
Mass density, ρ_p	7800 kg/m^3	8060 kg/m^3
Magnetostrictive Material	TdVib Galfenol	Metglas
Elastic constant, Y_{33}^H	40, GPa	105, GPa
Elastic compliance, s_{33}^H	$1/Y_{33}^H$, m^2/N	$1/Y_{33}^H$, m^2/N
Magnetic permeability, $\mu_{33,m}^T/\mu_0$	100	45×10^3
Piezomagnetic coefficient, $d_{33,m}$	17.5×10^{-9} , Wb/N	50.3×10^{-9} , Wb/N
Mass density, ρ_m	7800 kg/m^3	7180 kg/m^3
Other constants		
Total volume, V_0	2, mm^3	
Mechanical quality factor, Q_1	46.81	
Interface coupling coefficient, κ	62.2 %	

For a mass-spring-damper system, a general expression of the quality factor is

$$Q_{0/1} = \frac{\omega_{0/1} m}{b} \quad (5.13)$$

where $\omega_{0/1}$ are the resonance/antiresonance angular frequencies and m is the mass. However, the mechanical impedance Z of a ME transducer (presented in Chapter 4) is an indispensable function of the material properties and the composite geometry. Thus, it is required to approximate Z by an equivalent mass-spring model in order to estimate the damping constant.

For a given geometry of an ME laminated composite, the resonance and antiresonance frequencies are determined. Equivalent mass and spring constants are derived in terms of ω_0 and ω_1 as follows

$$m = \frac{\Delta K}{\omega_1^2 - \omega_0^2}, \quad (5.14)$$

$$K_0 = \Delta K \frac{\omega_0^2}{\omega_1^2 - \omega_0^2}. \quad (5.15)$$

Assuming that the mechanical quality factor at the anti-resonance frequency is identified, $Q|_{\omega_1} = Q_1$, the mechanical damping coefficient is calculated as

$$b = \frac{m\omega_1}{Q_1} = \frac{\Delta K}{Q_1} \frac{\omega_1}{\omega_1^2 - \omega_0^2}. \quad (5.16)$$

The equivalent mass-spring system does not alter either ω_0 or ω_1 . Therefore, it is sufficient to capture all the essential dynamics of the original system at these frequencies, which are of interest. More importantly, this approximate model also keeps the nature of the electromechanical coupling coefficient, $k_p^2 = 1 - \omega_0^2/\omega_1^2$, unchanged.

5.3.2 Demagnetization effects

A demagnetizing field is generated inside a ferromagnetic material when it is exposed to a magnetic field. The demagnetizing field is always opposed to the applied field; therefore, the effective internal field is less than the external one. This inevitable phenomenon reduces the magnetic energy absorbed by magnetostrictive material in use, and as a consequence, decreases the actual power transferred to the load. An analytical method to investigate the demagnetization effects for materials of a rectangular shape was developed by Joseph and Schlomann in 1965 [2], which could be the most convenient approach for ME laminated composites due to the similarity in geometry.

The relation between the magnetization M and the internal field H is

$$M = \chi_m H = (\mu_r - 1)H \quad (5.17)$$

where χ_m is the magnetic susceptibility and $\mu_r = \mu_{33,m}^T / \mu_0$ is the relative permeability of a given material, $\mu_r = \chi_m + 1$. Due to the demagnetization effects, the internal field is

$$H = H_0 - N_d M \quad (5.18)$$

where H_0 is the applied magnetic field and N_d is the demagnetization factor. Thus, the effective magnetic field is described with regard to the applied field and the demagnetization factor as follows

$$H = \frac{H_0}{1 + N_d(\mu_r - 1)}. \quad (5.19)$$

Assuming that the external field H_0 is applied along the z -axis as shown in Figure 5.1, the z -component of the demagnetization factor is given by [2]

$$\begin{aligned} N_d = N_d^{zz}(x, y, z) = & \frac{1}{4\pi} [\cot^{-1} f(x, y, z) + \cot^{-1} f(-x, y, z) \\ & + \cot^{-1} f(x, -y, z) + \cot^{-1} f(x, y, -z) \\ & + \cot^{-1} f(-x, -y, z) + \cot^{-1} f(x, -y, -z) \\ & + \cot^{-1} f(-x, y, -z) + \cot^{-1} f(-x, -y, -z)] \end{aligned} \quad (5.20)$$

where

$$\begin{aligned} f(x, y, z) = & \frac{[(a-x)^2 + (b-y)^2 + (c-z)^2]^{1/2}(c-z)}{(a-x)(b-y)}, \\ a = & w/2, \\ b = & t_m/2, \\ c = & L/2. \end{aligned} \quad (5.21)$$

An example of N_d at the center of the prism, $(x, y, z) = (0, 0, 0)$, is given in Figure 5.2, in which $w = 2$ mm. In general, $N_d(0, 0, 0)$ increases with either the decrease of the ratio L/w

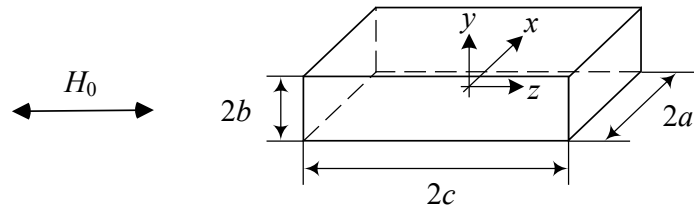


Figure 5.1. The coordinate system used in the calculations, adapted from [2]. Its origin is at the center of the rectangular prism.

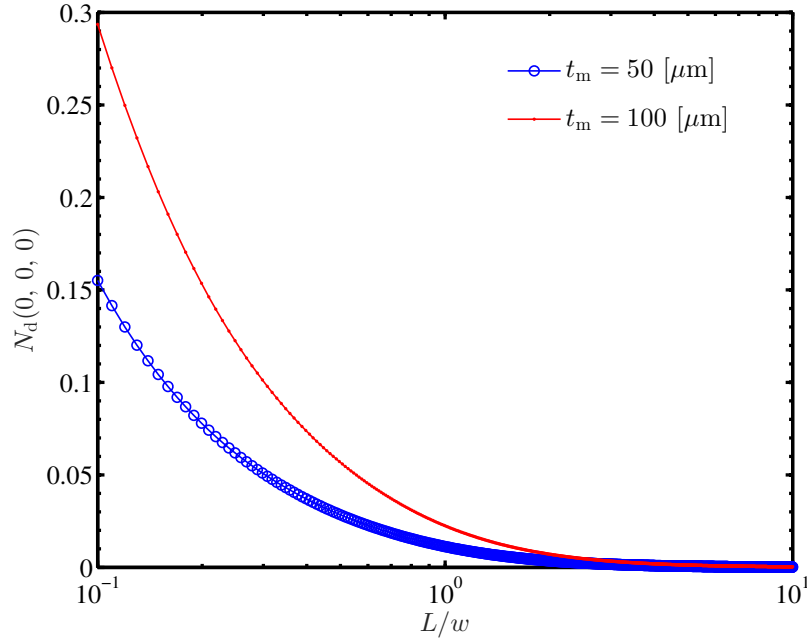


Figure 5.2. Variation of the demagnetization factor at the center of the rectangular prism with respect to the change of the ratio between the length and width.

or the increase of t_m . With the same t_m , if both L and w change but L/w keeps identical, then $N_d(0, 0, 0)$ does not change.

Finally, the output power is averaged over the volume as

$$P_L = \langle P_i(x_i, y_i, z_i) \rangle, i = 1, \dots, N \quad (5.22)$$

where N is the number of numerical samples. In practice, the effects of the demagnetizing field are embedded in the piezomagnetic coefficient, $d_{33,m}$. This constant is extracted from the experiment and can be considered as an effective value.

It is important to note that, in some circumstances, the presence of eddy currents in a magnetostrictive material gives rise to ohmic losses and consequently decreases its performance. However, the effects of the eddy-current are negligibly small when t_m is in the range of μm or sub-mm [3].

5.3.3 Safety standards

The maximum allowable magnetic field strength is determined by utilizing (i) the Institute of Electrical and Electronics Engineers (IEEE) standards on maximum permissible exposures (MPEs) for the head and torso under controlled environmental conditions [4, 5],

and (ii) the International Commission on Non-Ionizing Radiation Protection (ICNIRP) specifications on maximum occupational exposure to magnetic fields [6].

The two corresponding sets of standards are depicted in Figure 5.3, and the optimization is performed with each set. As a general trend, the maximum permissible field decreases with the increase of drive frequency. The reduction is even more critical when the operating frequency rises above 100 kHz. It should be noted that the output power is proportional to the square of the magnetic field amplitude. Thus, a lower drive frequency operation may be preferable as it may result in higher power generated at the implant.

5.3.4 Optimization problem formulation

The objective of the optimization is to maximize the power transferred to an electrical load P_L without violating a magnetic field safety limit, in which the geometric dimensions of the ME laminated composite are the variables of interest. The problem is then formulated as follows

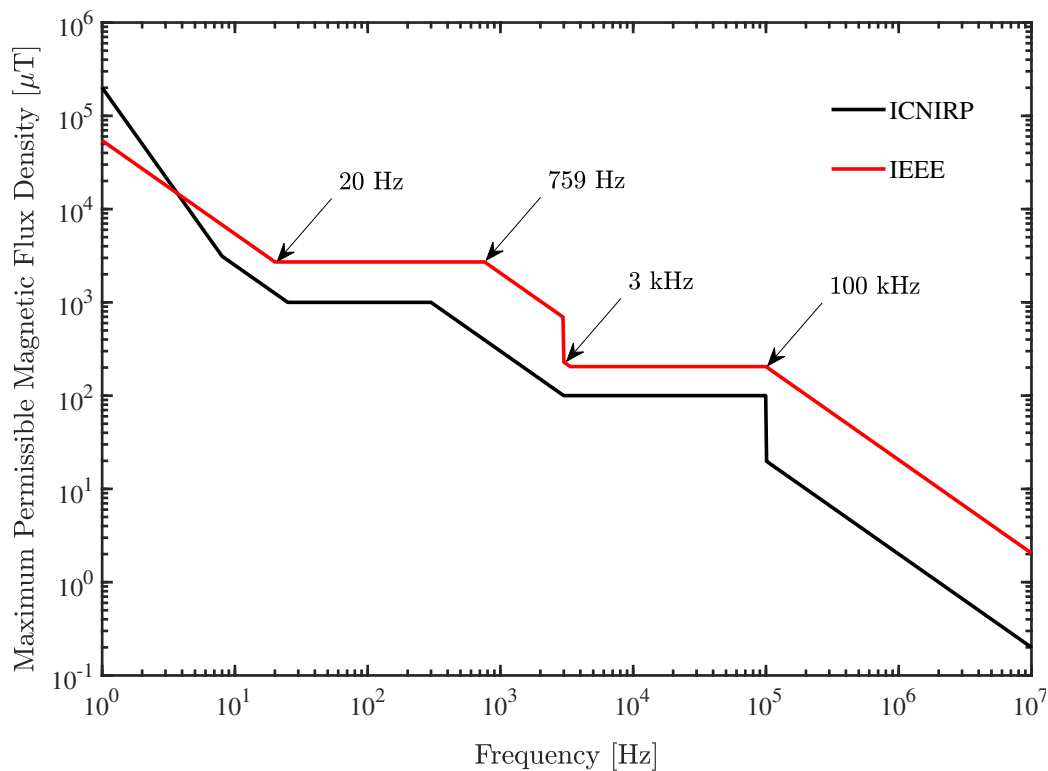


Figure 5.3. ICNIRP and IEEE safety standards on MPEs as functions of operating frequency.

$$\begin{aligned}
& \max_{L, w, t_m, t_p} && P_L(L, w, t_m, t_p) \\
& \text{subject to} && Lw(t_p + 2t_m) \leq V_0, \\
& && H_0 = H_s(f_{0/1})
\end{aligned}$$

where V_0 is a given volume of the laminate, and H_s is the maximum allowable magnetic field expressed as a function of either resonance or antiresonance frequency $f_{0/1} = \omega_{0/1}/(2\pi)$, depending upon which frequency is chosen to operate the ME WPTS. For such a complicated optimization problem with nonlinear constraints, the *patternsearch* algorithm in the Global Optimization Toolbox in MATLAB is used.

As can be seen in (5.10), it is always preferable to achieve higher Γ_m since $P_{0/1} \propto \Gamma_m^2$. In addition, increasing $M_{0/1}$ (i.e., the electromechanical figure of merit at the resonance or anti-resonance frequency) is also required so that the average output power P_L can reach the power available for transfer $P_{\text{avt}} = (\Gamma_m H)^2 / (8b)$. Here, $M_{0/1} \geq M_* = 2$ is the sufficient condition for $P_L = P_{\text{avt}}$.

Based on the definitions of Γ_m and M_0 , we have

$$\Gamma_m \propto (wt_m), \quad (5.23)$$

$$M_0 = \frac{1}{b} \frac{d_{31,p}^2}{\pi \bar{v} \epsilon_{33}^S (s_{11}^E)^2} (wt_p) \propto (wt_p). \quad (5.24)$$

These characteristics indicate that, for a given constant magnetic field, the optimization attempts to select a wide and thick laminated composite. Especially, extending the laminate width is more desired as it increases both Γ_m and M_0 simultaneously. However, this trend may no longer be valid or prioritized when the safety standards are applied, in which the allowable external field could vary with the change of the transducer length.

We now consider another perspective when the laminate volume is constrained. From (5.14) and (5.16), it can be inferred that $b \propto (wt_p/L)$. And since $P_{\text{avt}} \propto (1/b)$, the increase of w is not boundless. Widening w too large could lead to the rise of b and the corresponding drop of P_{avt} . Furthermore, assuming that L and w are chosen based on the relationship between $\{\Gamma_m, M_0\}$ and b , there should also be an optimal value of the ratio t_m/t_p . As the total thickness is now determined, both t_m and t_p cannot increase at the same time.

5.4 Results and Discussions

Without loss of generality, P_1 is chosen as the optimization objective. Different magnetostrictive and piezoelectric materials are considered and all the material properties are listed in Table 5.1. We first investigate the optimization of the transducer geometry with the use of Galfenol and PZT. We apply a total volume constraint of 2 mm^3 as a reasonable practical constraint for a very small biomedical implant. In the case where the safety concerns are disregarded and the external field is set at a constant (denoted as **Case I**), the optimal dimensions and transferred power are as follows, $L = 132.5 \text{ }\mu\text{m}$, $w = 9.69 \text{ m}$, $t_p = 0.24 \text{ }\mu\text{m}$, $t_m = 0.66 \text{ }\mu\text{m}$, and $P_L = 33.3 \text{ mW}$ with an applied field of $205 \text{ }\mu\text{T}$. This laminate is extremely wide, thin and short, coinciding with the tendency predicted by the theoretical model in Section 5.3.4. Although the output power is high, this geometry is infeasible in practice. In the following cases, the safety standards are applied.

Subject to the IEEE safety regulations, we divide the operating frequency into three breakpoint ranges, $F_E = [1, 19]$, $F_L = [20, 3000]$, and $F_H = [3001, 10^6]$ Hz; each range starts from one breakpoint to the next breakpoint in the **B**-field amplitude curve. It is convenient for the optimization while still ensuring to achieve the global solution throughout the frequency space. Let us examine the case when $f \in F_H$ (**Case II**). The optimization results in $L = 12.44 \text{ mm}$, $w = 5.06 \text{ mm}$, $t_p = 4.36 \text{ }\mu\text{m}$, and $t_m = 13.70 \text{ }\mu\text{m}$. The corresponding maximum output power is $P_L = 597 \text{ }\mu\text{W}$. It is interesting to note that the optimization process results in the length of the composite such that the operating frequency f_1 is exactly at 100 kHz . This could be the most suitable choice to balance the maximum allowable magnetic field and other parameters such as Γ_m and M_1 . In one hand, increasing L causes a possible decrease of w and/or $\{t_m, t_p\}$, which reduces Γ_m and/or M_1 . Simultaneously, a decrease of f_1 (as a consequence of expanding the length) below 100 kHz does not impact H_s . Therefore, a longer laminate does not give any benefit in overall. On the other hand, decreasing L could lead to a wide and thick ME laminate and enhance Γ_m and/or M_1 . However, H_s is significantly decreased with a further increase of f_1 , thus lowering the output power. It is worth noting that the effects of the demagnetization phenomenon on Galfenol are nearly the same with the variation of L in the neighborhood of 12.44 mm .

In order to justify the above interpretation, we further study the cases where the length of the laminate is chosen such that the antiresonance frequency f_1 (which is also the op-

erating frequency) is not at 100 kHz, and the output power is optimized in terms of other geometric parameters. The obtained results are depicted in Figure 5.4, showing the general trend that the delivered power drops when the transducer length is different from L_* (or equivalently, f_1 is away from 100 kHz).

If $f \in F_L$ (**Case III**), we get $L = 1.64$ m, $w = 0.15$ mm, $t_p = 1.04$ μ m, $t_m = 3.44$ μ m, and $P_L = 849$ μ W. In the same manner as in **Case II**, the optimization aims to select the operating frequency at the corner at which the trend of the maximum allowable field strength changes its direction (i.e., $f_1 = 759$ Hz). The optimum output power in this frequency range is higher than that of when $f \in F_H$ by a factor of 1.4. However, the geometry is again infeasible and impossible to implement in realistic scenarios. These results also show that there does not exist a practical solution when $f \in F_E$ (**Case IV**). Therefore, operating a ME WPTS in the kHz range is the best suited for real-world applications. From now on, we only consider $f \in F_H$.

Along with optimizing the transducer geometry, choosing appropriate materials is another important aspect. With the use of PZT (**Case II**), the electromechanical figure of

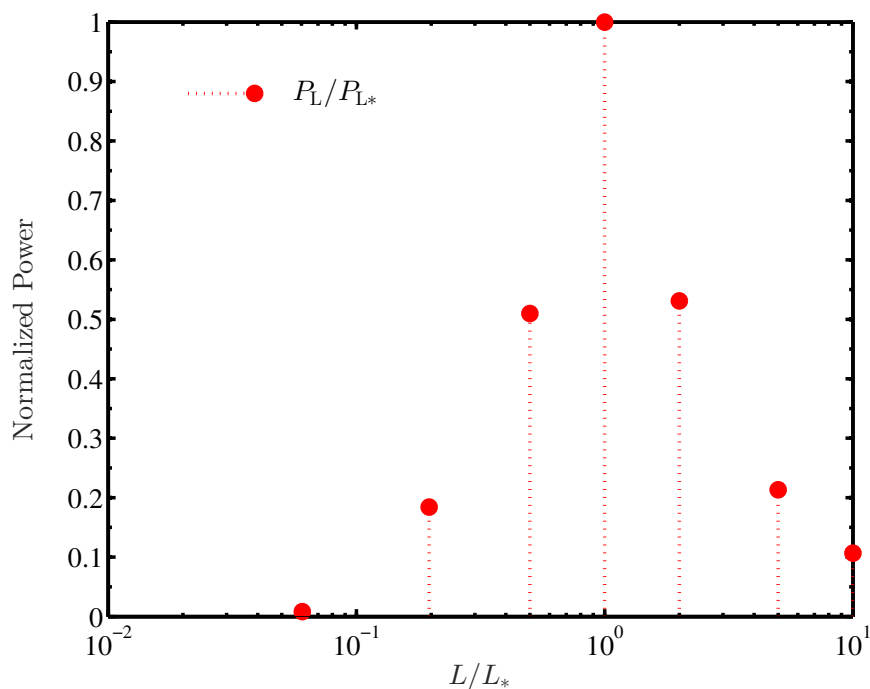


Figure 5.4. Comparison of optimized output power with different chosen length, normalized by the power (P_{L*}) and length (L_*) obtained in **Case II**.

merit is $M_1 = 0.91$, less than half of the desired value ($M_* = 2$). Thus, we are motivated to investigate the optimal performance using PMN-PT with a possible higher figure of merit (**Case V**). The obtained dimensions are $L = 12.05$ mm, $w = 30.78$ mm, $t_p = 0.58$ μm , and $t_m = 2.41$ μm , which leads to increases of ~ 50 % in figure of merit and 32 % in output power compared to **Case II**; in particular, in **Case V**, $M_1 = 1.36$ and $P_L = 789$ μW .

Even though the output power in **Case V** is promising, the optimal geometry may cause difficulties in practice. As the total thickness is only about 5.4 μm , the laminate is extremely flexible. It is hard not to create any bending curvature during the fabrication process; meanwhile, the ME composite must be flat to operate in the longitudinal mode. Taking this concern into account, we further analyze the optimization problem by adding a constraint on the thickness of the transducer, $t_0 = t_p + 2t_m \geq 100$ μm (**Case VI**). The optimized shape now becomes $L = 12.05$ mm, $w = 1.66$ mm, $t_p = 10.86$ μm , and $t_m = 44.57$ μm . And interestingly, the output power is $P_L = 736$ μW , reaching 93.3 % of the global optimum shown in **Case V**.

Among the three dimensions, the width may be the most important variable since it directly affects both the electrodynamic transduction factor and the electromechanical figure of merit. Therefore, exploring the sensitivity of the optimal solution on the variation of the width is of interest. An analysis is presented in Figure 5.5, in which L , t_p and t_m are optimized at each fixed value of w . The nominal geometry and power are taken from **Case VI** and denoted by L_0 , t_{p0} , t_{m0} , and P_{L0} . Throughout a wide range of $w \in [w_0/2, 2w_0]$, there always exists a set of other parameters for which the output power is not compromised. This is an essential property of the optimization problem as it provides more possibilities to realize an optimal system that satisfies practical constraints, while still delivering sufficient required power.

In order to further understand the role of the magnetostrictive phase, let us consider using Metglas instead of Galfenol. If subject to the total volume constraint only (**Case VII**), we obtain $L = 84.79$ mm, $w = 1.70$ mm, $t_p = 3.88$ μm , $t_m = 5.01$ μm , and $P_L = 2.76$ mW. Due to the extremely high permeability, the effects of the demagnetizing field on Metglas are much more significant than that on Galfenol. This characteristic leads to a considerable change in the trend of optimization. The length tends to increase for Metglas to reduce the impact of the demagnetization phenomenon. The optimal operating frequency is therefore

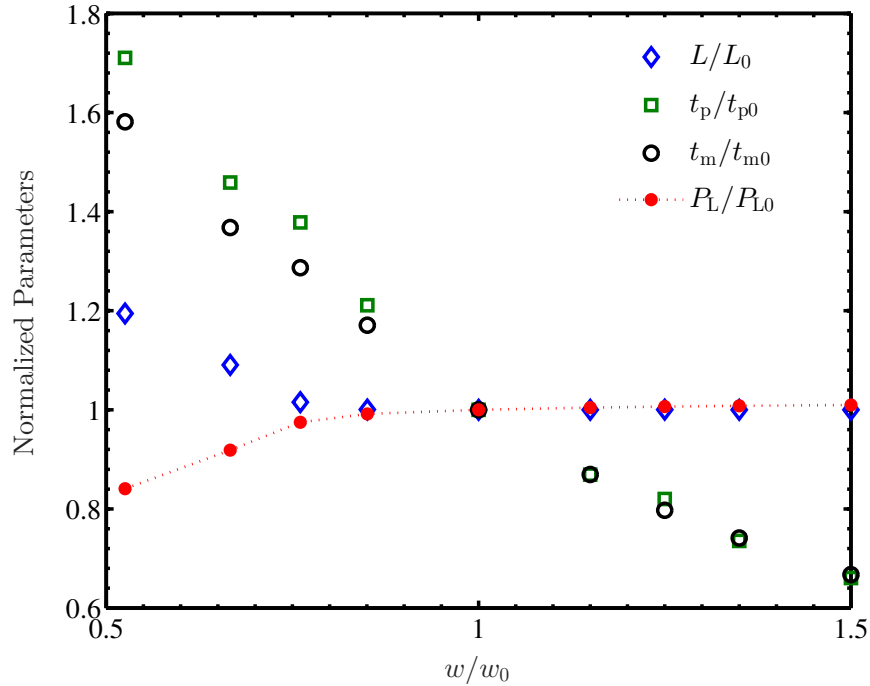


Figure 5.5. An analysis of sensitivity of the output power to the transducer width.

no longer at the 100-kHz corner but at $f_1 = 21.34$ kHz. We note that t_p and t_m are somewhat in the same range of those in **Case V**. Meanwhile, the width is substantially decreased to keep the total volume unchanged, which reduces both Γ_m and M_1 in terms of the geometry parameters. However, as Metglas possess a high piezomagnetic coefficient and a low compliance, Γ_m still reaches a high level ($\Gamma_m \propto (d_{33,m}/s_{33}^H)$), as does the transferred power. When both volume and thickness constraints are imposed (**Case VIII**), the composite length is enlarged with the increase of the magnetostrictive thickness. As the result, there is a considerable reduction in the width as well as the output power. The optimized solution is as follows: $L = 198.72$ mm, $w = 0.10$ mm, $t_p = 27.30$ μm , $t_m = 36.36$ μm , and $P_L = 227$ μW . The geometries determined in **Cases VII** and **VIII** are not applicable in practice, but these considerations provide meaningful perspectives that have not been revealed in previous studies (i.e., **Cases I–VI**). With the constraints of the volume, thickness and maximum applied field, Galfenol is preferable to Metglas.

Due to the similarity of the IEEE and ICNIRP standards, imposing the latter regulations does not alter the nature of the optimization problem. Taking **Case VI** with the ICNIRP criteria as an example (now denoted as **Case IX**), the optimal geometry is kept nearly

identical, as would be expected. However, since the field amplitude in this case is limited at a lower level, the output power is much less than that of **Case VI**. All the optimization results are summarized in Table 5.2.

It is worth emphasizing that the solutions presented in Figure 5.5 and Table 5.2 collide with the optimization trend predicted by theory in Section 5.3.4. There exists an optimal ratio between t_m and t_p , which is set by the properties of materials in use. In particular, this ratio is about 3.2, 4.1 and 1.3 for Gal/PZT, Gal/PMN-PT and Met/PMN-PT, respectively.

5.5 Future Work

Although the developed two-port model was successfully validated with the use of the material properties listed in Table 5.1, these constants may be subject to change when the dimensions of the ME laminate scale down to sub-mm or μm range, due to possible degradation of the materials. This potentially decreases either or both electrodynamic and electromechanical transduction factors. Furthermore, as the relative thickness between the magnetostrictive or piezoelectric layer and the bonding layer becomes smaller, the interface coupling may reduce, leading to an increase in the total mechanical loss (or equivalently, the mechanical damping coefficient). The combination of these effects could result in a significant drop in the output power, compared to those obtained by the optimization algorithm.

Table 5.2. Optimization results. Notations: Std. – Standard, Cstr. – Constraint, Gal – Galfenol, Met – Metglas. Constraints: (i) $Lw(t_p + 2t_m) \leq V_0$, and (ii) $(t_p + 2t_m) \geq 100 \mu\text{m}$.

Case	Std.	Materials	Cstr.	L , mm	w , mm	t_p , μm	t_m , μm	P_L , μW
I	No	Gal/PZT	(i)	132.5e-3	9.69e3	0.24	0.66	33.3e3
II	IEEE*	Gal/PZT	(i)	12.44	5.06	4.36	13.70	597
III	IEEE**	Gal/PZT	(i)	1.64e3	0.15	1.04	3.44	849
IV	IEEE***	Gal/PZT	(i)	–	–	–	–	–
V	IEEE*	Gal/PMN-PT	(i)	12.05	30.78	0.58	2.41	789
VI	IEEE*	Gal/PMN-PT	(i), (ii)	12.05	1.66	10.86	44.57	736
VII	IEEE*	Met/PMN-PT	(i)	84.79	1.70	3.88	5.01	2.76e3
VIII	IEEE*	Met/PMN-PT	(i), (ii)	198.72	0.10	27.30	36.36	227
IX	ICNIRP*	Gal/PMN-PT	(i), (ii)	12.04	1.64	11.45	44.98	175

* $f \in [3001, 10^6]$ Hz,

** $f \in [20, 3000]$ Hz,

*** $f \in [1, 19]$ Hz.

The following experimental plan is proposed as a means to validate future miniaturized devices once they are manufactured. The most important parameters of the circuit model are the mechanical impedance Z , the electrodynamic transduction factor Γ_m , the mechanical damping coefficient b , the electromechanical transduction factor Γ_p , and the nominal capacitance C_0 . In practice, the following approaches can be utilized to identify these parameters to complete the model.

First, C_0 can be found by a multimeter, and the output impedance Z_{out} can be measured as a function of the drive frequency (i.e., measured in a wide range of f or ω) by an impedance analyzer. The definition of Z_{out} is shown in Figure 5.6 and its expression is given by [7]

$$Z_{\text{out}} = \frac{jY(b + jX)}{b + j(X + Y)}, \quad (5.25)$$

$$X = \omega m - \frac{K_0}{\omega}, \quad (5.26)$$

$$Y = -\frac{\Gamma_p^2}{\omega C_0} \quad (5.27)$$

where jX is an mass-spring-equivalent approximation of Z . An example of the output impedance amplitude $|Z_{\text{out}}|$ is demonstrated in Figure 5.7. Based $|Z_{\text{out}}|$, the resonance and antiresonance frequencies (ω_0 and ω_1) and the squared electromechanical coupling factor $0 \leq k_p^2 = 1 - \omega_0^2/\omega_1^2 \leq 1$ can be approximately determined. In particular, ω_0 and ω_1 are the frequencies at which $|Z_{\text{out}}|$ attains its minimum and maximum, respectively.

The mechanical quality factor at the antiresonance frequency, Q_1 , can be extracted based on the free decay response of the open-circuit output, as presented in [8]. Due to the following relations,

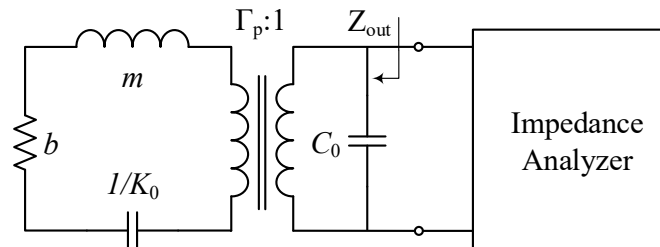


Figure 5.6. Schematic of impedance measurement.

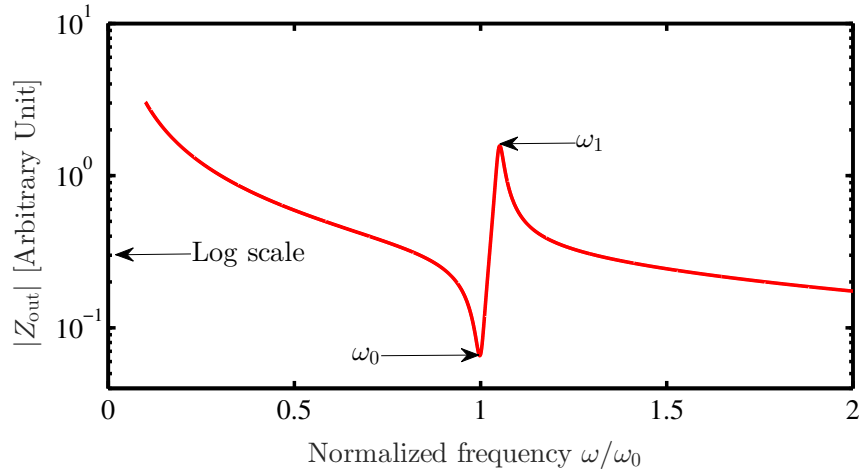


Figure 5.7. An example of the measured output impedance amplitude.

$$\omega_0 = \sqrt{\frac{K_0}{m}}, \quad (5.28)$$

$$\omega_1 = \sqrt{\frac{K_1}{m}}, \quad (5.29)$$

$$k_p^2 = \frac{\Delta K}{K_1} \quad (5.30)$$

where $\Delta K = \Gamma_p^2/C_0$ and $K_1 = \Delta K + K_0$, the mechanical damping coefficient, the equivalent mass, and the electromechanical transduction factor can be written in terms of the equivalent spring constant as

$$b = \frac{\omega_1 K_0}{Q_1 \omega_0^2}, \quad (5.31)$$

$$m = \frac{K_0}{\omega_0^2}, \quad (5.32)$$

$$\Gamma_p^2 = k_p^2 \omega_1^2 \frac{K_0}{\omega_0^2}. \quad (5.33)$$

If K_0 is known, then b , m and Γ_p are also identified. Substituting (5.31), (5.32), and (5.33) into (5.25), K_0 can be found by the least-squares optimization scheme

$$\min_{K_0 > 0} \sum_j^N [(|Z_{out}|_j^s)^2 - (|Z_{out}|_j^e)^2] \quad (5.34)$$

where $|Z_{out}|^s$ is the simulation results, $|Z_{out}|^e$ is the experimental data, and N is the number of experimental samples collected.

Finally, an effective value of the electrodynamic transduction factor Γ_m can be estimated from the measured amplitude of the open-circuit voltage, denoted as $|\widehat{V}_\infty|$, as follows [8]

$$\Gamma_m = |\widehat{V}_\infty| \frac{C_0 \omega_1 b}{H_0 \Gamma_p}. \quad (5.35)$$

where $|\widehat{V}_\infty|$ is measured at ω_1 . Up to this point, we have obtained a complete set of parameters that can be utilized to validate the model. Characteristics of the device that should be considered include frequency, load, and **B**-field responses.

The step-by-step procedure to identify the model parameters can be summarized as follows:

- Measure C_0 with a multimeter,
- Measure the frequency response of the output impedance,
- Determine ω_0 and ω_1 based on $|Z_{out}|$,
- Extract the mechanical quality factor Q_1 using free decay response,
- Determine K_0 by fitting simulations to measured values,
- Compute b , m and Γ_p from other coefficients,
- Measure the open-circuit voltage amplitude at ω_1 (i.e., $|\widehat{V}_\infty|$), and
- Estimate Γ_m from $|\widehat{V}_\infty|$.

In order to better comprehend the physical insights of the system performance at small sizes, a finite element analysis (FEA, also known as finite element method – FEM) is highly recommended. A few comparisons among four methods, (i) analytical model presented in Chapter 4, in which all parameters are derived as functions of material properties and transducer geometry, (ii) simplified model with key parameters identified from experiments (as presented in this Section), (iii) finite element simulations, and (iv) experimental data, could provide a further in-depth understanding and may fully explain the behavior of the system. Several examples are given as follows.

- Comparing the demagnetization effects in (i) and a corresponding study using (iii) could indicate whether the explicit relation between the effective magnetic field and the applied field in (5.19) is sufficiently accurate at small scale devices or not.
- The electrodynamic transduction factor Γ_m can be determined by FEM magnetostatic simulations. Adjusting $d_{33,m}$ (and/or s_{33}^H , depending on magnetostrictive material used) to fit the simulated result of Γ_m with that obtained in (ii) could show how much $d_{33,m}$ deviates from a theoretical prediction or values reported from other research in the literature.
- Similarly, the electromechanical transduction factor Γ_p can also be identified from a static piezoelectric analysis. A comparison between results from a FEM model and the empirical parameter identification in (ii) could show the possible deviation of $d_{31,p}$ (and/or s_{11}^E) from expected.
- FEA of stress transfer in composite could bring a more comprehensive understanding of the essential influences of the bonding layers to the interface coupling coefficient.
- Developing a complete FEM model for this multiphysics problem might require a more significant effort. However, it could help fulfill some factors that are neglected or underestimated in the analytical model; for instance, the physical mechanism of stress transfer between layers and how it affects the overall mechanical damping constant. Therefore, a full comparison between (iii) and (iv) is of great interest to investigate.

5.6 Conclusions

We have formulated an optimization problem to maximize the transferred power with respect to the shape of the ME laminated composite, subject to a volume constraint. In addition, the maximum permissible magnetic field strength is kept within the safety standards. We have revealed several important insights that can serve as a foundation to design an optimal ME WPTS. In a general principle, a ME transducer tends to be wide in order to enhance the electrodynamic transduction factor and electromechanical figure of merit. However, more interestingly, there exist local optima that satisfy possible practical

limitations (such as the minimum total thickness) while being close to the global optimum. We have also emphasized the effects of the magnetostrictive and piezoelectric material properties on the trend of the optimization parameters. The optimization model presented in this chapter can be utilized as a framework to further investigate the optimal solution with different sets of constraints and/or constitutive materials used.

From the obtained results, we realize that three primary factors drive high output power are as follows: (i) applied field strength; (ii) geometry that results in high Γ_m , which is somewhat equivalent to increasing the laminate width; and (iii) high $d_{33,m}$ and high stiffness (i.e., low s_{33}^H). The optimization chooses the 100 kHz corner as that gives high B-field and high Γ_m . Regarding (iii), Metglas would be preferable since it possesses better material constants than Galfenol. However, Metglas also has a larger permeability which amplifies the effect of the demagnetizing field. Therefore, if we constrain the geometry to not be very long and thin, the higher permeability of Metglas yields lower internal \mathbf{H} -field and thus Galfenol becomes more attractive.

5.7 References

- [1] A. Erturk and D. J. Inman, *Piezoelectric Energy Harvesting*, John Wiley & Sons Ltd., New York, 2011.
- [2] R. I. Joseph and E. Schlömann, "Demagnetizing field in nonellipsoidal bodies," *J. Appl. Phys.*, vol. 36, no. 5, pp. 1579–1593, 1965.
- [3] G. Liu, C. Zhang, W. Chen, and S. Dong, "Eddy-current effect on resonant magneto-electric coupling in magnetostrictive-piezoelectric laminated composites," *J. Appl. Phys.*, vol. 114, no. 2, pp. 027010, 2013.
- [4] IEEE, "IEEE standard for safety levels with respect to human exposure to electromagnetic fields, 0-3 kHz," *IEEE Std C95.6-2002*, pp. 1–0, Oct 2002.
- [5] IEEE, "IEEE standard for safety levels with respect to human exposure to radio frequency electromagnetic fields, 3 kHz to 300 GHz," *IEEE Std C95.1-2005 (Revision of IEEE Std C95.1-1991)*, pp. 1–238, April 2006.
- [6] International Commission on Non-Ionizing Radiation Protection., "Guidelines for limiting exposure to time-varying electric, magnetic, and electromagnetic fields (up to 300 GHz).," *Health Phys.*, vol. 75, Oct 1998.
- [7] B. D. Truong, S. Williams, and S. Roundy, "Experimentally validated model and analytical investigations on power optimization for piezoelectric-based wireless power transfer systems," *J. Intell. Mater. Syst. Struct.*, vol. 30, no. 16, pp. 2464–2477, 2019.

- [8] B. D. Truong and S. Roundy, "Experimentally validated model and power optimization of a magnetoelectric wireless power transfer system in free-free configuration," *Smart Mater. Struct.*, vol. 29, no. 8, pp. 085053, Jul 2020.

CHAPTER 6

APPROACHES TO SELF-BIASED MAGNETOELECTRIC TRANSDUCERS

This chapter is devoted to providing a short review on appropriate methods to eliminate the need for an external DC field bias.

6.1 Introduction

A magnetostrictive material usually requires a DC magnetic field bias while operating as a driven phase in a magnetoelectric (ME) laminated composite. It is primarily due to the dependence of the piezomagnetic coefficient ($d_{33,m}$) on the magnetostriction (λ) produced in the material by the bias field (H_b), $d_{33,m} = d\lambda/dH_b$ [1]. An external bias field is typically provided by using permanent magnets or a DC magnetic coil, which results in large device size, possible electromagnetic interference, and noise source.

Device miniaturization is one of the critical issues in realizing an implanted system. Therefore, developing an alternative method that exhibits strong ME effects in the absence of a DC magnetic field (here referred to as self-biased ME coupling) is essential. The first self-biased ME phenomenon was discovered in $\text{La}_{0.7}\text{Sr}_{0.3}\text{MnO}_3$ (LSMO)/PZT composites by Srinivasan *et al.* in 2001 [2], which is due to a large remanence in the LSMO layer at $H_b = 0$. However, this finding did not capture much attention of researchers until nearly a decade later, when the field of multiferroics and magnetoelectrics started shifting its focus from fundamental material discoveries to translational research. In 2010, Mandal *et al.* demonstrated a non-zero ME output voltage without a DC bias field in a graded ferrite/PZT laminate, in which internal magnetic fields were created by compositional gradients [3]. Since then, many efforts have been devoted to studying material replacements of the magnetostrictive phase in order to further enhance the ME coefficient [4].

In addition to the functionally graded approach, other researchers also developed dif-

ferent techniques to realize zero-biased ME coupling [5, 6, 7, 8, 9], which is expected to make further application-oriented breakthroughs over the next few years [10]. In this light, this chapter aims to present an overview of self-biased ME mechanisms in the literature and propose possible pathways forward for ME-based wireless power transfer systems (WPTSs), with a focus on potential use in biomedical applications. A more detailed and in-depth review of self-biased ME composites can be found in [11].

It is essential to note that the ME coefficient α_{ME} , defined by the rate of change of the induced electric field with respect to the applied magnetic field, is not the most appropriate criterion to evaluate the performance of a ME WPTS. Instead, separately evaluating the role of each phase, magnetostrictive and piezoelectric, is a more comprehensive view. In particular, the electrodynamic transduction factor (Γ_{m}) defines the physical bound of the power that can be transferred to the load, and the figures of merits ($M_{0/1}$) indicates whether the device is able to reach that limit or not [12]. Therefore, Γ_{m} and $M_{0/1}$ are more suitable criteria. However, α_{ME} could still be utilized as a preliminary examination to estimate how strong the self-biased ME coupling is.

6.2 Self-Biased Magnetolectric Composites

6.2.1 Magnetostriction hysteresis (MH)

The self-biased ME property can be accomplished in a two-phase system that consists of homogeneous ferromagnetic and piezoelectric materials [5]. Common ferromagnetic materials used in these configurations include, among others, Ni, FeNi, SmFe₂, and Fe-CoSiB. Figure 6.1 shows an example where a Ni-MFC (Macro Fiber Composite) bilayer exhibits a large response of $1.25 \text{ Vcm}^{-1}\text{Oe}^{-1}$ at an off-resonance low frequency of 1 kHz with $H_{\text{b}} = 0$. The mechanism behind this effect is related to the natural existence of ferromagnetic hysteresis, which results in a non-zero magnetostriction and piezomagnetic coefficient at zero-field bias. However, this method could pose significant challenges to the synthesis procedure of some structures such as FeCoSiB-AlN and Cobalt ferrite/PZT, due to the residual stress created during the film growth process. This issue is discussed in more detail in the next section.

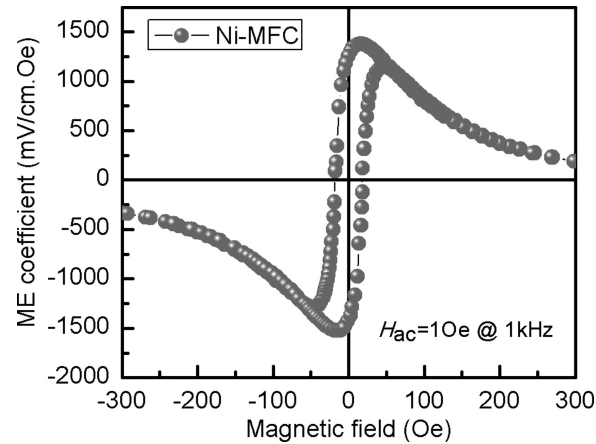


Figure 6.1. ME coefficient of Ni-MFC laminate as a function of DC bias field [5].

6.2.2 Built-in stress (BT)

For many cofired ME composites and thin-film heterostructures, the self-biased phenomenon is not only attributed to the magnetostriction hysteresis but also the built-in stress at the interface of the piezoelectric and magnetostrictive phases. These residual stresses typically result from the thermal treating process. Direct bonding techniques such as the cofiring and thin-film deposition greatly improve the mechanical coupling between the two constituent materials. Furthermore, the electrodynamic transduction factor is remarkably enhanced under a certain level of mechanical preloading [13]. However, the development of this research direction has been slow. Several obstacles can be mentioned as follows: (i) Cosintering two distinct phases through high-temperature thermal cycling are challenging due to the large difference in shrinkage rates and mismatch in thermal expansion. (ii) The residual strain needs to be well controlled and optimized; otherwise, it could trigger adverse effects and weaken the interface coupling.

6.2.3 Nonlinear magnetoelectric effect (NME)

The self-biased behavior of a ME transducer can be realized based on the nonlinear properties of some specific magnetostrictive materials in response to a bipolar AC magnetic excitation. Under this circumstance, the magnetostriction λ is non-zero even in the absence of the DC bias field. In particular, λ is dependent on (and can be expressed as a function of) the amplitude, fundamental frequency, and high-order harmonics of the AC applied magnetic field. Such a phenomenon was revealed for the first time by

Wang *et al.* in 2013 [6], as shown in Figure 6.2. A laminate composed of Metglas foils, Mn-doped PMN-PT crystal fibers and a pair of interdigitated electrodes was utilized for the investigation, which showed a maximum open-circuit output voltage of ~ 20 V at the resonance with an input field strength of 0.9 mT. However, the insight of how and why this nonlinear behavior occurs has not been addressed.

As an additional observation, Metglas may be the most common material that is widely used as a magnetostrictive phase to explore possible nonlinearities in ME systems [7]. However, since Metglas has a high permeability (over 45×10^3), the effective applied magnetic field, which is of interest, could be significantly reduced due to the influence of the demagnetizing field.

6.2.4 Exchange bias (EB)

Exchange bias (also known as exchange anisotropy) occurs due to the exchange interaction between the antiferromagnetic and ferromagnetic materials at their interface. The exchange bias phenomenon is characterized by a horizontal shift of the magnetization-magnetic field ($M - H$) hysteresis loop along the magnetic field (H) axis. A certain amount of this field shift is referred to as the exchange bias field. The shift of the magnetization (M) arising from exchange bias anisotropy coupling yields a corresponding shift in magnetostriction of the magnetostrictive phase. As a consequence, it is possible to achieve a

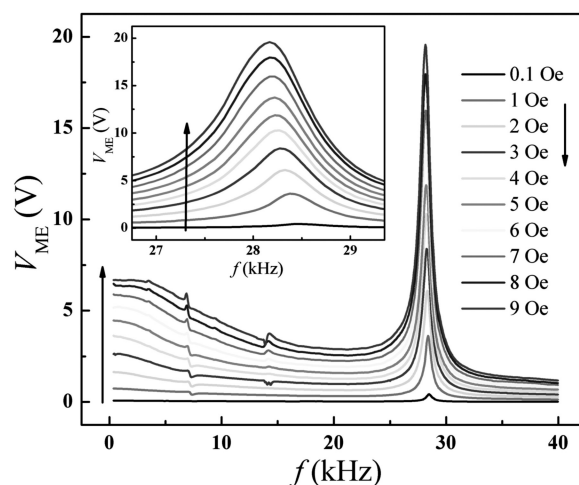


Figure 6.2. Open-circuit output voltage of a Metglas/PMN-PT heterostructure as a function of frequency under various amplitudes of the external bipolar AC magnetic field without the DC bias field [6].

non-zero piezomagnetic coefficient at the zero-bias field and hence the self-biased effects take place. Based on the exchange bias coupling, Lage and Meyners *et al.* developed a self-biased ME nanostructured composite, in which a multilayer laminate with the sequence of nonmagnetic-antiferromagnetic-ferromagnetic was utilized as the magnetostrictive phase and AlN was selected as the piezoelectric component [8]. This configuration exhibits a maximum magnetoelectric coefficient of $96 \text{ Vcm}^{-1}\text{Oe}^{-1}$ at the resonance frequency of 1.2 kHz, as shown in Figure 6.3. Such a self-biased ME structure could be promising for microscale devices. However, synthesizing a system with a complex multilayer stacked design, along with the need for field cooling and control of both film thickness and exchange bias inclination angle, is very challenging.

In order to reduce the fabrication process complexity and production cost, Li *et al.* proposed an alternative method with the use of a soft-hard biphasic ferromagnetic structure as a magnetostrictive phase [9]. A laminated composite consisted of annealed Metglas, Metglas and PZT was constructed for the study, demonstrating a giant ME coefficient of $12 \text{ Vcm}^{-1}\text{Oe}^{-1}$ at a low frequency of 1 kHz and $380 \text{ Vcm}^{-1}\text{Oe}^{-1}$ at the resonance frequency of 33.7 kHz, as shown in Figure 6.4. Amorphous Metglas foil is a homogeneous soft ferromagnetic material, which usually shows a symmetrical slim $M - H$ hysteresis loop with a quadratic behavior of λ with respect to H_b . However, after annealing under high

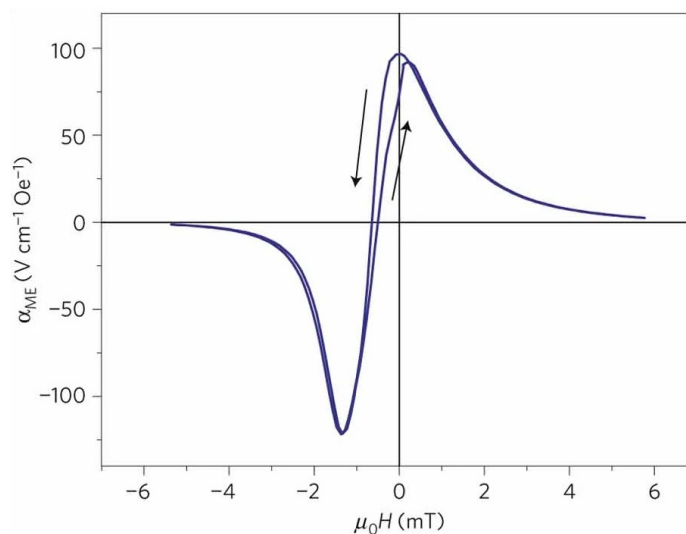


Figure 6.3. ME coefficient of a FeCoSiB-based transducer at zero bias field at resonance frequency [8].

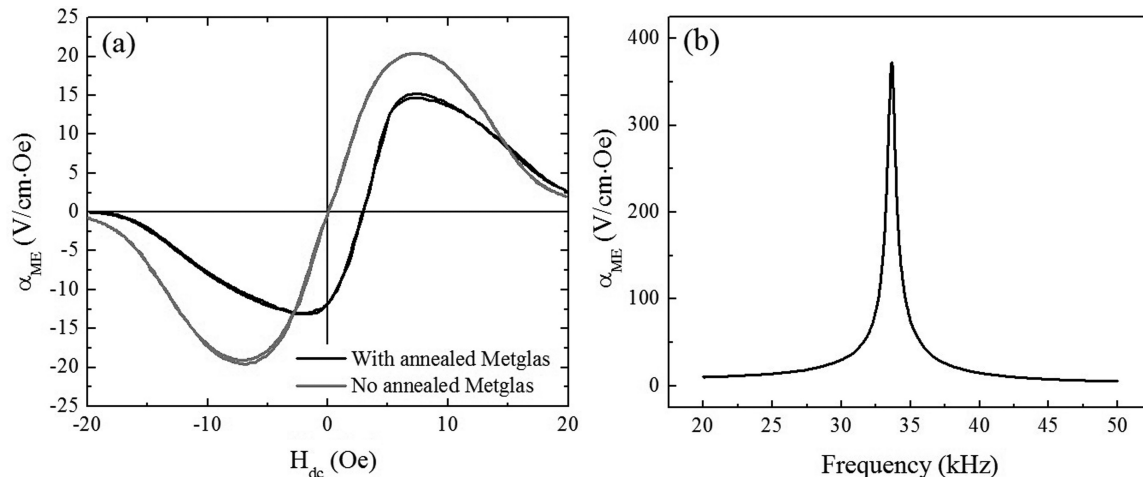


Figure 6.4. Performance of the ME composite. (a) ME coefficient as a function of DC bias field, measured at a frequency of 1 kHz, and (b) Frequency response of the ME coefficient at zero bias field [9].

temperature and premagnetizing, the annealed Metglas layers exhibit hard magnetic properties, and a unidirectional magnetization anisotropy is formed. The interaction between the soft and hard ferromagnetic materials creates a shift in the $M - H$ loop and leads to the appearance of the exchange bias phenomenon.

6.2.5 Functionally graded ferromagnetic effect (FGFE)

The concept of a magnetization-graded structure was first introduced by Mantese *et al.* in 2005 [14]. In this study, a magnetization graded sample of nickel-zinc ferrite was synthesized by creating a linear variation in the zinc concentration along the length of the sample. This technique resulted in a gradual change in magnetization in the longitudinal direction, and a small “built-in” internal magnetic field aligned with the magnetization-gradient was observed. With this finding as a foundation, in 2011, Mandal *et al.* revealed that the self-biased ME coupling could be achieved by using a ferromagnetic biphasic with stepped saturation magnetization [4]. An asymmetric configuration consisting of Ni and Metglas as magnetostrictive phase and PZT as piezoelectric material was investigated. Since Ni and Metglas have negative and positive magnetostriction, respectively, a transverse internal magnetic field is generated due to magnetization grading at the interface of Ni and Metglas layers. The interaction between this out-of-plane field and the applied

in-plane AC magnetic field produces a torque acting on the laminate. The kinetic energy of the bending vibration is converted to electrical form through the piezoelectric effects. A maximum ME coefficient of $46 \text{ Vcm}^{-1}\text{Oe}^{-1}$ was achieved at the resonance frequency of about 170 Hz. These interesting results inspired further study on functionally graded ME composites, based on the stepped magnetization.

Later investigations indicated that using a symmetric architecture could enhance the self-biased ME coefficient. A composite with the composition of $(\text{FeCuNbSiB})_n\text{-Ni/PZT/Ni-(FeCuNbSiB)}_n$ demonstrated a giant zero-biased ME coefficient of $89.2 \text{ Vcm}^{-1}\text{Oe}^{-1}$, as shown in Figure 6.5 [15]. Here, $n = 4$ is the number of layers of FeCuNbSiB ribbon. Both coefficients were measured at the longitudinal resonance frequency of 193.3 kHz. Besides Ni and FeCuNbSiB, other magnetostrictive materials could be considered such as (i) Samfenol, NiFe_2O_4 (NFO), and $\text{Ni}_{0.7}\text{Zn}_{0.3}\text{Fe}_2\text{O}_4$ (NZFO) as negative-magnetization phase, and (ii) Metglas, Ni-Fe alloy, Permendur, Terfenol-D, and Fe-Co alloy as positive-magnetization phase.

6.3 Proposals

Based on the analysis presented in the previous section and summarized in Table 6.1, magnetization-graded composites are perhaps the most promising solutions for use as a small-scale receiver of a ME WPTS. As the first sign, this configuration is capable of

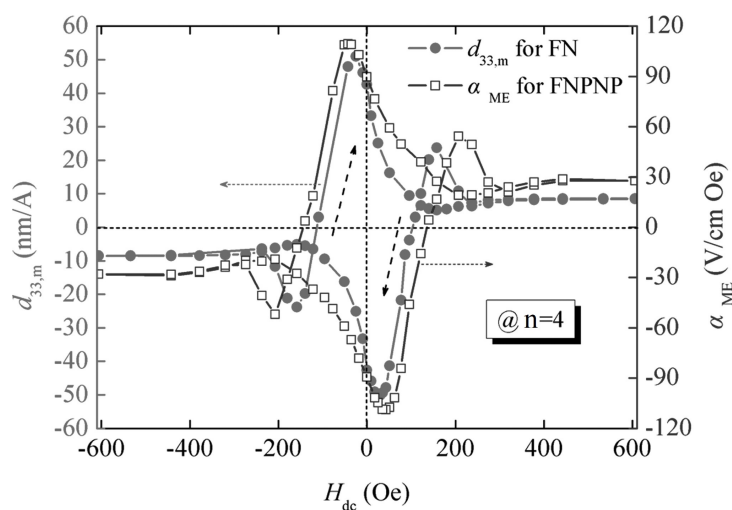


Figure 6.5. Piezomagnetic and ME coefficient as a function of DC bias field with four FeCuNbSiB layers. [15].

Table 6.1. A summary of self-biased ME techniques. Notation: Met = Metglas, A-Met = Annealed Metglas and FCNSB = FeCuNbSiB.

Mechanism	Material	Synthesis	$\alpha_{ME}, \text{Vcm}^{-1}\text{Oe}^{-1}$	Frequency
MH	Ni/MFC [5]	Epoxy	1.25	1 kHz
BS	LSMO/PZT [2]	Co-fire	16×10^{-3}	100 Hz
NME	Met/PMN-PT [6]	Epoxy	115, V Oe^{-1}	27 kHz
EB	FeCoSiB/AlN [8]	Magnetron-sputtered	96	1.2 kHz
EB	A-Met/Met/PZT [9]	Epoxy	380	33.7 kHz
FGFE	Met/Ni/PZT [4]	Epoxy	46	170 Hz
FGFE	FCNSB/Ni/PZT [15]	Epoxy	89	193.3 kHz

yielding a similar or higher ME coefficient, compared to other mechanisms. Secondly, with many negative- and positive-magnetization materials available, this approach offers more options in choosing suitable composition. It also should be noted that, as indicated in Chapter 5, Metglas may not be preferable to use as a driving layer of the magnetostrictive phase when the volume of a ME composite is constrained in the range of a few mm^3 (due to the demagnetization effects).

The mechanism behind the low-frequency bending-mode operation of the asymmetric structure was described fairly clearly in [4]. However, the developed model is not able to fully explain the observations presented in [15], in which the ME composite is symmetric and the longitudinal vibration is dominant. Therefore, seeking for an alternative theory to accurately capture the role of the transverse built-in magnetic field in the latter case is of great interest.

In order to establish the graded magnetization, it is required to create permanent magnetostriction in the two ferromagnetic layers. The most common approach for that purpose is to anneal the magnetostrictive phase for a specific amount of time under a certain level of DC magnetic field and temperature. The annealing procedure needs to be optimized depending upon the intrinsic magnetic properties of the materials in use.

The following steps are proposed to achieve the above goals.

- Similar to [15], Ni and FeCuNbSiB are chosen for the magnetostrictive phase. Ni serves as the driving material to capture the magnetic energy and transfer it to mechanical vibration. Meanwhile, FeCuNbSiB plays as a means to generate an internal field at the material interface. A particular laminate geometry is designed to minimize the effects of the demagnetization and eddy currents.

- Consider an appropriate annealing process with the DC magnetic field to premagnetize Ni/FeCuNbSiB.
- Fabricate and characterize a sub-cm size prototype as a concept device and evaluate the feasibility of the method.
- Develop a theoretical model to study the insight of the built-in internal magnetic field (which is parallel with the thickness direction), and examine its effects on the operation of the ME WPTS .
- Extend and adapt the optimization problem in Chapter 5 to design a microscale device and investigate the performance of a complete system that includes both transmitter and receiver sides.

6.4 References

- [1] X. J. Zheng and L. Sun, "A nonlinear constitutive model of magneto-thermo-mechanical coupling for giant magnetostrictive materials," *J. Appl. Phys.*, vol. 100, no. 6, pp. 063906, 2006.
- [2] G. Srinivasan, E. T. Rasmussen, B. J. Levin, and R. Hayes, "Magnetolectric effects in bilayers and multilayers of magnetostrictive and piezoelectric perovskite oxides," *Phys. Rev. B*, vol. 65, pp. 134402, Mar 2002.
- [3] S. K. Mandal, G. Sreenivasulu, V. M. Petrov, and G. Srinivasan, "Flexural deformation in a compositionally stepped ferrite and magnetolectric effects in a composite with piezoelectrics," *Appl. Phys. Lett.*, vol. 96, no. 19, pp. 192502, 2010.
- [4] S. K. Mandal, G. Sreenivasulu, V. M. Petrov, and G. Srinivasan, "Magnetization-graded multiferroic composite and magnetolectric effects at zero bias," *Phys. Rev. B*, vol. 84, pp. 014432, Jul 2011.
- [5] Y. Zhou, S. C. Yang, D. J. Apo, D. Maurya, and S. Priya, "Tunable self-biased magnetolectric response in homogenous laminates," *Appl. Phys. Lett.*, vol. 101, no. 23, pp. 232905, 2012.
- [6] Y. Wang, Y. Shen, J. Gao, M. Li, J. Li, and D. Viehland, "Nonlinear magnetolectric response of a metglas/piezofiber laminate to a high-frequency bipolar ac magnetic field," *Appl. Phys. Lett.*, vol. 102, no. 10, pp. 102905, 2013.
- [7] Y. Shen, J. Gao, Y. Wang, J. Li, and D. Viehland, "High non-linear magnetolectric coefficient in metglas/pmnm-pt laminate composites under zero direct current magnetic bias," *J. Appl. Phys.*, vol. 115, no. 9, pp. 094102, 2014.
- [8] E. Lage *et al.*, "Exchange biasing of magnetolectric composites," *Nat. Mater.*, vol. 11, April 2012.

- [9] M. Li, Z. Wang, Y. Wang, J. Li, and D. Viehland, "Giant magnetoelectric effect in self-biased laminates under zero magnetic field," *Appl. Phys. Lett.*, vol. 102, no. 8, pp. 082404, 2013.
- [10] R. Spaldin and N. A. Ramesh, "Advances in magnetoelectric multiferroics," *Nat. Mater.*, vol. 18, Mar 2019.
- [11] Y. Zhou, D. Maurya, Y. Yan, G. Srinivasan, E. Quandt, and S. Priya, "Self-biased magnetoelectric composites: An overview and future perspectives," *Energy Harv. Syst.*, vol. 3, no. 1, pp. 1 – 42, 01 Jan 2016.
- [12] B. D. Truong and S. Roundy, "Experimentally validated model and power optimization of a magnetoelectric wireless power transfer system in free-free configuration," *Smart Mater. Struct.*, vol. 29, no. 8, pp. 085053, Jul 2020.
- [13] S. Dong, J. Zhai, J. Li, D. Viehland, and E. Summers, "Strong magnetoelectric charge coupling in stress-biased multilayer-piezoelectric/magnetostrictive composites," *J. Appl. Phys.*, vol. 101, no. 12, pp. 124102, 2007.
- [14] J. V. Mantese, A. L. Micheli, N. W. Schubring, R. W. Hayes, G. Srinivasan, and S. P. Alpay, "Magnetization-graded ferromagnets: The magnetic analogs of semiconductor junction elements," *Appl. Phys. Lett.*, vol. 87, no. 8, pp. 082503, 2005.
- [15] C. Lu *et al.*, "Dynamic magnetostrictive properties of magnetization-graded ferromagnetic material and application in magnetoelectric composite," *J. Appl. Phys.*, vol. 115, no. 17, 2014.

CHAPTER 7

CONCLUSIONS

Dynamics and performance of three different techniques for wireless power transfer (WPT) technology with a focus on potential application to biomedical wearable and implantable devices are reported in this dissertation. We have developed equivalent circuit models for resonant inductive coupling, magneto-mechano-electric and magnetoelectric systems, in which the power transferred to a load resistance is the central objective of the investigation, rather than the transmission efficiency. Power optimization principles are investigated and rigorously validated with experimental data.

The dissertation starts with an analysis of the dynamics of a two-coil resonant inductive coupling (RIC) wireless power transfer system (WPTS) configured in series-series topology. In practice, there are circumstances where the parasitic capacitance of a coil cannot be neglected, resulting in the appearance of both resonance and antiresonance frequencies at the transmitter and receiver sides. This observation leads to an investigation of the optimal choice of the drive frequency to maximize the power delivered to a given load resistance. It is important to note that the resonance and antiresonance operation only occurs when the coil parasitic capacitance is present and is dominant at low-coupling regimes. Meanwhile, the frequency splitting phenomenon takes place at high coupling regardless of with or without the parasitic capacitance. In the latter case, the parasitic capacitance could cause an asymmetric property of the frequency splitting behavior. A numerical method is proposed to determine the coil parameters based on its measured impedance. We have also developed an analytical system model and formulated the closed-form solution of the output power. The experimental validations of these essential findings are carried out.

Although the RIC system seems to be a suitable candidate for powering biomedical implantable devices, the potential application of this technology could be limited when sub-

ject to safety standards due to its high-frequency operation (typically in the range of a few MHz to GHz). We have been seeking alternative approaches that are able to avoid these issues, and low-frequency architectures such as electromechanical- and electrodynamic-based systems become promising. However, an obstacle to evaluating and optimizing the performance of those mechanisms is that the system model of each device type has not been fully established in the literature. Therefore, we have developed and experimentally validated an equivalent circuit model of a magneto-mechano-electric (MME) WPTS utilizing a piezoelectric transducer and a permanent magnet as a receiver. Essential model parameters are expressed as functions of geometry and material properties only. We have demonstrated a power density of $152 \mu\text{W}/\text{cm}^3$ at an applied magnetic flux density of $300 \mu\text{T}$, which is typical with the use of piezoelectric technologies and is comparable to that of far-field WPT systems.

In the same manner, we have further extended the MME model for a symmetric structure where the piezoelectric beam is clamped at its center and the magnets are placed at the two ends. Although the prototype is implemented for the purpose of proof-of-concept, in which both the transmitter and receiver geometry have not been optimized yet, the measured results show that the MME transducer is still able to generate $4.93 \mu\text{W}$ with an input of $129 \mu\text{T}$ at a resonance frequency of 259.8 Hz . Moreover, according to the IEEE standards, the maximum permissible field at this frequency is 2.71 mT . With the same operating frequency and a magnetic field strength of 2.71 mT , the corresponding output power is 2.18 mW , which is sufficient to supply most of the body wireless-sensors. In order to examine the transmission efficiency, we have constructed and validated a complete system model that takes into account the dynamics of both transmitting and receiving sides. It is a unified model that can be applied to different types of receiver transducer such as MME, electrodynamic (i.e., electromagnetic resonator with magnet tip mass) and magnetoelectric (ME). With the use of a MME generator, an efficiency of $2.5 \times 10^{-3} \%$ is obtained.

As the efficiency of the MME configuration is extremely low due to weak coupling between the magnetic and mechanical domains, it is essential to find another architecture that balances the two following requirements: (i) operate at a reasonable low-frequency range to allow applying high magnetic field strength, and (ii) exhibit a higher coupling

between the magnetic and mechanical domains to increase the maximum power that can be transferred to the load. A WPTS utilizing the ME effects possesses such potential. To justify this hypothesis, we have investigated a comprehensive mathematical modeling framework and analytical solutions to the power optimization problem for a ME device and validated the findings by experiments. In addition, an efficiency of 0.12 % is attained at an antiresonance frequency of 70.47 kHz, which is comparable to an acoustic and RF energy transmission systems, or even a RIC device with mm-size. We have emphasized the essential role of the electrodynamic transduction factor on the performance of the ME WPTS and proposed alternative criteria to evaluate its performance instead of using the ME coefficient which has been introduced in the literature from a material point of view.

Accounting for practical considerations, we have further explored the variations of the maximum power delivered to the load under uncertainties in ME receiver position and orientation, as well as the effects of the field nonuniformity. As expected, the output power is more sensitive to the change of the orthogonal distance from the ME laminate origin to the coil plane than to the variation of the alignment in parallel with the coil diameter. We have also found that the generated power is proportional to the squared cosine of the orientation angle. Furthermore, for small-scale ME transducers, the field uniformity is not essentially required. For the particular experimental system being studied, the maximum transferred power of 4.91 mW is obtained at a distance of 30 mm between the centers of the coil and the ME receiver. The corresponding magnetic flux density in this case is 225.8 μT . As the distance increases to 60 mm, the generated power drops to 1.97 mW due to the decrease of the field strength. Subject to the IEEE safety standards, the largest allowable field amplitude that can be applied to the human body at 70.47 kHz is 205 μT ; correspondingly, the prototype under investigation is able to transfer up to 4.16 mW to a load resistance. This amount of power is sufficient to power most of the biosensors.

Based on the presented models, we have formulated an optimization problem that seeks for optimal geometry of the ME laminated composite to maximize the output power, subject to a total volume constraint of 2 mm³. The safety standards are simultaneously considered in the optimization formulation. In a general trend, the optimization results in a wide, short and extremely thin laminate. These characteristics could cause many complexities in the fabrication process. However, more interestingly, we have revealed

that this issue can be avoided by adding one more constraint on the total thickness of the resonator, while not compromising much the achieved power. In practice, the optimization framework can also be utilized for optimizing different material choices.